Fatigue analysis and design of arc-welded and laser-welded lap joints

Toe vs. root induced failure

S.T. Giesen

Fatigue analysis and design of arc-welded and laser-welded lap joints

Toe vs. root induced failure

by

S.T. Giesen

to obtain the degree of Master of Science
at the Delft University of Technology,
to be defended publicly on Wednsday September 20, 2023 at 13:00.

Student number: 5623405
Project duration: January 11, 2023 – September 20, 2023
Thesis committee: Dr. ir. J.H. den Besten,   TU Delft , chair
                        Ir. G. Bufalari,   TU Delft
                        Prof. dr. M. Veljkovic,   TU Delft
                        Prof. dr.-Ing. B. Hinrichsen,   Bremen University of applied sciences
Company Supervisor: Dipl.-Ing. P. Harpantides,   Abeking & Rasmussen SE

This thesis is confidential and cannot be made public until September 20, 2025.

An electronic version of this thesis is available at http://repository.tudelft.nl/.
Document number: MT.22/23.046.M

TUDelft

ABEKING & RASMUSSEN

Preface

Dear reader, within this document lies the culmination of my Master's study at the TU Delft, unveiling the research performed in the realm of fatigue focused on arc- and laser-welded lap joints. This endeavour has been a collaborative effort in partnership with Abeking & Rasmussen SE and the TU Delft, under the guidance of two supervisors: Henk den Besten, representing the academic facet, and Pantelis Harpantides, from the corporate sphere.

My affinity for ships has deep roots, stretching back to my young years, even though the sea is distant from my hometown. It's said that this connection blossomed during the annual summer holidays in the region of Zeeland, Netherlands. Following my undergraduate studies in shipbuilding in Bremen, my professional voyage continued at the structural department of Abeking & Rasmussen, igniting my interest in structural engineering. This connection between the Netherlands and the outstanding maritime Master's program at TU Delft eventually beckoned me. The course "Fatigue Strength of Marine Structures," given by Henk den Besten, opened a new fascinating topic.

Foremost, I extend my gratitude to Henk den Besten for the great support throughout this work. His incisive inquiries and challenges consistently drove me to explore beyond the surface, enriching my comprehension. I must also express appreciation to Abeking & Rasmussen, who have been reliable pillars throughout my academic journey. Within this organization, Pantelis Harpantides deserves special acknowledgement for making this research possible. The experiments gave me practical experience which I love. Hence, my gratitude extends to Photon AG for welding the specimens, with sincere thanks to Uriel Elliesen and Leo Pflugradt for their unwavering support. In addition, I extend my heartfelt thanks to Gabriele Bufalari, whose door was always open for my "casual" inquiries. Broder Hinrichsen's advice consistently reminded me of the real-world relevance my research needed to maintain within the engineering domain, a guidance I deeply cherish.

Lastly, I want to thank my family and friends who supported me while I was subjected to some mental fatigue - luckily it happened to be a run-out.

S.T. Giesen
Bremen, September 2023

Abstract

Fatigue might be the governing limit state in marine structures mainly induced by the waves and wind. Therefore, using a lap joint for the shell plating to replicate the appearance of a riveted joint for a retro yacht is critical due to the limited fatigue resistance. For this joint type cracks initiated at the root, which should always be avoided due to hard detectability, might appear. Arc- and laser-welded lap joints are researched to estimate fatigue resistance and reduce the risk of root failure.

The hot spot peak stress of weld toe and weld root notches is insufficient to reflect the fatigue strength, explaining why an effective notch stress parameter is used, able to deal with both weld toe and weld root notch induced fatigue. Semi-analytical weld notch stress formulations are established in order to avoid solid finite element modelling to capture the effective notch stress. Particular attention is paid to the lap joint characteristic extreme weld notch load carrying level. A second-order weld load carrying stress formulation is introduced. Since the (laser) weld is typically small in comparison to the plate thickness, a dedicated way of weld modelling is proposed, assuming a shell finite element type of formulation, allowing to capture the far field stress for both the weld toe and weld root notch accurately.

Fatigue tests are performed to obtain the laser-welded lap joint mid-cycle fatigue resistance information, including the material characteristic length as effective notch stress coefficient. Particular attention is paid to mean (residual) stress effects in comparison to the arc-welded joint equivalent to explain the fatigue performance.

Comparing the lap joint fatigue resistance in arc-welded and laser-welded configurations to the resistance of other joint types, the results turned out to be aligned. Investigating different material characteristic parameters, either an effective point or an effective line is used. A line based parameter shows a better performance. The main reason is that the actual notch stress gradient is explicitly considered. The mean (residual) stress seems to be larger for arc-welded joints. Furthermore, the mean (residual) stress correction seems at the same time to be one reason for toe induced- rather than expected root induced failure. For arc-welded joints, the change in failure location induced by stress level dependent secondary bending moments is another reason. The fatigue resistance parameter confidence for laser-weld weld joints is relatively low in comparison to the confidence for arc-welded ones, as a result of data size: respectively $\approx$190 and $\approx$3000.

When not considering the change in secondary bending moments in the fit of a $S_e - N$ curve, the overall fit parameters and quality do not change significantly for arc-welded lap joints. However, the influence on the effective stress range is substantial and changed the value on average by 4.7% and up to 14.7%.

Considering only the mid-cycle fatigue resistance, laser welding is superior to arc welding when exposed to low load and response ratios resulting from the lower residual stress level. The FAT class design curve of arc-welded joints for the hot spot structural stress concept with a load and response ratio of 0.5 can be used with a mean stress correction to estimate the fatigue resistance of laser welds.

Zusammenfassung

Dauerfestigkeit kann die maßgebliche Bemessungsgröße in maritimen Strukturen sein, die hauptsächlich durch Wellen und Wind verursacht wird. Daher ist die Verwendung einer Überlappungsverbindung für die Außenhaut, um das Aussehen einer Nietverbindung für eine Retro-Yacht nachzubilden, wegen der begrenzten Dauerfestigkeit kritisch. Bei dieser Verbindungsart können an der Wurzel beginnende Risse auftreten, die wegen der schweren Erkennbarkeit immer vermieden werden sollten. Lichtbogen- und lasergeschweißte Überlappungsverbindungen werden erforscht, um die Dauerfestigkeit abzuschätzen und das Risiko eines Wurzelversagens zu verringern.

Die Spitzenspannung von Schweißnaht- und Schweißwurzelkerben reicht nicht aus, um die Dauerfestigkeit widerzuspiegeln. Deshalb wird ein effektiver Kerbspannungsparameter benutzt, der sowohl die durch die Schweißnaht- als auch die Schweißwurzelkerbe induzierte Ermüdung berücksichtigt. Es werden halbanalytische Formulierungen für die Kerbspannungen aufgestellt, um ein Finite-Elemente Volumenmodell zur Erfassung der effektiven Kerbspannungen zu vermeiden. Besonderes Augenmerk wird auf die für Überlappungsverbindungen charakteristische, extreme Schweißnaht-Trag- fähigkeit gelegt. Hierfür wird eine Schweißnaht-Tragfähigkeitformulierung zweiter Ordnung eingeführt. Da die (Laser-)Schweißnaht im Vergleich zu den Plattendicken typischerweise klein ist, wird eine spezielle Art der Schweißnahtmodellierung vorgeschlagen, die von einer schalenförmigen Finite-Ele- mente-Formulierung ausgeht und es ermöglicht, die Strukturspannung sowohl für den Schweißnahtübergang als auch für die Schweißnahtwurzelkerbe genau zu erfassen.

Es werden Ermüdungstests durchgeführt, um Informationen über die Dauerfestigkeit der laser-geschweißten Überlappungsverbindung für mittlere Schwingzahlen zu erhalten, einschließlich der charakteristischen Materiallänge als effektiver Kerbspannungskoeffizient. Besonderes Augenmerk wird auf die Auswirkungen der Eigenspannungen im Vergleich zur lichtbogengeschweißten Verbindung gelegt, um die Dauerfestigkeit zu erklären.

Vergleicht man die Ermüdungsfestigkeit von Überlappungsverbindungen in lichtbogengeschweißten und lasergeschweißten Konfigurationen mit der Ermüdungsfestigkeit anderer Verbindungsarten, so zeigt sich, dass die Ergebnisse übereinstimmen. Es werden Parameter für die Materialeigenschaften untersucht, entweder mit einem effektiven Punkt oder einer effektiven Linie. Ein linienbasierter Parameter zeigt eine bessere Leistung. Der Hauptgrund ist, dass der tatsächliche Kerbspannungsgradient explizit berücksichtigt wird. Die mittlere Spannung (Eigenspannung) ist bei lichtbogengeschweißten Verbindungen größer. Die Korrektur der mittleren Spannung (Eigenspannung) ist gleichzeitig ein Grund für das Versagen am Nahtübergang und nicht das erwartete Versagen an der Wurzel. Bei lichtbogengeschweißten Verbindungen ist die Änderung des Versagensortes, die durch spannungsniveauabhängige sekundäre Biegemomente verursacht wird, ein weiterer Grund. Die Genauigkeit der Dauerfestigkeitsparameter für lasergeschweißte Schweißnähte ist im Vergleich zu lichtbogengeschweißten Schweißnähten relativ gering, was auf die Datengröße zurückzuführen ist: ca. 190 bzw. ca. 3000 Datenpunkte.

Wenn die spannungsabhängige Änderung der sekundären Biegemomente nicht berücksichtigt wird, verändern sich die Parameter und die Qualität der Anpassungskuve für lichtbogengeschweißte Überlappungsverbindungen nicht wesentlich. Der Einfluss auf die effektive Kerbspannung ist jedoch erheblich und verändert den Wert im Mittel um 4,7% und bis zu 14,7%.

Betrachtet man nur die Dauerfestigkeit für mittlere Schwingzahlen, so ist das Laserschweißen dem Lichtbogenschweißen bei niedrigen Lastverhältnissen aufgrund des geringeren Eigenspannungsniveaus überlegen. Die Bemessungskurve der FAT-Klasse von Lichtbogenschweißverbindungen für das Strukturspannungskonzept mit einem Lastverhältnis von 0,5 kann mit einer Mittelspannungskorrektur zur Abschätzung der Dauerfestigkeit von Laserschweißnähten verwendet werden.

Contents

List of Figures

List of Tables

Nomenclature

Abbreviations

AIC   Akaike information criterion

AENSC area method of the critical distance theories

A&R   Abeking & Rasmussen

BM   base material

CA   constant amplitude loading

CDF   cumulative probability density function

CDT   critical distance theories

ENSC   effective notch stress concept

FAT   fatigue class

FE   finite element

GMAW gas metal arc welding

GTAW   gas tungsten arc welding

HAZ   heat-affected zone

HCF   high cycle fatigue

HI   heat input

HSSSC hot spot structural stress concept

IIW   International Institute of Welding

LASER light amplification by stimulated emission of radiation

LBW   laser beam welding

LC   load carrying

LCF   low cycle fatigue

LENSC line method of critical distance theories

MCF   mid cycle fatigue

MLE   Maximum Likelihood Estimates

MSC   macroscopic stress concentration

msc   microscopic stress concentration

ND:YAG Neodymium-doped yttrium aluminium garnet

NLC   non load carrying

NSC   nominal stress concept

Latin Symbols

a^*	micro structural support point location
b^*	micro structural support radius
C	fatigue resistance constant
C_{bw}	weld load-carrying stress coefficient
C_{bw2}	2nd order weld load-carrying stress coefficient
D	Palmgren-Miner damage sum
d	average grain size
h_w	weld height
K_f	notch factor
K_t	theoretical stress concentration factor
L	material length parameter
l_w	weld length
m	fatigue resistance inverse slope
N	number of cycles until failure
N_i	allowable cycles per stress level
n_i	cycles at a certain stress level
pn	weld penetration
r	radial coordinate
r'	artificial radial coordinate
r_{lr}	remote mechanical load ratio
S	elastic stress range
S_n	nominal stress range
S_s	structural stress range
S_e	effective notch stress range
r_s	structural bending stress ratio
s	support factor for the fictitious notch radius
t_p	plate thickness
t_p'	artificial plate thickness
$T_{\sigma S}$	strength scatter index

Greek Symbols

α	notch angle
β	stress angle
χ_i	eigenvalue coefficient of asymptotic solution
χ_a, χ_s	first eigenvalue coefficient of (anti-)symmetry part
δK_{th}	fatigue crack propagation threshold
$\delta \sigma_0$	plain-specimen endurance limit
γ	load ratio coefficient
λ_i	eigenvalue (asymptotic solution)
λ_a, λ_s	first eigenvalue of (anti-)symmetry part
μ_i	stress component amplitude
μ_a, μ_s	stress amplitude of (anti-)symmetry part
ρ	notch radius
ρ_f	fictitious notch radius
ρ^*	micro structural support length
σ	Standard deviation
σ_b	bending contribution to the structural stress
σ_{bw}	weld load-carrying stress
σ_{eff}	Walker mean stress corrected stress
σ_f	far field stress distribution
σ_n	weld toe notch stress distribution
σ_N	Nominal stress
σ_{nr}	weld root notch stress distribution
σ_m	mean stress of the stress cycle
σ_{max}	maximum stress of the stress cycle
σ_{min}	minimum stress of the stress cycle
σ_{rr}	radial stress component (polar coordinate)
$\sigma_{r\theta}$	shear stress component (polar coordinate)
σ_s	structural stress at the toe
σ_{sr}	structural stress at the root
$\sigma_{\theta\theta}$	tangential stress component (polar coordinate)
φ	Airy stress function

1

Introduction

Marine structures sailing across the ocean are exposed to cyclic loading and response conditions, meaning fatigue can be a governing limit state. Stress concentrations, hot spots, typically appear at joints connecting the structural members, turn out to be the governing fatigue sensitive locations. Marine structures often serve at remote locations around the world. A failure could, therefore, lead to severe damage. Hence, avoiding fatigue damage is essential.

1.1. Motivation

A future yacht project at Abeking & Rasmussen (A&R) shall appear like a yacht built in the 1920s (fig. 1.1). At this time, joints connecting the ship's structural members were still riveted. However, this joining method is not feasible anymore because of the high production costs. To still achieve this particular look, the shell plating shall be lapped and welded (fig. 1.2). Nonetheless, lap joints are rarely used within the marine industry, partly as their fatigue strength is inferior to that of a generally used butt joint (Hobbacher et al., 2016). Laser welding does show a small weld geometry and a low heat input (HI), hence a minor distortion. This ensures a good appearance which is of particular importance for yachts. The fatigue resistance is influenced by laser welding (Remes et al., 2008). To still ensure a safe yacht, the fatigue resistance has to be known.
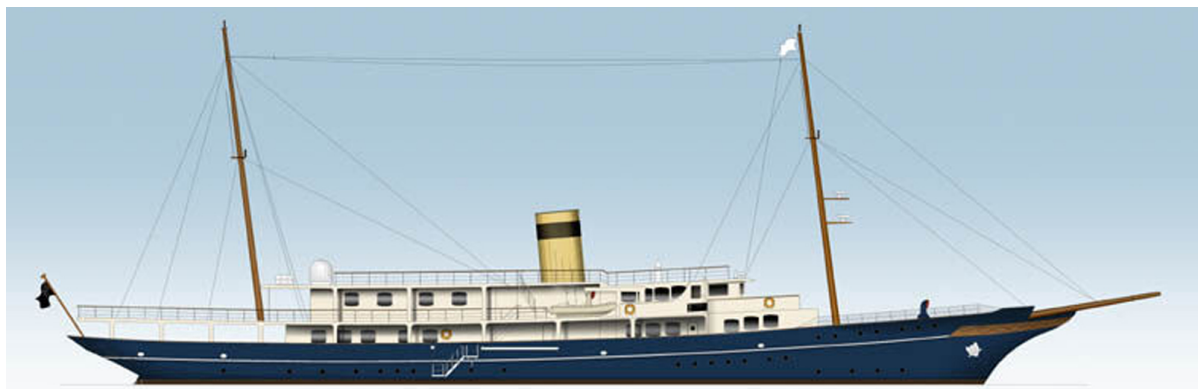
Figure 1.1: Profile view of possible future yacht project (Yacht Forums, 2022)

So far, the nominal stress concept (NSC) has been used at A&R. This concept poses significant limitations when assessing welds (Hobbacher et al., 2016). Firstly, this concept is not capable of predicting the failure location. Hence, the fatigue strength for a failure from the root and the toe must be assessed separately, where the lower fatigue strength is the governing one. For the given joint, the

fatigue strength for a root failure is only about 60% of that for a toe failure when arc welded (Hobbacher et al., 2016), possibly resulting in a highly conservative estimation.

Secondly, although the NSC was already used for the estimation of the fatigue strength of laser-welded, the needed geometric similarity between the specimen and designed joint makes it not applicable as no laser-welded lap joints were adapted for this concept yet (Fricke et al., 2015; Fricke and Robert, 2012).

Riveted Joint   Single lap joint DS (614)
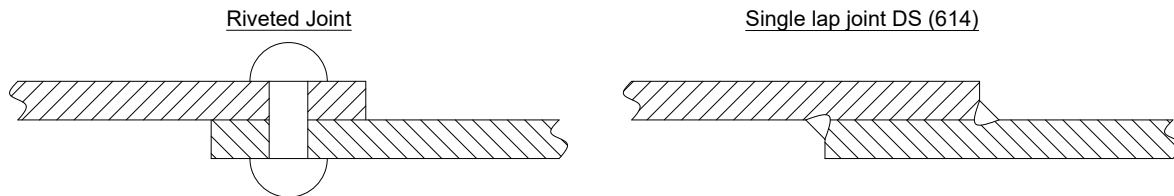
Figure 1.2: Proposed welded lap joint and riveted lap joint

Using laser-welding for a lap joint imposes the problem that no fatigue concept has been validated yet. Also, a more developed concept than the NSC should be chosen to predict the failure location and enhance fatigue performance. Therefore, the following problem statement is identified.

Problem Statement
No fatigue concept is validated to estimate the fatigue strength of laser-welded lap joints. Reliable fatigue strength and failure location estimation are required to ensure a safe structure.

1.2. Research goal
Validate a fatigue assessment concept for laser-welded lap joints. A fatigue damage criterion and the corresponding fatigue resistance curve must be established for common laser-welded joints in steel structures. Lap joint design guidelines will be provided to obtain weld toe-induced failure (WT) and prevent weld root-induced failure (WR).

1.3. Scope
The research is limited to **laser-welded lap joints** with **fillet welds** made of **steel** under **uniaxial loading (Mode-I)** with a **CA** in **MCF**. The fatigue resistance characteristics of **arc-welded joints** with the same limitations will be established for reference. A **fatigue assessment concept** will be validated for these limitations.

1.4. Relevance
Practical
So far, only the NSC has been used to estimate the fatigue strength of welds at A&R. However, this is not State-of-the-Art anymore and cannot give reliable predictions of failure locations. A more accurate fatigue assessment concept should be validated for day-to-day use. It is, moreover, enhancing the design of future ships and minimising the need for fatigue tests. In addition, investigating the fatigue behaviour of laser welds will help to avoid fatigue failure and enhance the knowledge acquired in the last years during the implementation of laser welding in projects.

Scientific
The contribution concerning science is validating a fatigue assessment concept for lap joints with fillet welds, both laser-welded and arc-welded, aiming to approve the good applicability of this concept. Furthermore, the semi-analytical formulations for the weld notch stress distribution, which shall be adopted, will help the concept as it will be usable for both arc- and laser-welded lap joints, especially for the automotive industry, as lap joints are common there.

Societal
The final aim of building a yacht might give ethical concerns as yachts are mostly pure pleasure vessels owned by wealthy people and, therefore, only offer a minimal contribution to society apart from the labour required to build and maintain it. In any case, as the possible yacht will look like an old yacht, the heritage and history of shipbuilding can also be named.

However, the focus of the proposed research is to provide a safe yacht and, therefore, ensure the life of the ones onboard.

1.5. Fundamentals
The development of fatigue cracks is a local, progressive damage process. The time to complete failure can be divided into three phases: initiation, growth, and fracture. The initiation covers the short crack growth at the micro/meso-scale level. In contrast, the growth includes the long crack growth up to the fracture at the macro-scale. The fracture phase is related to unstable crack growth and does not add significantly to the lifetime (Schijve, 2008).

The first part of the initiation is the cyclic slip, where slip bands in the material shift. Followed by this is the nucleation of a crack, which then grows into a microscopic crack. The crack growth phase takes over as soon as the stress intensity at the crack tip is high enough to overcome the grain boundaries (Schijve, 2008). Hence, initiation is related to the surface, and growth is to the bulk.

The microscopic stress concentration (msc) needed for initiation appear randomly over the whole material surface, and their distribution is highly stochastic. Therefore, initiation will likely occur at a macroscopic stress concentration (MSC). Welds are generally a MSC, making them prone to experience fatigue damage. In addition, the tensile residual stress introduced by welding leads to a higher stress level.

The through thickness weld notch stress distribution divided into three zones is needed to understand the fatigue behaviour (fig. 1.3). Zone 1 is mainly affected by the peak notch stress. It usually extends from the surface up to a few per cent of the thickness. The influence of the notch typically expands to around 10-20% of the thickness and is called zone 2. The far field stress dominates the remaining thickness, Zone 3 (den Besten, 2015).
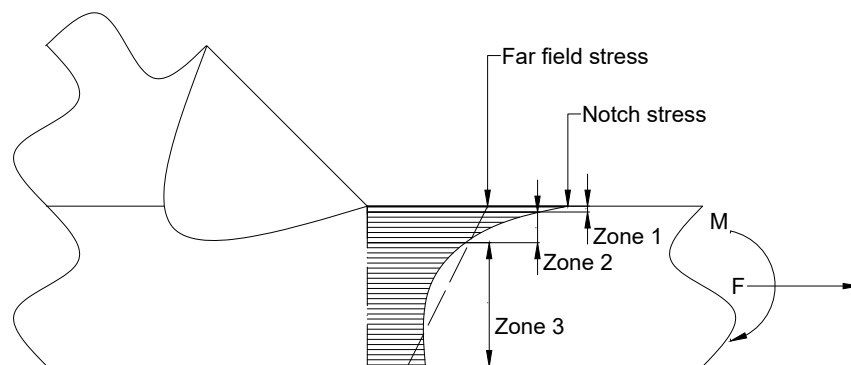
Figure 1.3: Schematic of different zones of notch stress

Wöhler first attempted to establish a model for the fatigue lifetime (Wöhler, 1860). However, only forty years later, Basquin established a simple formula to describe this behaviour (Basquin, 1910). The fatigue resistance data is plotted on a log-log scale, using the fatigue resistance constant (C) and the fatigue resistance inverse slope (m) as parameters. The input is given by elastic stress range (S) to obtain the number of cycles until failure (N) (eq. (1.1)). S is defined by the difference between the minimum stress of the stress cycle (σ_{min}) and the maximum stress of the stress cycle (σ_{max}). The Basquin equation is still predominantly used today, although other models also exist.

$$log(N) = log(C) - m * log(S) \tag{1.1}$$

The fatigue lifetimes can be divided into low cycle fatigue (LCF)- $N < 10^4$, mid cycle fatigue (MCF) -$10^4 < N < 4 * 10^6$- and high cycle fatigue (HCF) - $4 * 10^6 < N$. For marine structures, MCF and HCF are of main interest due to the long lifetime of ships reaching over 20 years. In the LCF, growth dominates, as macroplastic deformation appears, whereas, in the HCF, initiation is governing related to elastic behaviour (Schijve, 2008). Hence, these regions have different governing mechanisms. Initiation is a highly stochastic process due to the random location of the msc leading to an increasing scatter with increasing cycles (fig. 1.4).
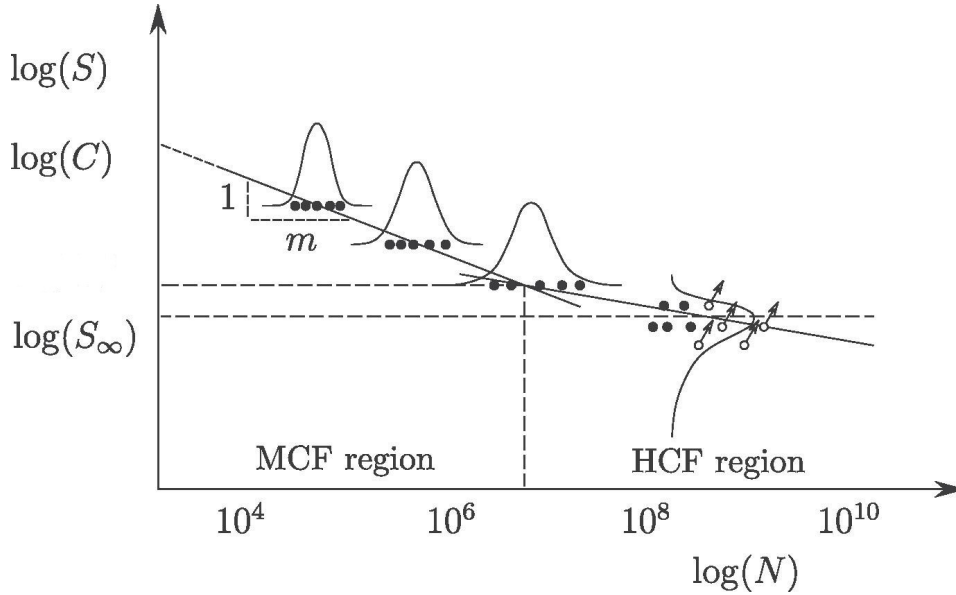
Figure 1.4: MCF and HCF fatigue resistance characteristics (Qin et al., 2020)

Due to the progressive behaviour of fatigue crack development, the damage accumulates over several cycles. To estimate the damage, a linear model, the so-called Palmgren-Miner rule, was proposed (Palmgren, 1924). The Palmgren-Miner damage sum (D) is defined by the cycles at a certain stress level (n_i) and the allowable cycles per stress level (N_i)(eq. (1.2)). This model only applies for constant amplitude loading (CA).

$$D = \sum_{i=1}^{k} \frac{n_i}{N_i} \tag{1.2}$$

The load in marine structures is largely driven by natural phenomena like wind and waves, which are dynamic and not constant. Hence, assessing the damage with CA shows limited applicability. As variable amplitude loading (VA) is complex, a spectral approach with different CA levels is mainly used as a compromise. The damage is calculated for each contribution of the spectrum and summed up over all the contributions.

Three different loading modes can induce a fatigue crack (Janssen et al., 2004) (fig. 1.5). Mode-I appears under normal and bending stress, which is governing for marine structures due to two reasons. Firstly, normal stresses govern thin-walled structures. Another reason is the construction method of stiffened panels. Here the hierarchy of the members, which yields an orthotropy, leads to normal stresses corresponding to Mode-I. Due to the explained reasons, marine structures are barely subjected to Mode-II. Mode-III corresponds to out-of-plane shear stress, which may occur in marine structures.
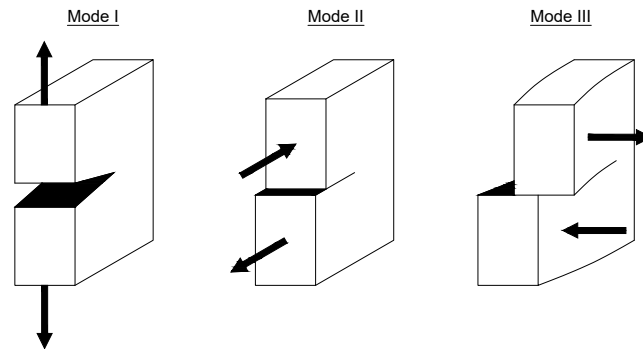
Figure 1.5: Three loading Modes

1.6. Outline

First, a literature view covers the current state-of-art to establish the research gap resulting in a hypothesis and the formulation of research questions (part I). Afterwards, the research is conducted (part II). The first part establishes the semi-analytical formulations and models to obtain the notch stress needed for the use of effective notch stress concept (ENSC) from a beam/shell model (chapter 6). Following the fatigue assessment of arc-welded lap joints with different fatigue resistance concepts (section 7.2), the same is done for laser-welded lap joints (section 7.3). An optimization of the weld geometry is added for application (section 7.4). In the end, the conclusion is drawn with the addition of the discussion and recommendations (part III)

Literature Review

<div style="text-align: right; font-size: 3em;">2</div>

Fatigue assessment concepts

Following an overview of fatigue assessment concepts (section 2.1), the NSC (section 2.2) and hot spot structural stress concept (HSSSC) (section 2.3) will be discussed for reference purposes. The ENSC (section 2.4) will be investigated as the one is potentially used to obtain a fatigue damage criterion and the corresponding fatigue resistance curve for laser-welded joints in steel structures.

2.1. Overview

To assess the fatigue lifetime of welds, different concepts have been established. These concepts have different assumptions and consist of a criterion and an accompanying fatigue resistance curve. The most prominent criteria differ in the following categories (den Besten, 2018):

- global and local

- intact and cracked geometry

- energy, stress or strain criterion

- point, line, area, or volume criterion

The first category divides concepts into the area of which information is considered, varying in either global or local information.

The next difference can be made by assuming an intact or cracked geometry. This is in line with the initiation and growth period of the crack. When looking at a weld, several crack nuclei appear (Schijve, 2008). Therefore, it seems like cracked geometry concepts are the best choice. However, a significant amount of time is spent in the notch-affected region; therefore, concepts assuming initiation are also valid (den Besten, 2015). Furthermore, marine structures are mainly exposed to MCF and HCF, where the initiation is dominant. The intact geometry concepts are coupled to a stress or strain concentration factor (SCF). A stress or strain intensity factor (SIF) corresponds to the cracked geometry concepts.

When measuring the load on the weld, energy, stress, or strain can be considered parameters. Strain criteria are primarily adaptations of a stress criterion. They mostly do not show different behaviour. However, stress is the easiest to obtain.

A point criterion cannot consider the different zones of the fatigue lifetime. More detailed approaches are line, area, or volume-based criteria.

Cracked geometry concepts need an estimation of the initial crack and a point where the transition between the initiation and growth periods happens. Both of these parameters are difficult to obtain (Schijve, 2008). Furthermore, the translation from the stress into a SIF requires added work. In addition, as marine structures are looked at, yielding MCF and HCF, intact geometry parameters are further considered in this chapter. For simplicity, only stress criteria are looked at. The energy criterion only offers significant advantages in multi-axial loading states, which are outside the scope of this research (den Besten, 2018). The concepts presented in this review are marked in fig. 2.1.
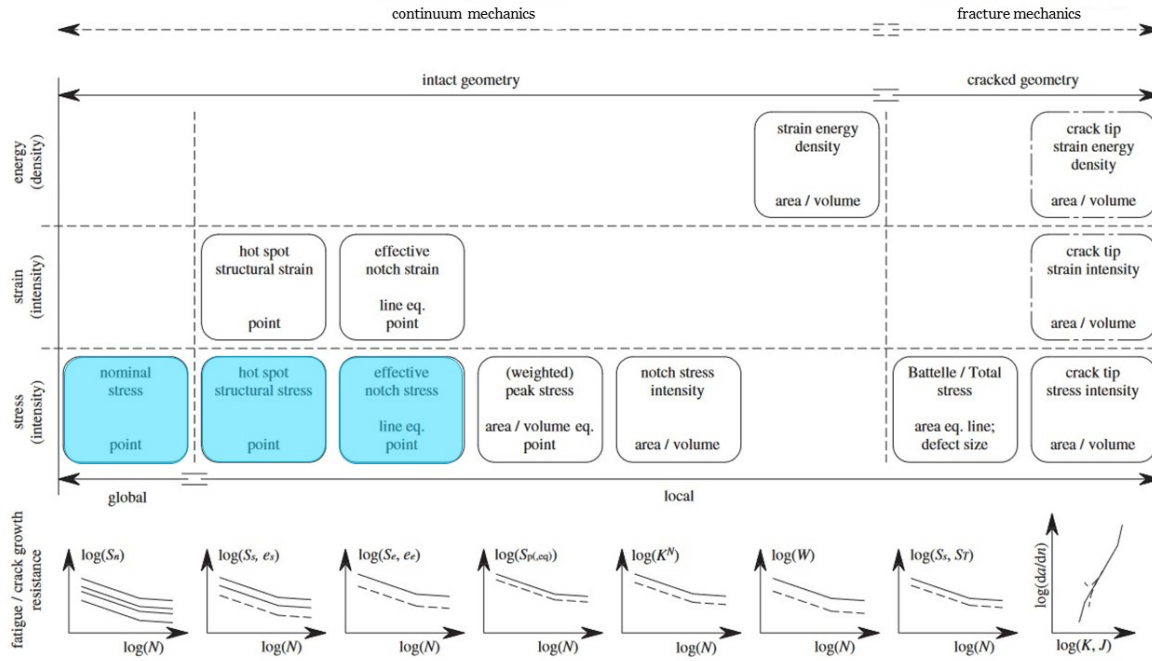
Figure 2.1: Overview of different fatigue concepts (den Besten, 2018)

2.2. Nominal stress concept

This concept is the only one adopting a global approach using the nominal stress range (S_n). It is an intact point criterion. Although, only integrating global information leads to the need for a structural detail for each different joint to include local information. Hence, each detail has its corresponding fatigue resistance curve and a structural detail reference stress. However, only the most prominent details of the infinite number of details are classified. The two most used collections of details are the fatigue class (FAT) by the International Institute of Welding (IIW) (Hobbacher et al., 2016) and the CAT from the CEN (Eurocode 3, 2007; Eurocode 9, 2007). Both collections have around 80 different details and use a Basquin type of equation. However, only the C is changed for each detail, showing the assumption that the failure mechanism is the same for all details as the m is not changed. The FAT and CAT classes are based on CA testing. This might limit accuracy in marine structures, which are mostly subjected to varying loads. Another assumption is neglecting the remote mechanical load ratio (r_{lr}), which is needed in addition to the incorporated range to define a stress cycle. However, this is reasoned by the residual stress, which is mostly highly tensile, reducing the influence of the mean stress.

The NSC results are satisfactory if geometry, material, loading & response, environment, and failure mechanism align with what the used code describes. However, defining the nominal stress from a FE-calculation of a complex structure leads to complications.

2.3. Hot spot structural stress concept

Local information is considered by using the structural stress range (S_s) $S_s = S_n * K_t$ and an intact geometry is assumed (Hobbacher et al., 2016; Eurocode 3, 2007; Eurocode 9, 2007). The theoretical stress concentration factor (K_t) is obtained by dividing the structural stress at the toe (σ_s) by the far field stress. However, the σ_s can be obtained straight from FE calculations eliminating the need to obtain the nominal stress. As the weld's local geometry information is not considered, an infinite amount of fatigue resistance curves are needed. The missing geometry information determines the self-equilibrium equivalent stress. The solution is to establish a fatigue resistance curve of a Basquin type for a load carrying (LC) and a non load carrying (NLC) weld with rules to decide on the load-carrying level.

As WR is hard to detect and should be avoided, the established rules by IIW and CEN only account for WT. However, it was shown that the concept could be adapted to root failure (Fricke, 2013).

Multiple methods can acquire S_s. Surface extrapolation is one method to obtain it (Hobbacher et al., 2016). This method can be used on real structures where different numbers and positions of extrapolation points from the weld toe for linear and non-linear extrapolation were established. The same approach can be adopted for FE-calculations. However, the values for S_s depend on the used mesh size (e.g. Fricke, 2001; Fricke et al., 2013). To avoid this problem, the through-thickness linearization was developed (Dong, 2005; Dong, 2001). This method gives the most accurate results. It can be either adopted for shell models, where the nodal forces naturally provide the membrane and bending structural stress, or for solid models, where the equilibrium of the nodal forces leads to the membrane and bending structural stress. The method, where a virtual node is introduced, was developed for hot spots at weld ends (Dong, 2005).

2.4. Effective notch stress concept

The notch radius (ρ) is highly stochastic, with measured values varying between 0 mm to 4 mm for arc-welding (Lassen et al., 2005; Darcis et al., 2006; Smith and Smith, 1982; Tricoteaux et al., 1995; Schubnell et al., 2020). Similar values with radii from 0.3 mm to 2 mm for laser welding were observed (Fricke & Robert, 2012). As laser beam welding (LBW) is performed with robots, the values vary less over the weld length. However, adopting one value for the weld radius is not deemed possible. Hence, a notch radius of $\rho = 0$ should ensure a conservative approach. Taking the peak stress at the notch for a related SCF K_t would lead to a too-conservative approach. A notch stress support hypothesis is adopted, a zone 1 and 2 parameter.

Different approaches were developed to obtain an effective notch stress range (S_e). The effective notch stress can be described as the multiplication of the σ_s by notch factor (K_f) $S_E = S_S * K_f$. Local information is considered, making it more detailed than the before explained NSC and HSSSC. Hence, this concept can be used to predict both root and toe-induced failure, which is essential for lap joints (Fricke, 2013; Baumgartner J., 2013). Furthermore, size effects are taken into account.

An overview of different approaches to incorporate the notch support is given below. The approaches b) to d) in fig. 2.2 are gathered under critical distance theories (CDT) (Taylor, 2008).
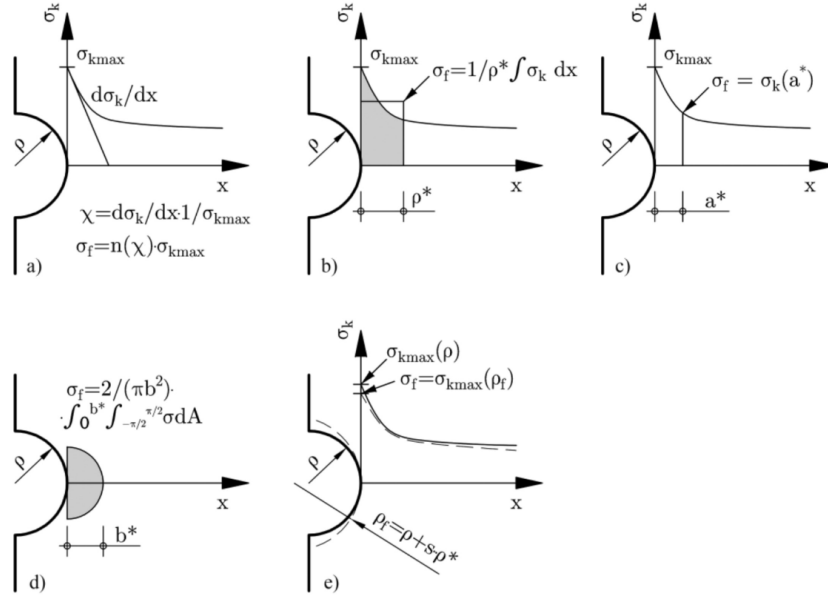
Figure 2.2: Overview of different notch support hypothesis (Lang et al., 2017)

2.4.1. Stress gradient approach

The concept marked with a) in fig. 2.2 uses the gradient of the stress distribution (Stieler, 1954). The gradient can be obtained with an analytical solution considering the radius or with FE-calculations. However, the analytical solution only considers the radius, not the opening angle. Yielding unsatisfactory results under certain circumstances. For FE-calculations, the value highly depends on the mesh size (Baumgartner J., 2013). Furthermore, this concept can hardly deal with small radii as the stress becomes asymptotic, making this concept not applicable for welds where $\rho = 0$ is assumed (Lang et al., 2017).

2.4.2. Line method

In this concept, the stress is averaged over a micro structural support length (ρ^*) which follows the assumed crack path, see fig. 2.2 b) (Neuber, 1985) (eq. (2.1)). This concept is based upon the theory of the microstructural support thesis, in which the areas with high local stress are relieved, and in surrounding areas, with lower load, the stress is increased (Neuber, 1968).

$$\sigma_e = \frac{1}{\rho^*} \int_0^{\rho^*} \sigma_n \left(\frac{r}{tp} \right) d \left(\frac{r}{tp} \right) \tag{2.1}$$

One needs the microstructural length and the weld stress distribution for the criterion. The microstructural length ρ^* is a material characteristic parameter directly obtained from experiments or semi-analytical formulas (see. section 2.4.6). The stress distribution can be obtained from FE-calculation. Here the mesh dependency is not as high as with the gradient concept, as averaging the stress yields a lower influence of the singularity at the notch. However, using the semi-analytical weld stress distribution (chapter 6) has the advantage of easier use, as no further FE-calculation is needed. Although the weld stress distribution was developed for SIF and not SCF, it showed promising results (den Besten, 2015; Qin et al., 2019; Qin et al., 2020). Therefore, using them for the line method of critical distance theories (LENSC) seems valid.

2.4.3. Point Method

Another way of establishing the S_e is taking the stress at a certain depth along the crack path, related to micro structural support point location (a^*)(Peterson, 1938; Moore, 1945), see fig. 2.2 c). However, the concept was initially developed for polished specimens where the surface layer is compressed, and the strength is enhanced (Peterson, 1938). Hence, the cracks were initiated underneath the surface. The initial values for a^* were established under this assumption. However, these values for a^* did not give accurate results for welded joints and were, therefore, adapted (Taylor, 2008). This method is mainly called the point method of the critical distance theories (PENSC). The a^* is generally obtained from experimental data with a maximum likelihood analysis (section 2.4.6). Furthermore, it depends on the material, the heat-affected zone (HAZ) and the filler material. Only taking the stress at a certain depth might have limitations when changing the notch radius. Hence, it depends not only on the material (G. Zhang et al., 2012).

2.4.4. Area method

Another option is to average the stress in the circular area around the notch see fig. 2.2 d) (Sheppard, 1991). It is also referred to as area method of the critical distance theories (AENSC), where the characteristic parameter micro structural support radius (b^*) is introduced. The microstructural support effect appears along the cracked line and around the whole notch. Hence, it is an area effect which is considered in this method. However, it assumes the same cross-section along a weld, yielding a quasi-2-D geometry. For a 3-D geometry like hotspots at weld ends, the volume method of the critical distance theories (VENSC) was developed, where the stress is averaged in a spherical volume around the notch (Bellett et al., 2005).

2.4.5. Fictitious notch radius concept

The most used concept currently is the fictitious notch concept, shown in fig. 2.2 e) (Neuber, 1985; Radaj and Vormwald, 2007). In this concept, the existing radius ρ is enlarged by multiplying the microstructural support length ρ^* with the support factor for the fictitious notch radius (s) to achieve the fictitious notch radius (ρ_f)(eq. (2.2)). The aim is to increase the notch radius so far that the maximum stress at the surface of the fictitious notch radius has the same value as the averaged stress along the crack path over ρ^* as in the LENSC. However, the s depends on the weld geometry and stress/strain conditions. This concept was developed as obtaining the through-thickness stress distribution was coupled to a great effort before FE-calculations were common.

$$\rho_f = \rho + s * \rho^* \tag{2.2}$$

The change in geometry leads to the loss of physical representation. In addition, the weld's opening angle, which significantly influences the stress, is no longer considered (G. Zhang et al., 2012). Furthermore, the root can be modelled with a U-hole or a keyhole, which leads to different results. The same applies to the utilised stress, the principal or the von Mises stress. These parameters have to align with those used to create the fatigue curve. Hence, it is impossible to establish one support factor for different conditions. Therefore, primarily the reference radius of 1 mm is used in engineering applications instead of calculating the ρ_f according to the conditions(Hobbacher et al., 2016).

2.4.6. Material characteristic length

All the CDT rely on a microstructural support length. The microstructural length is a material-dependent parameter independent of notch size and geometry. A formula was developed, where the material length parameter (L) is described with the plain-specimen endurance limit ($\delta\sigma_0$) and the fatigue crack propagation threshold (δK_{th}) (Tanaka, 1983; Taylor, 1999)(eq. (2.3)).

$$L = \frac{1}{\pi} \frac{\delta K_{th}}{\delta \sigma_0^2} \tag{2.3}$$

However, the relation between the characteristic parameters for the PENSC, LENSC and AENSC is different (fig. 2.3). Kawagoishi stated that the microstructural length depends on the grain size in the crack zone (Kawagoishi et al., 2000). Hence, ρ^* should be obtained with experiments, where it was found that $\rho^* = 3 * d$ with the average grain size (d) (Kawagoishi et al., 2000).
Another way to obtain the microstructural length for the different approaches is by using a maximum likelihood analysis with experimental data. Whether the principal stress or the von Mises stress has been used is essential.
For the LENSC a ρ^* of 1.23 mm is proposed when using $\rho = 0$ (Qin et al., 2019). Microstructural lengths of 0.4 mm and 0.31 mm were also proposed (Sonsino et al., 1999; G. Zhang et al., 2012). However, those results are obtained for the fictitious notch concept. Baumgartner established a value of 0.35 mm for the principal stress and 0.15 mm for the von Mises stress by using a fictitious notch radius of 0.05 mm to avoid a singularity but averaged the stress over the microstructural length (Baumgartner J., 2013).
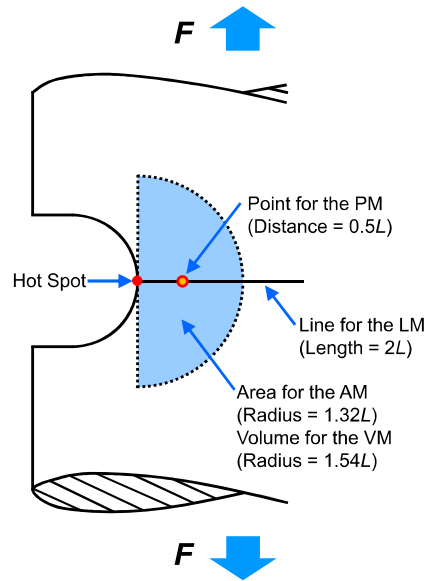
Figure 2.3: Characteristic length parameters of CDT (Liao et al., 2020)

For the PENSC, a value of 0.1 mm has been proposed by Baumgartner for principal stress under the same conditions as for LENSC (Baumgartner J., 2013). This result aligns with the correlation between a^* and ρ^* explained before. Other values of 0.15 mm and 0.21 mm were found with a sharp notch and the analytical formula (Taylor, 1999; Radaj, 1975).

All of these values were obtained for arc-welded joints. As the crack is initiated in the HAZ where the properties are affected by the welding method (section 3.3) the parameter will be different for laser-welded.

In general, significant differences between the obtained values can be seen. The different approaches with which the values were derived, and conditions like fictitious notch radii might be a reason.

2.4.7. Walker mean stress correction

The mean stress of the stress cycle (σ_m) influences the fatigue strength. The influence occurs as tensile stress enhances crack initiation and growth, whereas compressive stress inhibits those. The mean stress determines the time spent in the compressive and tensile zone (fig. 2.4). Higher mean stress reduces fatigue resistance. The mean stress is defined by r_{lr} (eq. (2.4)). It is, therefore, advised to keep the r_{lr} constant when fatigue tests are performed (Hobbacher et al., 2016).

$$r_{lr} = \frac{\sigma_{min}}{\sigma_{max}} \tag{2.4}$$

To avoid the need for an S-N curve for each r_{lr}, correction models were developed for fatigue assessment concepts like the ENSC where the effect of the mean stress is not included. Walker introduced a model where the influence of the mean stress is scaled by the load ratio coefficient (γ), a material-dependent parameter (Walker et al., 1970). A Walker mean stress corrected stress (σ_{eff}) is calculated with the uncorrected stress value, r_{lr} and γ (eq. (2.5)).
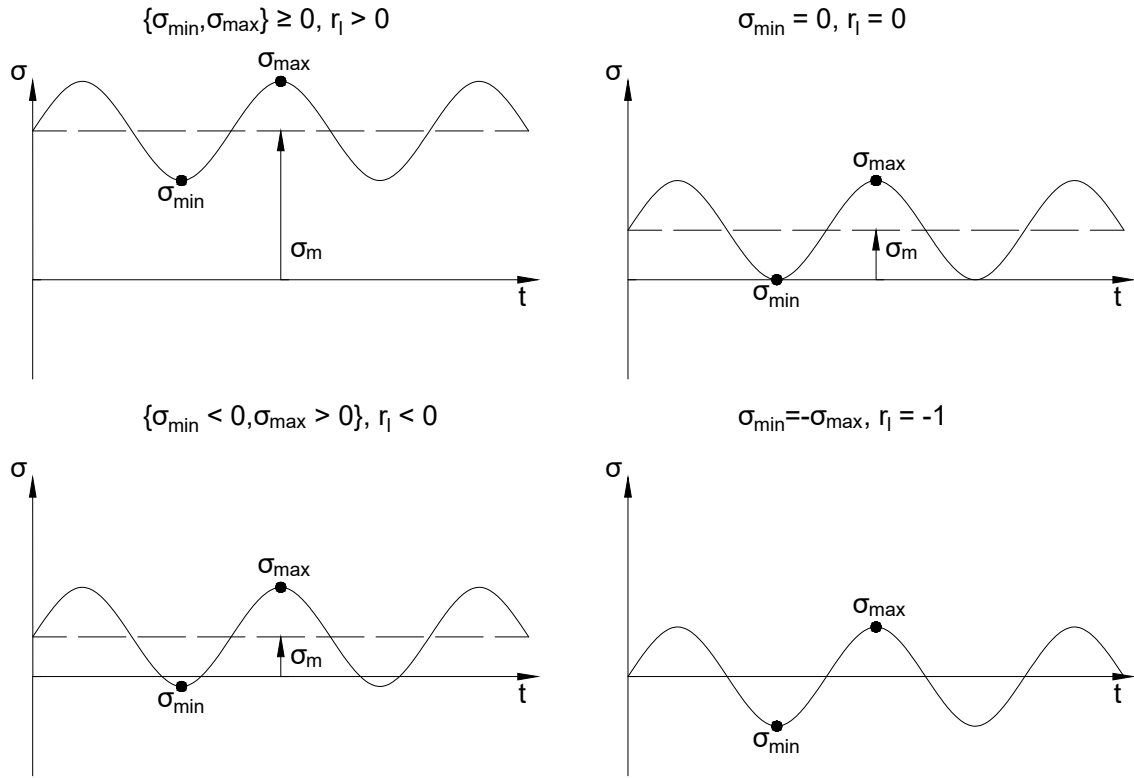
Figure 2.4: Overview of different r_{lr} values

This model is one of the most used ones, provides the most versatility and gives the most accurate results (Gaia da Silva et al., 2021; Dowling, 2009). For those reasons, it will be used in this thesis. In addition, the exponential behaviour of the walker model does provide a good fit for small stress ranges and high mean stresses. This applies especially in the MCF and HCF, which are important regions for marine structures.

$$\sigma_{eff} = \frac{\sigma}{(1 - r_{lr})^{1-\gamma}} \tag{2.5}$$

The values for γ must be determined by performing a regression analysis of experimental data with a non-zero r_{lr} similar to the material characteristic length. A higher value for γ yields a lower dependency on the mean stress effect. For a typical application, γ varies between 0.3 and 0.8. For arc welded steel joints, a value of 0.92 was obtained (Qin et al., 2019). This value shows a low dependency on the mean stress. However, only the mean stress of the loading is included and not the residual stress, which is highly tensile, most likely explaining the low dependency.

3

Laser welds

light amplification by stimulated emission of radiation (LASER)s provide another energy source for welding than an electric arc, which is commonly used in the marine industry (fig. 3.1). The higher energy density compared to arc welding yields different weld properties. However, the overall HI is lower due to the smaller welding area than arc welding. The different energy properties cause a change in microstructure, hardness and other factors. These lead to multiple advantages of LASER welds over arc welds.
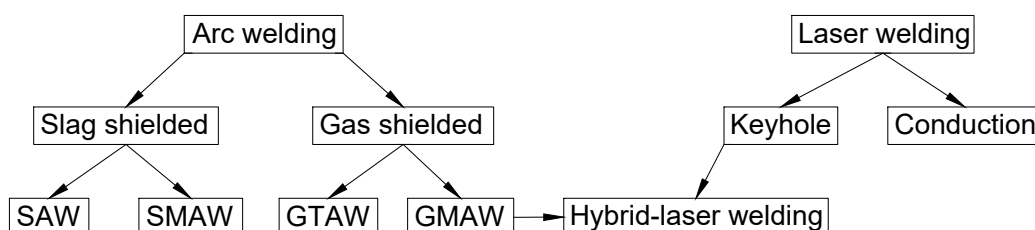
Figure 3.1: Welding methods in the marine industry

One of the most important advantages is the lower HI compared to other methods. This imposes several further upsides, like low distortion, low residual stress and a small HAZ. Another critical factor is the enhanced welding speed and the ease of automation (Cho et al., 2004). The high achievable penetration with keyhole welding gives the opportunity for new constructions like sandwich panels or full penetration with a single-sided weld (Fricke et al., 2016). More advantages are stated in table 3.1. However, LBW poses challenges as well. The needed tight fit and the low toughness of the weld are issues for the marine industry. A possible solution is the use of hybrid laser welding, where gas metal arc welding (GMAW) or shielded metal arc welding (SMAW) and LBW are combined (fig. 3.1). This process, however, is complex and has a higher HI than pure laser-welded. In addition, only minimal filler should be applied to the yacht because the HI shall be as low as possible. The more extensive weld geometry would destroy the appearance of a riveted joint. Due to these reasons, it is not considered an option for this application.

Characteristics	Comment
High energy density - "keyhole" type weld	Less distortion
High processing speed	Cost-effective
Rapid start/stop	Unlike arc process
Welds at atmospheric pressure	Unlike electron beam welding
No X-rays generated	Unlike electron beam
No filler required	No flux cleaning
Narrow weld	Less distortion
Relatively little HAZ	Can weld near heat-sensitive materials
Very accurate welding possible	Can weld thin to thick materials
Good weld bead profile	No clean-up necessary
No beam wander in magnetic field	Unlike electron beam
Little or no contamination	Depends only on gas shrouding
Relatively little evaporation loss of volatile components	Advantages with Mg and Li alloys
Difficult materials can sometimes be welded	General advantage
Relatively easy to automate	General feature of laser processing
Laser can be time-shared	General feature of laser processing

Table 3.1: Advantages of laser welding (Steen & Mazumder, 2010)

In this chapter, LBW will be explained by examining the different techniques (section 3.2) and sources (section 3.1). Followed by the introduction of the properties of laser welded joints (section 3.3), paying special attention to the ones that influence the fatigue properties. Lastly, the fatigue resistance of laser welded joints will be looked at (section 3.4).

3.1. Sources

The production of a monochromatic, coherent beam with high brightness makes the LASER useful for welding (Ion, 2005). However, the LASER utilised for welding must have sufficient power to melt the material. A LASER consists of a pumping source and an active medium between two mirrors (Dawes, 1992) (fig. 3.2). The pumping source stimulates the atoms of the active medium as electrons jump into higher levels in the shell. Suppose a photon hits an atom, which activation energy equals the photon's energy. In that case, the activated atom emits a photon with the same phase angle and polarisation and returns to the initial state. The mirrors reflect the LASER light through the active medium, enhancing the chance of photons to stimulate other atoms.

Two different kinds of active mediums are commonly used in the industry application, namely the CO_2 LASER and the Neodymium-doped yttrium aluminium garnet (ND:YAG) LASERs (Rooks, 2000).
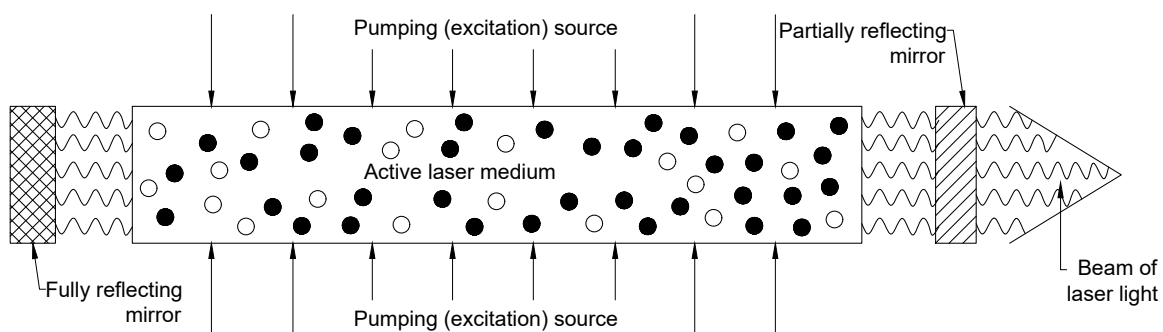
Figure 3.2: Basic elements of a laser (Dawes, 1992)

3.1.1. CO_2 laser

Since the 1980s, CO_2 LASERs have been used for welding. They can provide high powers of up to 45 kW (Caccese, 2010). However, the LASER beam has to be deflected with mirrors due to the wavelength of 10.7 nm (Rooks, 2000). This leads to limited application possibilities.

3.1.2. ND:YAG laser

ND:YAG LASERs were introduced later in the 1990s and only have a tenth of the wavelength of the CO_2 LASERs (Rooks, 2000). This provides several advantages, as this allows the LASER beam to be transported in a fibre cable and has a higher absorption rate for steel (Rooks, 2000). The transport in a fibre cable allows for flexible application in robots, for example. The higher absorption rate leads to higher efficiency. Only half of the energy is needed compared to a CO_2 LASER (Rooks, 2000). One downside of this kind of LASER is the lower power availability, where only recently LASER with in exceedance of 10kW power have been constructed (Caccese, 2010).

3.2. Techniques

A LASER beam is utilised as an energy source in laser welding. The power density of a LASER is higher than that of traditional welding methods (fig. 3.3). This enables high welding speeds and lower distortion due to a lower HI (Caccese, 2010). In general, there are two different methods of welding modes for LBW: keyhole and conduction welding. Both of them will be presented in the following part.
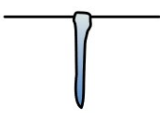
Process	Heat source intensity $(\mathrm{W\,m^{-2}})$	Fusion zone profile
Flux-shielded arc welding	$5 \times 10^6 - 10^8$	
Gas-shielded arc welding	$5 \times 10^6 - 10^8$	low / high
Plasma	$5 \times 10^6 - 10^{10}$	low / high
Laser or electron beam	$10^{10} - 10^{12}$	defocus / focus

Figure 3.3: Power densities of different welding processes (Steen & Mazumder, 2010)

3.2.1. Keyhole welding

The first method requires high energy levels (Caccese, 2010). The LASER is set up in such a way that the metal evaporates (fig. 3.4). This forms a so-called keyhole (Steen & Mazumder, 2010). To achieve this, an energy density of at least $10^4 \frac{W}{mm^2}$ is needed. After the formation of the keyhole, the power drops significantly (Ion, 2005). At the surface of the keyhole, the surface tension and the hydrostatic pressure of the surrounding melt pool and the pressure from the evaporating material have to equal each other to achieve a stable melt pool (Ion, 2005). The deep keyhole is possible due to multiple reflections of the LASER beam inside the keyhole (Ion, 2005). However, the high energy density also imposes the risk of forming a plasma in between the nozzle and the weld material (Zhou & Tsai, 2005). The plasma can absorb and scatter the LASER beam, lowering the available power for the actual weld. Using Helium can solve this problem (Ion, 2005). The number of physical phenomena, including keyhole formation, weld pool dynamics, material melting, and their interaction, show the complexity of this process.
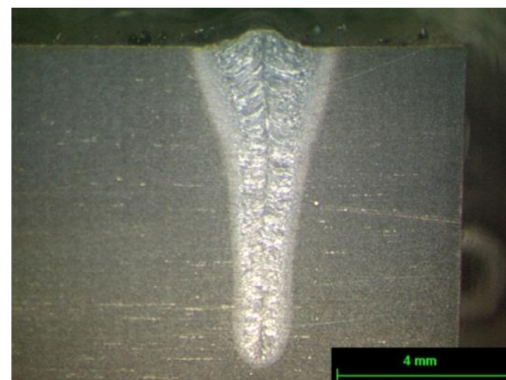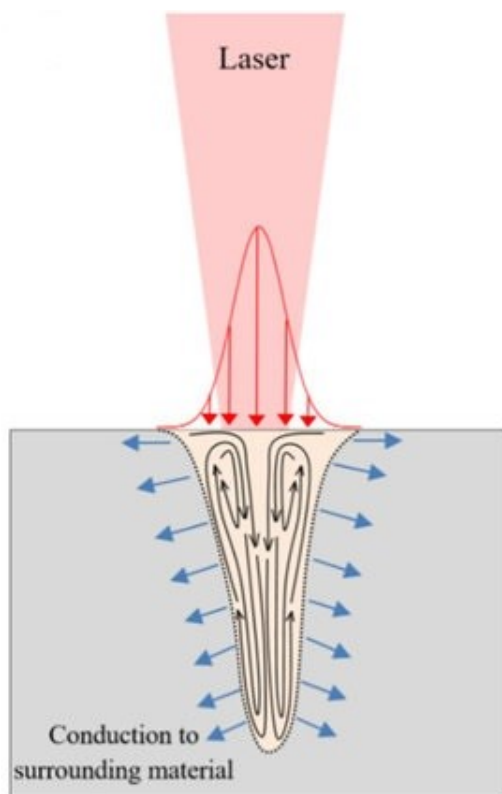
Figure 3.4: Schema of laser keyhole welding process (Balbaa et al., 2020)

Figure 3.5: Micrograph of keyhole laser weld (Cranfield University, 2022)

3.2.2. Conduction welding

Another way to use LASERs for welding is conduction welding (Caccese, 2010). For this method, lower powers of $10^3 \frac{W}{mm^2}$ are required, which can be achieved by either reducing the power or defocusing the LASER beam (Ion, 2005). This method is relatively similar to the more conventional methods like arc welding, as a hemispherical melt pool is formed (fig. 3.6)(Ion, 2005). This offers wide weld beads and low penetration (fig. 3.7). However, when thick parts should be welded, the distortion resulting from the needed high energy input might be significant (Ion, 2005). As only low energy is needed and the weld bead is wide, the LASER beam can be of lower quality.
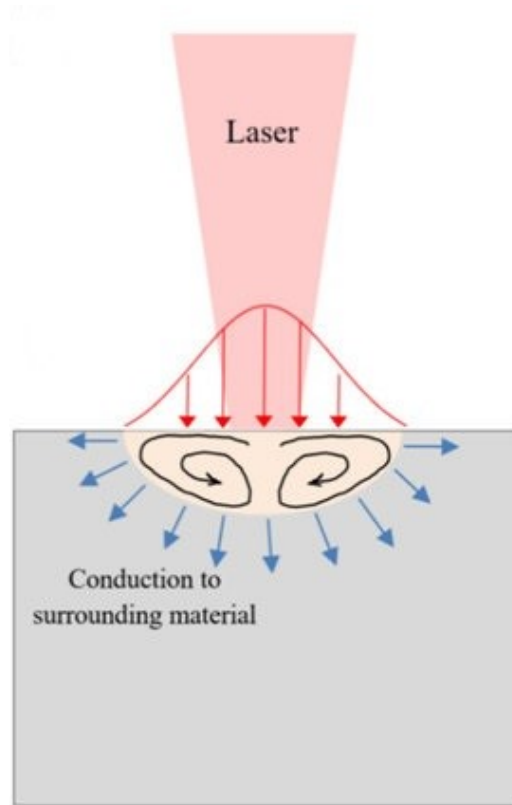
Figure 3.6: Schema of laser conduction welding process (Balbaa et al., 2020)
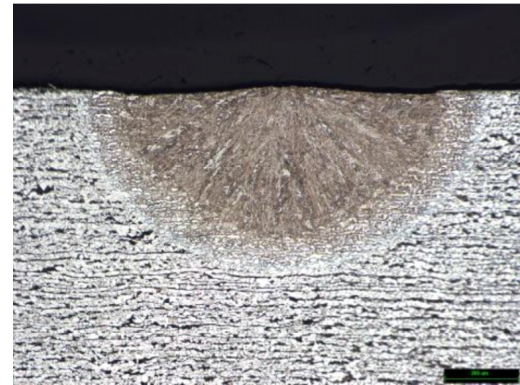
Figure 3.7: Micrograph of conduction laser weld (Cranfield University, 2022)

3.3. Keyhole welding properties

The keyhole welding method will be used given the advantages. Hence, its properties will be assessed. The energy density for LBW is high, but the heated area is small. Together with the high welding speed this results in a steep temperature gradient from the weld through the HAZ to the base material (BM), causing several material properties to change compared to arc welds. In addition, the different geometry of the laser weld is apparent. Therefore, the influence of HI and geometry on the properties will be discussed in this part.

3.3.1. Geometry

Using LBW with and without filler is generally possible. However, when not using filler material, several risks emerge. Firstly, if a perfect fit of the welding specimen is not given, a lack of fusion might appear (Caccese, 2010). In addition, the negation of filler can lead to an enhanced porosity in the weld (Remes et al., 2008). Furthermore, Roland showed that solidification cracking and heat distortion might also appear (Roland et al., 2004). Due to these reasons, it is recommended to use a filler, especially as a zero-gap is tough to achieve in the marine industry. However, less filler is typically used than in arc welds.

When looking at the geometry (fig. 3.8), the cross-section is smaller compared to arc welds, but a higher penetration is achieved. In addition, the weld height is usually smaller due to less addition of filler (Remes et al., 2008). Nevertheless, the weld shape also depends on the HI (Liu et al., 2017; Caiazzo et al., 2017). With low HI, the weld shows a perfect keyhole and a nail-like shape. Increasing the welding power leads to a more V-shape geometry. (fig. 3.8). Extending the weld pool to the root might happen at very high HI. In this case, vapour will also leave at the root, widening the melt pool and causing a peanut shape (fig. 3.8).
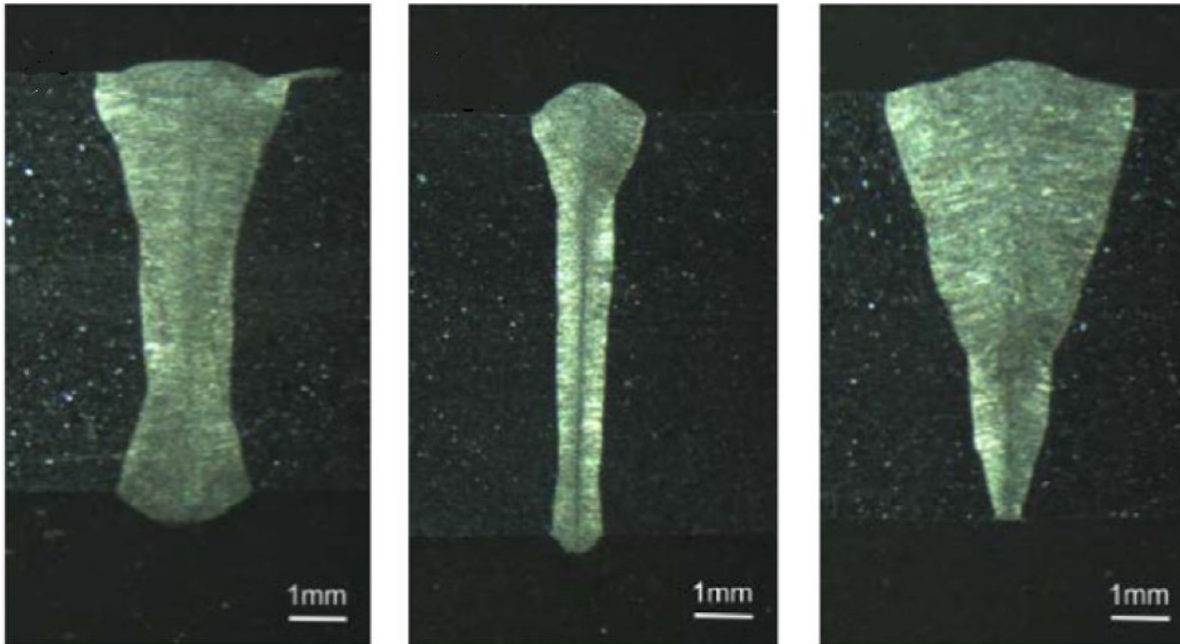
Figure 3.8: Laser weld bead geometries: Peanut shape, nail-shape, V-shape (Liu et al., 2017)

3.3.2. Micro-structure

Looking at the micro-structure in fig. 3.9, the smaller HAZ for laser-welded is obvious. For the GMAW process, the change in micro-structure is smoother, whereas the laser-welded process has a hard shift between the different zones (see. fig. 3.9).

Both processes show a different micro-structure in the weld material (WM) compared to the BM. However, for the laser-welded, it is closer to the one in the BM with a grain size of 4.6 µm compared to 29 µm for GMAW (Remes et al., 2008). The lower HI causes a smaller grain size and a more rapid solidification (Ion, 2005; Němeček et al., 2012). For steels commonly used in the shipbuilding industry, carbon contents exceed 0.12%, yielding a high risk of forming martensite inside the weld (Gerritsen and Howarth, 2005; Caccese, 2010). Martensite shows brittle behaviour and should, therefore, be avoided. This can be achieved by changing process parameters, like welding power and speed, or the filler material (Gerritsen & Howarth, 2005).
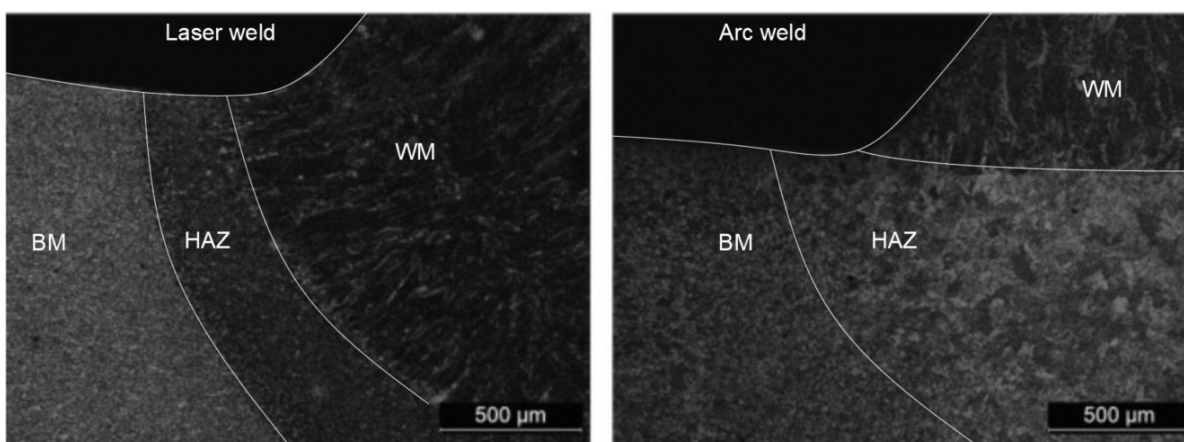
Figure 3.9: Micrograph of the transition zone from the base material to the weld material for laser and GMAW welding (Dourado et al., 2014)

3.3.3. Hardness

The micro-structure directly influences the weld's hardness, strength, and toughness. The hardness typically increases towards the weld. This can be seen in fig. 3.10, although the processes' profile and final values differ. For laser-welded, the hardness increase mainly occurs in the HAZ. Inside the weld, the hardness does not change significantly. In this case, the hardness constantly increases from the HAZ's start towards the weld material. In general, the maximum is observed in the HAZ for arc welding (Wu et al., 2020) and hybrid-laser welding (Fricke & Robert, 2012). For LBW a similar behaviour in contradiction to here shown distribution can be found as well (Fricke and Robert, 2012, Wan et al., 2018, Weldingh and Kristensen, 2003). However, both distributions are equally reported for LBW. One reason for the different reported distribution might be the smaller weld geometry of laser-welds, sometimes not allowing for tight measurement of hardness.

In addition, the hardness over match of laser-welded can be observed. The maximum value for submerged arc welding (SAW) is only 175 HV5, whereas, for laser-welded, it is 220 HV5. The base material S355 has a hardness of around 140 HV5. Similar observations were made in comparison to arc welding, where the hardness for LASER welds is reported to be up to 2.5 times higher than the hardness of the BM (Fricke and Robert, 2012; Oyyaravelu et al., 2016; Dourado et al., 2014; Němeček et al., 2012).

It was proven that toughness has an inversely proportional relation to hardness (Oyyaravelu et al., 2016). This poses a severe challenge to LBW as ductile and, therefore, tough behaviour is desired in marine structures. To achieve this the process parameters have to be balanced carefully.

However, an interesting breaking behaviour might occur at a highly overmatched WM. The crack might deviate from the over-matched weld into the base material (Gerritsen & Howarth, 2005). This appears as, for lower-strength materials, the crack driving force is higher. Therefore, a crack initiated in the weld metal with a high strength might deviate into the base metal. However, this is only sometimes applicable, and a purely brittle failure might still occur (Gerritsen & Howarth, 2005).
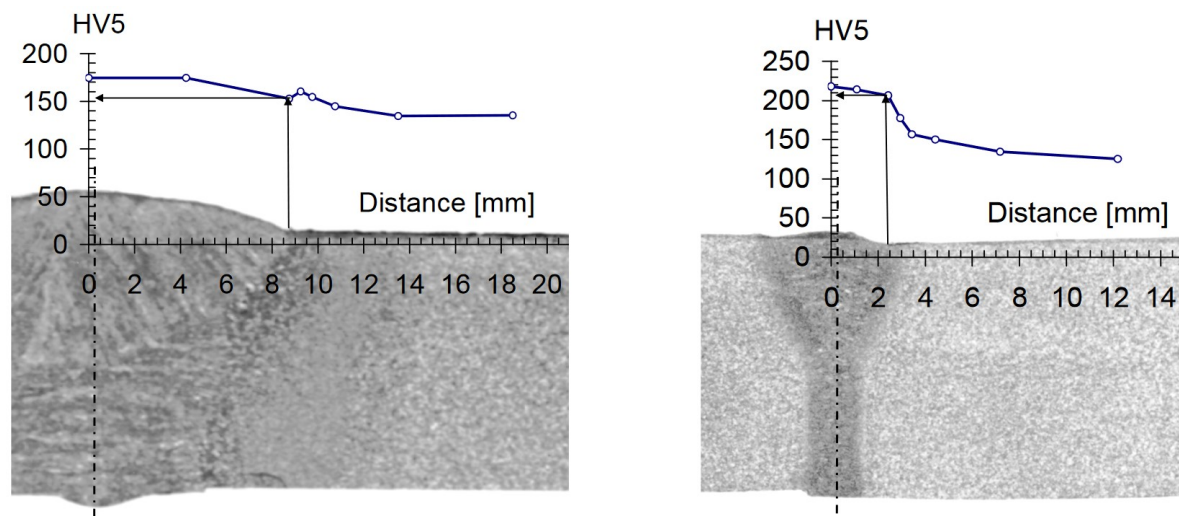
Figure 3.10: Hardness profile of SAW and Laser welding (Remes et al., 2008)

3.3.4. Defects

When welding, material flaws can occur due to the complex process. The same flaws as for GMAW might appear. However, some are prone to emerge in laser-welded due to the high energy density. For example, it is reported that solidification cracking and porosity are more likely appear (Gerritsen and Howarth, 2005; X. Zhang et al., 2010).

Several properties of a LASER weld are superior to other conventional welding processes. However, due to the energy density and the small weld, some challenges are imposed when balancing the process parameters to achieve an acceptable hardness and toughness of the weld.

3.3.5. Residual stress

Residual stress appears due to thermal expansion. The magnitude is highly dependent on the HI and the material, but the influence of constraints cannot be neglected (Cho et al., 2004). Before all, as for LBW a tight fit needs to be ensured the workpieces are mostly clamped. However, as expected, the low HI causes less residual stress than arc-welding methods (see fig. 3.11) (Moraitis & Labeas, 2008). The decrease in maximum residual stress is more than 30% in the given case (fig. 3.11).

In addition, the zone of residual stresses is smaller than for arc welding (X. Zhang et al., 2010; Moraitis and Labeas, 2008). In some cases, it was shown that the residual stress in weld metal was compressive (Yan et al., 2022). The extent of compression was mainly dependent on the oscillation of the LASER (Yan et al., 2022). The drop in residual stress in the weld metal can also be seen in fig. 3.11.
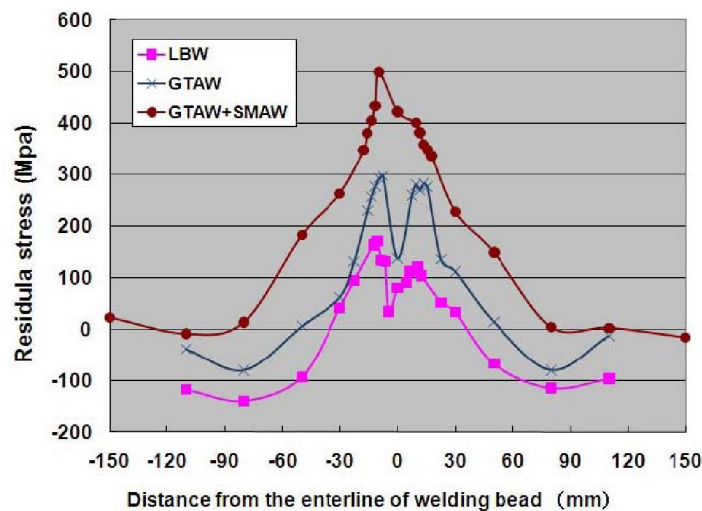
Figure 3.11: Residual stress perpendicular to the weld (X. Zhang et al., 2010)

3.4. Fatigue resistance

When looking at the fatigue performance of LASER welds, the laser-welding method, namely conduction or keyhole welding, and the addition of filler has to be accounted for. These factors influence fatigue performance, and therefore, comparing them is difficult. However, in the last years, more testing was performed on the fatigue performance of LASER welds.

In general, the fatigue performance of laser-welded is found to show different behaviour in comparison to arc welding (Ring and Dahl, 1994; Weldingh and Kristensen, 2003). However, only in the last years the amount of data was sufficient to make estimations of the actual performance (Baumgartner et al., 2012). A flatter S-N curve was shown to have a good fit with an inverse slope of $m = 5$ rather than the for arc-welded joints used inverse slope of $m = 3$ (Sonsino et al., 2010). The FAT value at $2 * 10^6$ cycles was observed to be the same for the different welding methods. Hence, laser-welded joints provide a better MCF and HCF fatigue performance and lower LCF fatigue performance than arc welds. However, in both cases, only thin-walled specimens of up to 3 mm thickness were considered. Fatigue tests with specimen thicknesses between 3 mm and 8 mm thickness showed that an inverse slope of $m = 5$ fits thicker joints as well (Fricke et al., 2015). A similar behaviour was already observed earlier, where the suggestion was to increase the inverse slope to $m = 10$. However, only butt joints were tested (Remes et al., 2008).

There are several reasons for the different fatigue behaviour of LASER welded joints. The most apparent change to other welding methods is the geometry. For arc-welded joints, a primary influence of weld flank angle was shown (Anthes et al., 1993, Anthes et al., 1994). On the contrary, for LASER welds, the notch depth and its root radius have a more significant influence on butt joints than the flank angle (Remes et al., 2008). As the smaller weld cross-section mostly leads to a higher stress concentration, it can be assumed that this adds to the lower fatigue performance at LCF as this is mostly growth dominated (Dourado et al., 2014).

When looking at the decreased HI of laser welding, the lower residual stresses come to mind first. Several studies have been performed showing that lower residual stresses lead to an increased fatigue lifetime (Sepe et al., 2020; Sonsino, 2009; Kang et al., 2008; Cho et al., 2004). A relief of residual stresses due to a post-weld treatment does only significantly influence the HCF, as in the LCF the additional stresses lead to plastic deformation of the weld and, therefore, a release of the residual stresses (Sonsino, 2009). In addition, post-weld treatment has a more considerable influence if the weld geometry does not have a crack-like geometry (Sonsino, 2009). Therefore, the lower residual stresses will likely contribute to better fatigue performance. Although the HI is lower, the energy density increases hardness and reduces the HAZ and weld material grain size. Both factors positively influence initiations, contributing to the enhanced HCF (Remes et al., 2008). However, when the LASER weld is subjected to a high pre-strain, the inverse slope changes to $m = 3$, meaning that the positive influence of the increased hardness and smaller grains is neglected (Remes et al., 2008). Hence, the influence of residual stress overcomes the one of micro-structure (Kang et al., 2008).

Multiple studies on the fatigue resistance of laser-welded have been performed (Sepe et al., 2020; Sonsino et al., 2010; Eibl, 2003; Fricke et al., 2016; Frank et al., 2011; Fricke and Robert, 2012). However, the thicknesses used mainly (<3 mm) are lower than the ones applied in the marine industry. Nevertheless, it was found for arc welds that a change in fatigue resistance appears around 7 mm (Baumgartner et al., 2020). Hence, the assessed joint might still be represented by a thin specimen.
In the marine industry, hybrid laser-welding is preferred due to the not-needed zero gap; hence, more fatigue data is available (Fricke and Robert, 2012; Gerritsen and Howarth, 2005). In addition, in recent years, LASER showed sufficient power for welding thicker plates.
Most studies assess the fatigue performance of penetration joints, as this is a unique joint geometry for LBW. This joint is mainly used in the automotive industry (Eibl, 2003). However, the opportunity of laser welded sandwich panels for the marine industry is also examined (Fricke et al., 2016; Frank et al., 2011).

For comparison purposes, 123 data points from literature for lap and other common joints in the marine industry are extracted (table 3.2 and fig. 3.12, detailed see appendix B). The tested specimens' thickness ranges from 3 mm up to 12 mm. The r_l is primarily close to zero (table 3.2). As described before, the flatter behaviour of an S-N curve for laser-welded can also be seen here (fig. 3.12).
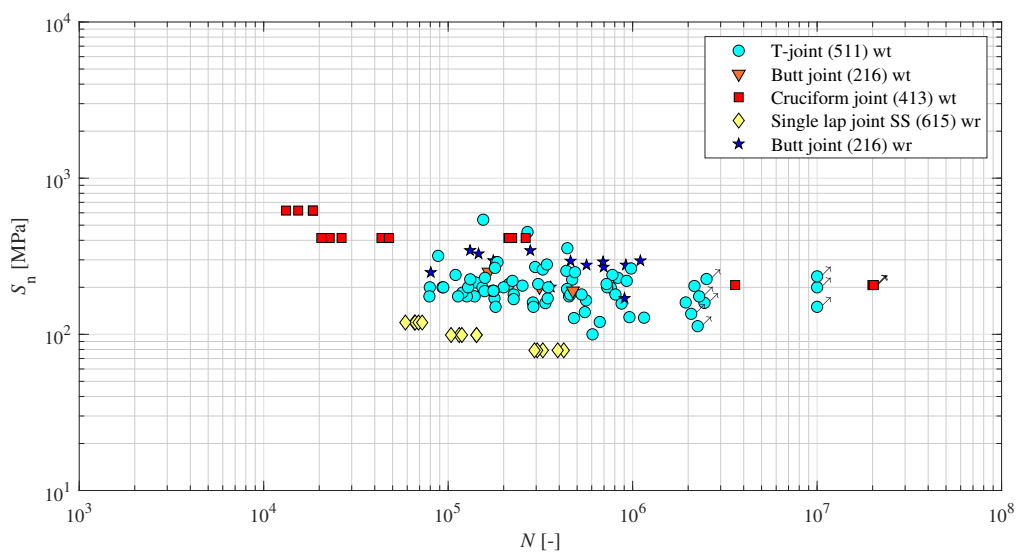
Figure 3.12: Nominal stress based fatigue resistance of laser welded joints from literature

Source	Yield strength [MPa]	code according to IIW	tp [mm]	r_{lr}	number
Fricke and Robert, 2012	350	511	4	0	45
			10	0	12
Remes et al., 2008	275	216	12	0	6
Dourado et al., 2014	350	615	3/2.5	0.01	15
Caccese et al., 2006	650	413	12.7	-1	17
Lillemäe et al., 2012	407	216	3	0	10
Laitinen et al., 2001	350/420	511	12	0.1	18

Table 3.2: Overview of experimental fatigue data for laser welded joints

Lap joints

Different geometries of lap joints are possible (fig. 4.1). The single lap joint with a double-sided weld (614) shall be implemented on the yacht. To achieve a broad view, the joints with a single-sided weld (615) and the double-sided joint (611) will be looked at as well (fig. 4.1). The codes used to describe the weld geometries are obtained from IIW (Hobbacher et al., 2016).
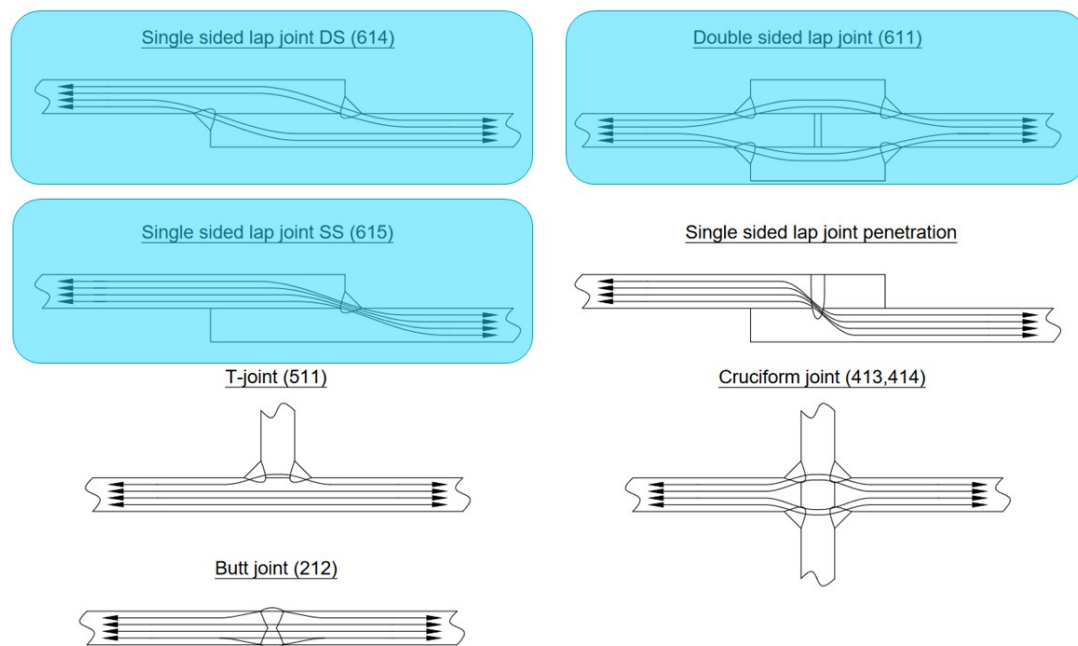
Figure 4.1: Overview of common joint geometries

4.1. Applications

Lap joints can be found in all industry areas. Although, in some, it is more prominent than in others. In the automotive industry, it is a common joint. There it is used as a substitution for butt joints, allowing for bigger tolerances. For the butt joints, the plates need to be cut to fit exactly, whereas, for a lap joint, it is not essential. This is further enhanced using a penetration weld instead of a fillet weld (fig. 4.1). In this case, there is no need to align the joint as the penetration can be placed anywhere along the lap. The fatigue resistance of this joint is decreased due to the small connected area compared to a fillet welded joint (Sonsino et al., 2010). As the automotive industry can provide more resources to test specific joints due to serial production, they can optimise joints to fit their demands.

Lap joints are also common in the building industry. Here, double lap joints (611) are often found, e.g. in the connection of two I-girders where two cover plates connect the web plates. Another example is using penetration welds to produce a corrugated sandwich panel for a bridge (Nilsson et al., 2020). Apart from specific projects like bridges, fatigue is not a common failure mechanism in the building industry due to the relatively constant and not cyclic loading & response conditions. Hence, explaining the common use of the easy-to-produce joint.

In marine structures, lap joints are rare nowadays. One reason is their insufficient fatigue resistance. An exemption are cover plates, which were described as NLC double lap joints (611) (Fricke & Feltz, 2010). Due to their stiffness-attracted load path, their fatigue resistance is better than those of the here-researched lap joints. Like the building industry, laser-welded sandwich panels are gaining more popularity in the marine industry (Frank et al., 2011; Gerritsen and Howarth, 2005). Here, also, lap joints with penetration welds are used sometimes. Looking at the past, though, lap joints were common in the marine industry as riveted joints.

4.2. Load path characteristics

All single lap joints introduce eccentricity yielding an additional bending moment (section 4.2.1). Since lap welds are typically not fully penetrated, a failure at the weld root might appear (section 4.2.2). The possible root failure, non-symmetry and eccentricity make lap joints quite specific.

4.2.1. Secondary bending moments

The influence of the secondary bending moments depends on several factors. One set of factors are the boundary conditions and applied forces (fig. 4.2). Similarly, the geometry, like lap length, plate thickness, and overall length, contributes. In addition to the secondary bending moment, a shear force is also introduced, pulling the two plates apart due to the deformation (Radaj et al., 2006).
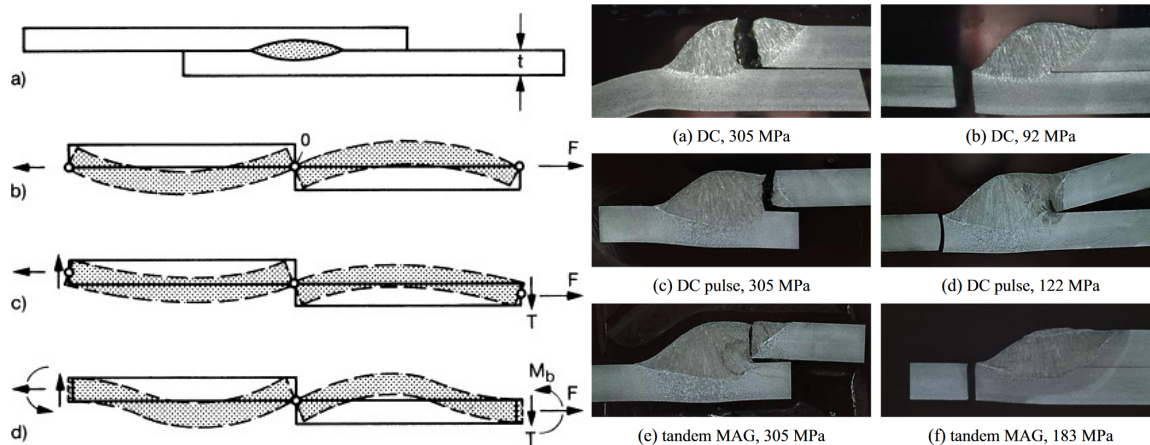
Figure 4.2: Schematic model of single-sided lap joint under different loading conditions (Radaj, 1990)

Figure 4.3: Fracture shape of 615 joint after fatigue test (Kim et al., 2017)

As the secondary bending moments depend on the load, their effect on the different fatigue regions is not linear. The non-linear deformation imposes the size of secondary bending moments. Hence, non-linear FE-calculations are needed to model the impact of secondary bending moments. When the influence of the secondary bending moments might be significant at the LCF due to high forces, the effect at the MCF and HCF might reduce significantly (Radaj et al., 2006). This behaviour was also observed in experiments by the change of failure location for different fatigue regions (Hwang et al., 2017; Baumgartner J., 2013; Bonnen et al., 2009; Kim et al., 2017). This behaviour was mainly observed for single joints (615) where WR occurred for high load levels and changed to WT for low load levels (fig. 4.3). In addition, the secondary bending moments influence the r_{lr}, as it depends on the minimum and maximum stress of the cycle, which do not scale proportionally due to secondary bending moments. A correlation for this behaviour has not been observed yet, however. For misaligned joints, the influence of secondary bending moments caused an increase of the stress by up to 45% (Hobbacher et al., 2016).

4.2.2. Root failure

For several fatigue concepts, it was shown that a prediction of root failure is possible (Fricke, 2013). However, the assessment of root failure still shows some challenges. Two particular root failure-related issues will be presented.

Firstly, it was calculated that the residual stress at the root of arc-welded fillet and butt welds could be compressive (Barsoum, 2008;Barsoum and Barsoum, 2009). A relation between the number of passes and the penetration was shown (Barsoum, 2008). For laser welds, compressive residual stress was shown in the weld metal for butt joints (Yan et al., 2022). Compressive residual stress positively influences fatigue life and enhances fatigue strength. This differs from the common toe failure where tensile residual stresses appear (Hobbacher et al., 2016). Hence, not including the residual stress in the failure criterion might lead to different toe and root failure results. It was observed for the peak stress method that the specimens did not fail at the predicted location; an explanation for this might be compressive residual stresses (Meneghetti, 2012; Fricke and Feltz, 2010).

In addition, the crack path might differ for different loading ratios. For a double joint (611), the influence of different loading ratios on the crack path was shown (fig. 4.4). For tension loading, the crack path extends through the weld metal close to the cover plate. Experiments also showed this behaviour (Fricke and Feltz, 2010, Baumgartner J., 2013). However, for compressive loading, the crack path develops along the weld bead into the baseplate (fig. 4.4). Nevertheless, this also depends on the joints' geometry.

Hence, not accounting for the residual stress at the root and the crack path might lead to inaccurate results for the assessment with the fatigue concepts.
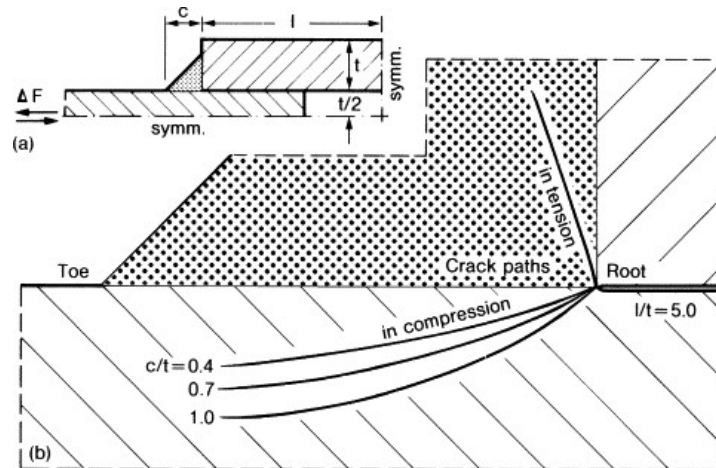
Figure 4.4: Predicted crack paths from the root for different r_{lr} of a double-sided lap joint (Nykänen, n.d.)

4.3. Fatigue resistance

The fatigue strength of lap welded joints is specific due to the previously described characteristics. The properties of the two welding methods will be addressed: arc- and laser-welding. Afterwards, unique design criteria for lap joints are introduced.

4.3.1. Arc-welded joints

Several studies investigated the fatigue strength of lap joints (table 4.1). It turned out that the double lap joints behave like a LC cover plate (Fricke & Feltz, 2010). Furthermore, it was shown that post-welding treatments like gas tungsten arc welding (GTAW) dressing or toe radius machining have a bigger positive impact in comparison to other joints (Shiozaki et al., 2018; Lee and Oh, 2015). This can be explained with the high MSC at the toe and, therefore, a greater impact of enhancement methods. A high scatter in the fatigue resistance was found for thin plates compared to the thicker specimens. This was explained by the more significant relative influence of changes in the welding process (Bonnen et al., 2009). Furthermore, for thin plates, it was found that they have a decreased fatigue resistance for a single lap joint (614) due to their lower resistance against bending induced by the secondary bending moments (Bonnen et al., 2009).

The generally assumed low influence of the yield strength of the material was proven as well (Bonnen et al., 2009). Another study showed that pores in the weld only significantly influence the LCF and the MCF (Kim et al., 2018).

A single lap joint (614) was shown to behave similarly in the HCF compared to riveted joints (Overbeeke et al., 1984). However, this highly depends on the design of the welded and riveted joint.

From the literature, experimental results of fatigue tests were gathered (see. table 4.1 and fig. 4.5, detailed see appendix A). 373 data points were found, equally spread over the three different geometries and failure locations. However, only thin specimens (< 3.6 mm) were found for the single lap joints. Furthermore, the r_{lr} has a limited range (table 4.1).
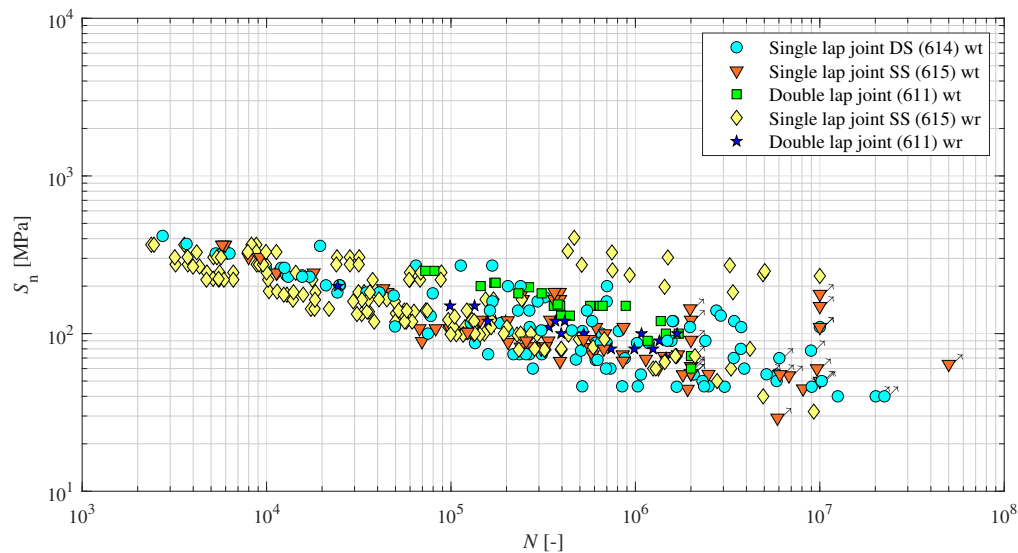
Figure 4.5: Nominal stress-based fatigue resistance of arc-welded lap joints from literature

Source	Yield strength [MPa]	geometry	tp [mm]	r_{lr}	number
Dourado et al., 2014	355	615	2.5/3	0.01	15
Fricke and Feltz, 2010	355	611	12	0	20
Bonnen et al., 2009	different	614	3.4	0.1	45
		615	3.4	0.1	40
Kim et al., 2017	590	615	2.3	0.1	14
Baumgartner J., 2013	340	614	1.5	0.1/0.5	20
		615	1.5	0.1/0.5	19
	355	614	3	0.1/0.5	17
		615	3	0.1/0.5	16
Meneghetti, 2012	355	611	10	0.1	23
Overbeeke et al., 1984	560	614	6	-1	28
Sharifimehr et al., 2016	780	615	3.55	0.1/0.62	6
Hwang et al., 2017	590	615	2.3/2.6	0.1	53
Matsuda and Yonezawa, 2022	509	615	2.9	0.1	15
Kim et al., 2018	590	615	2.6	0.1	42

Table 4.1: Overview of experimental fatigue data for lap joints

4.3.2. Laser-welded joints

As explained, the lap joint with a penetration weld is chiefly applied (section 4.1). For this joint, a large amount of fatigue data is available (Baumgartner et al., 2012; Sepe et al., 2020). Hence, only limited fatigue data is available for the investigated joints.

One study showed an increased fatigue resistance for a laser-welded single lap joint SS (615) compared to an arc-welded joint (Terasaki et al., 2001). However, the welding was performed with conduction laser welding and produced a big toe radius, partly explaining the enhanced fatigue strength (fig. 4.6). These results are not applicable as the keyhole welding method will be used.

The same joint geometry (615) was also welded with the keyhole welding method (fig. 4.7, see fig. 3.12 for fatigue data). Increased fatigue resistance was also observed compared to an arc-welded joint (Dourado et al., 2014). However, in this case, it was related to the enhanced properties of the welding process (see. section 3.4). In addition, it can be seen that a change in weld angle would improve the penetration, possibly avoiding the occurring root failure (fig. 4.7).
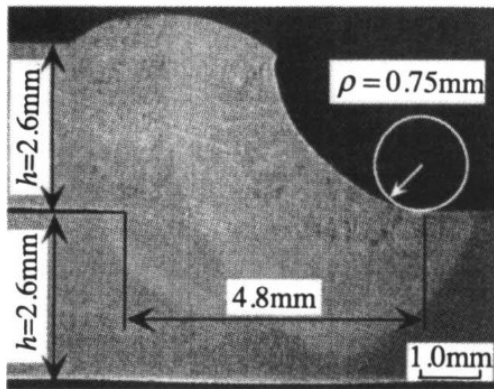
Figure 4.6: Micrograph conduction LBW lap joint (Terasaki et al., 2001)
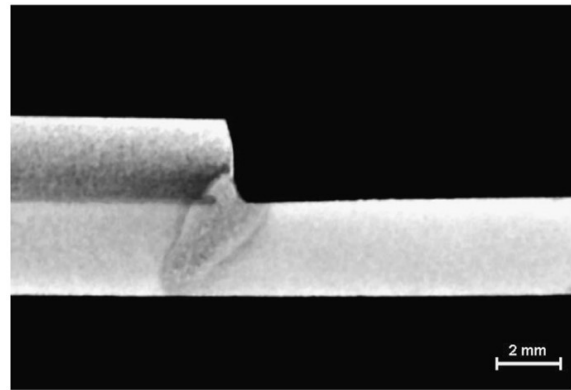
Figure 4.7: Micrograph keyhole LBW lap joint (Dourado et al., 2014)

4.3.3. Design aspects

Superficially, designing a lap joint might seem easy. However, the introduced eccentricity and the root failure are two main concerns of a proper design. In addition, to the normal design parameters of a welded joint, like the weld angle and penetration, the lap length is also to be considered.

The recommendations for lap joints are mostly based on engineering experience (File, 2001). This provides, in general, conservative results. The first studies have been performed to evaluate the influence of geometry on the fatigue strength of lap joints. A parametric study was performed for a cover plate that could be described as a NLC lap joint (Li et al., 2001). Here it was shown that an optimised weld geometry highly depends on the boundary conditions and the loading. Hence, every lap joint needs to be designed for its specific purpose. Furthermore, the appearance of a initial crack at the toe and root did not influence the failure location under pure membrane force and compressive bending stress at the weld toe (Li et al., 2001). The influence of porosity and weld bead shape on fatigue strength was also studied (Kim et al., 2018; Hwang et al., 2017). However, the limited data does not allow for any general conclusions.

As no general conclusions for a lap joint design can be drawn, each design needs to be evaluated by a fatigue concept. Here, multiple concepts were validated to be used to assess toe and root failure (Baumgartner J., 2013; Meneghetti, 2012; Fricke, 2013). However, more advanced concepts that consider the local contribution, like the ENSC, the peak stress method or the crack tip stress intensity, must be used to predict the failure location. None of these concepts were validated for the change in failure location for the single lap joint SS (615) described in section 4.2.1. However, it was shown that the crack path aligns with the path of the highest stress obtained from FE-calculations (Matsuda & Yonezawa, 2022).

5

Research Overview

A research gap (section 5.1) has been identified after the literature survey. A research hypothesis is defined (section 5.2), followed by the research questions (section 5.3).

5.1. Research gap

The ENSC shall be used for this thesis as it incorporates local information compared to the NSC and HSSSC. This allows for determining the failure location and only one fatigue resistance curve. In detail, the PENSC and LENSC methods should be evaluated.

The gradient method will not be included as it did not show a better performance than the PENSC and the LENSC for arc-welded lap joints (Baumgartner J., 2013). In addition, the gradient depends highly on the mesh size and cannot be obtained for $\rho = 0$, which is assumed for this thesis (Baumgartner J., 2013). Losing the physical representation leads to excluding the fictitious notch radius concept. Furthermore, using the LENSC instead of the fictitious notch stress concept increases fatigue performance by about 10% (Qin et al., 2019). The AENSC and VENSC are excluded as they only show improved behaviour under multiaxial loading and are more complex to implement (Liao et al., 2020). Lastly, it was revealed that the LENSC and the PENSC could be used to predict the failure location of arc-welded lap joints (Baumgartner J., 2013). So far, the LENSC and PENSC are not validated for laser-welded lap joints.

Furthermore, adapting the semi-analytical toe notch stress distribution for lap welds is missing, mainly a fitting function for the weld load-carrying stress. For the root stress distribution, it should be assessed if a similar breakdown of the stress contributions as for the toe stress distribution is possible. Here particular attention shall be paid to the influence of secondary bending moments in single lap joints, as the exact influence on the number of cycles and the loading ratio is unknown.

No experiments have yet been performed for laser-welded single lap joints DS (614). For the laser welded lap joint welded only from one side (615), no fatigue tests with thicknesses in exceedance of 3 mm have been performed. The obtained data from experiments will be used to establish the missing material characteristic parameter, ρ^*, a^* and γ, for laser welded joints and $S_e - N$ curves for the chosen concepts. Both fatigue assessment concepts should be validated to establish a prediction of the failure location.

5.2. Research hypothesis

Can the fatigue strength, separately, be estimated for each failure location of a laser- and arc-welded lap joint with the ENSC, and how is the fatigue performance?

5.3. Research questions

The following research questions lead to the answer to the research hypothesis.

1. How do the weld root and weld toe stress distribution for different laser- and arc-welded lap joint geometries look?

2. How do the secondary bending moments for a single-sided lap joint (614,615) influence the fatigue resistance?

3. What is the fatigue strength of arc-welded lap welds, and is it in line with the Mode-I fatigue resistance of other arc-welded joints in steel structures?

4. Can the LENSC and PENSC reliably predict the failure location for laser-welded joints?

5. Which of the two assessment concepts provides less conservative results?

6. How much does laser welding enhance the fatigue strength compared to arc welding?

7. What is the optimal geometry to avoid root failure and still show good fatigue strength?

II

Analysis & design

6
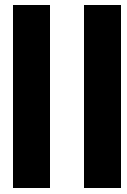
Through thickness weld notch stress distribution

The through thickness weld notch stress distribution along the radial coordinate (r) is needed to understand the fatigue behaviour and is, therefore, implemented in fatigue concepts like the ENSC (section 2.4). To obtain the weld notch stress, solid FE-calculations or the semi-analytical approach can be utilised (den Besten, 2015). When using a solid FE-model, the mesh must be fine enough to ensure no mesh dependency on the results. To avoid this time-consuming approach, a refined semi-analytical expression for the stress distribution was established (den Besten, 2015).

The following section will introduce the separate parts. First, the division into two parts, namely the self equilibrium equivalent part (section 6.2) and the equilibrium equivalent part (section 6.1), are introduced (fig. 6.1). The weld load-carrying stress formulation is refined for highly weld load-carrying joints (section 6.2.1). A linear superposition of the components with force and moment conditions yields the notch stress at the toe (section 6.3). The formulation for the root is established alike (section 6.4).
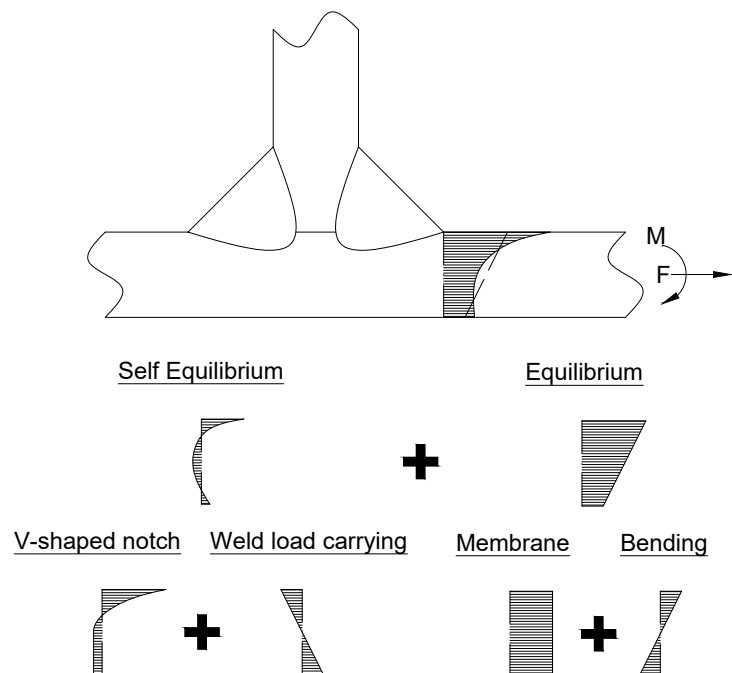
Figure 6.1: Schematic weld toe stress distribution of different contributions

Afterwards, parametric FE-studies are performed to introduce a fitting function for the C_{bw} and C_{bw2}. These fitting functions are established for the single lap joint DS (614) (section 6.6.3) and single lap joint SS (615) (section 6.6.4) for both the root and the toe. To obtain the far field stress from a beam/shell model, an enhanced model is introduced (section 6.7). The chapter is concluded with a discussion (section 6.8).

6.1. Equilibrium equivalent part

The equilibrium equivalent part is often referred to as far field stress distribution (σ_f). It mainly influences zone 3 of the stress distribution and comprises the membrane and the bending part (Niemi, 1995). The structural bending stress ratio (r_s) $r_s = \frac{\sigma_b}{\sigma_s}$ and σ_s can be obtained from FE-calculations with shell elements and from solid elements models with through thickness linearisation (section 2.3). Applying the surface extrapolation does not yield the necessary bending part bending contribution to the structural stress (σ_b). The σ_f formulation for the symmetrical case (eq. (6.1)) is similar to the one for the non-symmetrical case (eq. (6.2)).

$$\sigma_f\left(\frac{r}{t_p}\right) = \sigma_s\left\{1 - 2 * r_s * \frac{r}{t_p}\right\} \forall \left\{0 \leq \frac{r}{t_p} \leq 1\right\} \tag{6.1}$$

$$\sigma_f\left(\frac{r}{t_p}\right) = \sigma_s\left\{1 - 4 * r_s * \frac{r}{t_p}\right\} \forall \left\{0 \leq \frac{r}{t_p} \leq 0.5\right\} \tag{6.2}$$

6.2. Self equilibrium equivalent part

The self equilibrium equivalent part contains the weld load-carrying stress (section 6.2.1) and a V-shaped notch stress component (section 6.2.2) (den Besten, 2015). Their contribution to the force and moment integrated over the whole thickness is, by definition, zero.

6.2.1. Weld load carrying stress

The weld's geometry change induces the weld load carrying stress as the neutral axis shifts, generating a bending moment. The value of this stress distribution mainly depends on the geometry of the joint, particularly the weld size and penetration. This part has the primary influence on Zone 2. This influence is incorporated by the introduction of C_{bw}, which can be obtained by fitting the semi-analytical weld notch stress formulation to the solutions from a solid model or with a parametric fitting function (den Besten, 2015; Qin et al., 2019; Bufalari et al., 2022). The formulation was established for symmetrical (eq. (6.4)) and non-symmetrical joints (eq. (6.3)) (den Besten, 2015).

$$\sigma_{bw}\left(\frac{r}{t_p}\right) = \sigma_s * C_{bw} * \left\{2 * \frac{r}{t_p} - 1\right\} \forall \left\{0 \leq \frac{r}{t_p} \leq 1\right\} \tag{6.3}$$

$$\sigma_{bw}\left(\frac{r}{t_p}\right) = \sigma_s * C_{bw} * \left\{4 * \frac{r}{t_p} - 1\right\} \forall \left\{0 \leq \frac{r}{t_p} \leq 0.5\right\} \tag{6.4}$$

2nd order weld load carrying

For high load carrying geometries, the linear weld load carrying does not represent the apparent weld notch stress distribution (fig. 6.2). The maximum error occurs around half of the plate thickness and at the surfaces, appearing to be of quadratic shape for this arbitrary joint. This behaviour was already observed earlier, less pronounced though (den Besten, 2015).
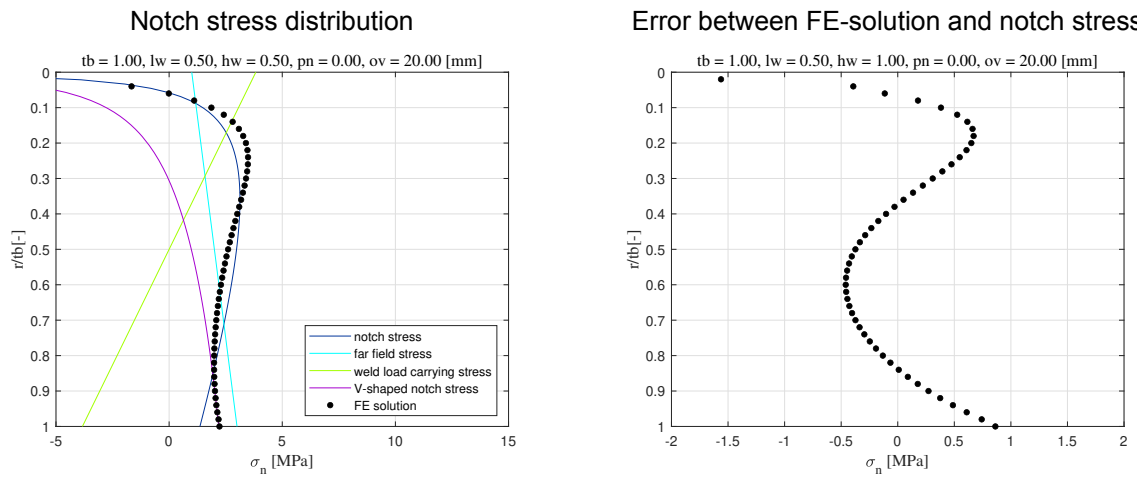
Figure 6.2: Example of through thickness stress distribution for single lap joint DS (614) at the toe with a high weld load carrying $(\sigma_s = 1, r_s = -1)$

Assuming for high load carrying load carrying joints, the neutral axis does not reach half of the plate thickness at the weld toe (fig. 6.3). In addition, the height difference between the neutral axes of the two plates enforces a moment on the weld leading to a bending behaviour inside the weld. This stress distribution follows the neutral axis. However, as the neutral axis has not reached half of the plate thickness at the location of the weld toe, the distribution only represents an upper part of the stress distribution, depending on the position of the neutral axis. The lower part results due to the force and moment equilibrium over the thickness. Hence, it has an opposite shape (fig. 6.3). In this case, the neutral axis is assumed to be at $0.25 * t_p$ at the location of the weld toe leading to the symmetrical behaviour. This triangular stress distribution shape is unrealistic as it is not continuous. Hence, a continuous quadratic shape is considered. Furthermore, the linear weld load carrying part induced by the change in the neutral axis is still apparent.
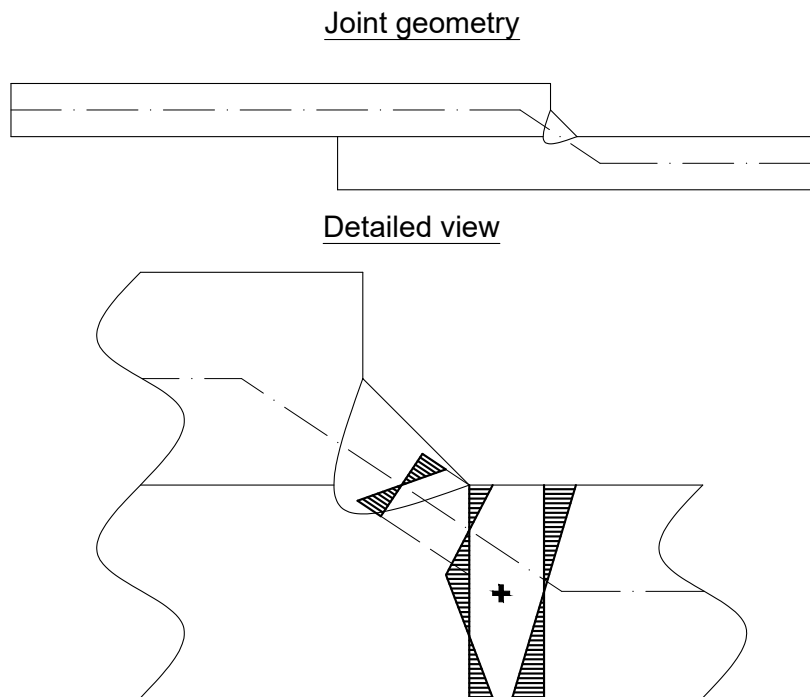
Figure 6.3: Schematic sketch of geometry and load carrying stress

To fulfil the independence of 2nd order weld load carrying formulation concerning the force and momentum equilibrium, the maximum is set to be at $0.5 * t_p$. C_{bw2} is introduced for scaling the influence of the 2nd order weld-load carrying. This leads to the following equations for the non-symmetrical and symmetrical case (eq. (6.5), eq. (6.6)).

$$\sigma_{bw}\left(\frac{r}{t_p}\right) = \sigma_s * \left\{ C_{bw} * \left[2 * \frac{r}{t_p} - 1 \right] + C_{bw2} * \left[\frac{1}{12} - \left(\frac{r}{tp} - \frac{1}{2} \right)^2 \right] \right\} \forall \left\{ 0 \leq \frac{r}{t_p} \leq 1 \right\} \tag{6.5}$$

$$\sigma_{bw}\left(\frac{r}{t_p}\right) = \sigma_s * \left\{ C_{bw} * \left[4 * \frac{r}{t_p} - 1 \right] + C_{bw2} * \left[\frac{1}{12} - \left(\frac{r}{tp} - \frac{1}{2} \right)^2 \right] \right\} \forall \left\{ 0 \leq \frac{r}{t_p} \leq 0.5 \right\} \tag{6.6}$$

Implementing the established equations for the arbitrary joint yields a better fit (fig. 6.4). However, as the Least Squares fitting aims for the best overall fit, there is some overshoot from $0.2 * t_p$ up to the notch. Furthermore, the highest value appears around $0.55 * t_p$, showing the incorrectness of the before-made assumption of the maximum being at $0.5 * t_p$, but that the maximum point might depend on the weld geometry and loading. However, the small error introduced by this and the increased effort to change the maximum point according to the joint geometry leads to the decision to keep the maximum position at $0.5 * t_p$.
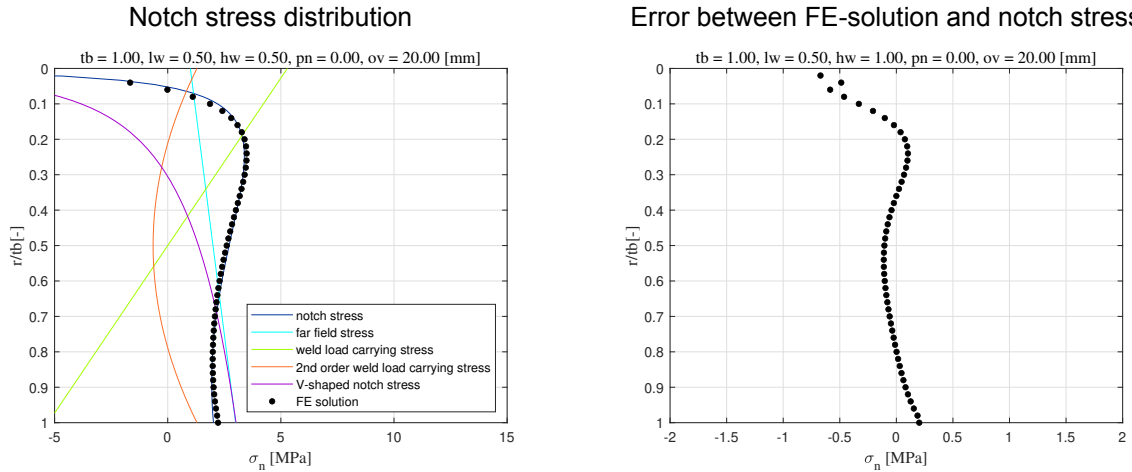
Figure 6.4: Example of through thickness stress distribution for single lap joint DS (614) at the toe with 2nd order weld load carrying ($\sigma_s = 1, r_s = -1$)

6.2.2. V-shaped notch stress

The missing contribution is the V-shaped notch stress distribution, covered by the Airy stress function (φ), contributing the most to zone 1 (Williams, 1952). A notch radius $\rho = 0$ and linear elastic continuum mechanics underpin this concept. The resulting stresses are given in a polar coordinate system. The function incorporates symmetrical and anti-symmetrical terms (eq. (6.7)).

$$\varphi = r^{\lambda+1} * [C_1 * cos\{(\lambda+1)\theta\} + C_2 * cos\{(\lambda-1) + \theta\} + C_3 * sin\{(\lambda+1)\theta\} + C_4 * sin\{(\lambda-1) + \theta\}] \tag{6.7}$$

The different stress contributions are related to different derivatives of the Airy stress function (eq. (6.8)). However, only the tangential stress component (polar coordinate) ($\sigma_{\theta\theta}$) and shear stress component (polar coordinate) ($\sigma_{r\theta}$) can introduce cracks. Therefore, the radial stress component (polar coordinate) (σ_{rr}) is neglected from now on.

$$\sigma_{rr} = \frac{1}{r}\frac{\partial \varphi}{\partial r} + \frac{1}{r^2}\frac{\partial^2 \varphi}{\partial \theta^2}$$

$$\sigma_{\theta\theta} = \frac{\partial^2 \varphi}{\partial r^2}$$

$$\sigma_{r\theta} = \frac{\partial}{\partial r}\left(\frac{1}{r}\frac{\partial \varphi}{\partial \theta}\right) \tag{6.8}$$

Including the boundary conditions of zero tangential ($\sigma_{\theta\theta}$) and shear stress ($\sigma_{r\theta}$) at the surface, the eigenvalue problem is obtained with notch angle (α) (eq. (6.9)) (den Besten, 2015).

$$\left.\begin{cases} \lambda sin(2\alpha) + sin(\lambda 2\alpha) = 0 \\ \lambda sin(2\alpha) - sin(\lambda 2\alpha) = 0 \end{cases}\right\} \forall (\lambda > 0, \lambda \neq 1) \tag{6.9}$$

The conditions for the eigenvalue include the finite strain energy (Barber, 2002) and no null-forms (den Besten, 2015). The solution will consist of at least one eigenvalue for the symmetric (Mode-I) and anti-symmetric (Mode-II) part corresponding first eigenvalue of (anti-)symmetry part (λ_a, λ_s) and first eigenvalue coefficient of (anti-)symmetry part (χ_a, χ_s) with stress angle (β). Including the boundary conditions in the equation for the tangential stress gives the final expression (eq. (6.10)) (den Besten, 2015).

$$\sigma_{\theta\theta}\left(\frac{r}{t_p}\right) = \sigma_s * \left\{ \left(\frac{r}{t_p}\right)^{\lambda_s - 1} \mu_s \lambda_s + 1[cos\{(\lambda_s + 1)\beta\} - x_s cos\{(\lambda_s - 1)\beta\}] \right. \tag{6.10}$$

$$\left. + \left(\frac{r}{t_p}\right)^{\lambda_a - 1} \mu_a \lambda_a + 1[sin\{(\lambda_a + 1)\beta\} - x_a sin\{(\lambda_a - 1)\beta\}] \right\}$$

6.3. Toe notch stress distribution

The crack path is assumed to progress vertically through the plate thickness for a Mode-I loading (den Besten, 2015; Baumgartner J., 2013). For this case, the linear superposition of the three before-mentioned contributions - σ_f, weld load-carrying stress (σ_{bw}) and $\sigma_{\theta\theta}$ - gives weld toe notch stress distribution (σ_n) (eq. (6.11)) (den Besten, 2015).

$$\sigma_n\left(\frac{r}{t_p}\right) = \sigma_s * \left\{ \left(\frac{r}{t_p}\right)^{\lambda_s - 1} \mu_s(\lambda_s + 1)[cos\{(\lambda_s + 1)\beta\} - x_s cos\{(\lambda_s - 1)\beta\}] \right.$$

$$\left. + \left(\frac{r}{t_p}\right)^{\lambda_a - 1} \mu_a(\lambda_a + 1)[sin\{(\lambda_a + 1)\beta\} - x_a sin\{(\lambda_a - 1)\beta\}] + C_{bw} * \left[2*\left(\frac{r}{t_p}\right) - 1\right] - 2r_s\left(\frac{r}{t_p}\right) \right\}$$

$$\tag{6.11}$$

The α and β are defined with the weld length (l_w) and weld height (h_w) :

$$\alpha = \frac{1}{2} * \left\{ \pi + arctan\left(\frac{h_w}{l_w}\right) \right\}$$

$$\beta = \alpha - \frac{\pi}{2}$$

The weld joint geometries can be divided into symmetry and non-symmetry ones regarding $\frac{t_p}{2}$. However, symmetrical joints are not covered by this thesis. Hence, only the non-symmetry solution is presented here. The stress amplitude of (anti-)symmetry part (μ_a, μ_s) can be obtained using force and moment conditions. The σ_n must have the same moment and force over the thickness as the σ_f (eq. (6.12)).

$$\int_0^1 \left\{ \sigma_n \left(\frac{r}{t_p} \right) \right\} d\left(\frac{r}{t_p} \right) = \int_0^1 \sigma_s \left\{ 1 - 2r_s \left(\frac{r}{t_p} \right) \right\} d\left(\frac{r}{t_p} \right)$$

$$\int_0^1 \left\{ \sigma_n \left(\frac{r}{t_p} \right) \right\} \left(\frac{r}{t_p} \right) d\left(\frac{r}{t_p} \right) = \int_0^1 \sigma_s \left\{ 1 - 2r_s \left(\frac{r}{t_p} \right) \right\} \left(\frac{r}{t_p} \right) d\left(\frac{r}{t_p} \right) \tag{6.12}$$

The solution of this system (eq. (6.12)) yields the μ_a, μ_s:

$$\mu_s = \frac{C_{bw}(\lambda_a + 1) + 3(\lambda_a - 1)}{6(\lambda_a - \lambda_s)[cos\{(\lambda_s + 1)\beta\} - \chi_s cos\{(\lambda_s - 1)\beta\}]}$$

$$\mu_a = -\frac{C_{bw}(\lambda_s + 1) + 3(\lambda_s - 1)}{6(\lambda_a - \lambda_s)[sin\{(\lambda_a + 1)\beta\} - \chi_a sin\{(\lambda_a - 1)\beta\}]}$$

6.4. Root notch stress distribution

Root failure typically occurs along the throat of a weld, but it depends on the loading conditions (Fricke, 2013; Nykänen, n.d.) (section 4.2.2). This introduces an artificial plate thickness (t_p') and artificial radial coordinate (r') along the crack path, correspondingly structural stress at the root (σ_{sr}) is added. In addition, symmetrical cases are rare and not apparent in this work. Hence, only the solution for the non-symmetrical joints is presented.

The Williams asymptotic solution, as presented before (section 6.2.2), describes the influence of the notch. However, $\alpha = 2\pi$ is assumed for the root due to the crack-like shape. Leading to a simplified formulation of $\sigma_{\theta\theta}$ (den Besten, 2015):

$$\sigma_{\theta\theta}\left(\frac{r'}{t_p'} \right) = \sigma_{sr} * \sum_{i=1}^n \left\{ \left(\frac{r'}{t_p'} \right)^{\lambda_i - 1} \lambda_i(\lambda_i + 1)(\mu_{1i}[cos\{(\lambda_i + 1)\beta\} - \chi_i cos\{(\lambda_i + 1)\beta\}] \right.$$

$$\left. - \mu_{3i}[sin\{(\lambda_i + 1)\beta\} - sin\{(\lambda_i - 1)\beta\}]) \right\}$$

with

$$\lambda_i = \frac{n}{2}, n = 1, 3, 5, 7, 9...$$

$$\chi_i = \frac{(\lambda_i + 1)}{(\lambda_i - 1)}$$

Using two terms of the Williams solution allows for fulfilling the moment and force condition, yielding eigenvalue (asymptotic solution) (λ_i) and eigenvalue coefficient of asymptotic solution (χ_i). In addition, making use of $\beta = \frac{\pi}{2}$ a simplified v-shaped notch stress formulation is obtained:

$$\sigma_{\theta\theta}\left(\frac{r'}{t_p'} \right) = -\sigma_{sr} \frac{3 * \sqrt{2}}{4 * \sqrt{\frac{r'}{t_p'}}} \left(15 * \left(\frac{r'}{t_p'} \right) * \mu_{1i} + 5 * \left(\frac{r'}{t_p'} \right) * \mu_{3i} - \mu_{1i} - \mu_{3i} \right)$$

Applying the same linear superposition of the three different contributions as for the toe distributions leads to weld root notch stress distribution (σ_{nr}) (eq. (6.13)).

$$\sigma_{nr}\left(\frac{r}{t_p} \right) = \sigma_{sr} * \left\{ \frac{3 * \sqrt{2}}{4 * \sqrt{\frac{r'}{t_p'}}} \left(15 * \left(\frac{r'}{t_p'} \right) * \mu_{1i} + 5 * \left(\frac{r'}{t_p'} \right) * \mu_{3i} - \mu_{1i} - \mu_{3i} \right) \right.$$

$$\left. + C_{bw} * \left[2 * \left(\frac{r'}{t_p'} \right) - 1 \right] - 2r_{sr}\left(\frac{r'}{t_p'} \right) \right\} \tag{6.13}$$

Only non-symmetrical joints are considered for a root-initiated crack. Utilizing moment and force conditions on σ_{nr} (eq. (6.14)) yields the stress component amplitude (μ_i) (eq. (6.15)).

$$\int_0^1 \left\{ \sigma_{nr}\left(\frac{r'}{t_p'}\right) \right\} d\left(\frac{r'}{t_p'}\right) = \int_0^1 \sigma_s \left\{ 1 - 2r_{sr}\left(\frac{r'}{t_p'}\right) \right\} d\left(\frac{r'}{t_p'}\right)$$

$$\int_0^1 \left\{ \sigma_{nr}\left(\frac{r'}{t_p'}\right) \right\}\left(\frac{r'}{t_p'}\right) d\left(\frac{r'}{t_p'}\right) = \int_0^1 \sigma_{sr}\left\{ 1 - 2r_{sr}\left(\frac{r'}{t_p'}\right) \right\}\left(\frac{r'}{t_p'}\right) d\left(\frac{r'}{t_p'}\right) \tag{6.14}$$

$$\mu_{1i} = \frac{\sqrt{2}(C_{bw} - 3)}{24}$$

$$\mu_{3i} = -\frac{\sqrt{2}(C_{bw} - 1)}{4} \tag{6.15}$$

6.5. Secondary bending moments

Single lap joints are eccentric joints. This characteristic introduces additional bending moments under tensile loading, resulting in additional joint deformation. Under bending, no secondary bending moments are apparent (Andrews, 1996). Hence, the magnitude of the secondary bending moments depends on the load applied and boundary conditions, a nonlinear effect (section 4.2.1). Therefore, every nominal stress introduces a different amount of additional secondary bending moments. Thus, multiplying S_n with one K_f to obtain S_e is not valid. The effective notch stress must be calculated for every nominal stress in the stress cycle. However, this is not practical as it demands excessive computation. Hence, it is assumed that the shape of the effective stress cycles still equals a sine curve defined by the maximum and minimum effective stress related to the maximum and minimum nominal stress.
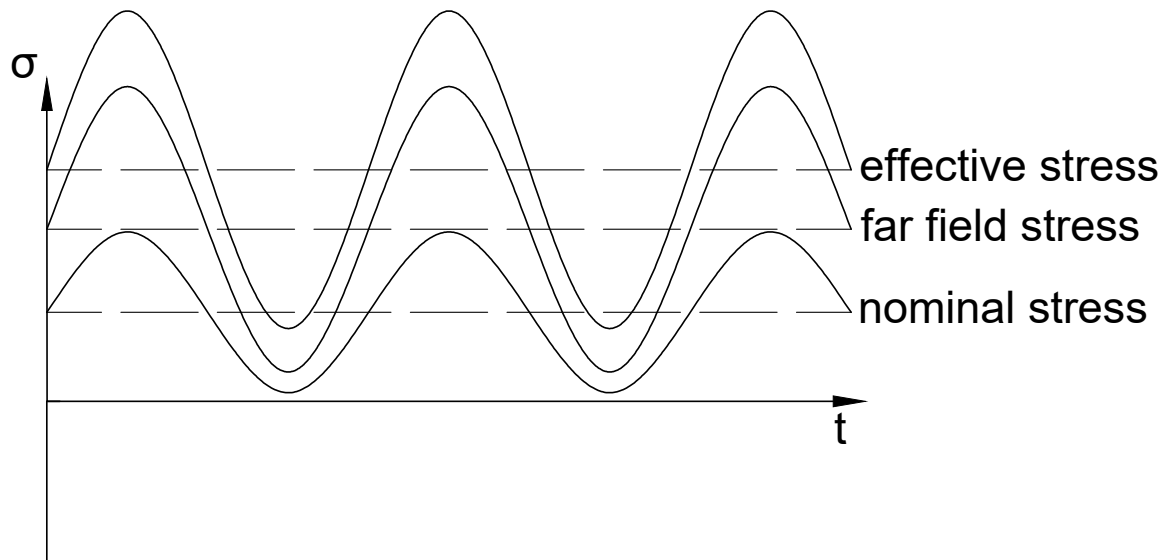
Figure 6.5: Schematic nominal, structural and effective stress cycle

Furthermore, the secondary bending moments are an effect introduced by the overall geometry, not the weld geometry specifically. Therefore, it is assumed that the secondary bending moments are far field related. Hence, the far field stress and the effective stress are proportional (fig. 6.5).

To prove this assumption, FE calculations under different nominal stresses are performed, simulating a Mode-I uniaxial tensile loading. To capture the secondary bending effects, the FE calculations are performed with non-linearity regarding the geometry. The modelled geometry is a single lap joint DS (614) similar to the one used for the experiments (section 7.3.1). The calculations are performed for $\sigma_N = 1, 100, 200, 300, 400 [MPa]$.

Firstly, the notch stress distributions are plotted as absolute values (fig. 6.6), showing the different nominal stresses. To compare them, they are normalized with the Nominal stress (σ_N). Here the eccentricity introduced bending can be seen proofing non-linearity between the nominal stress and the effective stress. Normalizing the notch stress with σ_s gives already a better fit. Especially in Zone-I, where the influence of σ_s is the more powerful than the one of r_s. Furthermore, the alignment over the whole thickness is improved. However, the bending contribution still separates the notch stress distributions of different nominal stresses. To account for the bending contribution, the far field contribution is subtracted. Hence, only the self equilibrium equivalent part is left. Now all five stress distributions align. Therefore, it is proven that the secondary bending moments are a far field related effect. Although, a slight difference is still likely to occur as the r_s is different for each nominal stress and a relation between r_s and C_{bw} is proven (Bufalari et al., 2022) (section 6.6).
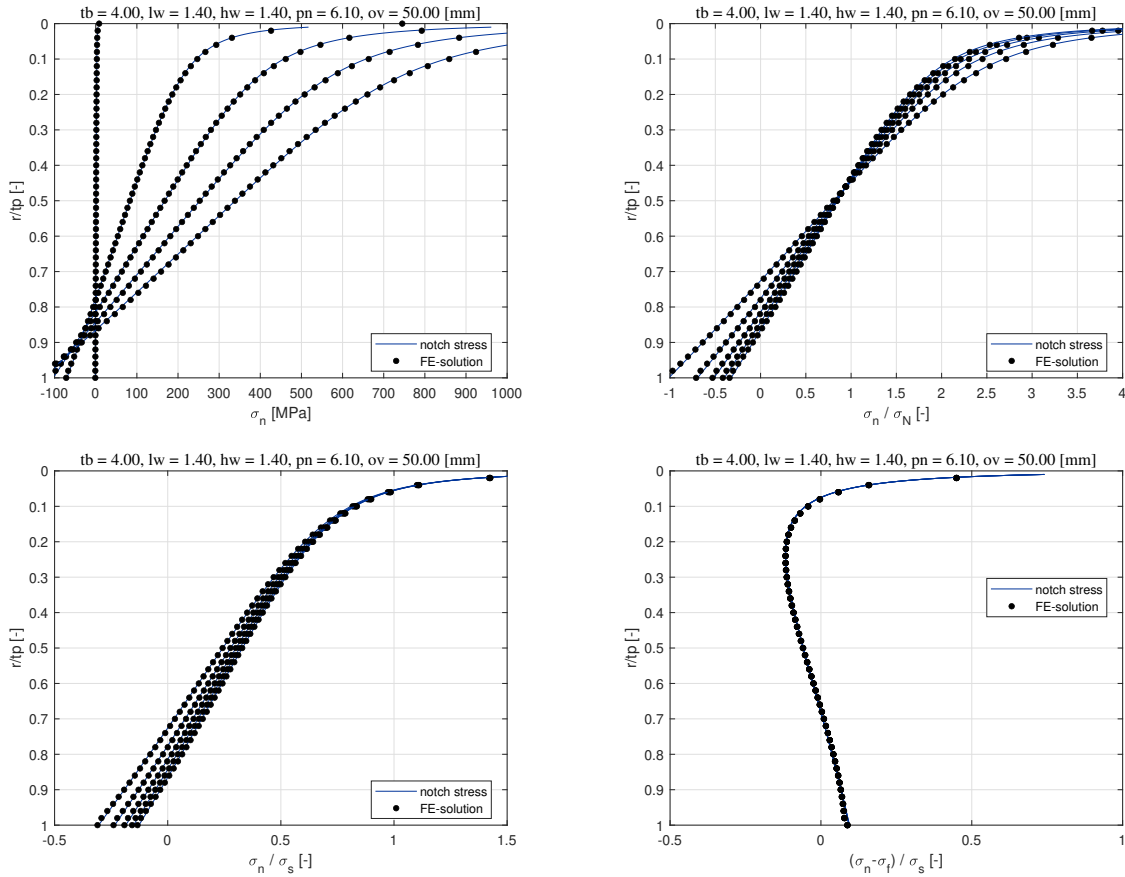
Figure 6.6: Through thickness stress distribution of single lap joint DS (614) at the toe under different nominal stresses

6.6. Weld load carrying fitting function

The fitting functions yielding C_{bw} and C_{bw2} for lap joints are developed in this section. Firstly, the methodology is introduced (section 6.6.1), followed by the Parametric FE-study (section 6.6.2). Afterwards, the fitting functions are established for the single lap joint DS (614) (section 6.6.3) and the single lap joint SS (615) (section 6.6.4).

6.6.1. Methodology

Initially, parametric FE studies are performed to obtain through thickness stress distributions. The nodal forces in the x-direction along the crack path for the root and the toe are extracted from the FE calculations. In case of geometries welded from two sides the right weld is examined (fig. 6.10). To obtain the far-field stress related σ_s and r_s through-thickness linearization is utilized (Dong, 2005). The nodal forces are transferred to stresses by dividing by the length represented by each element. A further division by the width is unnecessary, as all calculations are performed in unit width. These results are fitted with a nonlinear least squares approach from the Matlab Fit toolbox to the corresponding semi-analytical distribution by changing the C_{bw} and C_{bw2}. For this fitting, the point at the surface $\frac{r}{t_p} = 0$ is excluded due to the singularity.

Firstly, only cases with $-1 < rs < 1$ are included for the root. Extreme r_s arise when the σ_b and σ_m have a close absolute value but an opposite sign. Although these extreme r_s might be realistic, they do not allow finding a fitting function for the C_{bw} and are thus excluded.

Secondly, some extreme geometries do not allow the stresses to reach an equilibrium over the whole thickness at the location of the toe/root. In those cases, the stresses only reach over a certain fraction of the thickness (fig. 6.8). This behaviour cannot be covered with the established semi-analytical functions as these assume a stress distribution over the whole thickness. Hence, when trying to fit such a stress distribution to the semi-analytical formulas, non-realistic C_{bw} and C_{bw2} are achieved (fig. 6.8). Hence, the quality of the fit is, in this case, not good.

Attempts to capture these extreme geometries by restricting the maximal allowed C_{bw} and C_{bw2} values did not work, as some not extreme geometries show higher values than some extreme geometries do (fig. 6.7; here the maximum of 9 is derived from the final fitting fig. 6.16). Therefore, this restriction does not lead to a clear separation. Furthermore, locating these extreme geometries by the quality of fit between the semi-analytical stress distribution and the FE solution did not work either, as some extreme geometries with unrealistic C_{bw} and C_{bw2} values still showed a good fit (fig. 6.7). Hence, this restriction might work as an engineering-based approach but does not suffice the scientific standard.
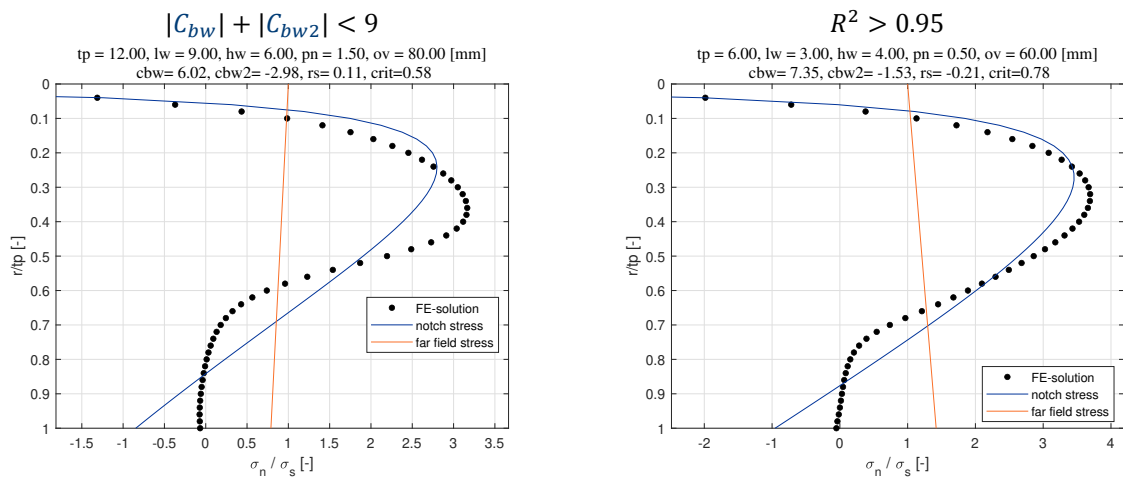
Figure 6.7: Example of possible restrictions for single lap joint DS (614) at the root

Therefore, a geometry-based criterion is developed. The criterion expresses the relation between the plate thickness and the height of an extension of the weld geometry until the location of the root reaches (X) (fig. 6.9; eq. (6.16)). The idea is to describe the position up to where the stresses reach. For this, it is assumed that the stresses follow the angle of the weld. This assumption seems reasonable looking at fig. 6.7 and fig. 6.8. Therefore, a criterion value bigger than one relates to geometries where the stress reaches over the whole thickness. This criterion is a simplified approach and does not entirely cover the complex behaviour. Hence, this might exclude geometries where an equilibrium over the whole thickness is reached and include ones where it is not.

tp = 8.00, lw = 2.00, hw = 2.00, pn = 0.50, ov = 100.00 [mm]
cbw= 39.09, cbw2= -86.34, rs= -0.33, crit=0.31
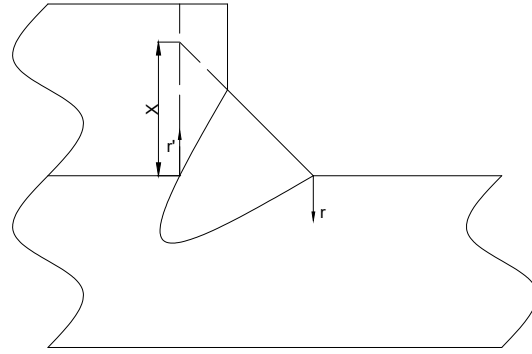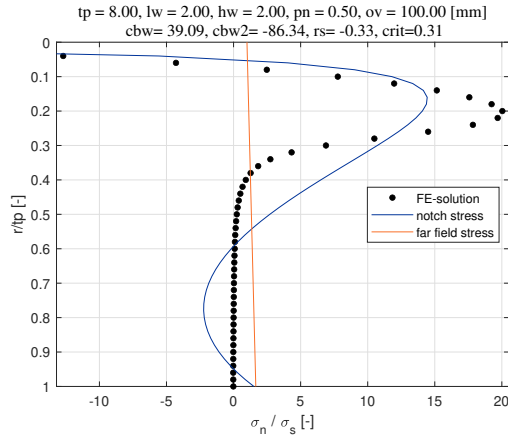
Figure 6.8: Example of extreme geometry for the root of a dou- Figure 6.9: Sketch of extreme criterion
ble lap joint DS (614)

$$Criterion = \frac{X}{t_p} = \frac{(pn + lw) * hw}{lw * t_p} \tag{6.16}$$

Lastly, using dimensionless parameters describing the weld geometry, an exponential fitting function for the C_{bw} and C_{bw2} is obtained. One fitting function modelling laser- and arc-welded joints for ease of use and better robustness is established with the MultiPolyRegress toolbox in Matlab. The fitting function is limited to have at least an R^2 of 0.95 and not more than 100 coefficients to provide usability by still achieving a reasonable accuracy. As done for other studies, the exponents for the dimensionless parameters are limited to 4 (Qin et al., 2019; Bufalari et al., 2022).

6.6.2. Parametric Finite-element-study

The parameters for the studies are chosen to fit typical values of arc- and laser-welded joints (table 6.1; fig. 6.10). Laser-welded joints typically show a smaller weld geometry and deeper penetration than arc-welded joints. Joint geometries where the weld height exceeds the thickness are not modelled. The lap length does not influence the single lap joint SS (615) as it is modelled without contact between the upper and lower plate. Hence, for this joint, only the lap length of 10 mm is modelled.
The FE calculations are performed in ANSYS with 42 plane elements to capture the nodal forces with linear elastic material behaviour (table 6.2). The element size is set to result in 50 elements over plate thickness (t_p) as done in other studies (Bufalari et al., 2022). In addition, the element size is growing between the lap part's penetration points to allow for reasonable calculation time (fig. 6.11). The left side of the FE model is clamped. On the right side, the forces are applied (eq. (6.17)), where the σ_s is always kept to equal 1 MPa.

Single lap joint DS (614)
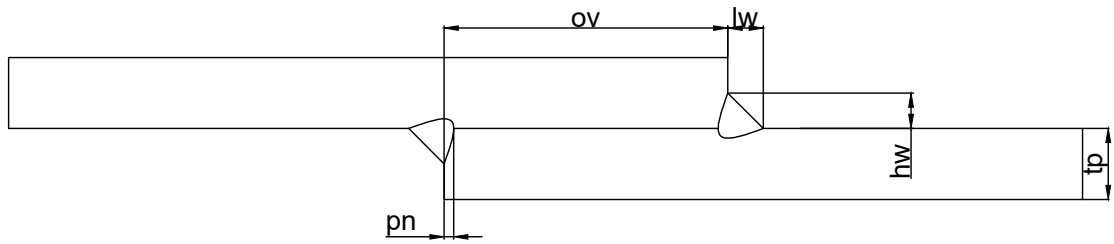
Single lap joint SS (615)
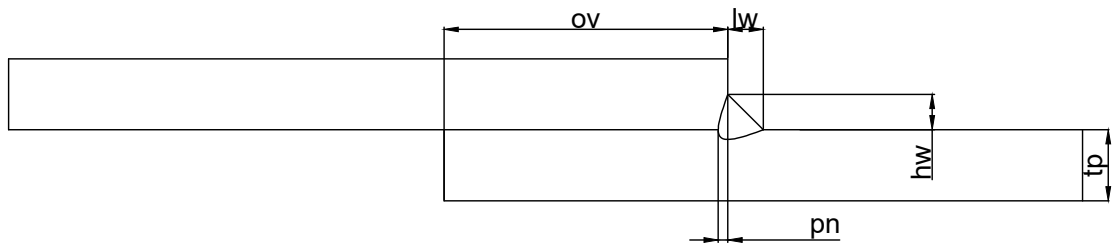
Figure 6.10: Weld geometry of single lap joints

	arc-welded	laser-welded
tp [mm]	2,4,6,8,10,12	
hw/lw [-]	0.5,0.75,1,1.5	
pn [mm]	0.5,1,1.5,2,3	2,3,4,6,8
ov [mm]	10,20,40,60,80,100	
r_s [-]	-1,-0.5,0,0.5,1	
hw [mm]	2,4,6,8	1,1.5,2,3

Table 6.1: Geometry parameters for the Finite-element-model

$$\sigma_b = r_s * \sigma_s$$
$$\sigma_n = \sigma_b * \left(\frac{1}{r_s} - 1 \right) \tag{6.17}$$
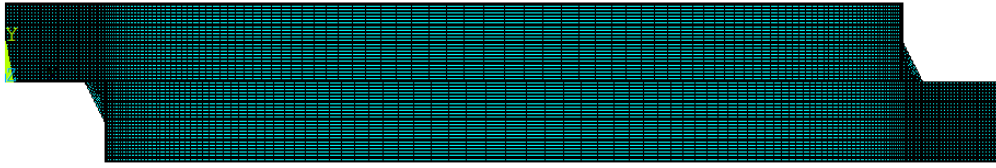
Figure 6.11: FE-model for a single lap joint DS (614)

E-modulus [MPa]	$2.10 * 10^5$
Poison ratio [-]	0.33
Density [kg/mm³]	$7.85 * 10^{-6}$

Table 6.2: Material properties of steel

6.6.3. Single lap joint DS (614)

The parametric study resulted in 23,680 unique geometries. The criterion is not employed in this fit. To decide whether 2nd order weld load carrying is needed, the relative error between the FE-solution and the semi-analytical stress distribution normalized with σ_s is calculated. The mean and standard deviation of the error are plotted over the normalized thickness (fig. 6.12). Due to the asymptotic behaviour of the notch stress, the error shows the same behaviour. Hence, considering the error close to the surface does not reflect the fit quality. For the toe, linear weld load carrying gives sufficient results, but the 2nd order behaviour is observed. The 2nd order weld load carrying shows an enhanced fit, coupled with the higher accuracy in Zone 2, which significantly influences the value of the S_e, resulting in using this one.
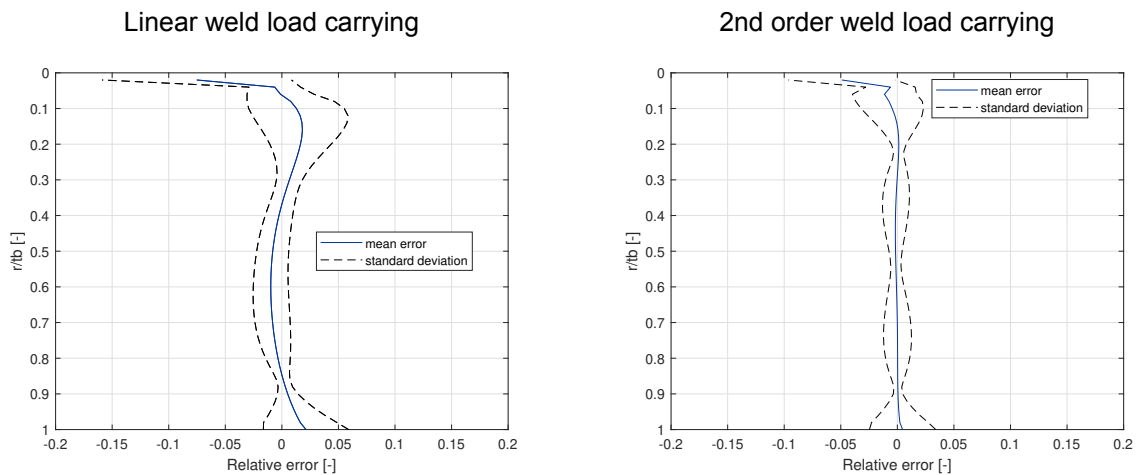
Figure 6.12: 2nd order weld load carrying relative error for single lap joint DS (614) at the toe

Looking at an arbitrary joint, the semi-analytical formulas provide a perfect fit (fig. 6.13). In addition, the C_{bw} and C_{bw2} values are already close to extreme values obtained for less load carrying joints (Qin et al., 2019). The results for the geometry with the highest C_{bw} and C_{bw2} do not show a good fit. However, this error is presumably caused by the fixed position of the maximum stress for the 2nd order weld load carrying formulation, as the maximum seems to be close to $0.75t_p$. Hence, not the same error type is observed compared to the one which the criterion was developed for. Interestingly, the

stresses close to the notch are compressive, although the structural stress is tensile. The negative r_s is likely to be the reason for this. Overall, the resulting fit from the semi-analytical formulas is sufficiently good, especially as the ENSC related material parameters are Zone 2 ones.
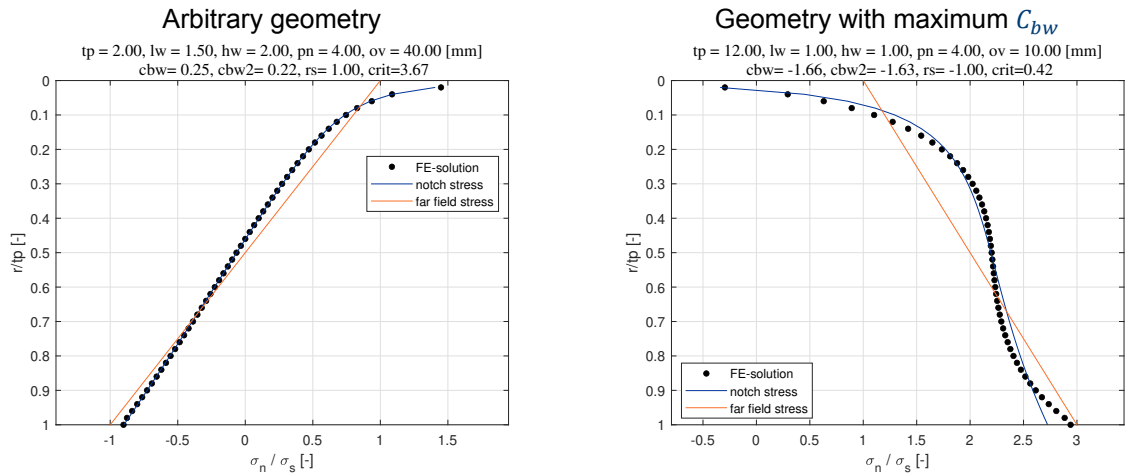
Figure 6.13: Example of through thickness stress distribution for single lap joint DS (614) at the toe

Geometries exceeding a value of 1 for the criterion for extreme geometries had to be excluded for the root. Together with the restriction on the r_s, 8334 geometries are looked at. For the root, the 2nd order behaviour is highly apparent. When accounted for, it significantly improves the mean and the standard deviation (fig. 6.14). The error occurring in the 2nd order weld load carrying, indicating a higher order behaviour, is caused by the assumed location of the maximum stress in the definition of the 2nd order weld load carrying. The maximum stress is set to be at $0.5t_p$, whereas the maximum, in this case on average, seems to be at $0.6t_p$.
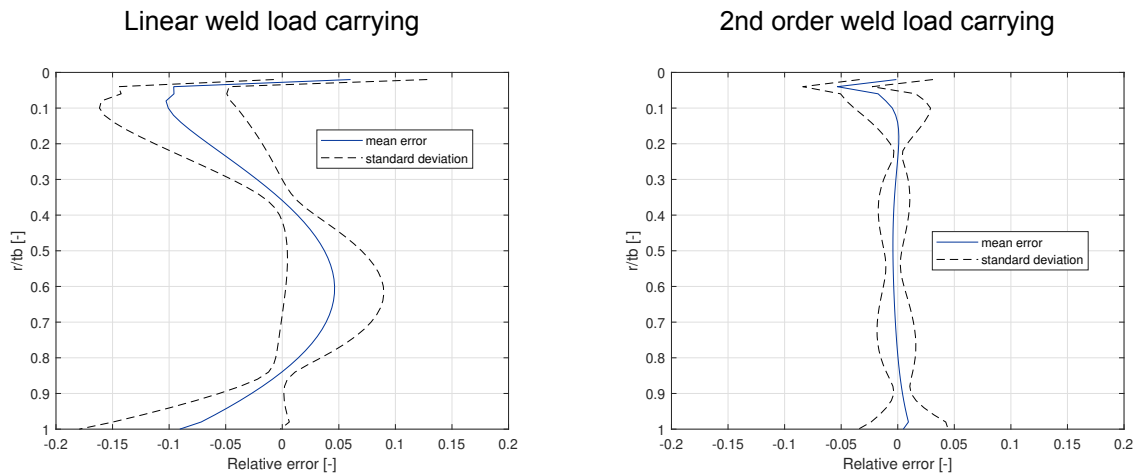
Figure 6.14: 2nd order weld load carrying relative error for single lap joint DS (614) at the root

Similar to the toe, the arbitrary joint geometry shows a good fit between the FE-solution and semi-analytical formulations (fig. 6.15). A worse fit is apparent when looking at the geometry with maximum C_{bw}. Here the criterion indicates that the stresses have reached the whole thickness. However, the actual stress distribution only reaches about $0.8t_p$ showing the weakness of this criterion. Despite this error, the fitting is still sufficient for a Zone 2 parameter.
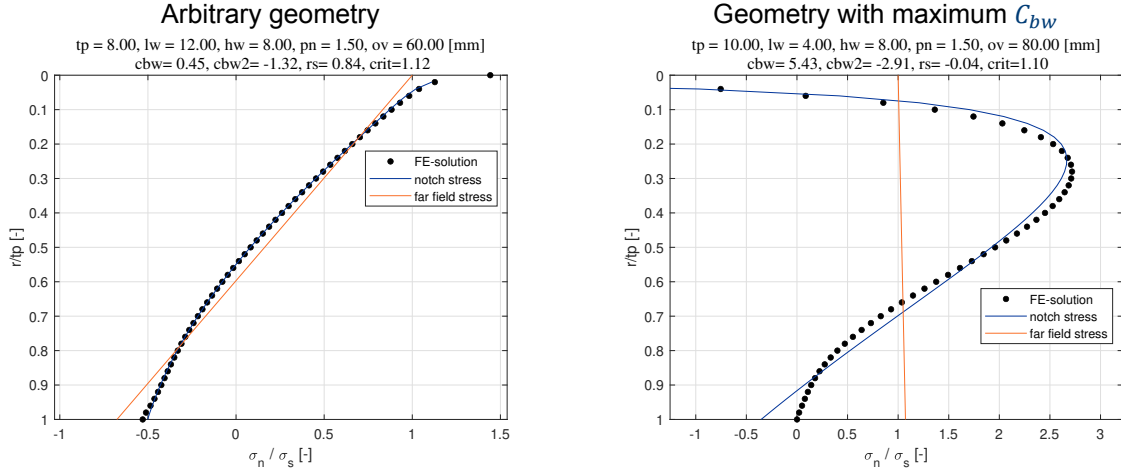
Figure 6.15: Example of through-thickness stress distribution for single lap joint DS (614) at the root

The non-dimensional parameters introduced for the fitting function at the toe are similar to the ones used before (Qin et al., 2019; Qin et al., 2020; Bufalari et al., 2022)(eq. (6.18)). The load path related parameter T is adapted to represent the lap length instead of the cross plate thickness of a cruciform/T-joint (Bufalari et al., 2022). In addition, the variability in the penetration of the weld resulted in an additional parameter linking the penetration to the weld height. A second load path related parameter is introduced as well. Here the lap length is correlated to the overall length of the weld obtained by adding the weld length and the penetration. Furthermore, r_s is used as a parameter for the fitting functions. Each non-dimensional parameter's exponent is chosen to provide the best result with the least number of coefficients under the given conditions (section 6.6.1).

$$P = \frac{pn}{hw}$$
$$T = log\left(\frac{ov * 0.5 + lw}{tb}\right)$$
$$O = \frac{ov}{lw + pn}$$
$$W = \frac{lw}{hw}$$
$$Q = \frac{lw}{tb} \tag{6.18}$$

For the C_{bw} a good fit is found for P, r_s, T^4, O^2, W and Q (eq. (C.1)). Firstly, the C_{bw} values are significantly larger than those discovered for other joints where values of 0.3 were extreme (Qin et al., 2019; Bufalari et al., 2022)(fig. 6.16). However, no joints with a similar high weld load-carrying level have been assessed yet. For C_{bw}, the laser-welded geometries show higher absolute values. The fitting function represents both welding geometry well, seen in the same scatter band.

For the C_{bw2}, a high dependency on C_{bw} is located. Furthermore, this allowed to reduce the amount of used dimensionless parameters to 5. A good fit is found for O, T^4, W, r_s and C_{bw} (eq. (C.2)). Both arc- and laser-welded geometries cover the whole range of C_{bw2} values (fig. 6.16). For $-0.5 < C_{bw} < 1$ of arc-welded geometries, the scatter is significantly higher than for the laser-welded geometries. In addition, the arc-welded geometries show higher values of C_{bw2}. A reason for the higher scatter cannot be identified. Overall, the fitting functions can represent both arc-welded and laser-welded geometries. Resulting in a fitting function for each the C_{bw} and C_{bw2}, which both show a sufficient accuracy (fig. 6.16).
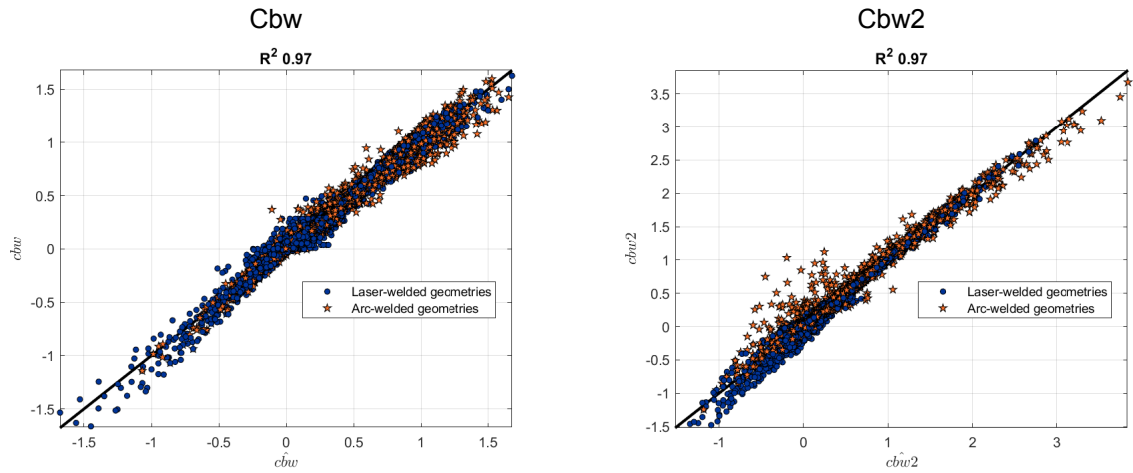
Figure 6.16: Goodness of fit scatter plot for the toe of the single lap joint DS (614)

For the fitting of the C_{bw} values at the root, most of the factors from the fitting for the toe do show a substantial influence. However, the Q is excluded due to insignificance. In exchange, S is added, linking the structural stress of the root and the toe (eq. (6.19)). Although this is not a direct parameter, as many factors are included in these values, no other parameter with a similar substantial influence is found.

$$S = \frac{\sigma_s}{\sigma_{sr}} \tag{6.19}$$

The optimum with regard to fitting quality and amount of coefficients is obtained at P^2, r_s, T^4, O, W, S (eq. (C.3)). The values of C_{bw} are twice as high as the C_{bw} for the toe (fig. 6.17). The C_{bw} exceeding values of 3 seems to be extreme cases, which are not captured by the criterion, as seen for the geometry with the maximum C_{bw} (fig. 6.15). Still, the weld load carrying of the root appears higher than that of the toe. Interestingly, no difference in extreme C_{bw} values for arc- and laser-welded geometries is observed, opposite to the toe. The C_{bw} values for arc-welded joints between 1 and 1.5 show an underestimation of the fitting function, indicating a relation not covered by the fitting function.

Similar to the C_{bw2} for the toe, the number of dimensionless parameters included is reduced with the optimum lying at P^4, T^2, O, W, r_s and C_{bw} (eq. (C.4)). The C_{bw2} fitting function shows a higher scatter for arc-welded geometries than for laser-welded geometries, similar to the toe. Furthermore, the range of the C_{bw2} values is similar to that of the toe. Most of the C_{bw2} values for laser-welded geometries are negative, whereas the ones for the arc-welded geometries are equally distributed.
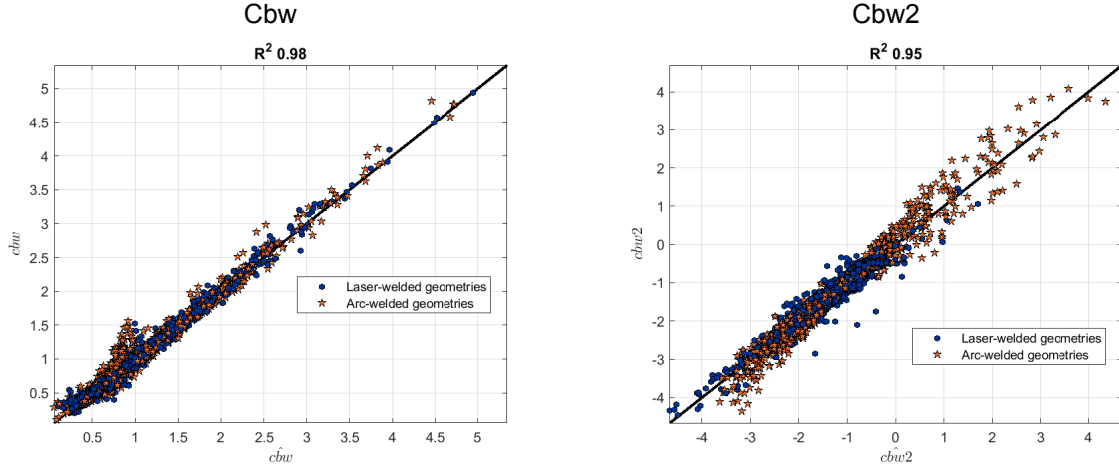
Figure 6.17: Goodness of fit scatter plot for the root of the single lap joint DS (614)

6.6.4. Single lap joint SS (615)

The parametric study yielded 4100 unique geometries. Contrary to the single lap joint DS (614), only one load path exists, leading to a higher weld load carrying. Hence, already for the toe, the geometries had to be restricted to values smaller than 1 for the criterion, minimizing the available geometries further to 1670.

Applying linear weld load carrying, the quadratic-shaped error behaviour indicates a 2nd order behaviour (fig. 6.18). However, the maximum error occurs at $0.7t_p$, contrary to the assumed $0.5t_p$ in the definition of the weld load carrying part. This might be the reason for the still noteworthy error when using 2nd order weld load carrying, as the shape of the error is similar to the linear one. However, the error's mean and standard deviation are reduced to a reasonable size. Hence, 2nd order weld load carrying for the toe is applied.
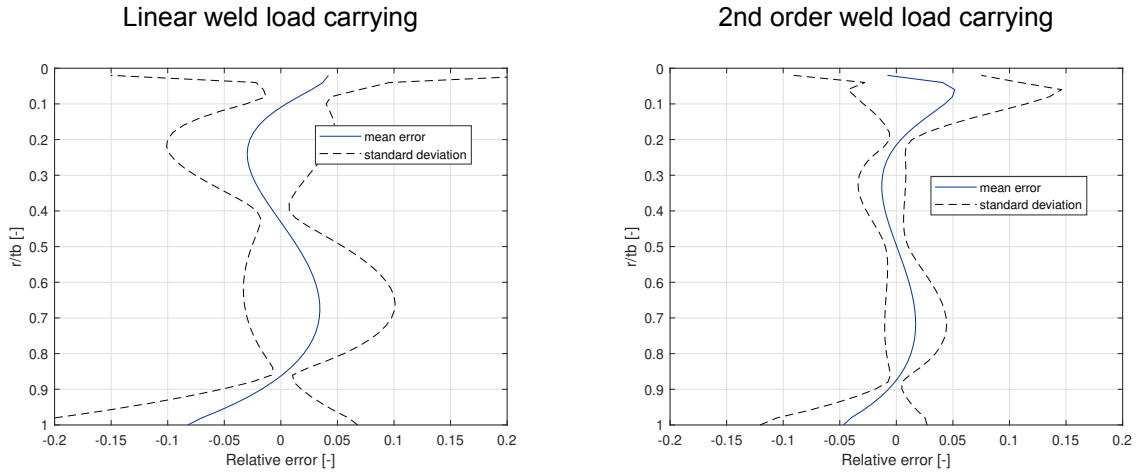
Figure 6.18: 2nd order weld load carrying relative error for single lap joint SS (615) at the toe

A good fit is observed for the arbitrary geometry (fig. 6.19). For the geometry with the maximum C_{bw} the negative r_s enforces compressive notch stress at the surface. Although the fit is decent, it is evident that semi-analytical formulations barely cover this example. The reason most likely for this is to set the maximum at $0.5t_p$ of the 2nd order weld load carrying. A maximum at $0.8t_p$ would provide a better fit. However, the fit quality is still sufficient, allowing to use this semi-analytical approach.

Arbitrary geometry

tp = 6.00, lw = 2.00, hw = 4.00, pn = 1.50, ov = 10.00 [mm]
cbw= 0.80, cbw2= 0.74, rs= 1.00, crit=1.17

Geometry with maximum C_{bw}

tp = 10.00, lw = 4.00, hw = 8.00, pn = 1.50, ov = 10.00 [mm]
cbw= -4.39, cbw2= -5.85, rs= -1.00, crit=1.10
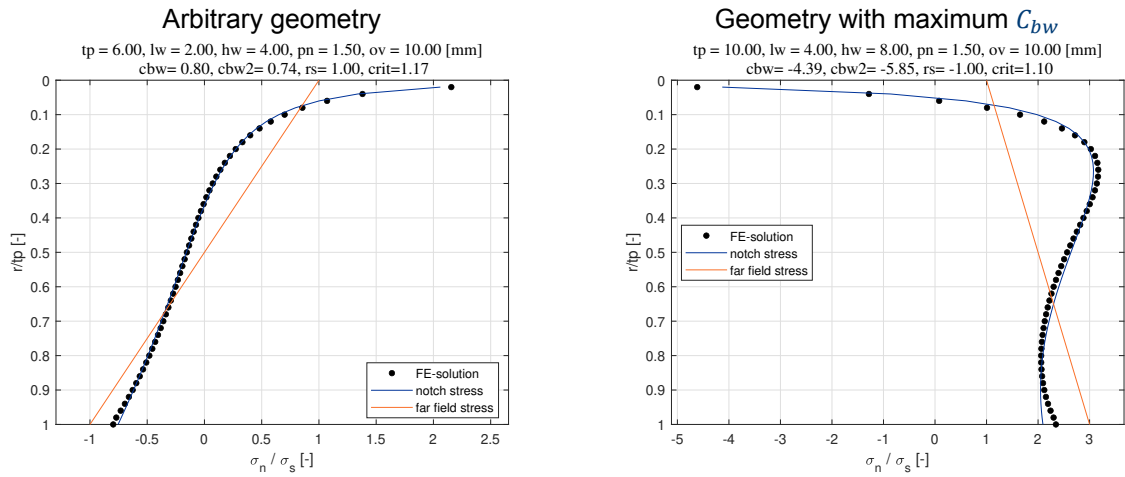
Figure 6.19: Example of through-thickness stress distribution for single lap joint DS (615) at the toe

By imposing the additional restriction of r_s in addition to the criterion at the root, the unique geometries are reduced to a total of 1533. Compared to the toe, the error is smaller for the linear weld load-carrying and shows a less pronounced 2nd order behaviour (fig. 6.20). This is opposite to the behaviour observed for the single lap joint DS (614). In addition, the location of maximum error over the thickness is closer to $0.5t_p$. Hence, 2nd order weld load carrying leads to an enhanced fit. Here, the mean error is only significant towards the surfaces, shown by 0.1 and 1 relative thickness values. Furthermore, the standard deviation and, therefore, the confidence bounds are quite tight. A shift in the location of the maximum stress for the weld load carrying likely causes the shape of the standard deviation error. Nonetheless, the alignment of the 2nd order weld load carrying with the FE solution confirms its appropriateness for utilization.

Linear weld load carrying

2nd order weld load carrying
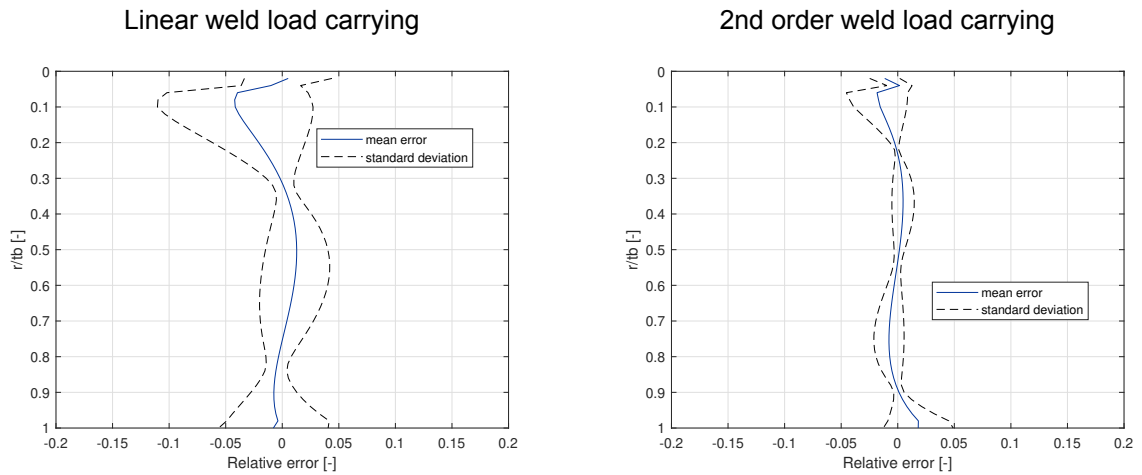
Figure 6.20: 2nd order weld load carrying relative error for single lap joint SS (615) at the root

As before, a good fit is evident when looking at the stress distribution of an arbitrary geometry (fig. 6.21). However, a significant error is prominent for the geometry with the maximum C_{bw} value. This is induced by the same phenomena as before, the different positions in maximum stress of the weld load-carrying part. In this case, it is around $0.7t_p$. However, the fit is still considered sufficient for a Zone 2 parameter.
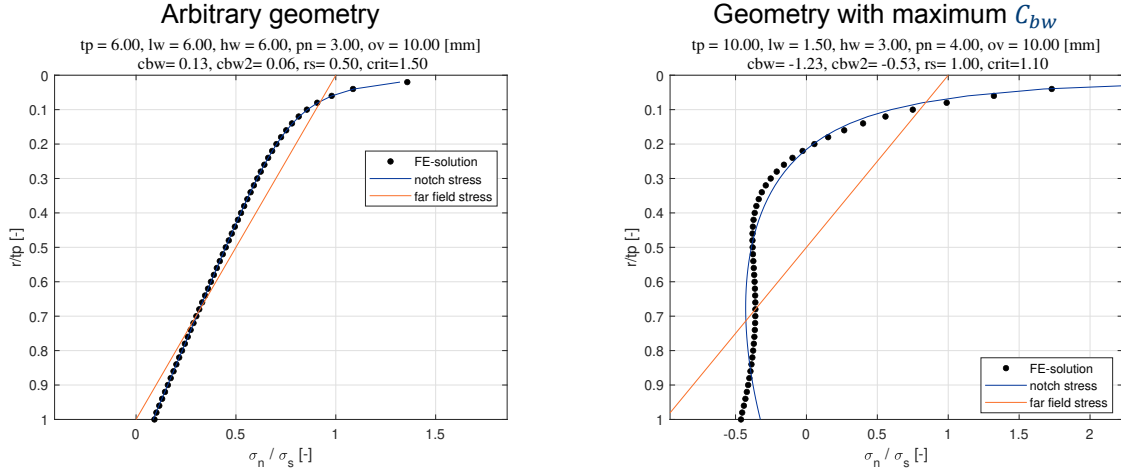
Figure 6.21: Example of through thickness stress distribution for single lap joint DS (615) at the root

Most of the non-dimensional parameters are duplicated from the fitting of the single lap joint DS (614). However, as only one load path exists, the second load path parameter O is redundant and the load path parameter T is adapted (eq. (6.20)). Moreover, it is noteworthy that the parameters Q and P exhibit negligible impact, resulting in their exclusion.

$$T = log\left(\frac{pn + lw}{tb}\right) \tag{6.20}$$

T^3, W and $r_s{}^4$ lead to the best fit for C_{bw} (eq. (C.5)). The absolute values of C_{bw} are similar to the ones observed for the single lap joints DS (614) (fig. 6.22). For the C_{bw}, the scatter band is minimal, and no significant differences between arc- and laser-welded geometries are observed (fig. 6.22).
For the C_{bw2} the parameters are reduced even further to T^4 and $C_{bw}{}^3$ (eq. (C.6)). The C_{bw2} values lower than -2 are likely to cover extreme cases similar to the ones of the C_{bw}. In addition, the scatter is increasing with the absolute value of C_{bw2}. However, both fitting functions show a good fit and can be used.
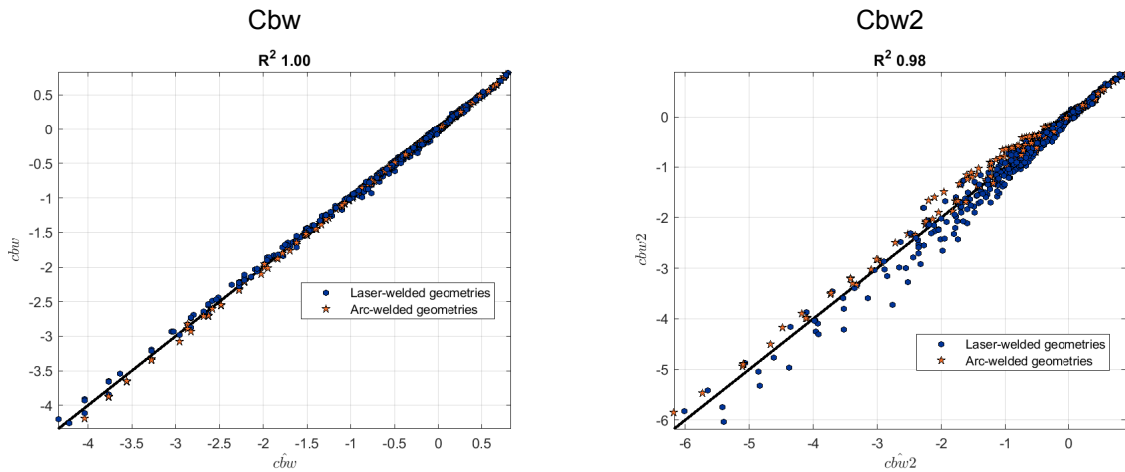
Figure 6.22: Goodness of fit scatter plot for the toe of the single lap joint SS (615)

The fitting function for the C_{bw} at the root is more complex than the one for the toe as five parameters are included, where P^4, T^4, W^3, S and $r_s{}^2$ yield the optimum (eq. (C.7)). Interestingly, the C_{bw} values for the root are smaller than the ones for the single lap joint DS (614) (fig. 6.23). A bigger diversion from the set location of the maximum weld load carrying stress might be a reason, as observed before

(fig. 6.21). Looking at the C_{bw} values, the ones with values lower than -0.5 are likely to be extreme cases. Furthermore, no difference between arc- and laser-welded geometries are observed. The C_{bw2} fitting function has a similar complexity as the one for the C_{bw} with five parameters, showing the optimum at P, T^3, W^2, r_s^3 and C_{bw}^2 (eq. (C.8)). The C_{bw2} mainly yields negative values contrary to the single lap joint DS (614). The laser-welded geometries only yield C_{bw2} values between -1 and 0.5, whereas the arc-welded geometries show a more extensive range with values from -2.5 up to 0. Overall, a good fit is obtained with both fitting functions.
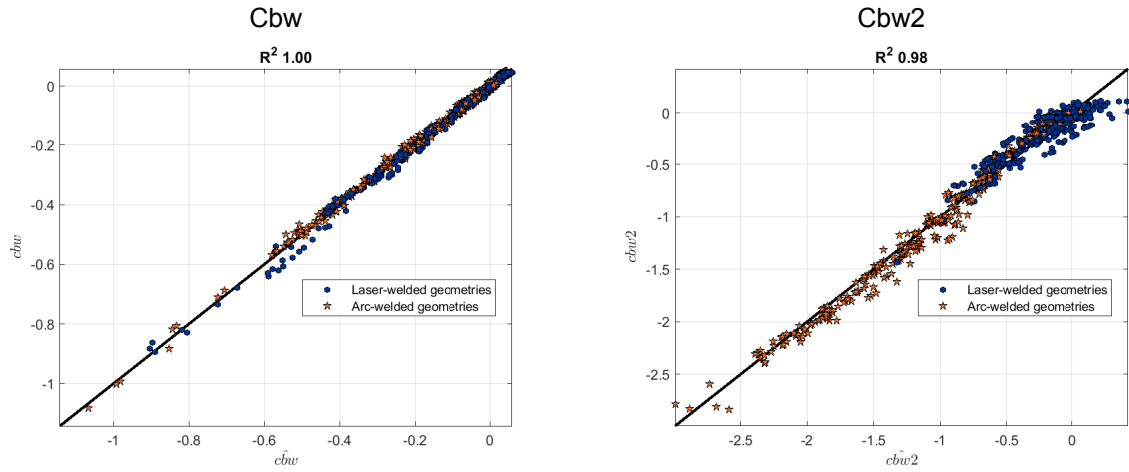
Figure 6.23: Goodness of fit scatter plot for the root of the single lap joint SS (615)

6.7. Far field stress from beam/shell model

The σ_s and r_s need to be obtained from FE calculations with non-linearity regarding the geometry to capture the secondary bending moments. As no solid model is needed for obtaining the C_{bw} and C_{bw2}, it should not be needed either for the σ_s and r_s. Beam/shell models allow for obtaining the σ_s and r_s with through-thickness linearization (Dong, 2005). However, so far, mostly the two components of the toe have been captured (den Besten, 2015; Qin et al., 2019). One method was established to obtain the far field stress at the root (Turlier et al., 2014). However, this model does yield high errors for the root and the toe in this case and is therefore excluded (table F.4). A reason for this is the high weld load carrying and, therefore, the high sensibility regarding the weld geometry.

To model the weld in more detail, the use of two beam/shell elements is proposed instead of one. The throat of the weld is modelled by one beam/shell, and the penetration is modelled by a second beam/shell (fig. 6.24). The beam/shell modelling the weld throat is positioned in the middle of the weld throat. It ends when reaching the weld boundaries from where it is vertically rigidly connected to the beam/shell of the corresponding plate. The thickness of the throat beam/shell is the same as established in literature (den Besten, 2015).

The penetration beam/shell is positioned in the middle of the penetration and runs vertically from the lower to the upper plate. The thickness of this beam/shell equals the penetration of the weld (eq. (6.21)). Other models were tested as well but did not provide accurate answers (appendix F).

The nodal force in the x-direction and the nodal moment around the z-axis for the σ_s and r_s are obtained at the projected location of the toe/root to the corresponding plate. These values are transformed into σ_s and r_s with through-thickness linearization (Dong, 2005) (eq. (6.22)).

$$t_{throat} = \frac{lw * hw}{\sqrt{lw^2 + hw^2}}$$
$$t_{penetration} = pn \tag{6.21}$$

$$\sigma_{membrane} = \frac{fx}{t_b}$$

$$\sigma_{bending} = \frac{6 * mz}{t_b^2}$$

$$\sigma_s = \sigma_{membrane} + \sigma_{bending}$$

$$rs = \frac{\sigma_{bending}}{\sigma_s} \tag{6.22}$$
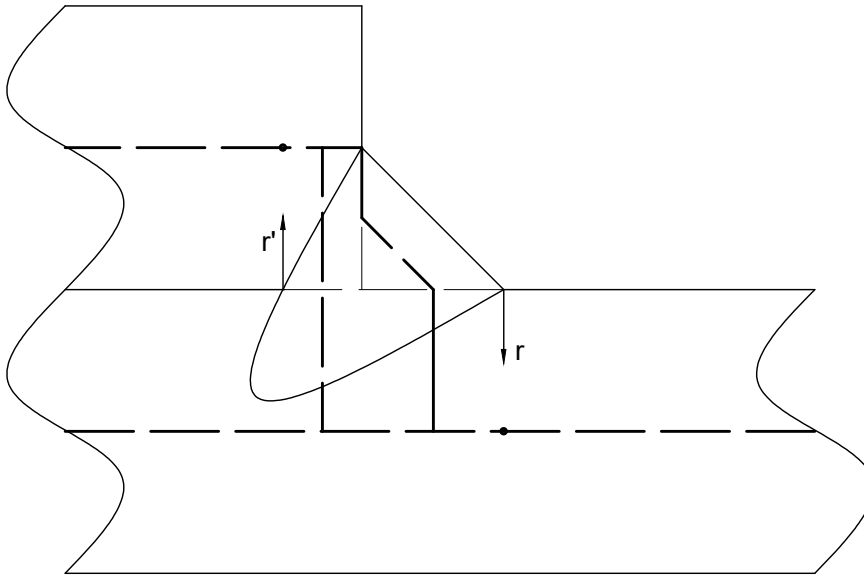
Figure 6.24: Weld geometry beam model

To validate this model, the error between the σ_s and r_s obtained from the introduced beam/shell model and a solid model is obtained. Four geometries close to the ones from the specimen (literature, experiments) are taken. The boundary conditions are set to the one of a uniaxial tensile Mode-I test. Hence, one side is fully clamped, whereas the other is only restricted in height, and the nominal stress is applied at the end of the specimen. The models are subjected to five different nominal stresses to show the change in secondary bending moments.

	Single lap joint DS (614)		Single lap joint SS (615)	
welding	laser	arc	laser	arc
tp [mm]	4	3	7	1.5
lw [mm]	1.4	5.3	1.4	1.45
hw [mm]	1.4	3	1.4	1.5
pn [mm]	6.1	1.7	6.1	1
ov [mm]	50	24	50	16
length [mm]	340	105	340	105

Table 6.3: Validation geometries beam model

The error for the structural stress components between the solid model and beam model, in general, increases with increasing applied nominal stress (table 6.4). However, the secondary bending is still captured by the beam model. In addition, the membrane part for all joints and locations has a non-significant error. Hence, the whole introduced error is caused by the bending part. Here the beam model is consistently under-predicting the bending for the toe of the single lap joints DS (614) and the root of the single lap joints SS (615). The opposite is observed for the corresponding other location of each joint.

Overall, this adapted model for welds to obtain the far field distribution at the root and the toe does yield accurate answers and incorporates the effect of changing secondary bending moments.

geometry	σ_n [Mpa]	toe				root			
		σ_m [-]	σ_b [-]	σ_s [-]	rs [-]	σ_m [-]	σ_b [-]	σ_s [-]	rs [-]
614 laser	1	0.00%	-0.46%	-0.32%	-0.14%	0.00%	0.05%	0.01%	0.03%
	100	0.00%	-1.21%	-0.80%	-0.41%	0.00%	0.67%	0.29%	0.38%
	200	0.00%	-1.36%	-0.87%	-0.49%	-0.01%	0.15%	0.06%	0.09%
	300	-0.01%	-1.74%	-1.09%	-0.66%	-0.06%	0.21%	0.07%	0.14%
	400	0.01%	-2.51%	-1.53%	-1.00%	-0.02%	0.82%	0.40%	0.41%
615 laser	1	0.00%	0.88%	0.64%	0.23%	0.00%	-0.88%	-0.66%	-0.22%
	100	-0.01%	1.54%	1.13%	0.41%	-0.01%	-2.15%	-1.61%	-0.55%
	200	0.00%	1.94%	1.43%	0.51%	0.00%	-3.03%	-2.25%	-0.80%
	300	0.01%	2.25%	1.65%	0.58%	0.01%	-3.74%	-2.76%	-1.00%
	400	0.02%	2.51%	1.85%	0.65%	0.02%	-4.33%	-3.19%	-1.18%
614 arc	1	0.00%	-2.73%	-1.70%	-1.05%	0.00%	1.68%	0.75%	0.92%
	100	0.00%	-3.33%	-2.05%	-1.31%	0.00%	2.00%	0.92%	1.08%
	200	0.00%	-3.86%	-2.34%	-1.56%	0.00%	2.18%	1.02%	1.15%
	300	0.00%	-4.33%	-2.58%	-1.80%	0.00%	2.27%	1.08%	1.18%
	400	0.00%	-4.76%	-2.80%	-2.02%	0.00%	2.29%	1.10%	1.17%
615 arc	1	0.00%	0.57%	0.41%	0.15%	0.00%	-0.60%	-0.45%	-0.15%
	100	0.00%	0.85%	0.62%	0.22%	0.00%	-1.93%	-1.44%	-0.50%
	200	0.01%	0.85%	0.63%	0.22%	0.01%	-2.74%	-2.01%	-0.74%
	300	0.06%	1.12%	0.83%	0.29%	0.05%	-3.21%	-2.33%	-0.89%
	400	0.21%	3.56%	2.63%	0.91%	0.18%	-1.75%	-1.22%	-0.54%
	Average	0.02%	2.12%	1.40%	0.73%	0.02%	1.83%	1.18%	0.66%

Table 6.4: Far field error of beam model for different geometries

6.8. Discussion

This chapter covered the research of the through thickness weld notch stress distribution. The before obtained semi-analytical formulas (den Besten, 2015) are refined with an additional weld load carrying term (section 6.6). This one covers the 2nd order behaviour occurring at highly weld load carrying geometries. Similar to the toe formulation, a linear superposition of the stress distribution components is proven to be valid for the root(section 6.4).

The secondary bending moments excited by the eccentricity of lap joints are investigated confirming the far field dependency of σ_s and r_s (section 6.5).

Fitting functions are established to obtain the weld load carrying coefficients, C_{bw} and C_{bw2}. For this, parametric FE studies are run for different weld geometries and r_s under unit σ_s. The resulting C_{bw} are more extreme than the prior observed ones (Bufalari et al., 2022; Qin et al., 2019). The weld load carrying coefficients obtained by fitting the semi-analytical formulations to the FE solutions are then related to dimensionless parameters yielding a fitting function. These fitting functions are obtained for single lap joints DS (614) and SS (615) correspondingly for the toe and the root. However, compared to ones developed in other studies, these needed to be significantly more complex to yield good results (Bufalari et al., 2022; Qin et al., 2019). Arc- and laser-welded geometries had shown similar relations and could be covered together.

The geometries had to be restricted by a criterion, as for some geometries the stress did not reach the whole thickness at the root/toe location (section 6.6.1). The semi-analytical formulations could not cover this behaviour. Furthermore, $-1 < r_s < 1$ is set for the root as extreme values did not allow for a fitting function.

Two phenomena did restrict the quality of the semi-analytical formulas. For some geometries the stress did not reach the whole thickness; for this relation, a criterion is developed. However, this is a simplified approach, not covering all geometries where the stress has not reached the whole thickness. Secondly, the location of the maximum weld load carrying stress set to $0.5t_p$ is not always correct. It was decided to set it to $0.5t_p$ to comply with force and momentum equilibrium correspondingly to the before obtained μ_a, μ_s.

Overall, the through thickness weld notch stress distribution of lap joints for the toe and the root can be covered by semi-analytical formulations. However, the applicable geometries are still limited due to the observed phenomena.

The possibility of obtaining the far field stress from a beam/shell model reduces computing time significantly. When applying a non-linear geometry dependency, the enhanced model can sufficiently capture the secondary bending moments .

7

Fatigue assessment

In this chapter, fatigue resistance is assessed with the different fatigue concepts introduced earlier (chapter 2). First, the used method is presented (section 7.1). Arc-welded joints are evaluated first (section 7.2), followed by the assessment of laser-welded joints (section 7.3). Lastly, the weld geometry for a laser-welded lap joint is optimized (section 7.4).

7.1. Modelling

The method used for the regression analysis, and implementation is explained first (section 7.1.1). Afterwards, the use of FE models to obtain the fatigue concept related criterion is elaborated (section 7.1.2).

7.1.1. Regression Model

In MCF, run-outs might already be part of the data set. This results in the need for a more advanced method than the most utilised Least Squares method. Hence, the maximum likelihood regression is used (den Besten, 2015; Dekking et al., 2005). This method is a statistical approach to estimate the parameters of the regression model by maximising the likelihood of the given data. These parameters are referred to as Maximum Likelihood Estimates (MLE). The data points are assumed to follow a particular probability distribution, which is generally assumed for fatigue resistance data.

The Likelihood formulation is the joint probability density of all data points to occur under the given parameters (θ)(eq. (7.1)). The corresponding probility density function (PDF) value is used for a failure, whereas, for a run-out, the joint probability for the failure to occur is used. Whether a failure or a run-out emerged is marked by σ, where $\sigma = 1$ equals a failure and $\sigma = 0$ shows a run-out.

$$L(\theta; N|S) = \prod_{j=1}^{n} \{f(N_j|S_j; \theta)\}^{\sigma_j} \{1 - F(N_j|S_j; \theta)\}^{1-\sigma_j} \tag{7.1}$$

Adapting the log-likelihood function leads to a summation instead of a multiplication allowing for more straightforward computation (eq. (7.2)). In addition, it neutralises the exponent appearing in the PDF and cumulative probability density function (CDF). This formulation is valid as the natural logarithm is a monotonically increasing function. The method is implemented in Matlab by minimising the negative log-likelihood with the fmincon function (eq. (7.3)). In addition, the limited amount of data available required bias corrected distributions.

$$L(\theta; N|S) = \sum_{j=1}^{n} \sigma_j ln\{f(N_j|S_j; \theta)\} + (1 - \sigma_j)ln\{1 - F(N_j|S_j; \theta)\} \tag{7.2}$$

$$min\{-L(\theta; N|S)\} \tag{7.3}$$

The fitting quality can be judged by the determined maximum log-likelihood value. As a model with more parameters generally provides a better fit, these values can only be compared when the number of parameters do not differ. Otherwise, the Akaike information criterion (AIC) has to be utilized (Akaike, 1973) (eq. (7.4)). In addition, the strength scatter index ($T_{\sigma S}$) is used to judge the fit.

$$AIC = -2\{L(MLE; N|S) - k\} \qquad (7.4)$$

7.1.2. Finite element model

The more advanced fatigue concepts (HSSSC and ENSC) use a criterion incorporating more details of the geometry. Some geometries do not fulfil the criterion established for the fitting functions (section 6.6.1). Therefore, FE calculations are utilised to obtain the stress distribution of the joints needed for those criteria. ANSYS with PLANE42 elements is used, modelling a quasi 3-D geometry under plane stress conditions. To account for the change in secondary bending moments, non-linear geometry dependency is used. Furthermore, contacts are used to avoid penetration. The applied boundary conditions are aligned with the testing conditions.
The FE calculations are run for five different nominal stresses for each series. Where the lowest stress is the overall minimum resulting from the stress cycles of the data points, the same applies to the highest stress. The in-between values are equally distributed. With the FE results, a polynomial transfer function is established for the notch stress in relation to the location along the crack path and the nominal stress to ensure continuous behaviour. Only the nominal stress is incorporated for the transfer function for the structural stress.
To incorporate the effect of secondary bending moments, the corresponding values for σ_{min} and σ_{max} are obtained separately. The S_s/S_e is then obtained by the difference between the minimum effective notch/structural stress and the maximum effective notch/structural stress. The r_{lr} is recalculated from these values as well.
In addition, for all fittings the mean stress is corrected according to Walker et al., 1970 (section 2.4.7).

7.2. Arc-welded joints

In this section, the fatigue resistance of arc-welded lap joints is assessed. First, the fatigue resistance data from lap joints is validated with fatigue resistance data from other welded joints (section 7.2.1). For comparison reasons the NSC (section 7.2.2) and HSSSC (section 7.2.3) are established. Afterwards, two concepts of the ENSC (section 7.2.4) are assessed. Lastly, the results are discussed (section 7.2.5).

7.2.1. Fatigue resistance data

Before using the fatigue resistance data obtained in the literature review for arc-welded lap joints (section 4.3), it has to be validated. For this purpose, arc-welded fatigue resistance data of other joint geometries is utilised ("Qin et. al.", 2023). In combination with a log(normal) distribution, the LENSC concept is used, in line with "Qin et. al.", 2023. ρ^* and γ are fixed due to the availability of data. Furthermore, the small amount of data from lap joints compared to the data from the other joints is likely not to influence the material-dependent parameters. Hence, the regression is only performed for log(C), m and Standard deviation (σ). As only MCF is in the scope of this thesis, all data points below 10^4 and exceeding $4 * 10^6$ cycles are excluded. Furthermore, series 1 and 2 are excluded as the small specimen thickness yielded an unacceptable high scatter of the results, and the applied ρ^* is close to the t_p (appendix A). This leads to a total of 272 data points for lap joints. The $S_e - N$ curve of the arc-welded lap joints and other joints (grey-coloured) is shown below (data from "Qin et. al.", 2023).
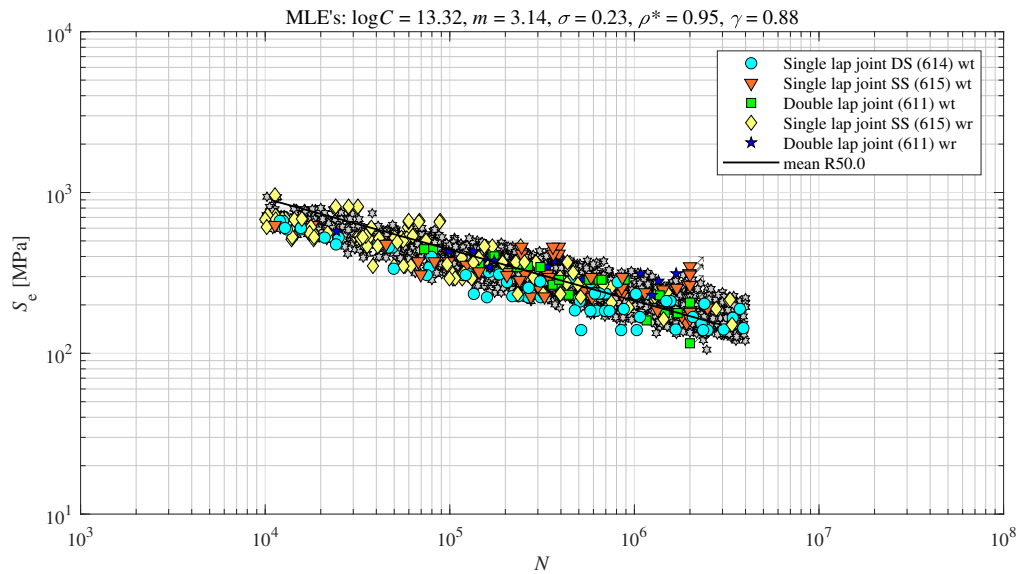
Figure 7.1: $S_e - N$ curve of arc-welded joints for data validation

Firstly, the data scatter of the lap joints, particularly the single lap joints (614,615), is higher than the one for the other joint geometries. The general small plate thickness of the single lap joints (614,615) might contribute to this higher scatter, as a smaller plate thickness leads to higher uncertainty. The single lap joint DS (614) toe failure data is typically below the median, indicating a worse fatigue performance. When looking at the curve parameters, the rise in scatter due to the lap joints is also apparent (table 7.1). However, the difference is small, similar to the other parameters. Hence, the assumption to keep the same material-dependent parameters is valid.

MLE	log(C)	m	σ
With lap joints	13.32	3.14	0.23
Without lap joints	13.36	3.15	0.22

Table 7.1: MLE of data validation for arc-welded lap joints

The change in secondary bending moments results in a more complex fitting. In addition, the curve parameters do not change significantly when not accounting for the change in secondary bending moments (table 7.2). Only a small change in the slope, as well as a different log(C), is observed, whereas the scatter even stays constant.

MLE	log(C)	m	σ
Including change in secondary bending moments	13.32	3.14	0.23
Excluding change in secondary bending moments	13.25	3.12	0.23

Table 7.2: Influence of secondary bending moments on MLE

However, when comparing the S_e for the single lap joints, the influence is consequential (fig. 7.2). The values differ up to 15% with an average of 4.7%. Hence, although the overall fit is barely influenced, the opposite is the case when looking at each fatigue resistance data point. Therefore, it is advised to incorporate the change in secondary bending moments in the fatigue assessment of eccentric joints.
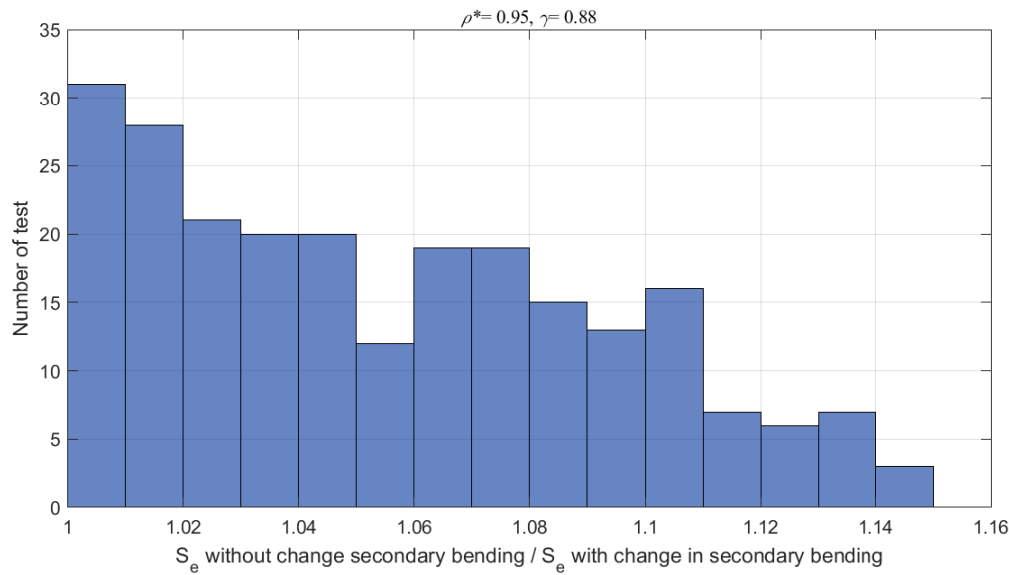
Figure 7.2: Influence of change in secondary bending moments on S_e

Overall, the fatigue resistance data of the lap joints lies within the scatter cloud of other joint geometries. Therefore, the data points are assumed to be valid for further use. In addition, it shows that the fatigue resistance of lap joints is in line with other arc-welded joints and the high influence of secondary bending moments.

7.2.2. Nominal stress concept assessment

For comparison, the NSC is considered. This concept is based on structural details and the nominal stress (section 2.2). To account for the mean stress influence and comply with the $r_{lr} = 0.5$ of the FAT, an adapted Walker mean stress correction is used (eq. (7.5)). No thickness correction is needed as all joints do not exceed the thickness of 25 mm. In addition, the engineering-based approach to account for the eccentricity of the single lap joints is excluded to keep the comparability to the other concepts.

$$S_{n,eff} = S_n \frac{(1 - 0.5)^{1-\gamma}}{(1 - r_{lr})^{1-\gamma}} \tag{7.5}$$

Using the log-likelihood regression with a bias correction, due to the limited number of data points, results for a log(Normal) and a log(Weibull) fitting are obtained (table 7.3). The log(Normal) distribution provides significantly better results than the more extreme log(Weibull) distribution, according to both σ and AIC value. The mean stress did not show an influence, which relates to the limited availability of r_{lr} in the literature data.

MLE	log(C)	m	σ	γ	AIC
Normal	11.02	2.77	0.43	1	738
Weibull	10.72	2.64	0.55	1	796

Table 7.3: MLE of NSC for arc-welded lap joints

Applying the log(normal) distribution yields a $T_{\sigma S} = 1 : 1.71$, which is larger than the commonly observed value of 1:1.5. This reflects the scatter observed in the $S_n - N$ plot (fig. 7.3). The m is smaller than the typical value of $m = 3$, possibly caused by the exclusion of HCF data with $N > 4 * 10^6$. The single lap joints (614, 615) appear to have a similar fatigue resistance opposite to the double lap joint (611) showing an increased fatigue resistance. The spread of the confidence bounds confirms the uncertainty related to the NSC (table 7.4).
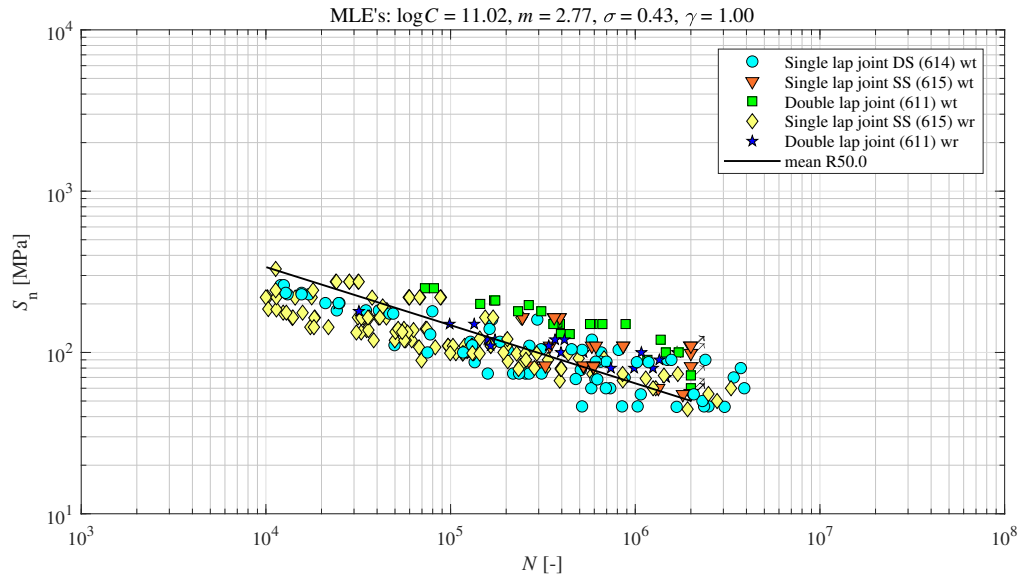
Figure 7.3: $S_n - N$ curve for NSC of arc-welded joints lap joints

Parameter	C75LB	MLE	C75UB
log(C)	10.68	11.02	11.34
m	2.61	2.77	2.93
σ	0.41	0.43	0.45
γ	0.96	1	1

Table 7.4: MLE and CB's for NSC of arc-welded lap joints

In addition, each structural detail is plotted with the corresponding FAT class curve (Hobbacher et al., 2016). The design curve is set with a reliability of 0.977 with 0.75 two-sided confidence bounds. All fatigue resistance data with $10^4 < N < 10^7$ is considered as 10^7 is the knuckly point for the FAT class. The value of γ is restricted to the MLE obtained before, $\gamma = 1$.

The eccentricity correction is included, as otherwise, the results do not align with the recommended FAT class (fig. 7.5). The upper and lower plate thickness is always the same, allowing to simplify the $k_{m,calculated}$. Multiplying the resulting $k_{m_{eff}}$ with the fatigue resistance data yields a design curve that better aligns with the recommended FAT class. The considerable distance between the quantile and the FAT design curve clearly shows the conservativeness coupled to this approach caused by the empirical formulation for eccentricity and the only global information taken into account.
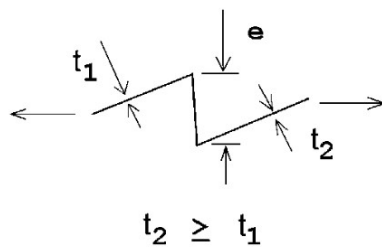
$$k_{m,eff} = \frac{k_{m,calculated}}{k_{m,alreadycovered}}$$
$$k_{m,alreadycovered} = 1.25$$
$$k_{m,calculated} = 1 + \frac{6e}{t_1} * \frac{t_1^{1.5}}{t_1^{1.5} + t_2^{1.5}} = 4$$

Figure 7.4: Axial misalignment correction according to Hobbacher et al., 2016
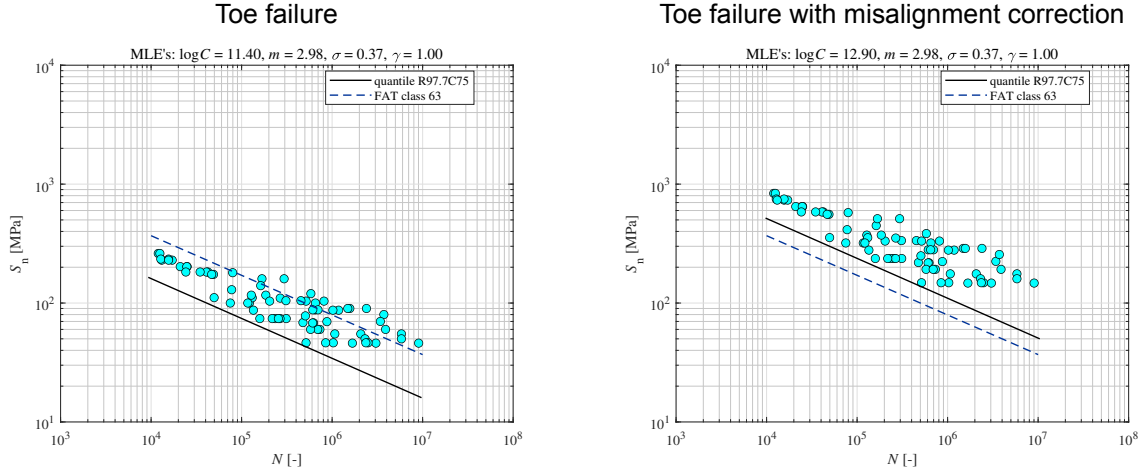
Figure 7.5: $S_n - N$ curve for NSC of arc-welded single lap joints DS (614)

For single lap joints SS (615), no FAT class has been proposed yet. Using the same methodology as before, the toe failure data complies with the FAT of the single lap joint DS (614) (fig. 7.6). The inverse slope value had to be restricted to $m = 3$. All data lies above the FAT design curve for the toe failure. For the root, a FAT class of 36 is below the quantile R97.7C75 design curve. Overall, for single lap joints SS (615), the same FAT classes as for single lap joints DS (614) are proposed.
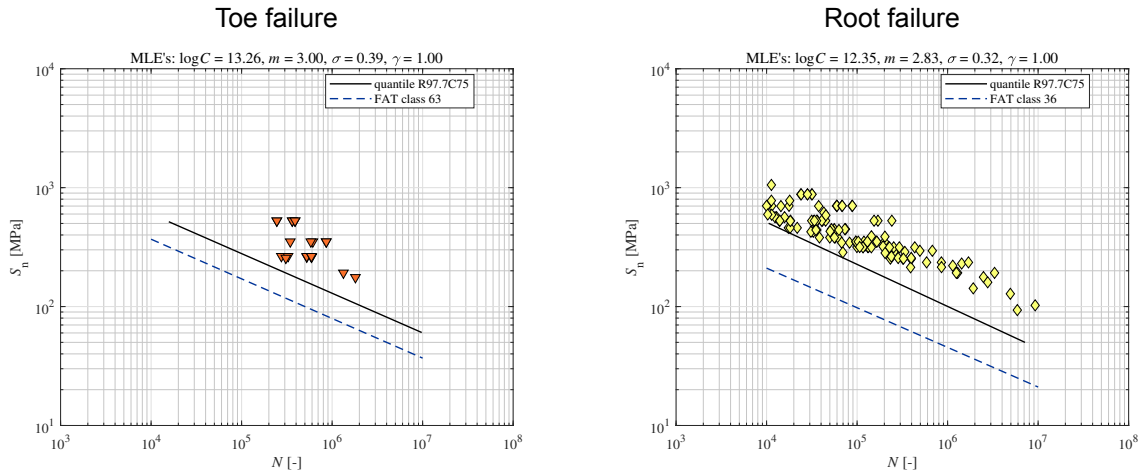
Figure 7.6: $S_n - N$ curve for NSC of arc-welded single lap joints SS (615)

Lastly, looking at the toe failure of double lap joints (611) (fig. 7.7), the FAT design curve shows a good fit with the design curve obtained from the fatigue resistance data. For the root, the quantile design curve shows a flatter behaviour with $m \approx 4$ compared to the FAT design curve, where the resistance aligns around $N = 3 * 10^4$ but for higher N, the quantile design curve shows enhanced fatigue resistance. However, low confidence due to the small amount of data is apparent. Still, the corresponding FAT value represents the fatigue resistance sufficiently for both root and toe failure.
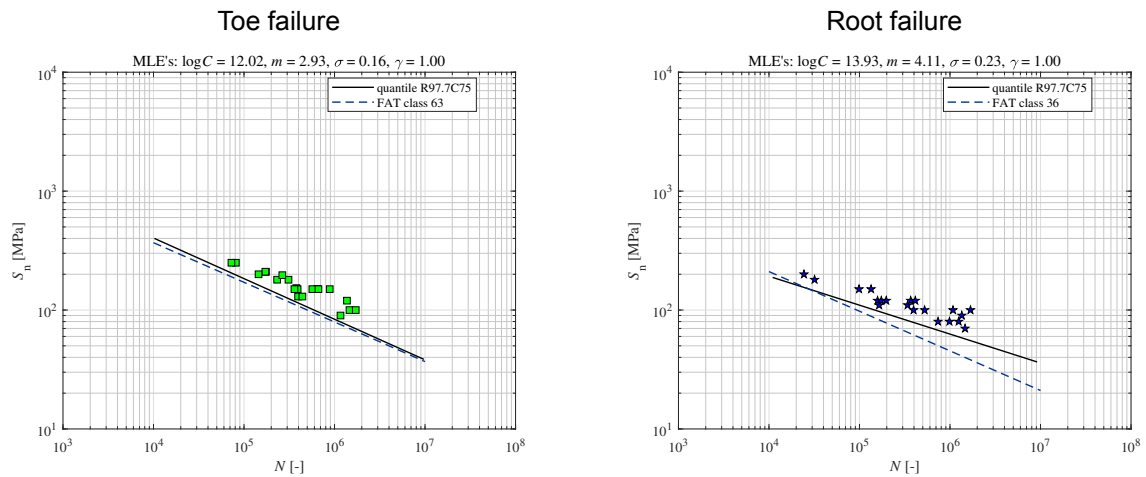
Figure 7.7: $S_n - N$ curve for NSC of arc-welded double lap joints (611)

7.2.3. Hot spot structural stress concept assessment

The HSSSC corresponding $S_s - N$ curve is established to allow for a comparison between arc- and laser-welded geometries. Taking local information into account by incorporating the S_s related far field stress respectively the change in secondary bending moments. To account for the mean stress, the same correction as used for the NSC is utilized (eq. (7.5)).

As for the NSC, the more simple log(Normal) distribution provides a better it than the log(Weibull) distribution (table 7.5). Interestingly, the inverse slope differs quite significantly from the typical value of $m = 3$. In addition, the performance parameter σ, AIC and $T_{\sigma S} = 1 : 1.90$ show a decreased fit quality compared to the NSC. This behaviour is the opposite of the expected, as the more detailed HSSSC should provide a more accurate fit.

MLE	log(C)	m	σ	γ	AIC
Normal	11.32	2.34	0.43	1	770
Weibull	11.40	2.39	0.57	1	840

Table 7.5: MLE of HSSSC for arc-welded lap joints

The double lap joints (611) with toe failure do lie beneath the rest of the fatigue resistance scatter band, causing a worse fit of the R97.7C75 quantile design curve compared to the FAT design curve (fig. 7.8). When excluding the double lap joints the quantile design curve aligns with the FAT design curve (fig. 7.9). However, no reason for the poor fit of the double lap joints is located. In addition, the implicitly included change in secondary bending moments might contribute to the higher scatter. Furthermore, the HSSSC does not account for the exact weld geometry or initial cracks at the weld, causing uncertainty.
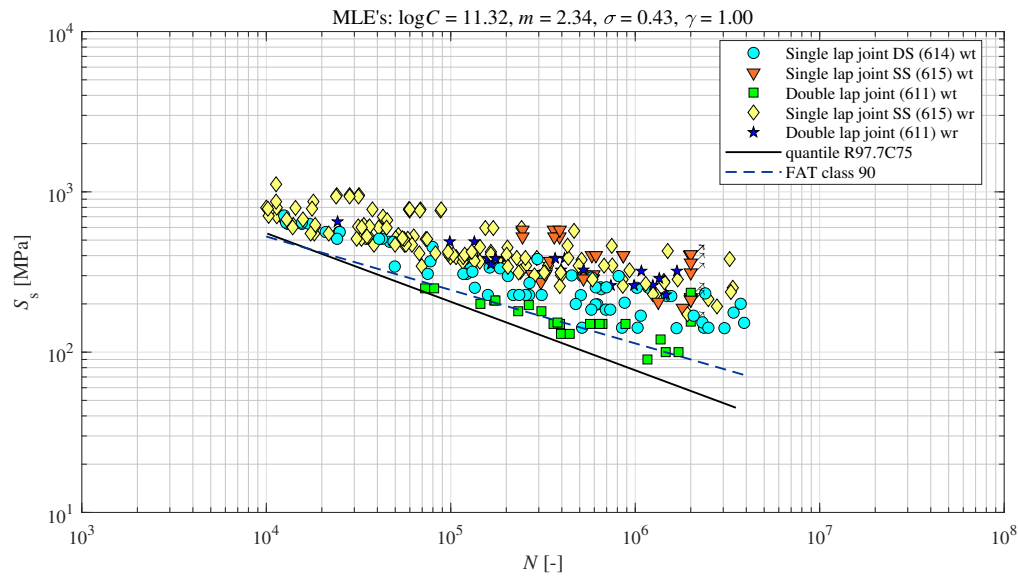
Figure 7.8: $S_S - N$ curve for HSSSC of arc-welded joints lap joints

For the here apparent load carrying joints, a FAT value of 90 is recommended (Hobbacher et al., 2016). The resulting quantile design curve has the same starting point at low cycles as the FAT design curve. However, due to the smaller m, it falls beneath the FAT design curve for a higher number of cycles. Here, the low fatigue resistance of the toe failure of the double lap joints is the reason.
Overall, the substandard quality is caused by the double lap joints (611). However, the comparable performance to the FAT design curve when excluding those shows the applicability (fig. 7.9).

Parameter	C75LB	MLE	C75UB
log(C)	10.99	11.32	11.64
m	2.20	2.34	2.48
σ	0.41	0.43	0.45
γ	0.98	1	1

Table 7.6: MLE and CB's for HSSSC of arc-welded lap joints

The not enhanced fit compared to the NSC is also reflected in the confidence bounds of the MLE (table 7.6).
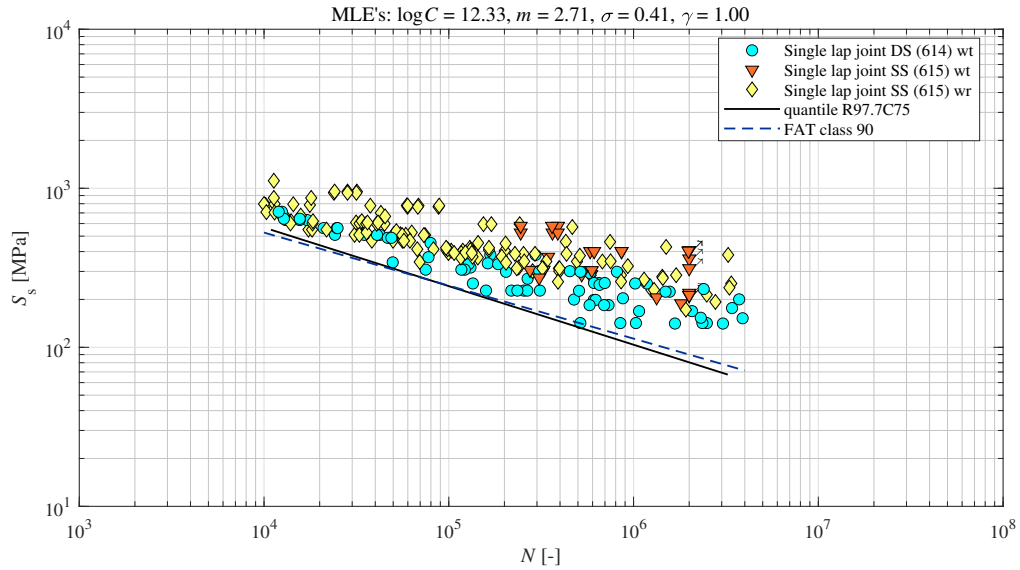
Figure 7.9: $S_S - N$ curve for HSSSC of arc-welded joints lap joints excluding double lap joints (611)

7.2.4. **Effective notch stress concept assessment**

Considering local information yields a more detailed approach like the ENSC. After the LENSC is assessed (section 7.2.4), the PENSC is looked into (section 7.2.4).

Line method assessment

Adopting the LENSC for the arc-welded lap joint fatigue resistance data with a Walker mean stress correction allows for obtaining γ, ρ^* and the corresponding $S_e - N$ curve. The change in secondary bending moments over the stress cycle results in nonlinearity (section 7.1.2).

Comparing the AIC of the fitting based on the log(Normal) and the log(Weibull) distribution (table 7.7), the higher flexibility of the log(Weibull) distribution does not yield a better fit. This result is in line with earlier done research (Qin et al., 2019). The other performance parameters for the log(Normal) distribution, σ and $T_{\sigma S} = 1 : 1.63$, indicate a worse fit than the typical values, respectively 0.25 and 1:1.5.

The material dependent parameter -ρ^* and γ- deviate significantly from the log(Normal) fit obtained generally for arc-welded joints (fig. 7.1). This might result from the missing thickness variation in the fatigue resistance data. Similarly, missing variation in the r_{lr} of the data is likely to be the reason for the observed γ, which has a value close to 1 for both distributions. Furthermore, the m is bigger than the commonly used value of $m = 3$ (Eurocode 3, 2007; Hobbacher et al., 2016). However, it is close to the one obtained for all arc-welded joints (section 7.2.1).

MLE	log(C)	m	σ	ρ^*	γ	AIC
Normal	13.46	3.28	0.33	1.09	1	618
Weibull	13.59	3.48	0.43	1.50	0.99	686

Table 7.7: Non-linear MLE of LESNC for arc-welded lap joints

To confirm the influence of secondary bending moments on the fitting shown earlier (section 7.2.1), the regression analysis was also performed with K_f and K_t obtained from $S_n = 1 MPa$ as it is done generally (table 7.8). Interestingly, the log(Weibull) distribution performs similarly whether the secondary bending moments are considered. The log(Normal) distribution shows a slightly better fit when secondary bending moments are considered. Furthermore, a difference in m is apparent when secondary bending moments are considered or not, showing the different influences on different stress levels.

MLE	log(C)	m	σ	ρ^*	γ	AIC
Normal	13.14	3.17	0.33	1.21	1	629
Weibull	13.25	3.32	0.43	1.52	1	684

Table 7.8: Linear MLE of LENSC for arc-welded lap joints
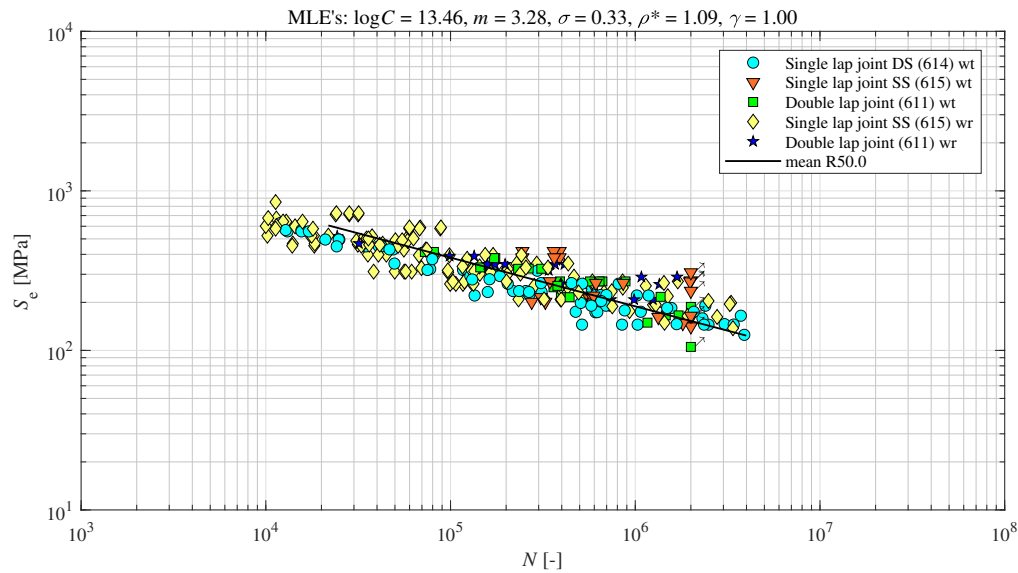
Figure 7.10: $S_e - N$ curve for LENSC of arc-welded joints lap joints

All fitting parameters show a allowable confidence (table 7.9). However, the missing amount of data and the lack of quality are apparent. The lack of quality data is most apparent in the $\log(C)$, m and ρ^* values.

Parameter	C75LB	MLE	C75UB
log(C)	13.11	13.46	13.81
m	3.14	3.28	3.42
σ	0.31	0.33	0.35
ρ^*	1.01	1.09	1.18
γ	0.99	1	1

Table 7.9: MLE and CB's for LENSC of arc-welded lap joints

Considering secondary bending moments does enhance the complexity of applying an ENSC. The observation of a reduced AIC, indicating improved model fitting alongside a more accurate representation of reality, strongly supports the decision to incorporate the change of secondary bending moments. As the more complex log(Weibull) distribution does yield an enhanced fit, the log(Normal) distribution is sufficient.

For this combination, the scatter between WT and WR is similar, and both fit in the same scatter cloud (fig. 7.10). Although the scatter should increase with a higher lifetime due to the change in the governing mechanism from growth to initiation, this data shows a more constant scatter.

Point Method assessment

Assuming the effective notch stress is related to the stress at a point at the length a^* along the crack path leads to the use of the PENSC. Similar to the ρ^* of the LENSC the a^* is a material dependent parameter.

Looking at the parameters of the log(Normal) and log(Weibull) distribution, the parameters are very similar (table 7.10). However, the log(Normal) distribution provides a better fit according to AIC comparable to the results of the LENSC (section 7.2.4). The other performance parameters are $\sigma = 0.35$ and $T_{\sigma S} = 1 : 1.67$.

MLE	log(C)	m	σ	a^*	γ	AIC
Normal	12.74	3.12	0.35	0.53	1	653
Weibull	12.49	3.03	0.46	0.54	1	724

Table 7.10: Non-linear MLE of PENSC for arc-welded lap joints

When not accounting for the change in secondary bending moments, the fitting in general gets slightly worse, indicated by the higher AIC (table 7.11). A small change in the slope also shows the influence of the secondary bending moments.

MLE	log(C)	m	σ	a^*	γ	AIC
Normal	12.64	3.07	0.37	0.54	1	689
Weibull	12.63	3.08	0.47	0.57	1	748

Table 7.11: Linear MLE of PENSC for arc-welded lap joints

Due to the above results, the change in secondary bending moments is taken into account and a log(Normal) fit is used. Overall, both WT and WR fit in the same scatter cloud (fig. 7.11).
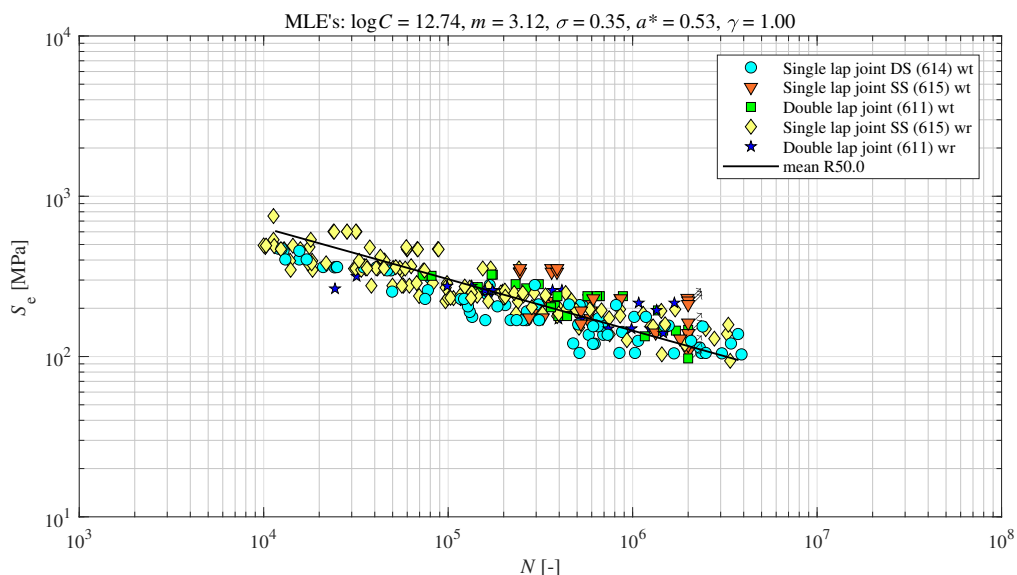
Figure 7.11: $S_e - N$ curve for PENSC of arc-welded joints lap joints

The most fitting parameter shows decent confidence (table 7.12).

Parameter	C75LB	MLE	C75UB
log(C)	12.39	12.74	13.09
m	2.98	3.12	3.26
σ	0.33	0.35	0.36
a^*	0.51	0.53	0.56
γ	0.99	1	1

Table 7.12: MLE and CB's for PENSC of arc-welded lap joints

7.2.5. Discussion

Firstly, the data obtained from the literature for arc-welded lap joints is considered usable (section 7.2.1). The change in secondary bending moments only slightly influenced the overall fit, both on the curve parameters and the fit quality. However, the significant influence on the S_e value of each data point results in the implementation. Confirmed by the application of the LENSC and PENSC where considering the change in secondary bending moments results in a better fit. However, for the PENSC, the negative influence when not implementing the secondary bending moments is bigger than for the LENSC.

A log(Normal) distribution provided better results for all applied fatigue concepts. The NSC yielded a significant scatter, as expected (section 7.2.2). However, the fatigue resistance data from the literature did align quite well with the corresponding FAT design curves, showing the conservativeness of the NSC. Utilizing the HSSSC to obtain a $S_s - N$ curve did show a worse performance than the NSC (section 7.2.3). This is unexpected but is caused by the poor fatigue resistance of double lap joints. Therefore, excluding this data the arc-welded lap joints could be represented with a FAT design curve. For the applied effective notch stress concepts, LENSC and PENSC, a factor of 2 was obtained between ρ^* and a^*. In contrary to the semi-analytical $\rho^* = 4 * a^*$ (section 2.4.6). In literature, only fittings were found where a fictitious notch radius while applying the LENSC and PENSC was modelled. This generally leads to smaller values of the material-dependent parameters as the singularity at the surface is less effective. However, there a relation close to a factor 3 was obtained (Baumgartner et al., 2011; Baumgartner et al., 2015; Baumgartner J., 2013). Furthermore, for mild notches, a deviation to $\rho^* = 2 * a^*$ was proposed (Baumgartner et al., 2020) Hence, the here obtained factor of 2 between the two values is still considered to be realistic.

The PENSC generally provides slightly worse results than the LENSC in this study. This behaviour was also observed before (Baumgartner J., 2013; Hensel et al., 2022). A main factor contributing to the worse performance of the PENSC is based on the method, as taking the stress at a single point is more sensible to changes than an averaged stress. Hence, the LENSC is considered superior due to a more robust and better fit.

Some failures are initiated at the weld toe, although a failure at the root is predicted. For the LENSC the S_e at the root was in some cases 20% higher than at the toe, and still toe failure occurred (fig. 7.12). Lower values occur at the PENSC.
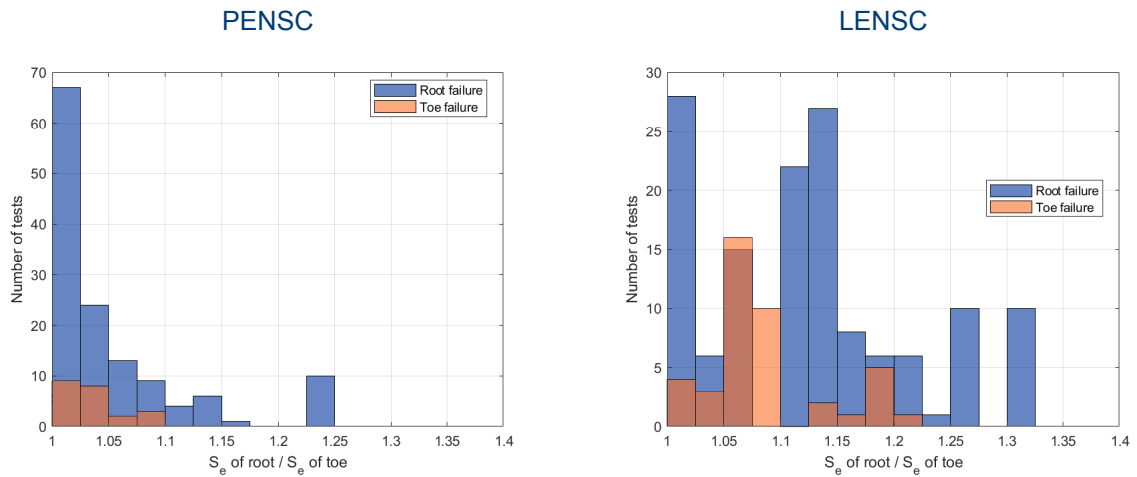
Figure 7.12: Histogram effective stress at the toe and the root

The wrongly predicted toe failures occurred when the secondary bending moments caused a change in failure location for the single lap joints SS (615) (fig. 7.13). The failure location of the single lap joints DS (614) was always predicted correctly. Hence, although the change in secondary bending moments is accounted for this does not result in a reliable prediction of the failure location. In addition, no root failures occurred where toe failures were expected. This enables the avoidance of hard detectable root failure. No mean stress influence is found resulting from the low available range of r_{lr} as discussed before.
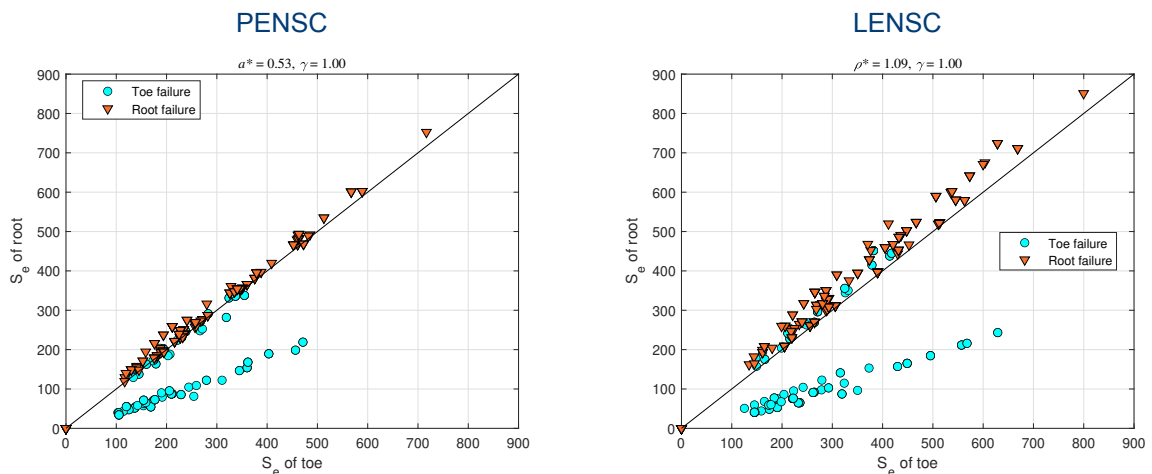
Figure 7.13: Effective stress at the toe and the root

7.3. Laser-welded joints

After obtaining fatigue resistance data from experiments (section 7.3.1), this and data from literature are assessed by different fatigue concepts, namely the NSC (section 7.3.3), the HSSSC (section 7.3.4) and the ENSC (section 7.3.5). The section is concluded with a discussion (section 7.3.6).

7.3.1. Fatigue testing

The limited availability of fatigue resistance data for laser-welded single lap joints DS (614) imposed the need for experiments (section 5.1). Firstly, this section introduces the specimens. Afterwards the experimental set-up is presented, followed by validation of the idealized weld shape.

Specimen

The specimen design follows the joint design, which shall be used at the yacht, meaning a single lap joint DS (614) with a lap of 50 mm and a thickness of 7 mm (fig. 7.14). To capture size effects, a second thickness of 4 mm is introduced. Furthermore, the single lap joint DS (614) is welded from both sides, likely yielding WT. As WR should be assessed as well, specimens with a weld only on one side are introduced, single lap joints SS (615). This leads to 4 different series (table 7.13). Three stress levels are tested with three tests each, resulting in 9 specimens per series. To capture γ, the mean stress correction, two different r_{lr} per series are tested. Overall, this leads to 18 needed specimens per series. For one series, a $r_{lr} = -1$ is tested to capture compressive cycles as well.

SINGLE SIDE WELDED

BOTH SIDES WELDED
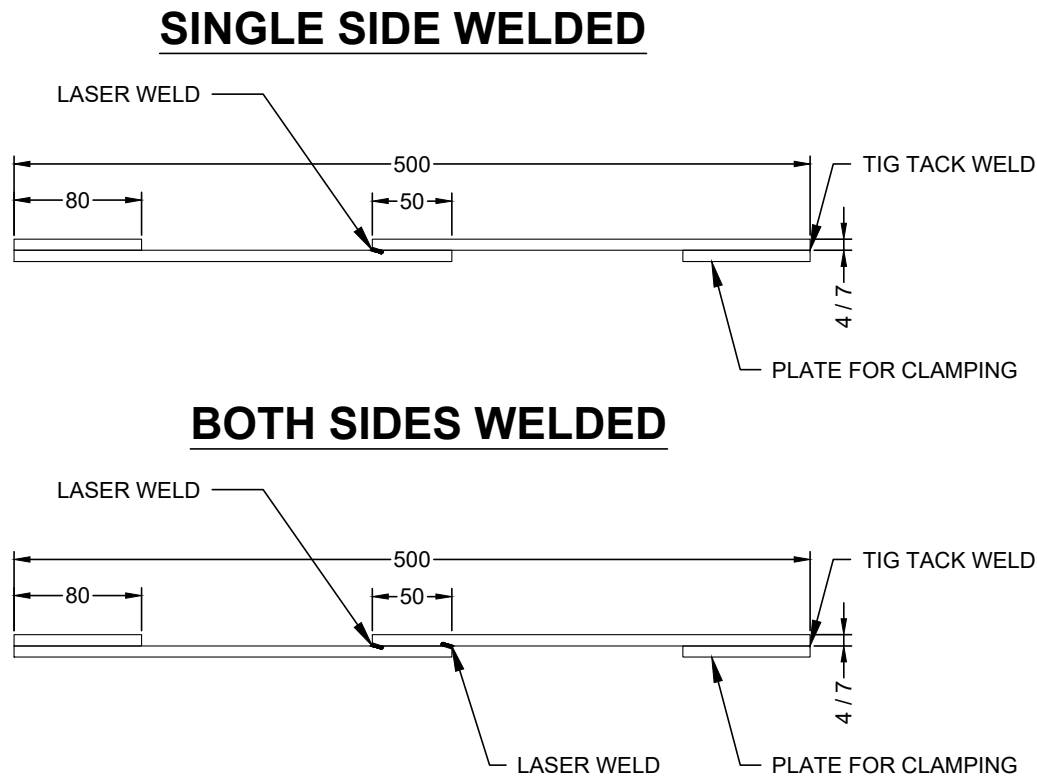
Figure 7.14: Side view of specimens

Name	4DS	4SS	7DS	7SS
Geometry	614	615	614	615
Welding	double-sided	single-sided	double-sided	single-sided
Thickness [mm]	4	4	7	7
Number	26	17	39	20

Table 7.13: Overview of specimen series for experiments

The specimens are made of S355 G1 S (1.0583). The welding is performed at the Photon AG using the 3-D laser-welding plant from A&R (fig. 7.16). This plant allows for welding 3-D deformed parts common in shell plating of marine structures. The welding characteristics are constant for each plate thickness (table 7.14). G4Si1 was used as a filler. The welding is performed under the lowest possible weld angle to ensure a high penetration avoiding WR for the single lap joint DS (614).

Specimen thickness [mm]	7	4
Laser power [kW]	8	7.5

Table 7.14: Laser welding parameter

The weld geometries obtained are typical for laser welds resulting in a high weld penetration (pn) and a small h_w and l_w (table 7.15). However, the small weld dimensions are hard to measure precisely and may introduce uncertainty when applying the ENSC. In addition, the relative change in geometry along the weld is more substantial in smaller weld geometries even if performed with a robot as common for LBW.

Specimen thickness [mm]	7	4
h_w [mm]	1.4	1.8
h_w [mm]	1.4	0.9
pn [mm]	6.1	5.1

Table 7.15: Laser weld geometry properties

When looking at the macrographs (fig. 7.15) both show the typical geometry of keyhole weld similar to the one observed in the literature review (section 3.3.2). The weld for the 7 mm thick specimen shows the parallel boundaries of the keyhole. Closer to the material surface, a circular weld bead appears due to less heat conduction possibilities closer to the surface than deeper inside the material. In addition, in both cases, the laser power could be lowered as the WM exceeds the penetration; for the 7 mm specimens, this is more the case than for 4 mm thick ones. Both welds show a radius at the weld toe; gravity likely influenced this behaviour (Barsoum & Jonsson, 2011). A slight undercut appears in both welds for the upper transition from WM to BM. The weld geometry is bulkier for the 4 mm thick specimens compared to the 7 mm thick ones, related to the amount of filler added during the welding process.

The small HAZ can be seen when looking at the microstructure, typical for laser welds. Furthermore, a slight difference in the microstructure between the HAZ and the BM is apparent, similar to the observations from the Literature study section 3.3.2.
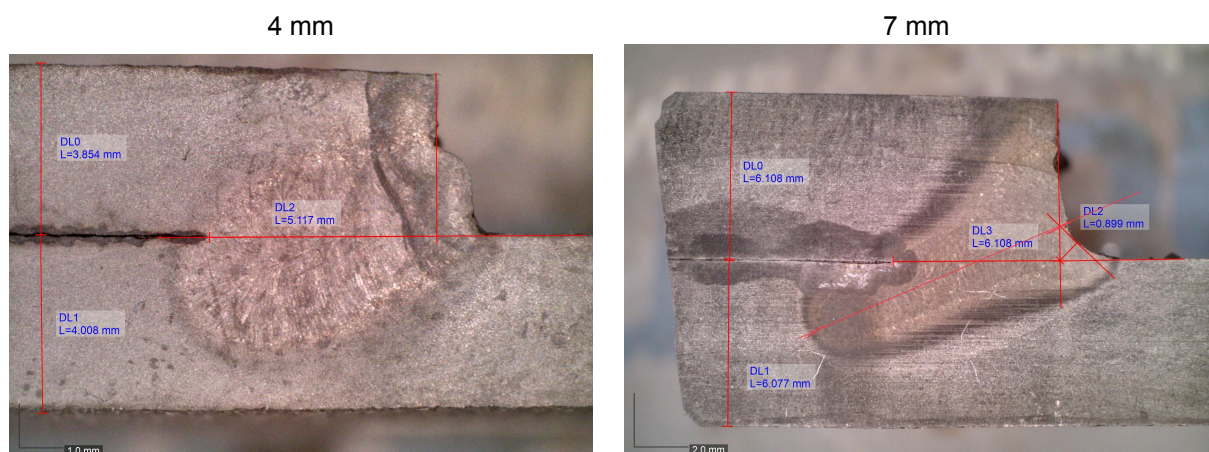
Figure 7.15: Macrograph of laser welds for the different thicknesses of the specimens

The specimens are clamped during the welding process to ensure a zero gap between the plates (fig. 7.16). This introduces residual stresses. However, it represents the industrial production process as a zero-gap is needed for good weld quality. For production purposes, 800 mm long panels are welded and afterwards sawed into the 50 mm wide specimen (fig. E.1). The flash of the sawing at the edges is removed with a flap grinder. Here, it is avoided to produce round edges.
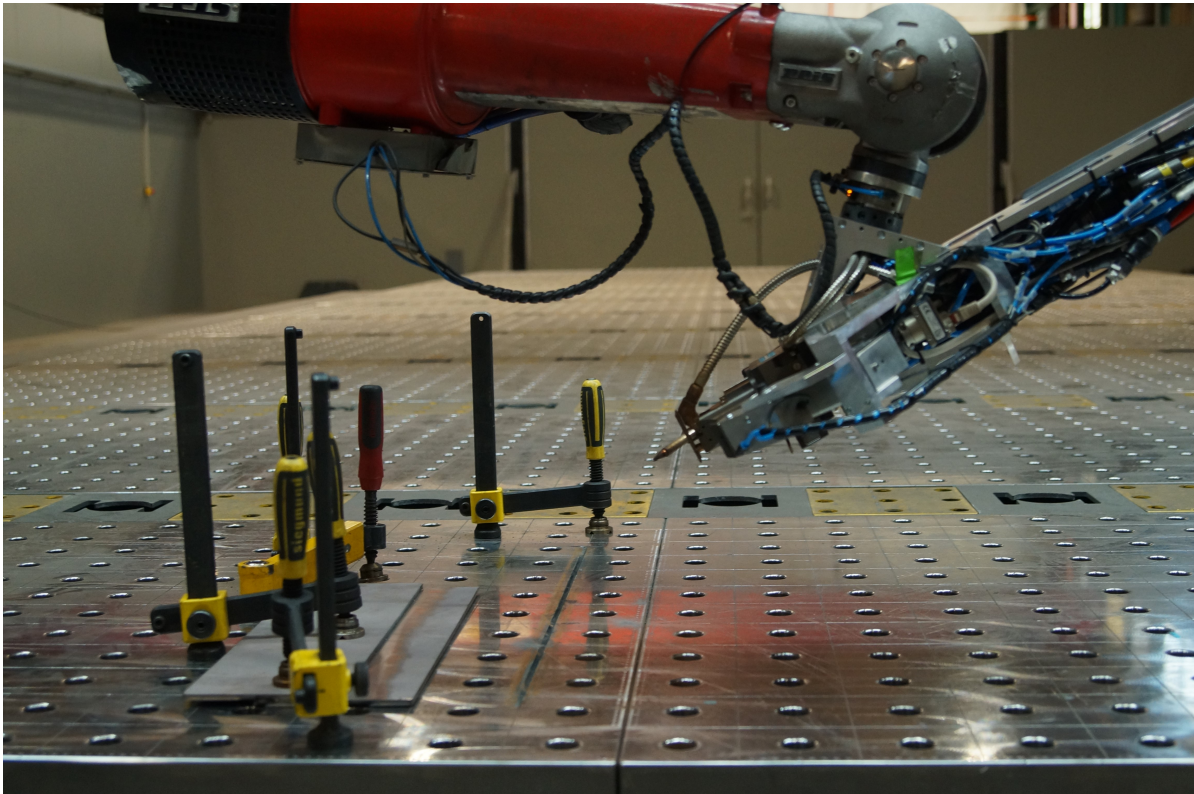
Figure 7.16: Laser welding set up

Some issues in the production process lead to limited availability of the series welded from a single side (table 7.13). This resulted in the decision to only test two specimens at each stress instead of three for the single lap joints SS (615). However, overall more specimens than needed are obtained.

Experimental set up

The testing is performed under CA uniaxial Mode-I loading. The servohydraulic machine used for the fatigue tests is an INSTRON 8854 (table 7.16). The machine features a digital controller and a fatigue-rated load cell. The length between the clamping grips is adapted to 340 mm, fitting the specimen.

max. force [kN]	250
max. torsion moment [Nm]	2000
fmax [Hz]	30

Table 7.16: Properties of INSTRON 8854

Figure 7.17: Experimental set up

Due to the secondary bending moments imposed on the machine, the lower grip connected to the load cell moved sideways. To assess the effect of this sideways movement, the magnitude of the sideways movement is captured. For this, a specimen of the 7DS series is clamped in the machine and subjected to a static load in steps of 10 kN from 10 kN up to 60 kN. For every load step, three pictures are taken. Using the thickness of the specimen as a reference and taking the average of the three pictures, the sideways movement at every load step is obtained. A linear relation between the applied force and the resulting movement is observed (fig. 7.18). Under dynamic load, a movement of 1 mm with a force of 20 kN under 20 Hz is observed. Hence, a dynamic factor 4 is assumed to fit the static results to the dynamic ones.
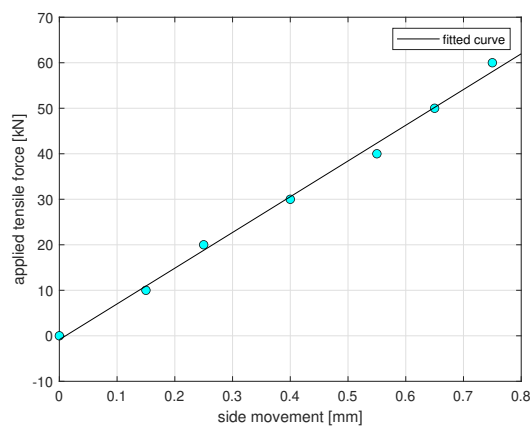
Figure 7.18: Clamp movement under static load

Performing an FE-calculation where the specimen is allowed to move sideways at the clamped side (fig. 7.19) resulted in the need for obtaining the stiffness. The spring is assumed to have a constant stiffness due to the proportional behaviour observed between the force and the movement (fig. 7.18). The stiffness is set to fit the resulting deformation of 1 mm under 20 kN of load.
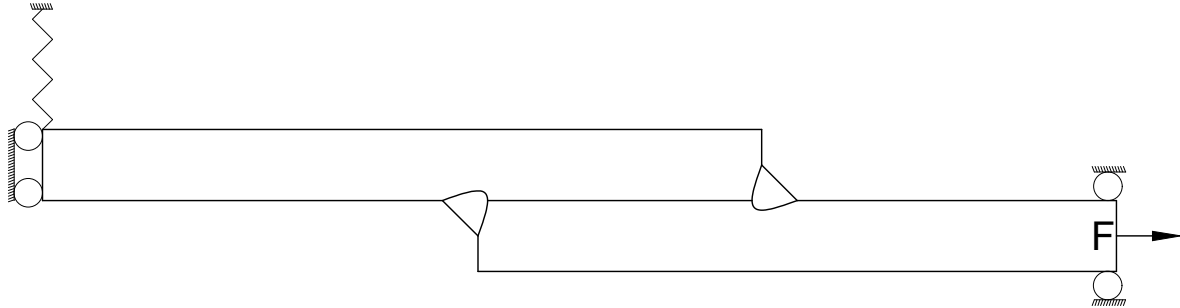
Figure 7.19: FE-model boundary conditions with spring

For the experimental results the S_e are calculated with and without a spring under the obtained ρ^* and γ (fig. 7.20). No significant change in S_e is apparent. Therefore, the insignificance of the sideways movement of the clamp is verified.
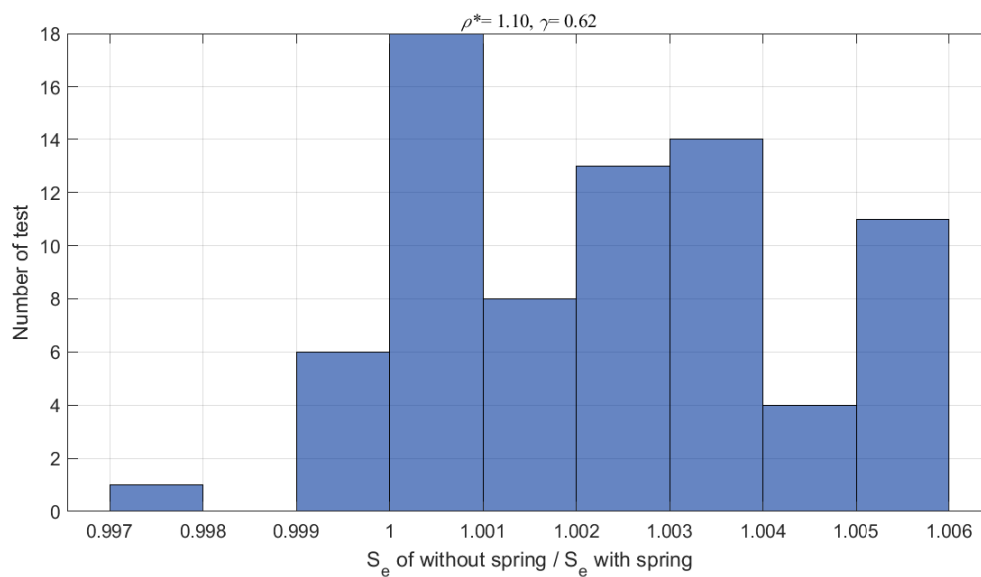
Figure 7.20: Impact of sideways movement on S_e

Finite-element-model

For this research the weld shall be modelled in a triangular shape. However, the real weld shape is different (fig. 7.21). Therefore, FE-calculations under a nominal tensile stress of $500MPa$ for the specimens are performed for both shapes.
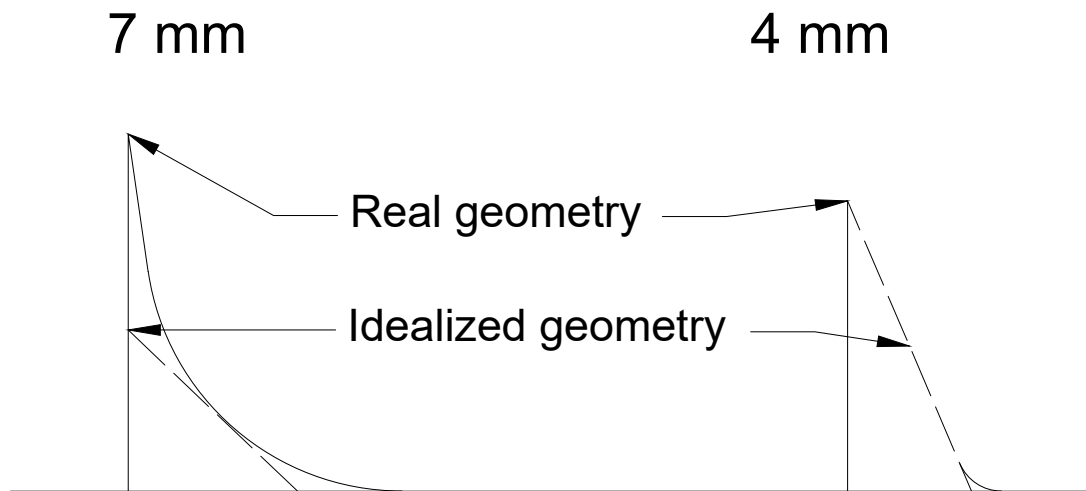
Figure 7.21: Shape of real and idealized geometry of welds based on fig. 7.15

The 7SS series showed the most extreme results. However, the weld notch stress distribution is not significantly influenced by the difference in shape (fig. 7.22). At the toe there is no influence, caused by the not apparent change in cross section and the calculation of the stresses only from the nodal forces in x-direction. Only the x-direction is taken into account as the crack appears vertical through the thickness. In addition, for the root, there is only a negligible influence. This results from a different weld load carrying behaviour due to the slight change in weld geometry. Hence, using the idealized weld geometry is allowed for obtaining the notch stress distribution. All results can be found in appendix E.2.
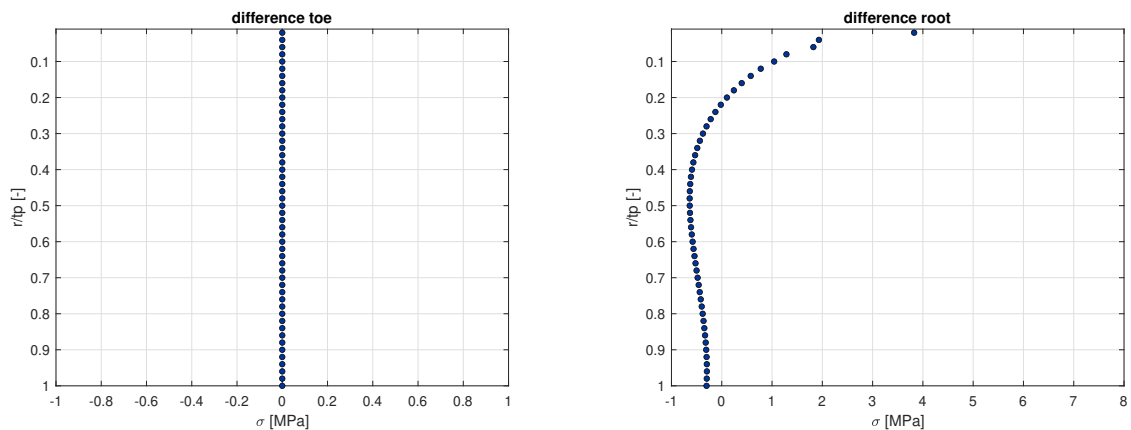
Figure 7.22: Difference in weld notch stress distribution for 7 SS series with $\sigma_n = 500 MPa$

7.3.2. Fatigue resistance data

The number of cycles until complete failure is obtained from the experiments. Overall, 80 experiments are performed (fig. 7.23; table E.1). Although HCF is excluded from this thesis, the inaccurate estimation of stress levels lead to a few data points in this region.

Looking at the results, the scatter increases for lower stress levels as generally assumed. This applies to both the SS and DS joints. The scatter for the $r_{lr} = 0.5$ is the smallest; the other two r_{lr} shows a higher scatter. Changing the r_{lr} caused, as expected, a vertical shift in the data where bigger r_{lr} yield a shorter lifetime, respectively higher stress levels and more minor r_{lr} show the opposite behaviour.

The DS joints show a better fatigue resistance than the SS joints based on S_n. This is expected as only one weld leads to a higher stress concentration. For the SS joints root failure is expected. However, all 7 mm thick specimens apart from one failed at the toe. Showing a similar behaviour to arc-welded lap joints (section 7.2.5).

The results show a flattening behaviour already at $N = 10^6$ whereas, for arc-welded joints, it is predominantly assumed to be at $N \approx 10^7$ (Hobbacher et al., 2016; Qin et al., 2020). This indicates a better HCF fatigue resistance.
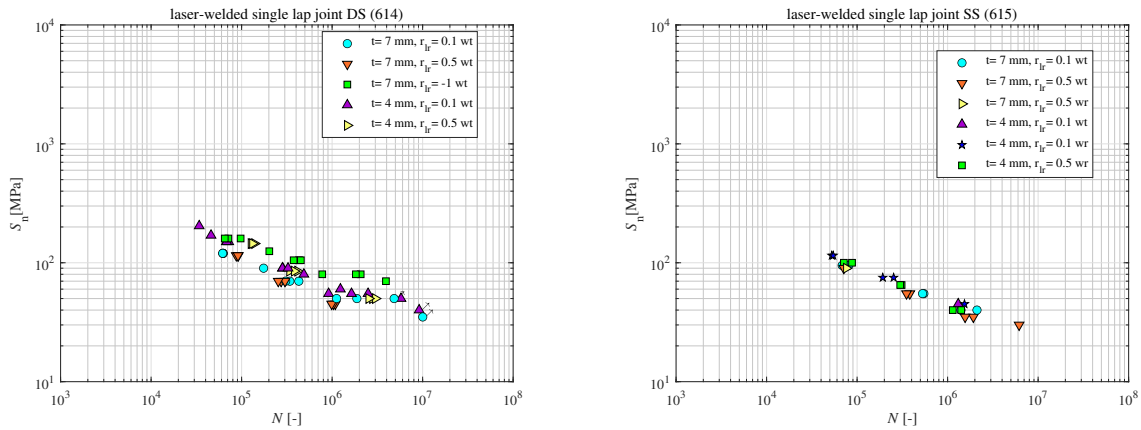
Figure 7.23: Fatigue resistance data obtained from experiments

7.3.3. Nominal stress concept assessment

Only experimental data is assessed to keep comparability to the arc-welded lap joints (section 7.2.2). As observed before, the log(Normal) distribution provides a more accurate result (table 7.17). The inverse slope is close to the expected value of $m = 3$. In addition, the fit is already quite good with $T_{\sigma S} = 1 : 1.82$ and $\sigma = 0.24$. However, the γ is at the lower bound observed for arc-welded joints with values between 0.7 and 1.0. This shows the higher dependency on the mean stress level.

MLE	log(C)	m	σ	γ	AIC
Normal	10.58	2.75	0.27	0.70	141
Weibull	10.58	2.76	0.36	0.71	166

Table 7.17: MLE of NSC for experimental data

Looking at the $S_n - N$ curve, the DS joints show a better fatigue resistance in line with the experiments (section 7.3.2; fig. 7.24). For the SS joints, no difference is apparent between WR and WT. One set of outliers is apparent at $N = 1.5 * 10^5$. These are tests performed at $r_{lr} = -1$. The rest of the data shows already a good fit.
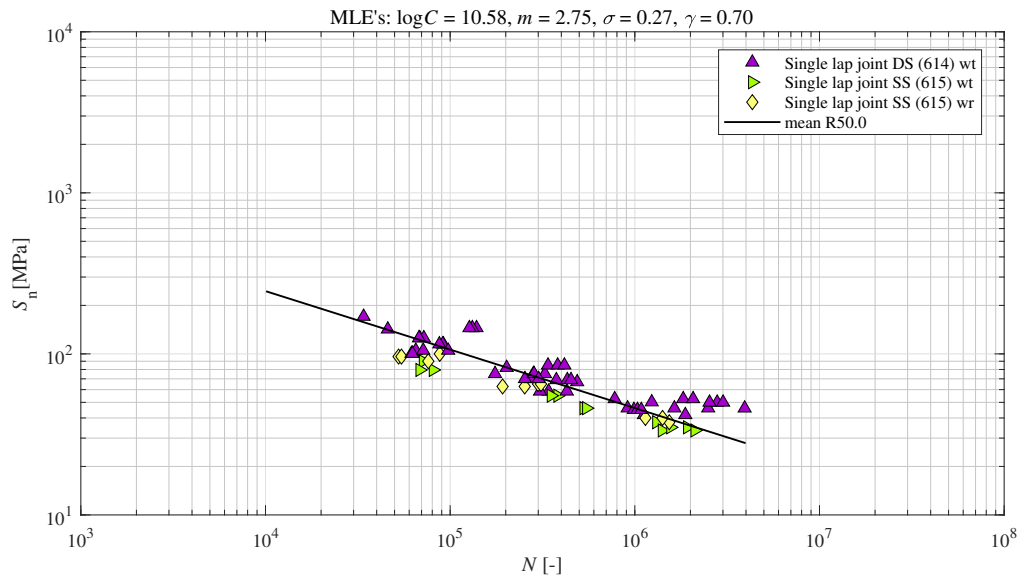
Figure 7.24: $S_n - N$ curve for NSC of experimental data

The confidence bounds reflect the fit (table 7.18). Only the γ shows a wide range, although special attention was paid during the experiments to cover different r_{lr}.

Parameter	C75LB	MLE	C75UB
log(C)	10.21	10.58	10.94
m	2.55	2.75	2.95
σ	0.24	0.27	0.29
γ	0.64	0.70	0.76

Table 7.18: MLE and CB's for NSC of experimental data

No FAT classes are determined so far for laser-welded joints. Therefore, the resultant quantile design curve R97.7C75 is compared to the corresponding FAT design curve for arc welding. To incorporate a consistent correction of the mean stress effect $\gamma = 0.70$ is adapted as obtained above.

For the butt joints (216), m is set to 3 as the relation of scatter over the available stress range is too big to fit a reasonable curve (fig. 7.25). As the weld is fully penetrating, a root failure is initiated at the bottom of the plate instead of the top. The quantile design curve yields smaller values than the FAT design curve. However, all data, excluding one test point, lie above the FAT design curve. The high scatter causes a low certainty. Hence, this FAT class might still represent laser welds.

The scatter is lower for single lap joints DS (614), causing a closer quantile design curve. The eccentricity is accounted for in the same way as for arc-welded joints (section 7.2.2). This curve lies above the FAT design curve and shows a similar slope. Here the laser-welded joints are represented by the FAT class for arc-welded joints.
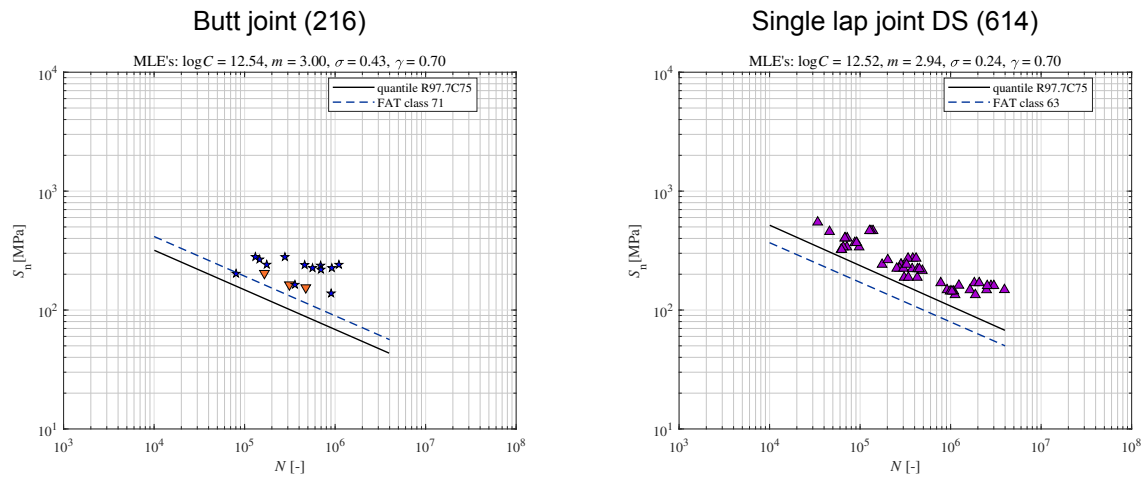
Figure 7.25: $S_n - N$ curve for NSC of laser-welded joint Part I

Opposite to the other two joint types, the fatigue resistance data of T-joints is already partly below the FAT design class (fig. 7.26). In addition, serious scatter is apparent, yielding a low quantile design curve. This data does not comply with the arc-welded FAT class design curve. The reason for this is a significant deformation of the specimens caused by the welding process which is not taken into account in the NSC (Fricke & Robert, 2012). For the HSSSC and ENSC, this deformation is taken into account by the FE calculations.

The amount of available data for the cruciform join (413), results in limited applicability. However, although the $t_p = 12.7mm$ and values of $m \approx 5$ appear predominantly for thin plates, the inverse slope does have a value of 4.66. Although this restricted data does not comply with the FAT design curve, this must not generally hold.
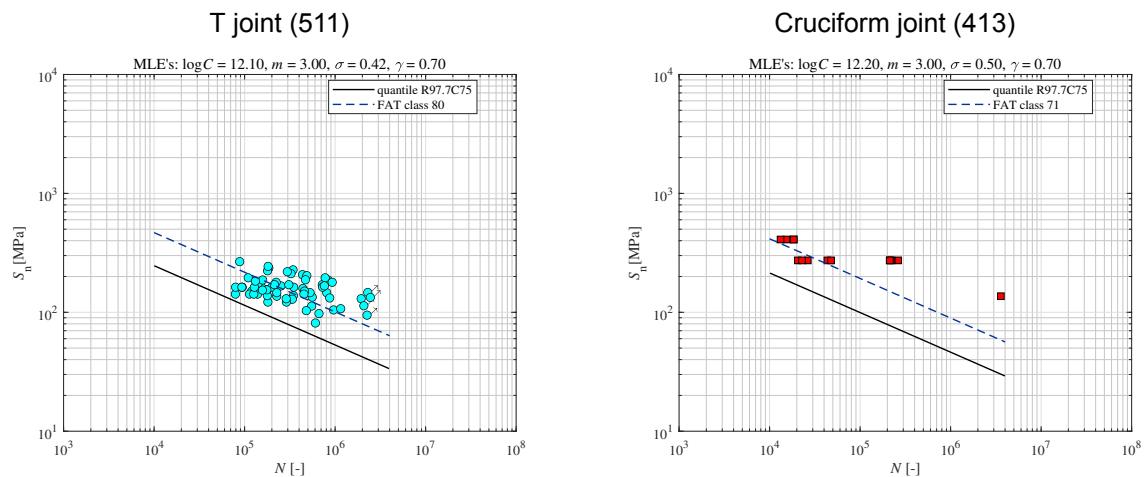
Figure 7.26: $S_n - N$ curve for NSC of laser-welded joint Part II

A flatter slope is also observed for the toe failure of single lap joints SS (615) (fig. 7.27). However, in this case, it lies consistently above the FAT design curve, due to the small scatter. For this joint, the fatigue resistance can be represented by the FAT class value of the arc welded joint. Even more extreme behaviour is apparent for the WR, where the quantile design curve shows values more than twice as high as the FAT design curve.
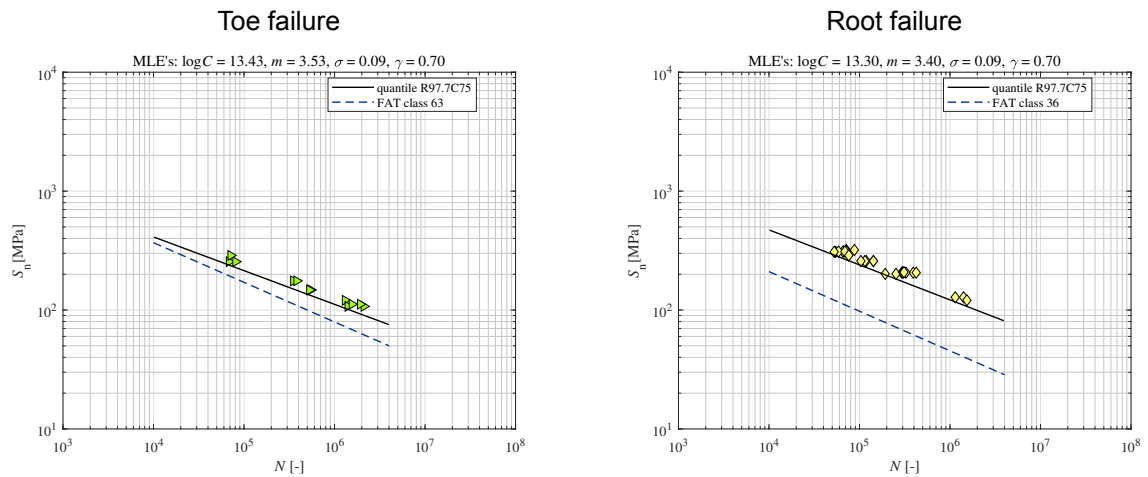
Figure 7.27: $S_n - N$ curve for NSC of laser-welded single lap joints SS (615)

7.3.4. Hot spot structural stress concept assessment

Utilizing the HSSSC enhances the fit. The AIC is close to 100 for the log(normal) distribution together with the $T_{\sigma S}$ of 1:1.74. The slope and the γ do not differ significantly between the distributions. However, the log(Normal) distribution yields better results.

MLE	log(C)	m	σ	γ	AIC
Normal	12.80	3.07	0.20	0.69	102
Weibull	12.99	3.16	0.28	0.68	127

Table 7.19: MLE of HSSSC for experimental data

The quantile design curve aligns with the FAT design curve showing the applicability of the FAT class for arc-welded structures. Furthermore, both WR and WT lie in the same scatter cloud proofing the usability of the HSSSC.
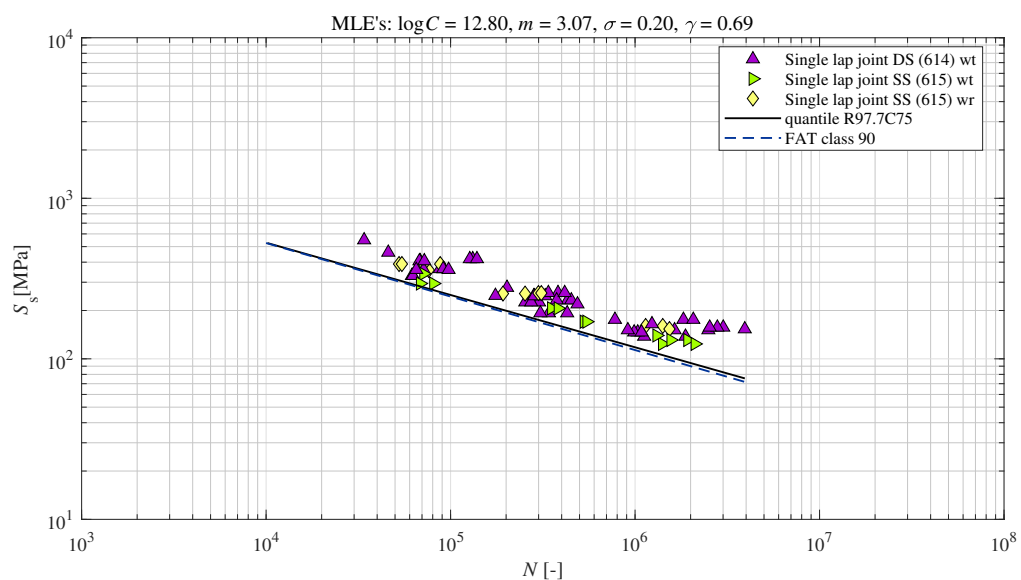
Figure 7.28: $S_s - N$ curve for HSSSC of experimental data

The confidence bounds are still large, related to uncertainty (table 7.20).

Parameter	C75LB	MLE	C75UB
log(C)	12.42	12.80	13.16
m	2.91	3.07	3.23
σ	0.18	0.20	0.22
γ	0.65	0.69	0.73

Table 7.20: MLE and CB's for HSSSC of experimental data

7.3.5. Effective notch stress concept assessment

Two notch stress hypotheses are evaluated, namely the LENSC (section 7.3.5) and the PENSC (section 7.3.5). For both methods, first, a fit is established with both the experimental results (75 data points) and the data from the literature (111 data points) (appendix B). However, series 14 of the literature data is excluded as the penetration weld from one side resulted in a complete outlier. Secondly, a fit for only the experimental data is obtained to compare the performance to the other fatigue concepts and arc-welded lap joints.

Line method assessment

Due to the better performance of σ and AIC, a log(normal) distribution is taken (table 7.21). In addition, the choice of distribution significantly influences the curve and material parameter.
The m is close to the typical value of $m = 3$. The ρ^* is in the proximity of the one for arc-welded joints $\rho^* = 0.95$. However, it is larger than observed for laser welds in literature where a $\rho = 0.05$ is used, implicitly yielding smaller ρ^* (Hensel et al., 2022; Marulo et al., 2017). The same relation is observed for arc welding when introducing a $\rho = 0.05$ (section 2.4.6). The γ is in line with the before observed ones for the NSC (section 7.3.3) and HSSSC (section 7.3.4).

MLE	log(C)	m	σ	ρ^*	γ	AIC
Normal	12.62	2.93	0.31	1.10	0.62	408
Weibull	12.96	3.06	0.40	1.05	0.52	454

Table 7.21: MLE of LENSC for laser-welded joints

At the upper end of the MCF, significant scatter starts to appear, indicating a knuckle point at $N = 10^6$. For the rest, the scatter is rather constant. The cruciform joints lie at the boundaries of the scatter cloud, possibly caused by the number of cycles obtained at a doubled initial opposite to complete failure (Caccese et al., 2006). For the rest of the joints, the scatter appears around the proposed $S_e - N$ curve yielding $T_{\sigma s} = 1 : 2.01$.
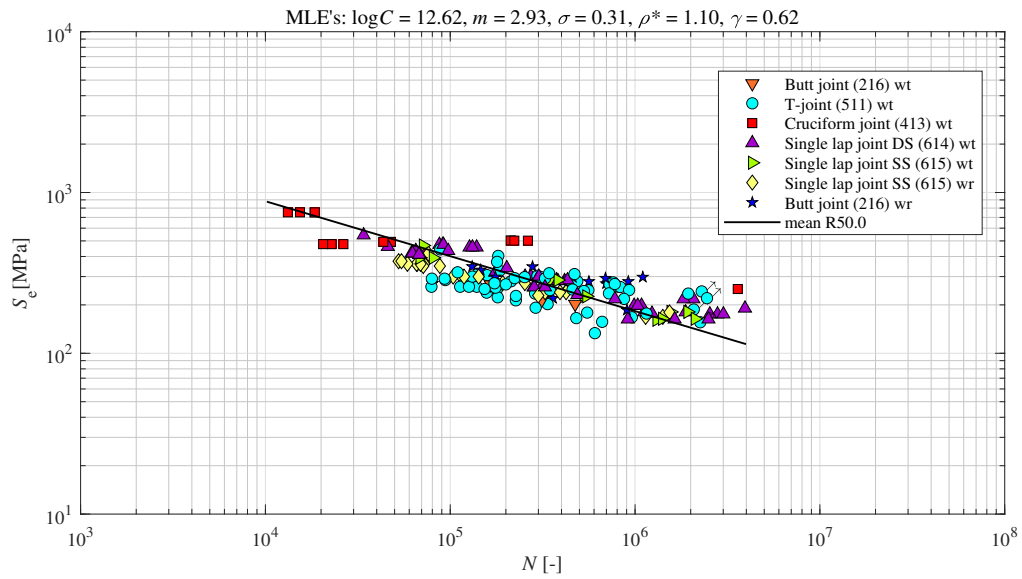
Figure 7.29: $S_e - N$ curve for LENSC of laser-welded joints joints

The confidence bounds are still fairly wide possibly caused by the larger amount of data compared to before and the added material dependent parameter (table 7.22).

Parameter	C75LB	MLE	C75UB
log(C)	12.19	12.62	13.08
m	2.75	2.93	3.11
σ	0.29	0.31	0.32
ρ^*	1.02	1.10	1.16
γ	0.57	0.62	0.67

Table 7.22: MLE and CB's for LENSC of laser-welded joints

Limiting the fit to lap joints results in a good fit. The γ did not change, opposite to the ρ^* showing the same value as for arc-welded joints. The fit is enhanced compared to the HSSSC with $\sigma = 0.18$ and $T_{\sigma s} = 1 : 71$.
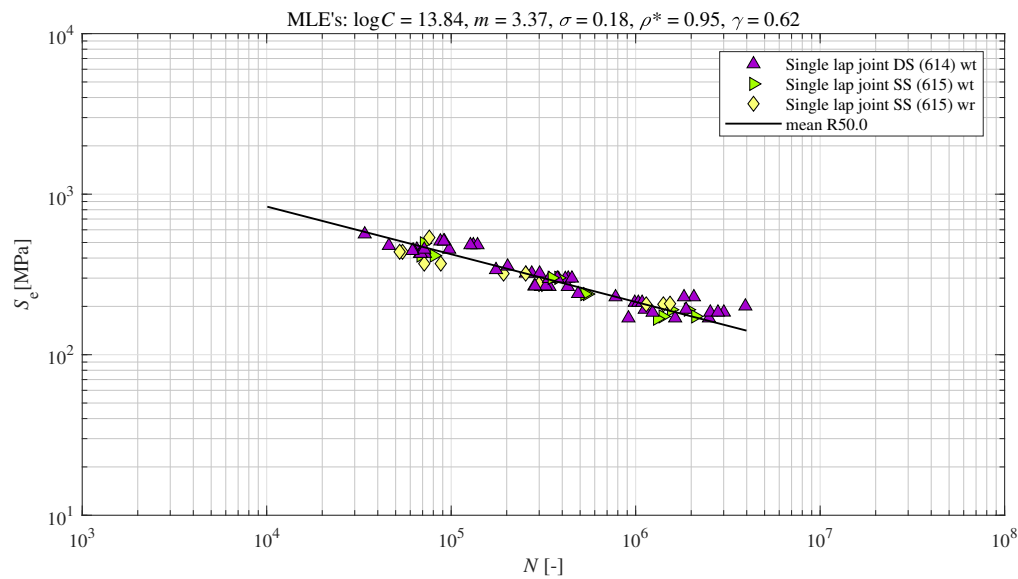
Figure 7.30: $S_e - N$ curve for LENSC of experimental data

Parameter	C75LB	MLE	C75UB
log(C)	13.45	13.84	14.23
m	3.21	3.37	3.53
σ	0.17	0.18	0.20
ρ^*	0.86	0.95	1.03
γ	0.59	0.62	0.65

Table 7.23: MLE and CB's for LENSC of experimental data

Point Method assessment

The values for the curve and material parameter obtained by the two distributions differ greatly (table 7.24). As commonly observed so far, the log(normal) distribution provides a better fit. Still, the performance is slightly worse than the one of the LENSC (section 7.3.5). Especially, the steeper slope of $m = 2.46$ is noticeable, resulting from the different notch hypotheses. In addition, the a^* is only about a tenth of the observed ρ^*. This diverts from any observed factor in literature where a factor of 0.25 is observed for laser welds (Marulo et al., 2017; Hensel et al., 2022). However, the absolute value is comparable to the literature's $a^* = 0.1, 0.08mm$. The geometry of laser welds is small; hence, the relative errors appearing are significant. Secondly, only a limited amount of data is available. Furthermore, already for arc-welded joints, a dependency of the fit on the quality of data is found (section 7.2.4).

MLE	log(C)	m	σ	a^*	γ	AIC
Normal	11.89	2.46	0.33	0.14	0.79	429
Weibull	12.70	2.76	0.41	0.12	0.65	465

Table 7.24: MLE of PENSC for laser-welded joints

The same scatter behaviour as observed for the LENSC is apparent, yielding a $T_{\sigma S}$ of 1:2.26 (fig. 7.31).
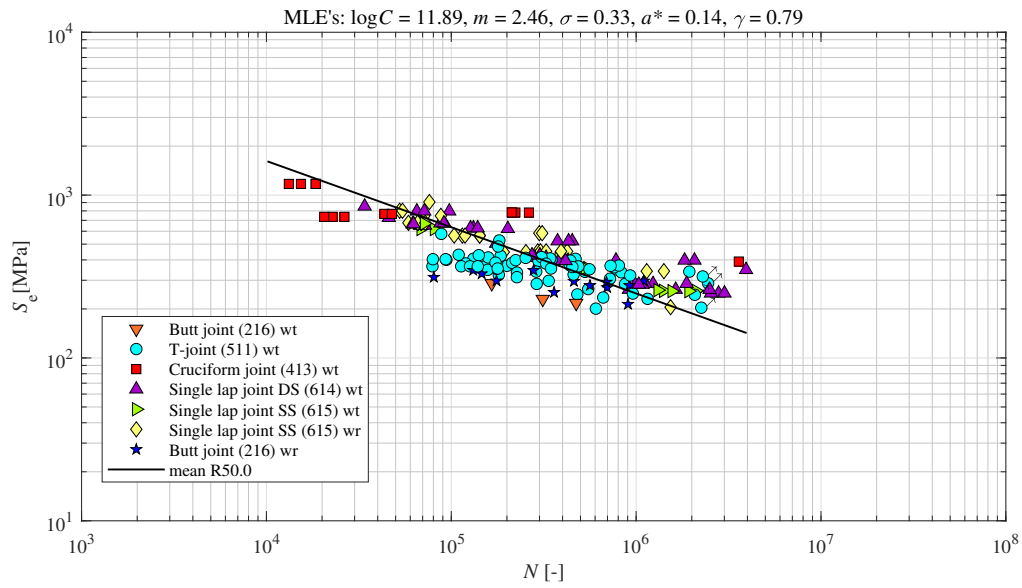
Figure 7.31: $S_e - N$ curve for PENSC of laser-welded joints

The confidence bounds of the curve parameter are approximately the same as for the LENSC (table 7.25). However, the material parameters show bigger relative confidence bounds.

Parameter	C75LB	MLE	C75UB
log(C)	11.46	11.89	12.33
m	2.28	2.46	2.64
σ	0.31	0.33	0.35
a^*	0.12	0.14	0.15
γ	0.72	0.79	0.86

Table 7.25: MLE and CB's for PENSC of laser-welded joints

The a^* only changed slightly when only examining lap joints compared to all joints (fig. 7.32). However, the γ is lower.

Compared to the HSSSC (section 7.3.4), the fit is slightly enhanced with a $T_{\sigma S}$ of 1:1.85. The scatter observed at the root failures is higher than the one for the toe failure.
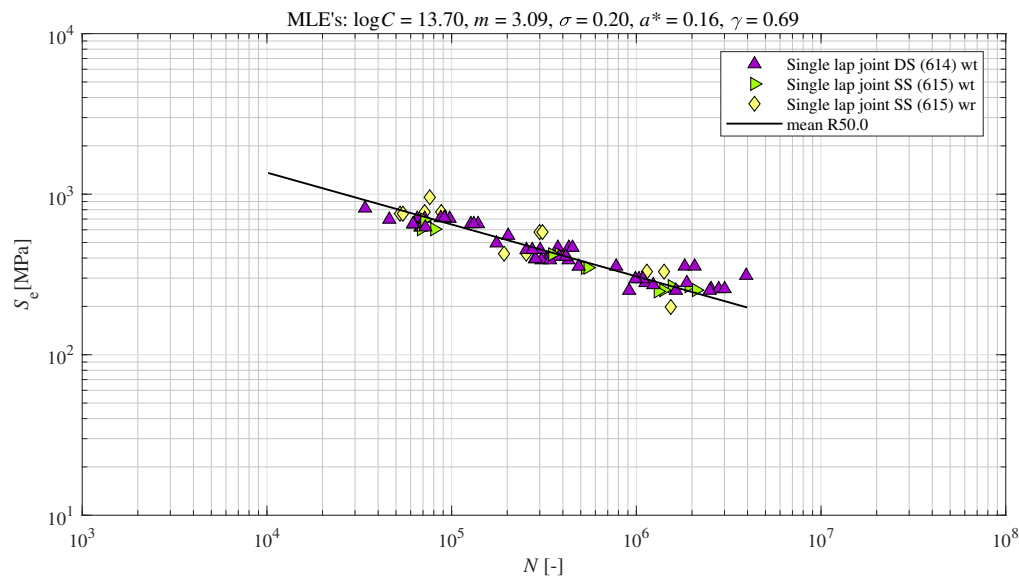
Figure 7.32: $S_e - N$ curve for PENSC of experimental data

Compared to the assessment with all laser-welded joints the fit for only lap joints tighter the confidence bounds apear caused by the small scatter apparent in the fatigue resistance data (table 7.26).

Parameter	C75LB	MLE	C75UB
log(C)	13.29	13.70	14.11
m	2.93	3.09	3.25
σ	0.18	0.20	0.22
a^*	0.12	0.16	0.18
γ	0.65	0.69	0.73

Table 7.26: MLE and CB's for PENSC of experimental data

7.3.6. Discussion

First, experiments are performed, yielding 80 new data points (section 7.3.1). Different stress levels, r_{lr} and specimens are tested to capture different influences. The sideways movement of the lower clamp, which is observed during the experiments, only has a negligible influence on the S_e.

When using the NSC, the laser-welded joints can largely be represented by the corresponding FAT design curve of arc-welded joints (section 7.3.3). Compared to arc-welded joints, a smaller γ is already observed (0.70). The primary influence for this parameter is the residual stress which is lower for laser-welded joints (section 3.3.5). Hence, the influence of the mean stress is more prominent.

For the HSSSC, the laser-welded lap joints did perfectly fit the FAT design curve of arc-welded joints (section 7.3.4). A similar behaviour is found in literature (Fricke et al., 2015). The γ is very close to the one of the NSC with a value of 0.69 but an improved fit is apparent compared to the NSC. In addition, the scatter is smaller for laser-welded joints than for arc-welded joints. Robots performed all laser-welded joints, so the human factor does not introduce uncertainty. However, the small amount of available data might also be a reason.

For the LENSC, the material parameters differ from the ones for arc-welded joints. For laser-welded joints, a $\rho^* = 1.10$ is proposed compared to the one for arc-welded joints of $\rho^* = 0.95$ ("Qin et. al.", 2023). Only looking at the material characteristics; microstructure (section 3.3.2), hardness (section 3.3.3); of laser welds ρ^* should be smaller (Atzori et al., 2005). However, laser welds have a smaller toe weld radius than arc welds (section 2.4). Therefore, as $\rho = 0$ is assumed, the ρ^* needs to be bigger. Resulting in a higher geometrical influence than the one from the material. The proposed γ

is similar in all concepts is similar with values between 0.62 and 0.8. Opposite to observations in literature (section 3.4), the $m = 2.93$ is close to the one of arc-welded joints $m = 3.15$ ("Qin et. al.", 2023). Furthermore, the knuckle point related to HCF seems to be at $N = 10^6$ as the material characteristics indicate a better initiation behaviour than arc-welded joints. Hence, a better HCF fatigue resistance is expected (section 3.4). A similar knuckle point is observed in literature (Sonsino et al., 2010).

For a few data points, the LENSC does not predict the correct failure location (fig. 7.34). No clear border value can be obtained. In addition, failure occurred at the root when predicted at the toe.
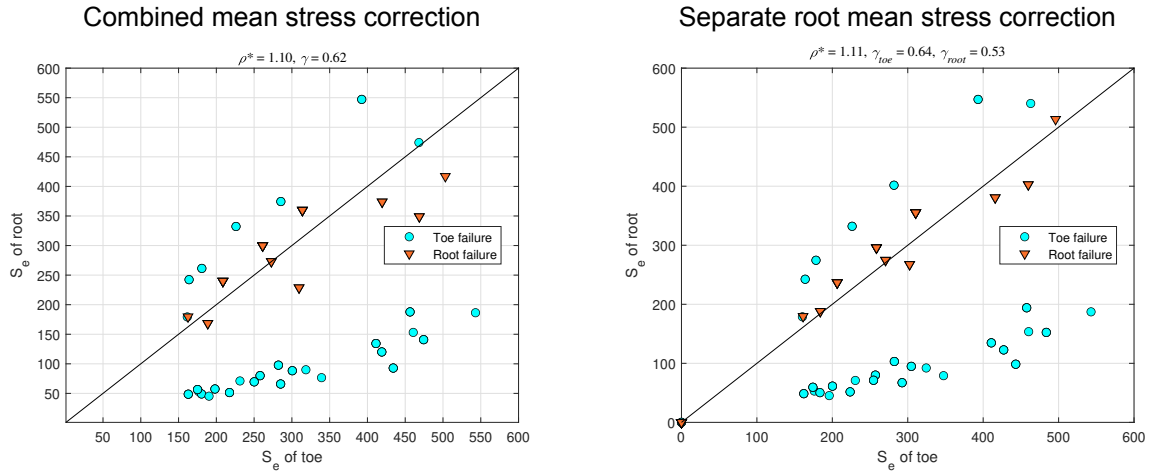
Figure 7.33: Influence of residual stress at the root
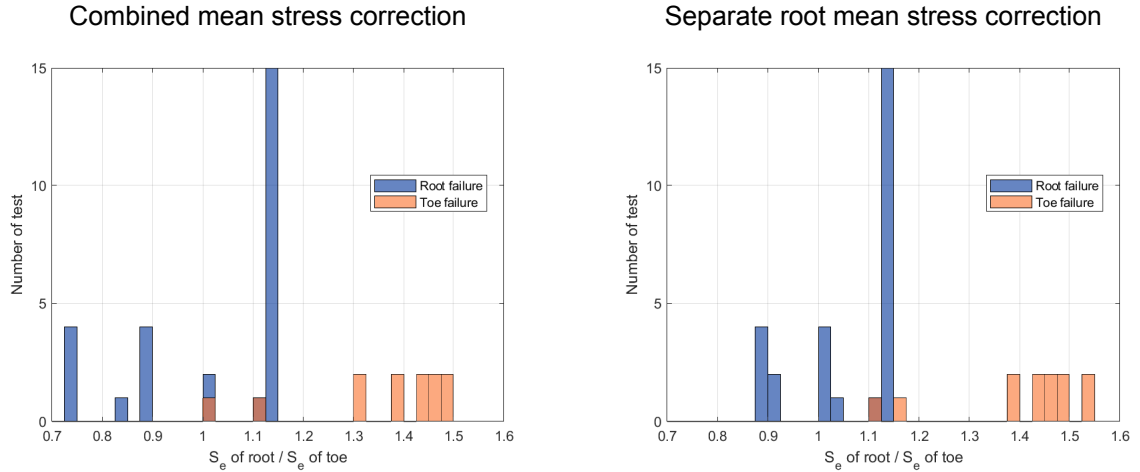
Figure 7.34: Influence of residual stress at the root

To validate the influence of the different residual stress at the root the γs are obtained separately for each failure location (fig. 7.35). The curve parameters and ρ^* did not change significantly. However, the γ obtained for the root is significantly lower, whereas the one for the toe is close to the one obtained before $\gamma = 0.62$. This indicates a lower residual stress at the root of laser-welded joints. The general fit quality is not improved with this adaptation. In addition, the occurring toe failure predicted root failures are still apparent with the same error (fig. 7.33). However, the root failures are closer to be predicted as those. Hence, the residual stress difference between the failure locations partly causes the wrong prediction.
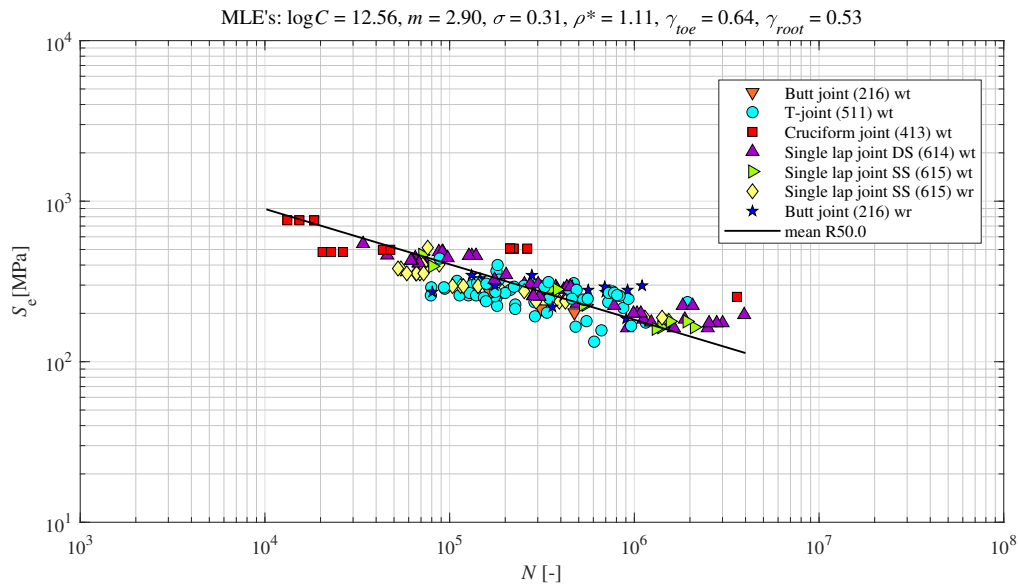
Figure 7.35: Fitting with separate mean stress correction with LENSC

When using the PENSC the prediction of the failure locations is even worse (fig. 7.36). In combination with the worse general fit, the mean stress influence is not elaborated for the PENSC.
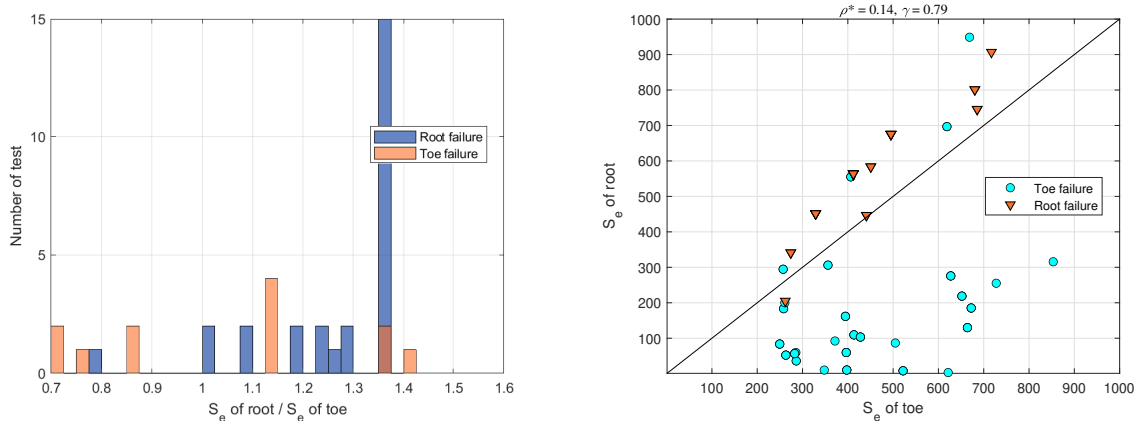
Figure 7.36: Influence of residual stress at the root

No relation can be obtained between the a^* for the arc-welded and laser-welded joints, where the one for arc-welded joints is a factor 4 bigger. Neither the material characteristics nor the weld geometry explain this relation. It seems to result from the PENSC when only taking one point to obtain the stress results in a high dependency on the amount and quality of the available data. Furthermore, the slope change likely results from the a^*.

Overall, the fatigue resistance of laser-welded joints is not significantly better than that of arc-welded joints. The apparent improvement in the MCF is so small that using the design curves of arc-welded joints is advised. In addition, the slope is similar to the one of arc-welded joints. However, the influence of the mean stress is higher for all fatigue concepts related to smaller γ. The material-dependent ρ^* is slightly bigger and likely caused by the smaller toe radius. For the PENSC, no explanation is found for the relation between the a^*s for arc- and laser-welded joints. Hence, it is advised to use the LENSC due to its robustness, although the PENSC only provides slightly less accurate results.

7.4. **Weld geometry optimization**

When welding is performed, the weld angle, as well as the width of the laser beam, can be varied. For the laser welds, a perpendicular relation between the surface of the weld throat and the keyhole direction is observed (fig. 7.37). However, this only holds as long as the weld angle is not too extreme, as gravity causes a different geometry (fig. 7.15). Furthermore, a penetration deep enough into the material is assumed. The amount of filler added is assumed to lead to a triangular weld geometry, opposite to the one observed for the 4 mm thick specimen (fig. 7.15). Hence, a laser weld can be described by the weld width and the corresponding weld angle yielding a triangular weld shape (fig. 7.38).
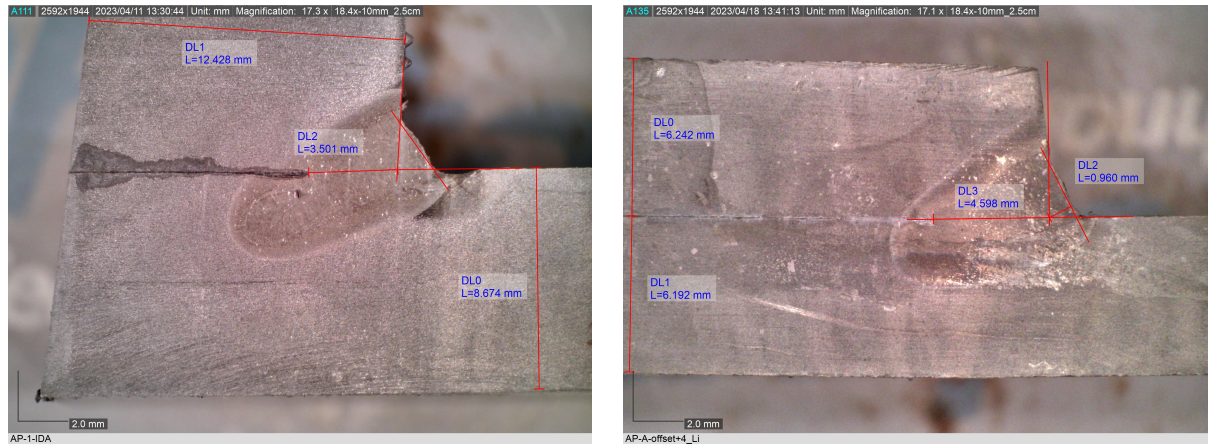
Figure 7.37: Macrographs of earlier weld tests
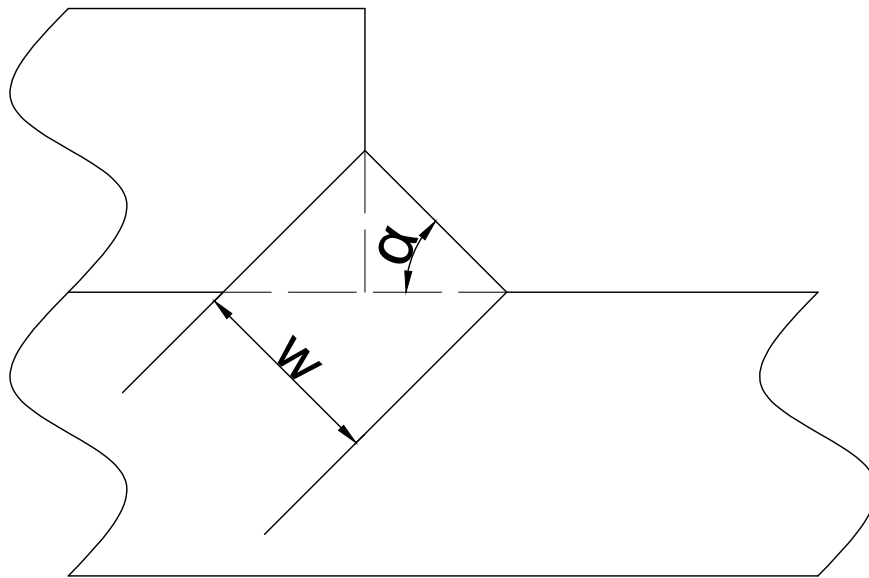
Figure 7.38: Model for optimization of weld angle and weld thickness

For the used 7 mm thick single lap joint DS (614) specimen from the experiments, the weld angle is varied (α) from 25° until 60° and correspondingly, the weld thickness (w) is varied from 1 mm until 3 mm. **c!** (**c!**)alculations are performed as the criterion established to cover geometries where the stress

is distributed over the whole thickness is not fulfilled. The effective stress is obtained by using the
LENSC with the established ρ^* (section 7.3.5).
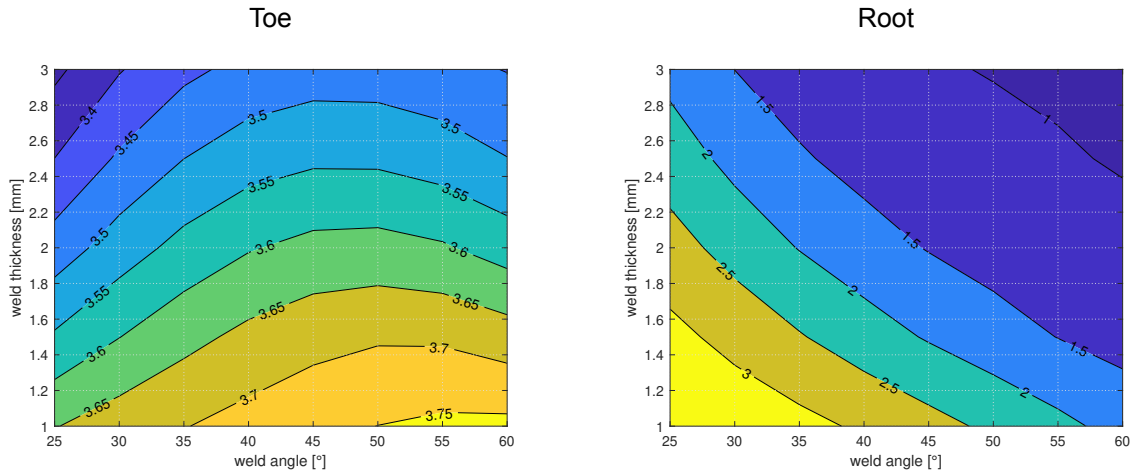
Figure 7.39: S_e/S_n at Sn= 100 MPa

First, a S_n of $100MPa$ with $r_{lr} = 0.1$ is applied (fig. 7.39). A bigger weld thickness relates to lower
effective stress for the toe and the root. However, a maximum occurs with a position dependent on
the weld thickness for the weld angle at the toe. Hence, small or high weld angles must be chosen for
low effective stress. The V-shaped notch contribution is small for the low weld angle, but the weld load
carrying is high due to the small penetration. The influence of the V-shaped notch contribution gets
more significant for higher weld angles, and the weld load-carrying influence decreases due to higher
penetration. Around 45° a maximum occurs as both contributions of the self equilibrium equivalent
stress have a high value.
For the root, no such behaviour is observed. Here, a higher weld angle results in lower stress. This
can be related to the increase in penetration, the main factor for the stress at the root.
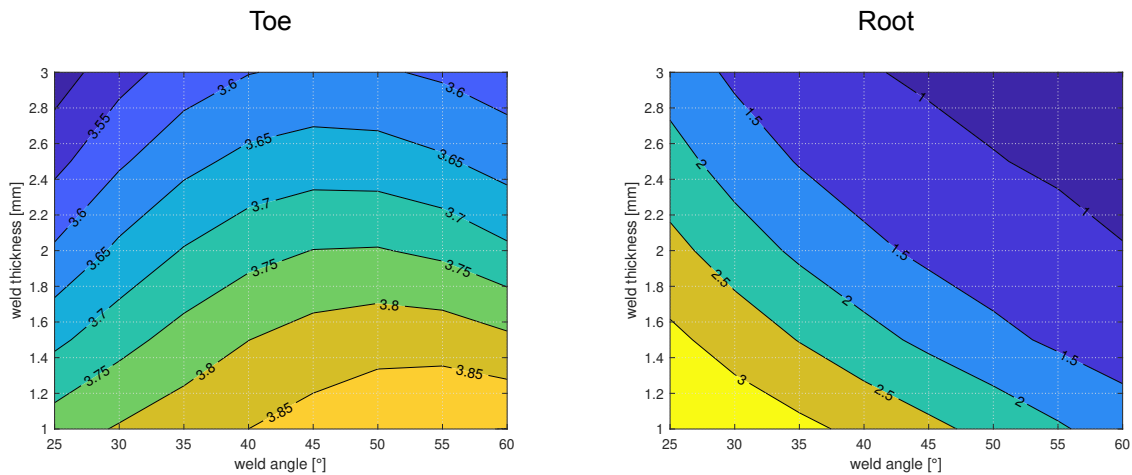
Figure 7.40: S_e/S_n at Sn= 30 MPa

When a S_n of $30MPa$ is applied the patterns are the same as observed for the application of $100MPa$
(fig. 7.40). However, the change in the influence of secondary bending moments is apparent, meaning
the effective stresses do not scale proportional to the applied stress. Lower S_n cause relatively high S_e.
This influence is higher for the toe than for the root. Dividing the S_e of the toe by one of the root gives
insight into the failure location (fig. 7.41). For all here given joints, the failure always occurs at the toe,
even for the ones with a small weld angle and small weld thickness. However, with a lower S_n, a failure
at the root is generally more likely.
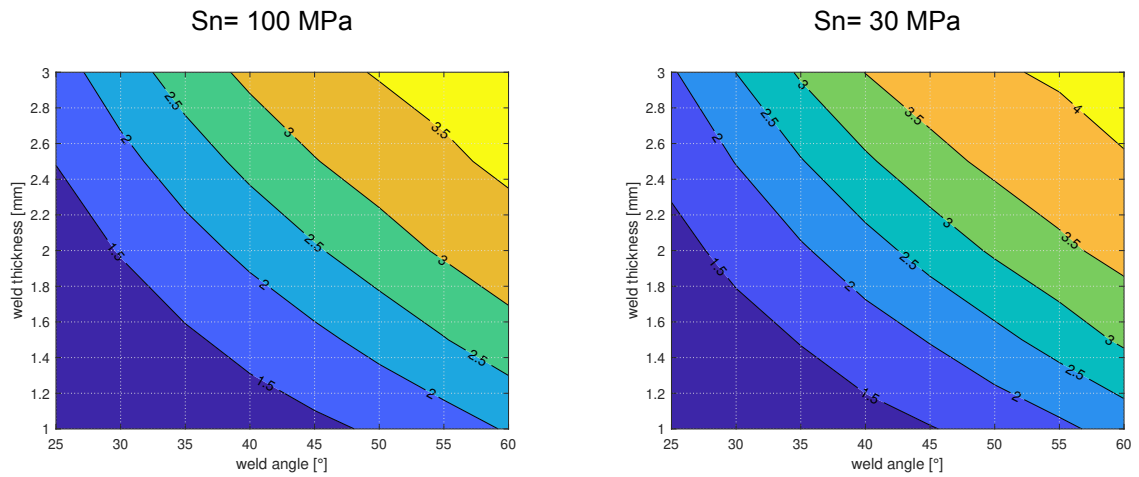
Figure 7.41: S_{e-toe}/S_{e-root} of optimization

From this, the following conclusions are drawn. A higher weld thickness always positively influences fatigue resistance. The fatigue resistance depends on the weld angle. Therefore, small or high weld angles should be chosen where a small weld angle provides better fatigue resistance. However, the safety that no root failure might occur is lower. Hence, it is advised to use welds with a high weld angle and a high weld thickness, even more for welds under low stress than ones subjected to high stress.
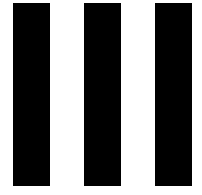
Judgement & future work

<div align="right">

8

</div>

<div align="right">
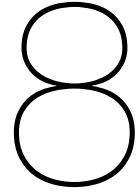
Conclusion

</div>

The problem statement in combination with the literature review yielded the
Research hypothesis:
Can the fatigue strength, separately, be estimated for each failure location of a laser- and arc-welded lap joint with the ENSC, and how is the fatigue performance?
To answer the different parts of the research gap, research questions were established section 5.3. The corresponding answers are presented in the following part leading to the result of the research hypothesis :

1. **How do the weld root and weld toe notch stress distribution for different laser- and arc-welded lap joint geometries look?**

    The weld root notch stress distributions follow the same principles for the toe. Hence, a semi-analytical formulation for the root is established (section 6.4).
    Lap joints have a high weld load carrying level which introduces a 2nd order weld load carrying behaviour, different from other joints (section 6.2.1). The maximum stress occurs around $0.5t_p$. Some extreme geometries do not allow the stresses to reach the whole thickness of the plate. Semi-analytical formulations cannot capture this behaviour (section 6.6.1). Hence, a criterion is developed to exclude these geometries.
    The C_{bw} and C_{bw} fitting functions are developed covering both laser- and arc-welded joints, as they follow the same principles (section 6.6).
    The stress distributions of lap joints show a higher weld load carrying than the one of other welded joints.

2. **How do the secondary bending moments for a single-sided lap joint (614,615) influence the fatigue resistance?**

    The secondary bending moments are a far field related phenomenon that occurs under uniaxial loading (section 6.5). The influence of the secondary bending moments changes correlatively to the applied stress. Hence, they are not proportional to the applied nominal stress. Furthermore, the influence on the root and toe changes over the applied stress.
    The overall fit of the $S_e - N$ curve is insignificantly influenced by the change in secondary bending moments. However, each S_e is noticeably influenced (section 7.2.1).

3. **What is the fatigue strength of arc-welded lap welds, and is it in line with the Mode-I fatigue resistance of other arc-welded joints in steel structures?**

    Arc-welded lap joints do align with the fatigue resistance of arc-welded joints (section 7.2.1). However, the scatter is slightly higher, which can be related to the literature data, limited to the small thickness, causing higher relative errors.

4. **Can the LENSC and PENSC reliably predict the failure location for arc- and laser-welded joints?**

   In general, both concepts can predict the failure location of arc- and laser-welded joints (section 7.2.5; section 7.3.6). Nevertheless, both concepts show partly a wrong prediction of root failure. For the arc-welded joints, it is caused by the influence of secondary bending moments. For laser-welded joints, wrong predictions for both failure locations occur. Here, a reason is the difference in residual stress at the failure locations. Where the mean stress influence at the root is higher than the one at the toe.

5. **Which of the two assessment concepts provides less conservative results?**

   Overall, the LENSC provides slightly better results for arc- and laser-welded joints (section 7.2.5; section 7.3.6). In addition, the performance of the PENSC depends on the amount and quality of data used to establish the $S_e - N$ curve, making it unreliable.

6. **How much does laser welding enhance the fatigue resistance compared to arc welding?**

   Laser welding only enhances the fatigue resistance compared to arc welding in the MCF at low r_{lr} (section 7.3.6). The same FAT design curve for $r_{lr} = 0.5$ can be used with a mean stress correction. In addition, the material-dependent parameters of the ENSC are different for laser welds. The higher influence of the mean stress is especially apparent. The slope is similar to the one recommended for arc-welded joints $m = 3$.

7. **What is the optimal geometry to avoid root failure and still show good fatigue strength?**

   For single lap joints DS (614), a high penetration and corresponding high weld angle are recommended, yielding a low weld load carrying (section 7.4). Nonetheless, fatigue resistance is better at a small weld angle corresponding to a high V-shaped notch stress contribution. However, the probability of a root failure is enhanced, especially at lower stress levels. Welds with angles around 45° should be avoided as those show high effective stress.
   A thicker weld yields better fatigue resistance in this case.

The research hypothesis can be split into two parts. The first one is the validation of the ENSC to predict the failure location. This is partly covered by research question 4. Both assessed concepts LENSC and PENSC can reliably predict toe failure. However, some predicted root failures resulted in toe failure.

The fatigue performance of arc-welded lap joints is in line with other arc-welded joints; see research question 3. Against the expectations, the fatigue resistance of laser-welded lap joints is not better than the one for arc-welded joints in the MCF; see research question 6. However, the material-dependent parameters do differ compared to arc-welded joints.

Research goal

Validate a fatigue assessment concept for laser-welded lap joints. A fatigue damage criterion and the corresponding fatigue resistance curve must be established for common laser-welded joints in steel structures. Lap joint design guidelines will be provided to obtain weld toe and prevent weld root failure.

The above-stated research goal is fulfilled with the performed research.

9
Discussion

The research gave new insight into the through thickness weld notch stress distribution of highly load weld carrying joints. In addition, a semi-analytical formulation similar to the one for the toe is adapted for the root.

A 2nd order weld load carrying behaviour is apparent for welds with a high weld load carrying. A corresponding formulation is developed (section 6.2.1). For simplicity, the point of maximum stress is set at $0.5 * t_p$, allowing for no effect on the force and moment equilibrium. Regardless, for multiple geometries, the point of maximum stress is not at half of the thickness. In addition, the stress distribution do not reach over the whole thickness for extreme geometries. However, the semi-analytical formulations can only be applied when the notch stress distribution covers the whole thickness. Therefore, a geometry engineering-based criterion is established to exclude these extreme geometries. Nevertheless, an influence of the loading seems to be apparent, leading to unexact results of the criterion. Still, the criterion excludes most extreme geometries. Therefore, the formulation did not yield a perfect fit for all geometries (section 6.8).

The secondary bending moments are a non-linear far field related phenomenon and do not need to be implemented in the semi-analytical formulations but in calculating the far field stress.

In general, arc- and laser-welded geometries can be described with the same formulations, showing applicability regardless of the geometry. This allowed to establish C_{bw} and C_{bw2} fitting functions covering both welding methods. The fitting functions are more complex than the ones so far established. In addition, the range of fitted geometries is limited.

Overall, existing semi-analytical formulations are adapted and extended to cover highly weld load-carrying joints with the failure location at the toe and the root.

The fatigue assessment compared multiple concepts for arc- and laser-welded geometries. The fatigue resistance data for arc-welded lap joints does align with the fatigue resistance of other arc-welded joints when utilizing the LENSC. However, the increased scatter is influenced by the small thickness of the data. Against the expectations, laser welding does not noticeably enhance the fatigue resistance in the MCF. Applying the HSSSC, the quantile design curve aligns with the FAT design curve for arc-welded joints (section 7.3.4). Furthermore, the m is found to be equal to the recommended value of $m = 3$ for arc welded joints (Hobbacher et al., 2016). This is in contrast to other observations where flatter $S - N$ curves with values around $m = 5$ are found (Sonsino et al., 2010, Remes et al., 2008, Fricke and Robert, 2012). The influence of the microstructure and hardness seems negligible in the MCF, and the crack growth is more dominant than expected. This aligns with the only small change in the material dependent parameter, ρ^* and a^*. However, a transition into the HCF is observed at $N \approx 10^6$, compared to $N10^7$ assumed for arc welds (Hobbacher et al., 2016). This indicates a better HCF resistance, which cannot be assured due to the limitation of this thesis to MCF. Furthermore, the mean stress influence for laser-welded joints is significantly higher than for arc-welded ones. This is related to the lower residual stress for laser welds. The amount and diversity of fatigue resistance data of laser-welded joints are singular so far and therefore give more certainty to the findings. However, comparing the number of data points for laser-welded joints ($\approx$190 data points) to one of the arc-welded joints ($\approx$3000 data points) the lack of available data prohibits the conclusion of exact trends.

A change in slope is observed, and a more realistic representation yields the inclusion of the change in secondary bending moments. Although including this only results in a slightly better fit. However, the influence on the S_e of each data point is significant and cannot be neglected.

As expected, the NSC reflects a conservative approach, which is also needed due to the high scatter apparent confirmed by this research. The FAT design curve only recommended a better fatigue resistance than the experimental results for a few joints. In general, an increased performance is observed when using more advanced fatigue assessment concepts. For arc-welded lap joints, the HSSSC posed an exception as it showed a higher scatter than the less sophisticated NSC. Of the two assessed ENSC, the LENSC yielded better performance for both arc- and laser-welded joints. The value of a^* seems to be dependent on the number and quality of the data used for the fit. This is proved when the PENSC is applied to the laser-welded data. There the a^* is only a tenth of the reasonable ρ^*, whereas in literature, a third is observed (Baumgartner et al., 2011; Baumgartner J., 2013; Baumgartner et al., 2015). Furthermore, the small welding dimensions of laser welds cause significant uncertainty when obtaining the geometry parameter (h_w, l_w, pn). In addition, a dependency of a^* on the notch radius of the weld was proven before (G. Zhang et al., 2012).

Both ENSC show problems in reliably predicting the failure location. For the arc-welded joints, the change in failure location caused by secondary bending moments cannot be predicted. Although the change in secondary bending moments is already implemented. For the laser-welded joints, the different residual stress levels at the failure locations are proven to be one influence for the wrong prediction of the failure location. However, a still significant error is apparent. Therefore, using the ENSC for the failure location prediction is not reliable.

10

Recommendations

Regarding the through thickness weld notch stress distribution, several recommendations can be given. Firstly, the position of the maximum stress in the 2nd order weld load carrying yielded a significant error. Hence, a formulation should be developed covering the different positions of the maximum stress and the corresponding relation to the geometry and load. Another issue are the geometries, where the stress had not reached the whole thickness. The criterion developed allows for a good first guess. However, excluding all geometries where this problem occurred is not sufficient. Here, including the loading is recommended to obtain a more robust criterion.

For the C_{bw} and C_{bw2} fitting functions, a wider range of geometries should be assessed, allowing for better applicability within engineering. Furthermore, the C_{bw} and C_{bw2} fitting functions for the double lap joints (611) should be established to cover the full range of lap joints.

The difference between the LENSC and PENSC is small in this work and the literature for arc-welded joints. Hence, the comparison between LENSC and PENSC should be broadened to cover all joint geometries as well as the HCF. In addition, the prediction of both concepts of the failure location is sometimes incorrect, caused by the influence of secondary bending moments. Here, more data should be assessed to manifest this reason.

The amount of laser-welded fatigue resistance data is insufficient to accurately estimate the material-dependent parameter, ρ^* and γ. Therefore, more tests should be conducted and extracted from the literature. This data should also be assessed regarding HCF. Here more advanced $S-N$ curve models shall be implemented with fatigue limits. Particularly, the HCF is of interest as the experimental data indicates an earlier transition to the HCF as well as better behaviour. Similar to the arc-welded joints, some failure locations are predicted wrong by the ENSC concepts. Hence, the above-made recommendations should be extended to cover laser-welded joints as well.

Lastly, the adapted beam/shell model is only validated for single lap joints. Proving the usability for different weld geometries is recommended to simplify the assessment of root-initiated fatigue failure.

11
Implementation

The findings of this research shall be integrated into engineering design. To show the approach the following Roadmap is provided:

```
        ┌─────────────────────────────┐
        │  Joint geometry and loading │
        └─────────────────────────────┘
                      │
                      ▼
              ◇ CBW fitting
                functions can be used?    ──no──▶  ┌─────────────────┐
                (section 6.6.1) ◇                  │  Non-linear FE  │
                      │                            │   solid model   │
                     yes                           └─────────────────┘
                      ▼                                     │
        ┌─────────────────────────┐                        │
        │     Non-linear FE       │                        │
        │    bar/shell model      │                        │
        │     (section 6.7)       │                        │
        └─────────────────────────┘                        │
                      │                                     │
                      ▼                                     │
        ┌─────────────────────────┐                        │
        │   Establish Cbw         │                        │
        │    (section 6.6)        │                        │
        └─────────────────────────┘                        │
                      │                                     │
                      ▼                                     │
     ╱──────────────────────────────────────╲              │
    ╱ Calculate Se with given ρ* and γ        ╲◀───────────┘
    ╲──────────────────────────────────────────╲
```
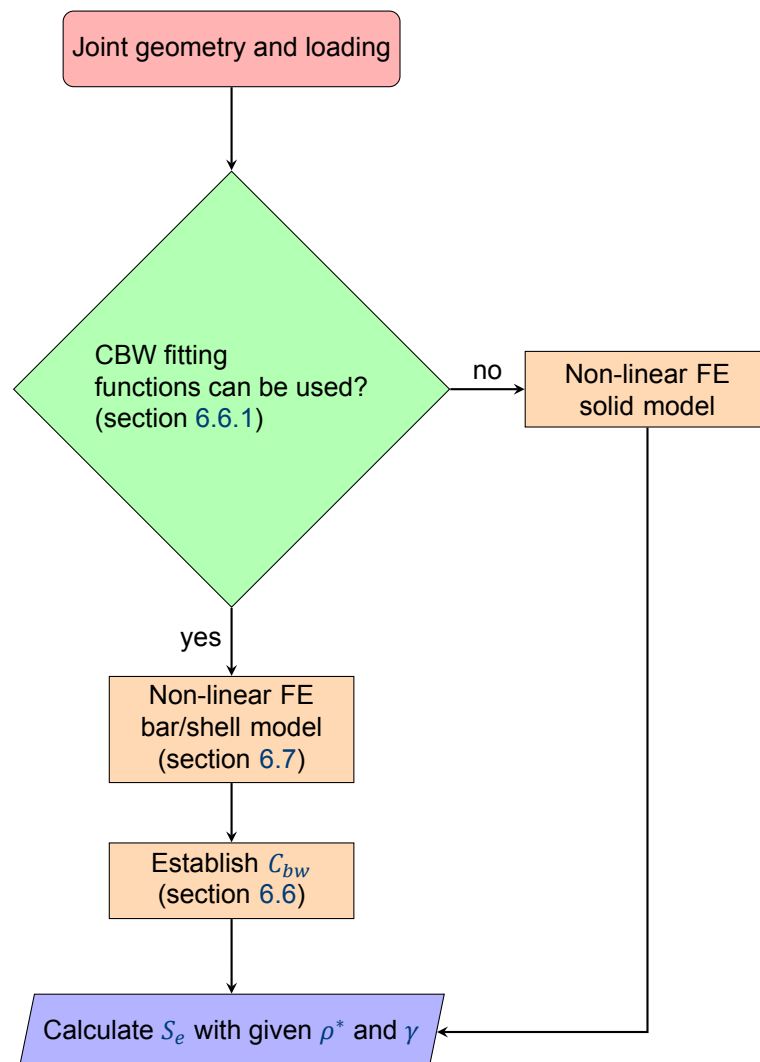
The geometry of the weld shall be established from a macrograph, as the welding geometries of laser welds are quite small and this allows obtaining the penetration. As macrographs are produced to check the welding parameters, this does not pose additional work.

The established C_{bw} fitting functions are still quite limited, but in case they can be applied the developed beam/shell model can be used. Otherwise, a solid-model has to be created. For both the influence of non-linear geometry has to be taken into account due to the significant influence of secondary bending moments. This requires a calculation of the minimum and maximum stress of the cycle. When the accuracy can be lower, an engineering-based approach can be taken where only unit stress is applied. This one shows conservative results (section 7.2.1).

With the stress distribution either obtained from a solid model or from the semi-analytical formulations the S_e can be established with the corresponding ρ^* and γ. Afterwards, the established design quantile design curves R97.7C75 can be used to obtain the N_i (fig. 11.1; fig. 11.2).
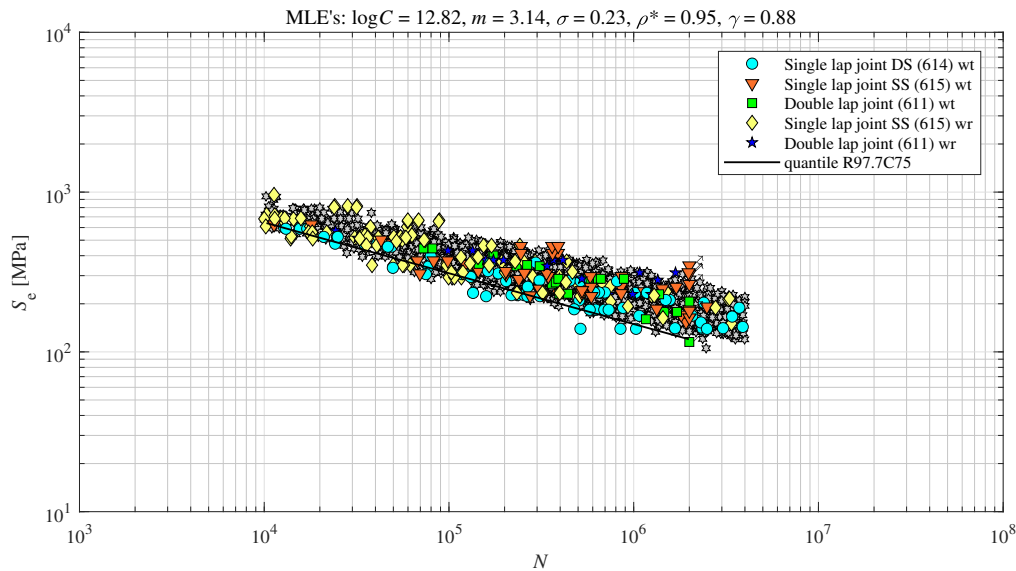
Figure 11.1: $S_e - N$ design curve for arc-welded joints
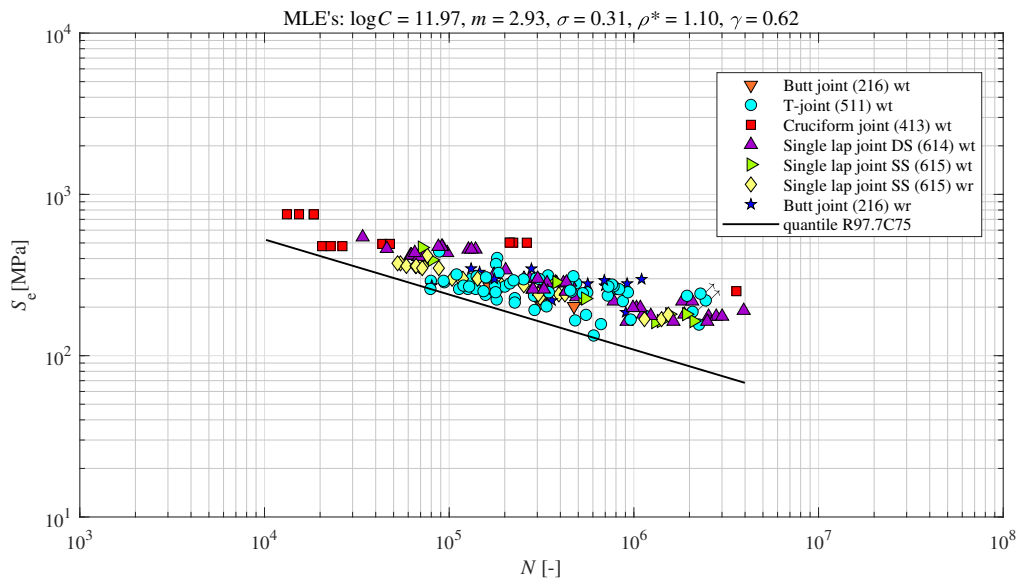
Figure 11.2: $S_e - N$ design curve for laser-welded joints

Bibliography

Akaike, H. (1973). Information theory and an extension of the maximum likelihood principle. *Proceedings of the 2nd International Symposium on Information Theory*, 267–281.

Andrews, R. M. (1996). The effect of misalignment on the fatigue strength of welded cruciform joints. *Fatigue & Fracture of Engineering Materials & Structures*, *19*(6), 755–768. https://doi.org/https://doi.org/10.1111/j.1460-2695.1996.tb01320.x

Anthes, R., Kottgen, V., & Seeger, T. (1993). Notch shape factors of butt joints and double-t butt joints.

Anthes, R., Köttgen, V., & Seeger, T. (1994). Effect of the weld geometry on the fatigue strength of butt and double-t joints. *Schweissen und Schneiden*, E–153.

Atzori, B., Meneghetti, G., & Susmel, L. (2005). Material fatigue properties for assessing mechanical components weakened by notches and defects. *Fatigue & Fracture of Engineering Materials & Structures*, *28*(1-2), 83–97. https://doi.org/https://doi.org/10.1111/j.1460-2695.2004.00862.x

Balbaa, M., Mekhiel, S., Elbestawi, M., & McIsaac, J. (2020). On selective laser melting of inconel 718: Densification, surface roughness, and residual stresses. *Materials & design*. https://doi.org/10.1016/j.matdes.2020.108818

Barber, R. (Ed.). (2002). *Solid mechanics and its applications*. Kluwer Academic Publishers.

Barsoum, Z. (2008). Residual stress analysis and fatigue of multi-pass welded tubular structures. *Engineering Failure Analysis*, *15*(7), 863–874. https://doi.org/https://doi.org/10.1016/j.engfailanal.2007.11.016

Barsoum, Z., & Barsoum, I. (2009). Residual stress effects on fatigue life of welded structures using lefm. *Engineering Failure Analysis*, *16*(1), 449–467. https://doi.org/https://doi.org/10.1016/j.engfailanal.2008.06.017

Barsoum, Z., & Jonsson, B. (2011). Influence of weld quality on the fatigue strength in seam welds. *Engineering Failure Analysis*, *18*(3), 971–979. https://doi.org/https://doi.org/10.1016/j.engfailanal.2010.12.001

Basquin, O. (1910). The exponential law of endurance tests. *Proc Am Soc Test Mater*, *10*, 625–630.

Baumgartner, J., Bruder, T., & Hanselka, H. (2012). Fatigue strength of laser beam welded automotive components made of thin steel sheets considering size effects [Modern Local Design Concepts for the Fatigue Assessment of Welded Structures – Industrial Applications]. *International Journal of Fatigue*, *34*(1), 65–75. https://doi.org/https://doi.org/10.1016/j.ijfatigue.2011.01.022

Baumgartner, J., Lipp, K., Bruder, T., & Kaufmann, H. (2011). Design methods for reliable fatigue assessment of pm components. *Materialwissenschaft und Werkstofftechnik*, *42*(10), 894–903. https://doi.org/https://doi.org/10.1002/mawe.201100869

Baumgartner, J., Hobbacher, A. F., & Rennert, R. (2020). Fatigue assessment of welded thin sheets with the notch stress approach – proposal for recommendations. *International Journal of Fatigue*, *140*, 105844. https://doi.org/https://doi.org/10.1016/j.ijfatigue.2020.105844

Baumgartner, J., Schmidt, H., Ince, E., Melz, T., & Dilger, K. (2015). Fatigue assessment of welded joints using stress averaging and critical distance approaches. *Welding in the World*, *59*. https://doi.org/10.1007/s40194-015-0248-x

Baumgartner J., S. H., Ince E. (2013). Erweiterung des kerbspannungskonzepts auf nahtübergänge von linienschweißnähten an dünnen blechen. *FAT-Schriftenreihe*, *259*. https://www.vda.de/de/aktuelles/publikationen/publication/fat-schriftenreihe-259

Bellett, D., Taylor, D., Marco, S., Mazzeo, E., Guillois, J., & Pircher, T. (2005). The fatigue behaviour of three-dimensional stress concentrations. *International Journal of Fatigue*, *27*(3), 207–221. https://doi.org/https://doi.org/10.1016/j.ijfatigue.2004.07.006

Bonnen, J., Mandapati, R., Kang, H., Iyengar, R., Khosrovaneh, A., Amaya, M., Citrin, K., & Shih, H.-C. (2009). Durability of advanced high strength steel gas metal arc welds. *SAE International Journal of Materials and Manufacturing*, *2*, 155–171. https://doi.org/10.4271/2009-01-0257

Bufalari, G., den Besten, H., & Kaminski, M. L. (2022). Mode-iii fatigue of welded joints in steel maritime structures: Weld notch shear stress distributions and effective notch stress based resistance.

International Journal of Fatigue, *165*, 107210. https://doi.org/https://doi.org/10.1016/j.ijfatigue.2022.107210

Caccese, V. (2010). 9 - fatigue in laser welds. In X. Sun (Ed.), *Failure mechanisms of advanced welding processes* (pp. 218–257). Woodhead Publishing. https://doi.org/https://doi.org/10.1533/9781845699765.218

Caccese, V., Blomquist, P., Berube, K., Webber, S., & Orozco, N. (2006). Effect of weld geometric profile on fatigue life of cruciform welds made by laser/gmaw processes. *Marine Structures*, *19*(1), 1–22. https://doi.org/https://doi.org/10.1016/j.marstruc.2006.07.002

Caiazzo, F., Alfieri, V., Cardaropoli, F., & Sergi, V. (2017). Investigation on edge joints of inconel 625 sheets processed with laser welding. *Optics* & *Laser Technology*, *93*, 180–186. https://doi.org/https://doi.org/10.1016/j.optlastec.2017.03.011

Cho, S.-K., Yang, Y.-S., Son, K.-J., & Kim, J.-Y. (2004). Fatigue strength in laser welding of the lap joint. *Finite Elements in Analysis and Design*, *40*(9), 1059–1070. https://doi.org/https://doi.org/10.1016/j.finel.2003.08.010

Cranfield University. (2022). *An introduction to laser welding*. https://camvaceng.com/case-study/an-introduction-to-laser-welding/ (accessed: 17.03.2023)

Darcis, P., Lassen, T., & Recho, N. (2006). Fatigue behaviour of welded joints part 2: Physical modeling of the fatigue process. *Welding Journal (Miami, Fla)*, *85*, 19–26.

Dawes, C. (1992). Chapter 1 - light and lasers. In C. Dawes (Ed.), *Laser welding* (pp. 1–15). Woodhead Publishing. https://doi.org/https://doi.org/10.1533/9781845698843.1

Dekking, F. M., Kraaikamp, C., Lopuhaä, H. P., & Meester, L. E. (2005). *A modern introduction to probability and statistics: Understanding why and how* (Vol. 488). Springer.

den Besten, H. (2015). *Fatigue resistance of welded joints in aluminium high-speed craft: A total stress concept* (Doctoral dissertation). Delft University of Technology. https://doi.org/10.4233/uuid:370b3d44-f4a6-403e-9629-d36174c3aca4

den Besten, H. (2018). Fatigue damage criteria classification, modelling developments and trends for welded joints in marine structures. *Ships and Offshore Structures*, *13*(8), 787–808.

Dong, P. (2001). A structural stress definition and numerical implementation for fatigue analysis of welded joints. *International Journal of Fatigue*, *23*(10), 865–876. https://doi.org/https://doi.org/10.1016/S0142-1123(01)00055-X

Dong, P. (2005). A Robust Structural Stress Method for Fatigue Analysis of Offshore/Marine Structures. *Journal of Offshore Mechanics and Arctic Engineering*, *127*(1), 68–74. https://doi.org/10.1115/1.1854698

Dourado, M., Soares, D., Barbosa, J., Marques Pinho, A., Meireles, J., Branco, P., Ribeiro, C., & Rei, C. (2014). A comparative study of fatigue behaviour of mag and laser welded components using reliability analysis. *Materials Science and Engineering: A*, *606*, 31–39. https://doi.org/https://doi.org/10.1016/j.msea.2014.03.067

Dowling, N. E. (2009). Mean stress effects in strain–life fatigue. *Fatigue & Fracture of Engineering Materials & Structures*, *32*(12), 1004–1019. https://doi.org/https://doi.org/10.1111/j.1460-2695.2009.01404.x

Eibl, M. (2003). *Berechnung der schwingfestigkeit laserstrahlgeschweißter feinbleche mit lokalen konzepten* (Doctoral dissertation). Technische Universität. Darmstadt. http://tuprints.ulb.tu-darmstadt.de/376/

Eurocode 3. (2007). *Design of steel structure-part 1-9: Fatigue* [EN-1993-1-9]. CEN.

Eurocode 9. (2007). *Design of aluminium structures-part 1-3: Structures suspectible to fatigue* [EN-1993-1-3]. CEN.

File, D. (2001). Designing welded lap joints. *Welding Innovation*, *18*(3).

Frank, D., Remes, H., & Romanoff, J. (2011). Fatigue assessment of laser stake-welded t-joints. *International Journal of Fatigue*, *33*(2), 102–114. https://doi.org/https://doi.org/10.1016/j.ijfatigue.2010.07.002

Fricke, W. (2001). *Recommended Hot Spot Analysis Procedure For Structural Details of FPSOs And Ships Based On Round-Robin FE Analyses* (Vol. All Days) [ISOPE-I-01-353].

Fricke, W., Codda, M., Feltz, O., Garbatov, Y., Remes, H., Risso, G., Rizzo, C., & Romanoff, J. (2013). Round robin study on local stress and fatigue assessment of lap joints and doubler plates. *Ships and Offshore Structures*, *8*(6), 621–627. https://doi.org/10.1080/17445302.2012.762727

Fricke, W., Remes, H., Feltz, O., Lillemäe, I., Tchuindjang, D., Reinert, T., Nevierov, A., Sichermann, W., Brinkmann, M., Kontkanen, T., Bohlmann, B., & Molter, L. (2015). Fatigue strength of laser-welded thin-plate ship structures based on nominal and structural hot-spot stress approach. *Ships and Offshore Structures*, *10*(1), 39–44. https://doi.org/10.1080/17445302.2013.850208

Fricke, W. (2013). Iiw guideline for the assessment of weld root fatigue. *Welding in the World*, *57*, 753–791.

Fricke, W., & Feltz, O. (2010). Fatigue tests and numerical analyses of partial-load and full-load carrying fillet welds at cover plates and lap joints. *Welding in the World, Le Soudage Dans Le Monde*, *54*, R225–R233. https://doi.org/10.1007/BF03263508

Fricke, W., Robert, C., Peters, R., & Sumpf, A. (2016). Fatigue strength of laser-stake welded t-joints subjected to combined axial and shear loads. *Welding in the World*, *60*(3), 593–604.

Fricke, W., & Robert, C. (2012). *Qualitätsgerechte 3d laser-schweißbearbeitung innovativer schiffskonstruktionen*. TU Hamburg Arbeitsbereich Schiffbau.

Gaia da Silva, D., Lockwood, J., Liang, W., & Topper, T. (2021). Mean stress effect in stress-life for hard steels. *International Journal of Fatigue*, *146*, 106101. https://doi.org/https://doi.org/10.1016/j.ijfatigue.2020.106101

Gerritsen, C., & Howarth, D. (2005–June 9). A review of the development and application of laser and laser-arc hybrid welding in european shipbuilding.

Hensel, J., Köhler, M., Uhlenberg, L., Diniz e Castro, J., Dilger, K., Faß, M., & Baumgartner, J. (2022). Laser welding of 16mncr5 butt welds with gap: Resulting weld quality and fatigue strength assessment. *Welding in the World*, *66*, 1–15. https://doi.org/10.1007/s40194-022-01306-4

Hobbacher, A., et al. (2016). *Recommendations for fatigue design of welded joints and components* (Vol. 47). Springer.

Hwang, I., Kim, D.-Y., Jeong, G., Kang, M., Kim, D., & Kim, Y.-M. (2017). Effect of weld bead shape on the fatigue behavior of gmaw lap fillet joint in ga 590 mpa steel sheets. *Metals*, *7*(10). https://doi.org/10.3390/met7100399

Ion, J. (2005). *Laser processing of engineering materials: Principles, procedure and industrial application*. Elsevier.

Janssen, M., Zuidema, J., & Wanhill, R. (2004). *Fracture mechanics: Fundamentals and applications*. CRC Press.

Kang, H. T., Lee, Y.-L., & Sun, X. J. (2008). Effects of residual stress and heat treatment on fatigue strength of weldments. *Materials Science and Engineering: A*, *497*(1), 37–43. https://doi.org/https://doi.org/10.1016/j.msea.2008.06.011

Kawagoishi, N., Chen, Q., & Nisitani, H. (2000). Significance of the small crack growth law and its practical application. *Metallurgical and Materials Transactions A*, *31*, 2005–2013. https://doi.org/10.1007/s11661-000-0228-6

Kim, D.-Y., Hwang, I., Jeong, G., Kang, M., Kim, D., Seo, J., & Kim, Y.-M. (2018). Effect of porosity on the fatigue behavior of gas metal arc welding lap fillet joint in ga 590 mpa steel sheets. *Metals*, *8*, 241. https://doi.org/10.3390/met8040241

Kim, D.-Y., Kim, D., Kang, M., & Kim, Y.-M. (2017). Improvement of fatigue strength of lap fillet joints by using tandem mag welding in a 590-mpa-grade galvannealed steel sheet. *The International Journal of Advanced Manufacturing Technology*, *93*. https://doi.org/10.1007/s00170-017-0828-6

Laitinen, R., Porter, D., Dahmen, M., Kaierle, S., & Poprawe, R. (2001). Comparative study on the weldability of different shipbuilding steels: Japan welding society. 7th international symposium. proceedings. today and tomorrow in science and technology of welding and joining. vol. 1.

Lang, R., Ladinek, M., & Lener, G. (2017). Über die anpassung eines fortschrittlichen stützwirkungsansatzes für das kerbspannungskonzept. *Stahlbau*, *86*(6), 470–482. https://doi.org/https://doi.org/10.1002/stab.201710494

Lassen, T., Darcis, P., & Recho, N. (2005). Fatigue behavior of welded joints part 1 - statistical methods for fatigue life prediction. *Welding Journal (Miami, Fla)*, *84*, 183–187.

Lee, K., & Oh, S. (2015). Development of durability enhancement technology for arc weldings in advanced high strength steel (ahss) chassis parts. *Journal of Welding and Joining*, *33*, 50–56. https://doi.org/10.5781/JWJ.2015.33.4.50

Li, X., Partanen, T., Nykänen, T., & Björk, T. (2001). Finite element analysis of the effect of weld geometry and load condition on fatigue strength of lap joint. *International Journal of Pressure Vessels and Piping*, *78*(9), 591–597. https://doi.org/https://doi.org/10.1016/S0308-0161(01)00066-7

Liao, D., Zhu, S.-P., Correia, J. A., De Jesus, A. M., & Berto, F. (2020). Recent advances on notch effects in metal fatigue: A review. *Fatigue & Fracture of Engineering Materials & Structures*, *43*(4), 637–659. https://doi.org/https://doi.org/10.1111/ffe.13195

Lillemäe, I., Lammi, H., Molter, L., & Remes, H. (2012). Fatigue strength of welded butt joints in thin and slender specimens. *International Journal of Fatigue*, *44*, 98–106. https://doi.org/https://doi.org/10.1016/j.ijfatigue.2012.05.009

Liu, S., Mi, G., Yan, F., Wang, C., & Jiang, P. (2017). Correlation of high power laser welding parameters with real weld geometry and microstructure. *Optics & Laser Technology*, *94*, 59–67. https://doi.org/https://doi.org/10.1016/j.optlastec.2017.03.004

Marulo, G., Baumgartner, J., & Frendo, F. (2017). Fatigue strength assessment of laser welded thin-walled joints made of mild and high strength steel. *International Journal of Fatigue*, *96*, 142–151. https://doi.org/https://doi.org/10.1016/j.ijfatigue.2016.11.016

Matsuda, K., & Yonezawa, T. (2022). Investigation of fatigue strength of root of lap fillet welds of thin sheet and improvement method. *Theoretical and Applied Fracture Mechanics*, *122*, 103667. https://doi.org/https://doi.org/10.1016/j.tafmec.2022.103667

Meneghetti, G. (2012). The use of peak stresses for fatigue strength assessments of welded lap joints and cover plates with toe and root failures. *Engineering Fracture Mechanics*, *89*, 40–51. https://doi.org/https://doi.org/10.1016/j.engfracmech.2012.04.007

Moore, H. (1945). A study of size effect and notch sensitivity in fatigue tests of steel. *ASTM*, *45*, 507–531.

Moraitis, G., & Labeas, G. (2008). Residual stress and distortion calculation of laser beam welding for aluminum lap joints. *Journal of Materials Processing Technology*, *198*(1), 260–269. https://doi.org/https://doi.org/10.1016/j.jmatprotec.2007.07.013

Němeček, S., Mužík, T., & Míšek, M. (2012). Differences between laser and arc welding of hss steels [Laser Assisted Net shape Engineering 7 (LANE 2012)]. *Physics Procedia*, *39*, 67–74. https://doi.org/https://doi.org/10.1016/j.phpro.2012.10.015

Neuber, H. (1968). Über die berücksichtigung der spannungskonzentration bei festigkeitsberechnungen. *Konstruktion*, *20*(7), 245–251.

Neuber, H. (1985). *Kerbspannungslehre* (Vol. 3). Springer.

Niemi, E. (Ed.). (1995). *Stress determination for fatigue analysis of welded components*. Woodhead Publishing. https://doi.org/https://doi.org/10.1016/B978-1-85573-213-1.50009-4

Nilsson, P., Al-Emrani, M., & Atashipour, S. R. (2020). Fatigue-strength assessment of laser welds in corrugated core steel sandwich panels. *Journal of Constructional Steel Research*, *164*, 105797. https://doi.org/https://doi.org/10.1016/j.jcsr.2019.105797

Nykänen, T. (n.d.). On fatigue crack growth simulation in a transverse double lap joint. *IIW Doc XIII-1583-95*.

Overbeeke, J., Alting, T., Flipsen, J., Feringa, H., & Jonkers, P. (1984). *The fatigue strength of welded, bolted and riveted joints in high strength, low alloy steel*. Technische Hogeschool Eindhoven.

Oyyaravelu, R., Kuppan, P., & Arivazhagan, N. (2016). Metallurgical and mechanical properties of laser welded high strength low alloy steel. *Journal of Advanced Research*, *7*(3), 463–472. https://doi.org/https://doi.org/10.1016/j.jare.2016.03.005

Palmgren, A. (1924). Die lebensdauer von kugellagern. *VDI-Zeitschrift*, *68*(1924), 339–341.

Peterson, R. (1938). Methods of correlating data from fatigue tests of stress concentration specimens. *Stephen Timoshenko 60th anniversary volume*, 179.

Qin, Y., den Besten, H., Kaminski, M., & Palkar, S. (2019). Fatigue design of welded double-sided t-joints and double-sided cruciform joints in steel marine structures: A total stress concept. *Fatigue & Fracture of Engineering Materials & Structures*, *42*. https://doi.org/10.1111/ffe.13089

Qin, Y., den Besten, H., Palkar, S., & Kaminski, M. (2020). Mid- and high-cycle fatigue of welded joints in steel marine structures: Effective notch stress and total stress concept evaluations. *International Journal of Fatigue*, *142*, 105822. https://doi.org/10.1016/j.ijfatigue.2020.105822

"Qin et. al.", Y. (2023). *Averaged effective notch stress fatigue resistance data* [unpublished].

Radaj, D. (1975). Notch stress analysis for fillet welds using the finite element method. *Schweißen & Schneiden*, *27*, 86–89.

Radaj, D., Sonsino, C., & Fricke, W. (2006). 9 - structural stress or strain approach for spot-welded and similar lap joints. In D. Radaj, C. Sonsino, & W. Fricke (Eds.), *Fatigue assessment of welded joints by local approaches (second edition)* (Second Edition, pp. 366–432). Woodhead Publishing. https://doi.org/https://doi.org/10.1533/9781845691882.366

Radaj, D., & Vormwald, M. (2007). *Ermüdungsfestigkeit: Grundlagen für ingenieure*. Springer. https://doi.org/10.1007/978-3-540-71459-0

Radaj, D. (1990). *Design and analysis of fatigue resistant welded structures*. Woodhead Publishing.

Remes, H., et al. (2008). *Strain-based approach to fatigue strength assessment of laser-welded joints* (Doctoral dissertation). Helsinki University of Technology.

Ring, M., & Dahl, W. (1994). Fatigue properties of laser-beam weldments on high-strength steels. *Steel research*, *65*(11), 505–510.

Roland, F., Manzon, L., Kujala, P., Brede, M., & Weitzenbock, J. (2004). Advanced Joining Techniques in European Shipbuilding. *Journal of Ship Production*, *20*(03), 200–210. https://doi.org/10.5957/jsp.2004.20.3.200

Rooks, B. (2000). Lasers become the acceptable face of precision welding and cutting. *Industrial Robot: An International Journal*, *27*, 103–108. https://doi.org/10.1108/01439910010315409

Schijve, J. (2008). *Fatigue of structures and materials*. Springer Netherlands. https://books.google.nl/books?id=PFsJhYgvOG8C

Schubnell, J., Jung, M., Le, C. H., Farajian, M., Braun, M., Ehlers, S., Fricke, W., Garcia, M., Nussbaumer, A., & Baumgartner, J. (2020). Influence of the optical measurement technique and evaluation approach on the determination of local weld geometry parameters for different weld types. *Welding in the World*, *64*(2), 301–316. https://doi.org/10.1007/s40194-019-00830-0

Sepe, R., Wiebesiek, J., & Sonsino, C. M. (2020). Numerical and experimental validation of residual stresses of laser-welded joints and their influence on the fatigue behaviour. *Fatigue & Fracture of Engineering Materials & Structures*, *43*(6), 1126–1141. https://doi.org/https://doi.org/10.1111/ffe.13180

Sharifimehr, S., Fatemi, A., Cha, S. C., Bae, M.-K., & Hong, S.-H. (2016). Fatigue behavior of ahss lap shear and butt arc welds including the effect of periodic overloads and underloads. *International Journal of Fatigue*, *87*, 6–14. https://doi.org/https://doi.org/10.1016/j.ijfatigue.2015.12.009

Sheppard, S. D. (1991). Field Effects in Fatigue Crack Initiation: Long Life Fatigue Strength. *Journal of Mechanical Design*, *113*(2), 188–194. https://doi.org/10.1115/1.2912768

Shiozaki, T., Yamaguchi, N., Tamai, Y., Hiramoto, J., & Ogawa, K. (2018). Effect of weld toe geometry on fatigue life of lap fillet welded ultra-high strength steel joints. *International Journal of Fatigue*, *116*, 409–420. https://doi.org/https://doi.org/10.1016/j.ijfatigue.2018.06.050

Smith, I. F. C., & Smith, R. A. (1982). Defects and crack shape development in fillet welded joints. *Fatigue & Fracture of Engineering Materials & Structures*, *5*(2), 151–165. https://doi.org/https://doi.org/10.1111/j.1460-2695.1982.tb01231.x

Sonsino, C., Bruder, T., & Baumgartner, J. (2010). S-n lines for welded thin joints — suggested slopes and fat values for applying the notch stress concept with various reference radii. *Welding in the World*, *54*(11), 375–392. https://doi.org/https://doi.org/10.1007/BF03266752

Sonsino, C. (2009). Effect of residual stresses on the fatigue behaviour of welded joints depending on loading conditions and weld geometry [Fatigue assessment of welded connections]. *International Journal of Fatigue*, *31*(1), 88–101. https://doi.org/https://doi.org/10.1016/j.ijfatigue.2008.02.015

Sonsino, C., Radaj, D., Brandt, U., & Lehrke, H. (1999). Fatigue assessment of welded joints in almg 4.5mn aluminium alloy (aa 5083) by local approaches. *International Journal of Fatigue*, *21*(9), 985–999. https://doi.org/https://doi.org/10.1016/S0142-1123(99)00049-3

Steen, W. M., & Mazumder, J. (2010). *Laser material processing*. springer science & business media.

Stieler, M. (1954). *Untersuchungen über die dauerschwingfestigkeit metallischer bauteile bei raumtemperatur* (Doctoral dissertation). Technische Hochschule Stuttgart.

Tanaka, K. . (1983). Engineering formulae for fatigue strength reduction due to crack-like notches. *International Journal of Fracture*, *22*, R39–R46.

Taylor, D. (1999). Geometrical effects in fatigue: A unifying theoretical model. *International Journal of Fatigue*, *21*(5), 413–420. https://doi.org/https://doi.org/10.1016/S0142-1123(99)00007-9

Taylor, D. (2008). The theory of critical distances [Critical Distance Theories of Fracture]. *Engineering Fracture Mechanics*, *75*(7), 1696–1705. https://doi.org/https://doi.org/10.1016/j.engfracmech.2007.04.007

Terasaki, T., Sobue, T., & Kitamura, T. (2001). Study on fatigue strength of laser welded lap joint. *QUARTERLY JOURNAL OF THE JAPAN WELDING SOCIETY*, *19*, 507–512. https://doi.org/10.2207/qjjws.19.507

Tricoteaux, A., Fardoun, F., Degallaix, S., & Sauvage, F. (1995). Fatigue crack initiation life prediction in high strength structural steel welded joints. *Fatigue* & *Fracture of Engineering Materials* & *Structures*, *18*(2), 189–200. https://doi.org/https://doi.org/10.1111/j.1460-2695.1995.tb00154.x

Turlier, D., Klein, P., & Bérard, F. (2014). Fea shell element model for enhanced structural stress analysis of seam welds. *Welding in the World*, *58*. https://doi.org/10.1007/s40194-014-0134-y

Walker, K., Pendleberry, S., & McElwee, R. (1970). Effects of environment and complex load history on fatigue life. *ASTM STP*, *462*(1).

Wan, Z., Guo, W., Jia, Q., Xu, L., & Peng, P. (2018). Hardness evolution and high temperature mechanical properties of laser welded dp980 steel joints. *High Temperature Materials and Processes*, *37*(6), 587–595. https://doi.org/doi:10.1515/htmp-2017-0007

Weldingh, J., & Kristensen, J. K. (2003). Hybrid yag-laser/mag welding quality and stablility. *E. Proceedings 9th Conference on laser materials processing in the nordic countries*, (9), 15–24.

Williams, M. L. (1952). Stress singularities resulting from various boundary conditions in angular corners of plates in extension. https://doi.org/10.1115/1.4010553

Wöhler, A. (1860). Versuche über die festigkeit der eisenbahnwagenachsen. *Zeitschrift für Bauwesen*, *10*(1860), 160–161.

Wu, S., Qin, Q., Hu, Y., Branco, R., Li, C., Williams, C., & Zhang, W. (2020). The microstructure, mechanical, and fatigue behaviours of mag welded g20mn5 cast steel. *Fatigue & Fracture of Engineering Materials & Structures*, *43*(5), 1051–1063. https://doi.org/https://doi.org/10.1111/ffe.13215

Yacht Forums. (2022). *Classic yacht argosy-general*. https://www.yachtforums.com/threads/classic-yacht-argosy.35756/ (accessed: 16.03.2023)

Yan, S., Meng, Z., Chen, B., Tan, C., Song, X., & Wang, G. (2022). Prediction of temperature field and residual stress of oscillation laser welding of 316ln stainless steel. *Optics* & *Laser Technology*, *145*, 107493. https://doi.org/https://doi.org/10.1016/j.optlastec.2021.107493

Zhang, G., Sonsino, C. M., & Sundermeier, R. (2012). Method of effective stress for fatigue: Part ii – applications to v-notches and seam welds. *International Journal of Fatigue*, *37*, 24–40. https://doi.org/https://doi.org/10.1016/j.ijfatigue.2011.09.016

Zhang, X., Ashida, E., & Tarasawa, S. (2010). Properties of welded joint for narrow gap laser welding of austenitic stainless steels. *International Congress on Applications of Lasers* & *Electro-Optics*, *2010*(1), 632–637. https://doi.org/10.2351/1.5062092

Zhou, J., & Tsai, H. (2005). 2 - welding heat transfer. In Z. Feng (Ed.), *Processes and mechanisms of welding residual stress and distortion* (pp. 32–98). Woodhead Publishing. https://doi.org/https://doi.org/10.1533/9781845690939.1.32

A
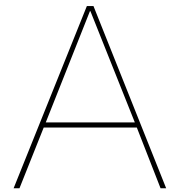
Arc-welded lap joint fatigue resistance data
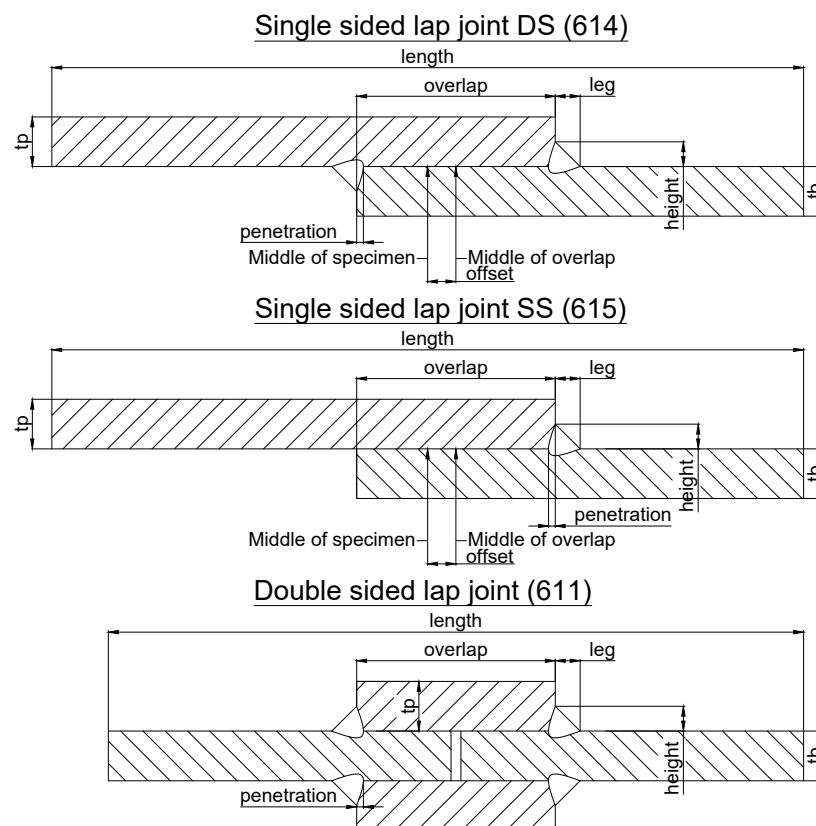
Figure A.1: Naming convention for arc-welded lap joints

source	series	yield strength [MPa]	geometry	rs []	tp [mm]	tb [mm]
Baumgartner J., 2013	1	340	614	0	1.5	1.5
Baumgartner J., 2013	2	340	615	0	1.5	1.5
Baumgartner J., 2013	3	355	614	0	3	3
Baumgartner J., 2013	4	355	615	0	3	3
Meneghetti, 2012	5	355	611	0	10	10
Meneghetti, 2012	6	355	611	0	10	10
Dourado et al., 2014	7	355	615	0	2.5	3
Fricke and Feltz, 2010	8	355	611	0	12	12
Fricke and Feltz, 2010	9	355	611	0	12	12
Overbeeke et al., 1984	10	560	614	0	6	6
Overbeeke et al., 1984	11	560	614	0	6	6
Bonnen et al., 2009	12	1000	614	0	3.4	3.4
Bonnen et al., 2009	13	285	614	0	3.4	3.4
Bonnen et al., 2009	14	420	614	0	3.4	3.4
Bonnen et al., 2009	15	330	614	0	3.4	3.4
Bonnen et al., 2009	16	285	615	0	3.4	3.4
Bonnen et al., 2009	17	420	615	0	3.4	3.4
Bonnen et al., 2009	18	330	615	0	3.4	3.4
Bonnen et al., 2009	19	1000	615	0	3.4	3.4
Kim et al., 2018	20	590	615	0	2.3	2.3
Hwang et al., 2017	21	590	615	0	2.3	2.3
Hwang et al., 2017	22	590	615	0	2.3	2.3
Hwang et al., 2017	23	590	615	0	2.6	2.6
Hwang et al., 2017	24	590	615	0	2.6	2.6
Kim et al., 2017	25	590	615	0	2.6	2.6
Kim et al., 2017	26	590	615	0	2.6	2.6
Kim et al., 2017	27	590	615	0	2.6	2.6
Matsuda and Yonezawa, 2022	28	506	615	1	2.9	2.9
Matsuda and Yonezawa, 2022	29	506	615	1	2.9	2.9
Sharifimehr et al., 2016	30	780	615	0	3.55	3.55

Table A.1: Overview of arc-welded lap joint fatigue test series Part I

source	series	length [mm]	overlap [mm]	offset [mm]	weld dimensions penetration [mm]	leg [mm]	height [mm]
Baumgartner J., 2013	1	105	27.1	0	1.8	1.5	1.5
Baumgartner J., 2013	2	105	16.1	0	1.85	1.5	1.5
Baumgartner J., 2013	3	105	24	0	1.74	5.3	3
Baumgartner J., 2013	4	105	22.8	0	1.4	5.4	3
Meneghetti, 2012	5	480	100	0	0	4.3	4.3
Meneghetti, 2012	6	480	100	0	0	8.5	8.5
Dourado et al., 2014	7	450	30	0	1.2	4	3
Fricke and Feltz, 2010	8	480	100	0	1.2	4.3	4.3
Fricke and Feltz, 2010	9	480	100	0	0	9.9	9.9
Overbeeke et al., 1984	10	360	70	0	1.1	4.4	6
Overbeeke et al., 1984	11	360	70	0	1.1	4.4	6
Bonnen et al., 2009	12	135	25	0	0	3.4	3.4
Bonnen et al., 2009	13	135	25	0	0	3.4	3.4
Bonnen et al., 2009	14	135	25	0	0	3.4	3.4
Bonnen et al., 2009	15	135	25	0	0	3.4	3.4
Bonnen et al., 2009	16	140	25	-12.5	0	3.4	3.4
Bonnen et al., 2009	17	140	25	-12.5	0	3.4	3.4
Bonnen et al., 2009	18	140	25	-12.5	0	3.4	3.4
Bonnen et al., 2009	19	140	25	-12.5	0	3.4	3.4
Kim et al., 2018	20	175	25	0	1.9	4.4	2.3
Hwang et al., 2017	21	175	25	0	3.2	3.3	2.3
Hwang et al., 2017	22	175	25	0	3.9	2.9	2.3
Hwang et al., 2017	23	175	25	0	4.8	4.3	2.6
Hwang et al., 2017	24	175	25	0	3.3	3.3	2.6
Kim et al., 2017	25	100	25	0	3.8	2.3	2.6
Kim et al., 2017	26	100	25	0	4.1	3.6	2.6
Kim et al., 2017	27	100	25	0	3.6	4.6	2.6
Matsuda and Yonezawa, 2022	28	65	10	-7	2.2	2.5	2.9
Matsuda and Yonezawa, 2022	29	65	10	-7	4.1	2	2.9
Sharifimehr et al., 2016	30	82	38	0	3.8	3.6	3.6

Table A.2: Overview of arc-welded lap joint fatigue test series Part II

series	num.	rl []	failure	Sn [MPa]	cycles []	series	num.	rl []	failure	Sn [MPa]	cycles []
1	1	0.1	wt	200.0	2.39E+05	3	4	0.5	wt	110.0	2.67E+05
1	2	0.1	wt	140.0	5.46E+05	3	5	0.5	wt	80.0	3.73E+06
1	3	0.1	wt	270.0	1.67E+05	3	6	0.5	wt	100.0	6.54E+05
1	4	0.1	nd	110.0	1.00E+07	3	7	0.5	wt	160.0	2.95E+05
1	5	0.1	wt	360.0	1.95E+04	3	8	0.5	wt	90.0	1.49E+06
1	6	0.1	wt	120.0	1.60E+06	3	9	0.5	wt	160.0	1.68E+05
1	7	0.1	wt	270.0	6.46E+04	3	10	0.5	wt	90.0	1.57E+06
1	8	0.1	wt	170.0	3.22E+05	3	11	0.5	wt	120.0	5.82E+05
1	9	0.1	wt	120.0	3.43E+06	3	12	0.5	wt	70.0	3.41E+06
1	10	0.1	wt	270.0	1.13E+05	3	13	0.5	wt	60.0	3.89E+06
1	11	0.1	wt	140.0	2.31E+05	3	14	0.5	wt	50.0	5.83E+06
1	12	0.1	wt	140.0	2.75E+06	3	15	0.5	wt	40.0	1.25E+07
1	13	0.1	wt	200.0	2.04E+05	4	1	0.1	wr	140.0	5.20E+04
1	14	0.1	wt	110.0	3.75E+06	4	2	0.1	wr	60.0	3.30E+06
1	15	0.5	wt	140.0	2.66E+05	4	3	0.5	wr	100.0	1.93E+05
1	16	0.5	wt	110.0	1.98E+06	4	4	0.5	wr	80.0	2.84E+05
1	17	0.5	wt	120.0	1.59E+06	4	5	0.5	wr	60.0	1.25E+06
1	18	0.5	wt	130.0	2.90E+06	4	6	0.5	wr	140.0	7.33E+04
1	19	0.5	wt	160.0	6.99E+05	4	7	0.5	wr	100.0	1.34E+05
1	20	0.5	wt	200.0	7.02E+05	4	8	0.5	wr	60.0	1.29E+06
2	1	0.1	wr	80.0	4.18E+06	4	9	0.5	wr	140.0	7.44E+04
2	2	0.1	wr	160.0	4.96E+04	4	10	0.5	wr	80.0	3.96E+05
2	3	0.1	wr	100.0	1.52E+05	4	11	0.5	wr	140.0	5.59E+04
2	4	0.5	wr	100.0	2.39E+05	4	12	0.5	wr	50.0	2.77E+06
2	5	0.5	nd	60.0	9.65E+06	4	13	0.5	wr	40.0	4.93E+06
2	6	0.5	wr	120.0	1.34E+05	4	14	0.5	wr	32.0	9.28E+06
2	7	0.5	wr	160.0	2.95E+04	4	15	0.5	nd	50.0	1.00E+07
2	8	0.5	nd	64.0	5.00E+07	4	16	0.5	wt	80.0	3.08E+05
2	9	0.5	wr	128.0	1.05E+05	4	17	0.5	wt	60.0	1.33E+06
2	10	0.5	wr	140.0	7.29E+04	4	18	0.5	wt	55.0	1.81E+06
2	11	0.5	wr	72.0	1.65E+06	5	1	0.1	wr	100.0	3.96E+05
2	12	0.5	wr	140.0	5.76E+04	5	2	0.1	wr	150.0	1.34E+05
2	13	0.5	wr	72.0	1.67E+06	5	3	0.1	wr	80.0	1.25E+06
2	14	0.5	wr	72.0	2.10E+06	5	4	0.1	wr	200.0	2.44E+04
2	15	0.5	wr	100.0	2.72E+05	5	5	0.1	wr	80.0	9.86E+05
2	16	0.5	wr	140.0	1.22E+05	5	6	0.1	wr	80.0	7.38E+05
2	17	0.5	wr	66.0	1.44E+06	5	7	0.1	wr	180.0	3.19E+04
2	18	0.5	wt	80.0	6.74E+05	5	8	0.1	wr	150.0	9.88E+04
2	19	0.5	wt	100.0	6.83E+05	5	9	0.1	wr	70.0	1.47E+06
3	1	0.1	wt	180.0	7.97E+04	5	10	0.1	wr	100.0	5.24E+05
3	2	0.1	wt	90.0	2.40E+06	5	11	0.1	nd	72.0	2.00E+06
3	3	0.5	wt	140.0	1.63E+05	6	1	0.1	wt	153.0	3.79E+05

Table A.3: Arc-welded lap joint fatigue test data Part I

series	num.	rl []	failure	Sn [MPa]	cycles []	series	num.	rl []	failure	Sn [MPa]	cycles []
6	2	0.1	wt	196.6	2.65E+05	9	7	0	wt	180.0	2.32E+05
6	3	0.1	wt	100.0	1.46E+06	9	8	0	wt	210.0	1.75E+05
6	4	0.1	wt	250.0	7.26E+04	9	9	0	wt	210.0	1.72E+05
6	5	0.1	wt	100.0	1.72E+06	9	10	0	wt	150.0	6.41E+05
6	6	0.1	wt	200.0	1.45E+05	10	1	-1	wt	100.0	7.50E+04
6	7	0.1	wt	250.0	8.13E+04	10	2	-1	wt	100.0	1.17E+05
6	8	0.1	nd	60.0	2.00E+06	10	3	-1	wt	100.0	1.22E+05
6	9	0.1	wt	150.0	3.61E+05	10	4	-1	wt	74.0	2.18E+05
6	10	0.1	wt	130.0	3.96E+05	10	5	-1	wt	74.0	2.35E+05
6	11	0.1	wt	130.0	4.41E+05	10	6	-1	wt	74.0	2.55E+05
6	12	0.1	wt	90.0	1.16E+06	10	7	-1	wt	60.0	5.78E+05
7	1	0.01	wr	119.0	5.61E+04	10	8	-1	wt	60.0	6.93E+05
7	2	0.01	wr	119.0	5.72E+04	10	9	-1	wt	60.0	7.32E+05
7	3	0.01	wr	119.0	4.99E+04	10	10	-1	wt	55.0	1.07E+06
7	4	0.01	wr	119.0	6.16E+04	10	11	-1	wt	55.0	2.07E+06
7	5	0.01	wr	119.0	3.83E+04	10	12	-1	wt	55.0	5.83E+06
7	6	0.01	wr	99.0	1.33E+05	10	13	-1	wt	50.0	2.31E+06
7	7	0.01	wr	99.0	1.07E+05	10	14	-1	wt	50.0	1.02E+07
7	8	0.01	wr	99.0	1.17E+05	10	15	-1	wt	46.0	1.68E+06
7	9	0.01	wr	99.0	9.95E+04	10	16	-1	wt	46.0	3.05E+06
7	10	0.01	wr	99.0	1.31E+05	10	17	-1	wt	46.0	9.04E+06
7	11	0.01	wr	79.0	3.98E+05	10	18	-1	nd	40.0	2.01E+07
7	12	0.01	wr	79.0	3.94E+05	10	19	-1	nd	40.0	2.24E+07
7	13	0.01	wr	79.0	3.25E+05	11	1	-1	wt	111.0	4.97E+04
7	14	0.01	wr	79.0	3.21E+05	11	2	-1	wt	74.0	1.59E+05
7	15	0.01	wr	79.0	2.33E+05	11	3	-1	wt	74.0	2.66E+05
8	1	0	wr	120.0	1.58E+05	11	4	-1	wt	74.0	3.11E+05
8	2	0	wr	110.0	3.40E+05	11	5	-1	wt	46.3	5.15E+05
8	3	0	wr	110.0	1.65E+05	11	6	-1	wt	46.3	8.48E+05
8	4	0	wr	100.0	1.68E+06	11	7	-1	wt	46.3	1.03E+06
8	5	0	wr	100.0	1.08E+06	11	8	-1	wt	46.3	2.36E+06
8	6	0	wr	120.0	1.74E+05	11	9	-1	wt	46.3	2.49E+06
8	7	0	wr	90.0	1.35E+06	12	1	0.1	wt	110.7	1.31E+05
8	8	0	wr	120.0	4.14E+05	12	2	0.1	wt	68.5	4.76E+05
8	9	0	wr	120.0	1.97E+05	12	3	0.1	wt	416.5	2.73E+03
8	10	0	wr	120.0	3.68E+05	12	4	0.1	wt	370.6	3.68E+03
9	1	0	wt	150.0	3.91E+05	12	5	0.1	wt	229.4	1.31E+04
9	2	0	wt	150.0	6.64E+05	12	6	0.1	wt	322.4	5.30E+03
9	3	0	wt	120.0	1.37E+06	12	7	0.1	wt	322.4	5.75E+03
9	4	0	wt	150.0	5.69E+05	12	8	0.1	wt	322.4	6.29E+03
9	5	0	wt	150.0	8.86E+05	12	9	0.1	wt	229.4	1.56E+04
9	6	0	wt	180.0	3.10E+05	12	10	0.1	wt	229.4	1.71E+04

Table A.4: Arc-welded lap joint fatigue test data Part II

series	num.	rl []	failure	Sn [MPa]	cycles []	series	num.	rl []	failure	Sn [MPa]	cycles []
12	11	0.1	wt	68.1	6.23E+05	16	7	0.1	wr	90.0	2.56E+05
12	12	0.1	wt	68.0	6.09E+05	16	8	0.1	wr	90.0	3.37E+05
12	13	0.1	nd	55.2	5.14E+06	16	9	0.1	wr	82.4	2.39E+05
13	1	0.1	wt	104.7	3.09E+05	16	10	0.1	wr	71.9	1.43E+06
13	2	0.1	wt	87.1	1.35E+05	16	11	0.1	nd	54.1	6.80E+06
13	3	0.1	wt	104.7	4.52E+05	17	1	0.1	wr	185.9	1.03E+04
13	4	0.1	wt	174.1	4.89E+04	17	2	0.1	wr	184.7	1.14E+04
13	5	0.1	wt	174.1	4.67E+04	17	3	0.1	wr	137.6	3.51E+04
13	6	0.1	wt	87.1	1.18E+06	17	4	0.1	wr	137.6	3.59E+04
13	7	0.1	wt	87.1	1.02E+06	17	5	0.1	wr	137.6	6.30E+04
13	8	0.1	wt	69.8	8.76E+05	17	6	0.1	wr	73.5	5.86E+05
14	1	0.1	wt	182.4	2.42E+04	17	7	0.1	wr	73.5	8.54E+05
14	2	0.1	wt	182.4	3.48E+04	17	8	0.1	wr	73.5	1.70E+06
14	3	0.1	nd	78.0	8.96E+06	17	9	0.1	nd	55.1	6.08E+06
14	4	0.1	wt	129.4	7.76E+04	18	1	0.1	wr	132.9	5.85E+04
14	5	0.1	wt	103.8	2.04E+05	18	2	0.1	wr	68.9	1.14E+06
14	6	0.1	wt	103.8	5.16E+05	18	3	0.1	wr	176.5	1.24E+04
14	7	0.1	wt	78.0	5.07E+05	18	4	0.1	wr	176.5	1.29E+04
14	8	0.1	wt	103.8	8.13E+05	18	5	0.1	wr	176.5	1.58E+04
14	9	0.1	wt	182.4	4.24E+04	18	6	0.1	wr	134.1	5.03E+04
14	10	0.1	wt	182.4	4.09E+04	18	7	0.1	wr	134.1	5.47E+04
14	11	0.1	wt	234.1	1.28E+04	18	8	0.1	wr	102.4	1.23E+05
14	12	0.1	wt	234.1	1.56E+04	18	9	0.1	wr	88.2	2.04E+05
15	1	0.1	wt	261.2	9.90E+03	18	10	0.1	wr	67.1	8.56E+05
15	2	0.1	wt	202.4	2.48E+04	18	11	0.1	wr	55.3	2.49E+06
15	3	0.1	wt	202.4	2.50E+04	18	12	0.1	nd	44.7	8.11E+06
15	4	0.1	wt	202.4	2.10E+04	19	1	0.1	wr	222.4	5.13E+03
15	5	0.1	nd	69.9	6.03E+06	19	2	0.1	wr	222.4	5.49E+03
15	6	0.1	wt	116.5	1.85E+05	19	3	0.1	wr	132.9	3.09E+04
15	7	0.1	wt	261.2	1.20E+04	19	4	0.1	wr	132.9	3.28E+04
15	8	0.1	wt	261.2	1.25E+04	19	5	0.1	wr	89.3	6.96E+04
15	9	0.1	wt	116.5	1.28E+05	19	6	0.1	wr	66.8	3.90E+05
15	10	0.1	wt	87.6	6.11E+05	19	7	0.1	wr	44.5	1.92E+06
15	11	0.1	wt	87.6	6.49E+05	19	8	0.1	nd	29.2	5.89E+06
15	12	0.1	wt	87.6	6.98E+05	20	1	0.1	wt	243.0	1.80E+04
16	1	0.1	wr	143.5	1.74E+04	20	2	0.1	wt	121.0	2.03E+05
16	2	0.1	wr	143.5	1.82E+04	20	3	0.1	wt	365.0	5.96E+03
16	3	0.1	wr	143.5	2.18E+04	20	4	0.1	wt	243.0	1.13E+04
16	4	0.1	wr	107.6	6.75E+04	20	5	0.1	wt	305.0	9.23E+03
16	5	0.1	wr	107.6	8.26E+04	20	6	0.1	wt	305.0	7.99E+03
16	6	0.1	wr	107.6	9.86E+04	20	7	0.1	wt	305.0	9.57E+03

Table A.5: Arc-welded lap joint fatigue test data Part III

series	num.	rl []	failure	Sn [MPa]	cycles []	series	num.	rl []	failure	Sn [MPa]	cycles []
20	8	0.1	wt	365.0	5.83E+03	23	5	0.1	wr	219.6	6.80E+04
20	9	0.1	wt	365.0	5.74E+03	23	6	0.1	wr	219.6	5.98E+04
20	10	0.1	wt	183.0	4.52E+04	23	7	0.1	wr	329.4	9.92E+03
20	11	0.1	wt	193.0	4.29E+04	23	8	0.1	wr	274.5	2.83E+04
20	12	0.1	wt	122.0	1.44E+05	23	9	0.1	wr	274.5	3.16E+04
20	13	0.1	wr	92.0	6.78E+05	23	10	0.1	wt	164.7	3.62E+05
20	14	0.1	wr	92.0	4.94E+05	23	11	0.1	wt	164.7	3.90E+05
21	1	0.1	wr	219.6	1.02E+04	23	12	0.1	wr	329.4	1.13E+04
21	2	0.1	wt	82.8	2.75E+05	23	13	0.1	wr	329.4	8.80E+03
21	3	0.1	wt	82.8	3.26E+05	24	1	0.1	wr	163.8	1.39E+04
21	4	0.1	wr	219.6	1.77E+04	24	2	0.1	wr	163.8	1.83E+04
21	5	0.1	wr	329.4	7.91E+03	24	3	0.1	wr	109.8	9.70E+04
21	6	0.1	wr	274.5	9.56E+03	24	4	0.1	wr	109.8	1.31E+05
21	7	0.1	wr	274.5	9.10E+03	24	5	0.1	wr	219.6	6.60E+03
21	8	0.1	wr	219.6	5.87E+03	24	6	0.1	wr	163.8	3.29E+04
21	9	0.1	wr	164.7	3.57E+04	24	7	0.1	wr	274.5	3.74E+03
21	10	0.1	wr	164.7	4.07E+04	24	8	0.1	wr	274.5	3.21E+03
21	11	0.1	wr	164.7	4.49E+04	24	9	0.1	wr	219.6	5.51E+03
21	12	0.1	wr	109.8	2.01E+05	24	10	0.1	wr	219.6	4.72E+03
21	13	0.1	wr	109.8	1.19E+05	24	11	0.1	wt	81.9	5.94E+05
21	14	0.1	wr	109.8	1.03E+05	24	12	0.1	wr	109.8	1.65E+05
21	15	0.1	wt	81.9	5.90E+05	24	13	0.1	wt	81.9	5.25E+05
21	16	0.1	nd	55.8	2.00E+06	24	14	0.1	nd	55.8	2.00E+06
22	1	0.1	wr	218.7	3.76E+04	25	1	0.1	wt	92.0	5.90E+05
22	2	0.1	wt	109.8	6.12E+05	25	2	0.1	wr	244.0	4.75E+03
22	3	0.1	wr	327.6	4.18E+03	25	3	0.1	wr	244.0	5.56E+03
22	4	0.1	nd	110.0	1.98E+06	25	4	0.1	wr	122.0	1.65E+05
22	5	0.1	wr	329.4	6.11E+03	25	5	0.1	wr	244.0	6.60E+03
22	6	0.1	wr	274.5	8.84E+03	25	6	0.1	wt	92.0	5.24E+05
22	7	0.1	wr	274.5	9.91E+03	25	7	0.1	wr	122.0	9.67E+04
22	8	0.1	wr	219.6	5.93E+04	25	8	0.1	wr	122.0	1.30E+05
22	9	0.1	wr	164.7	2.42E+05	25	9	0.1	wr	366.0	3.58E+03
22	10	0.1	wr	164.7	1.70E+05	25	10	0.1	wr	305.0	3.73E+03
22	11	0.1	wr	164.7	1.54E+05	25	11	0.1	wr	183.0	1.84E+04
22	12	0.1	wt	109.8	8.62E+05	25	12	0.1	wr	183.0	1.40E+04
22	13	0.1	wt	109.8	5.82E+05	25	13	0.1	nd	62.0	2.00E+06
22	13	0.1	wt	109.8	8.60E+05	25	14	0.1	wr	183.0	3.38E+04
23	1	0.1	wr	219.6	8.80E+04	25	15	0.1	wr	305.0	3.18E+03
23	2	0.1	wt	164.7	2.45E+05	25	16	0.1	wr	366.0	2.37E+03
23	3	0.1	wr	274.5	2.39E+04	25	17	0.1	wr	366.0	2.45E+03
23	4	0.1	nd	99.0	2.00E+06	26	1	0.1	wt	122.0	3.45E+05

Table A.6: Arc-welded lap joint fatigue test data Part IV

series	num.	rl []	failure	Sn [MPa]	cycles []
26	2	0.1	nd	91.0	2.00E+06
26	3	0.1	wr	183.0	3.15E+04
26	4	0.1	wr	243.0	1.44E+04
26	5	0.1	wr	244.0	1.14E+04
26	6	0.1	wr	244.0	1.00E+04
26	7	0.1	wr	183.0	3.63E+04
26	8	0.1	wr	266.0	4.33E+03
26	9	0.1	wr	266.0	3.99E+03
26	10	0.1	wr	305.0	5.15E+03
26	11	0.1	wr	305.0	5.66E+03
26	12	0.1	wr	305.0	5.38E+03
26	13	0.1	wr	183.0	4.14E+04
27	1	0.1	wr	244.0	8.87E+04
27	2	0.1	wt	183.0	2.45E+05
27	3	0.1	wr	305.0	2.83E+04
27	4	0.1	nd	122.0	2.00E+06
27	5	0.1	wr	305.0	3.18E+04
27	6	0.1	wr	244.0	6.85E+04
27	7	0.1	wr	244.0	5.99E+04
27	8	0.1	wr	305.0	2.41E+04
27	9	0.1	wr	366.0	8.28E+03
27	10	0.1	wr	366.0	8.80E+03
27	11	0.1	wt	183.0	3.64E+05
27	12	0.1	wt	183.0	3.89E+05
28	1	0.1	wr	334.0	4.30E+05
28	2	0.1	wr	273.0	5.12E+05
28	3	0.1	wr	252.0	7.51E+05
28	4	0.1	wr	235.0	9.31E+05
28	5	0.1	wr	198.0	1.44E+06
28	6	0.1	wr	183.0	3.38E+06
28	7	0.1	nd	178.0	1.00E+07
28	8	0.1	nd	149.0	1.00E+07
29	1	0.1	wr	405.0	4.66E+05
29	2	0.1	wr	327.0	7.46E+05
29	3	0.1	wr	304.0	1.50E+06
29	4	0.1	wr	271.0	3.25E+06
29	5	0.1	wr	249.0	5.03E+06
29	6	0.1	wr	238.0	4.92E+06
29	7	0.1	wr	232.0	1.00E+07
30	1	0.1	wr	98.4	2.28E+05
30	2	0.1	wr	98.4	2.54E+05
30	3	0.1	wr	98.4	4.34E+05

series	num.	rl []	failure	Sn [MPa]	cycles []
30	4	0.1	wr	98.4	2.93E+05
30	5	0.62	wr	98.4	1.16E+05
30	6	0.62	wr	98.4	1.44E+05

Table A.7: Arc-welded lap joint fatigue test data Part V

B

Laser-welded joint fatigue resistance data
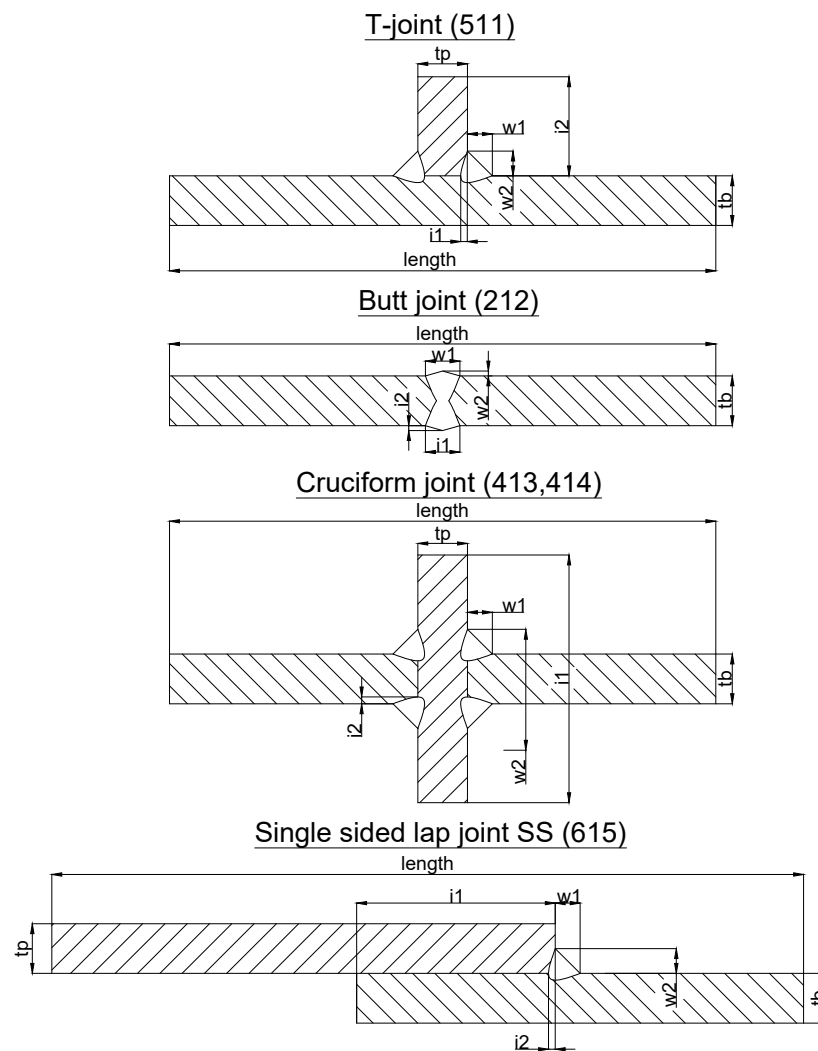
Figure B.1: Naming convention for laser-welded joints

source	series	yield strength [MPa]	geometry	tp [mm]	tb [mm]	i1 [mm]	i2 [mm]	w1 [mm]	w2 [mm]	length [mm]
Fricke and Robert, 2012	1	355	511	5	4	80	1.45	1.1	0.8	600
Fricke and Robert, 2012	2	355	511	5	4	80	1.3	0.25	0.3	600
Fricke and Robert, 2012	3	355	511	5	4	80	1.3	1.15	1	600
Fricke and Robert, 2012	4	355	511	5	4	80	2	0.7	1.1	600
Fricke and Robert, 2012	5	355	511	5	4	80	2	0.7	1.1	600
Fricke and Robert, 2012	6	355	511	10	10	80	3	1	2	600
Remes et al., 2008	7	275	216	12	12	1.68	0.53	2.85	0.06	250
Laitinen et al., 2001	8	420	511	12	12	100	6	1.2	1.2	500
Lillemäe et al., 2012	9	407	216	3	9	1	0.2	3	0.4	250
Dourado et al., 2014	10	355	615	3	3.6	30	1.2	0.25	0.25	450
Caccese et al., 2006	11	650	413	12.7	12.7	95	6.35	7	7	355
Caccese et al., 2006	12	650	413	12.7	12.7	95	6.35	2	2	355
Caccese et al., 2006	13	650	413	12.7	12.7	95	6.35	4.5	4.5	355
Laitinen et al., 2001	14	420	511	12	12	100	6	1.2	1.2	500

Table B.1: Overview of laser-welded joint fatigue test series

series	num.	rl []	failure	Sn [MPa]	cycles []	series	num.	rl []	failure	Sn [MPa]	cycles []
1	1	0	wt	170	3.46E+05	5	8	0	wt	200	7.95E+04
1	2	0	wt	160	1.94E+06	5	9	0	wt	175	1.13E+05
1	3	0	wt	190	1.77E+05	5	10	0	wt	175	7.91E+04
1	4	0	wt	210	3.08E+05	5	11	0	wt	175	1.26E+05
1	5	0	wt	200	3.49E+05	6	1	0	wt	290	1.85E+05
1	6	0	wt	180	8.07E+05	6	2	0	wt	255	4.37E+05
1	7	0	wt	175	4.52E+05	6	3	0	nd	235	1.00E+07
1	8	0	wt	190	1.74E+05	6	4	0	wt	280	3.43E+05
1	9	0	wt	170	1.78E+05	6	5	0	wt	220	9.28E+05
1	10	0	wt	160	2.88E+05	6	6	0	wt	230	8.32E+05
1	11	0	wt	150	1.81E+05	6	7	0	nd	200	1.00E+07
1	12	0	wt	200	9.41E+04	6	8	0	wt	210	7.22E+05
2	1	0	wt	190	1.76E+05	6	9	0	wt	250	4.87E+05
2	2	0	wt	225	1.32E+05	6	10	0	wt	260	3.26E+05
2	3	0	wt	200	7.28E+05	6	11	0	wt	270	2.96E+05
2	4	0	wt	220	2.23E+05	6	12	0	wt	240	7.77E+05
2	5	0	wt	180	5.29E+05	7	1	0	wr	170	9.04E+05
2	6	0	nd	150	1.00E+07	7	2	0	wt	190	4.74E+05
2	7	0	wt	230	1.58E+05	7	3	0	wt	251	1.66E+05
2	8	0	wt	210	2.14E+05	7	4	0	wr	249	8.05E+04
2	9	0	wt	240	1.10E+05	7	5	0	wr	201	3.60E+05
2	10	0	wt	200	1.28E+05	7	6	0	wt	201	3.12E+05
2	11	0	wt	200	2.00E+05	8	1	0.1	wt	318	8.83E+04
3	1	0	wt	100	6.06E+05	8	2	0.1	wt	290	1.82E+05
3	2	0	wt	189	1.57E+05	8	3	0.1	wt	224	4.70E+05
3	3	0	wt	150	2.90E+05	8	4	0.1	wt	199	7.61E+05
3	4	0	wt	180	2.27E+05	8	5	0.1	nd	159	2.45E+06
3	5	0	wt	200	1.53E+05	8	6	0.1	nd	175	2.29E+06
3	6	0	wt	120	6.63E+05	8	13	0.1	wt	266	1.79E+05
4	1	0	wt	129	9.61E+05	8	14	0.1	wt	180	4.59E+05
4	2	0	wt	139	5.51E+05	8	15	0.1	wt	157	8.71E+05
4	3	0	wt	158	3.37E+05	8	16	0.1	wt	128	1.15E+06
4	4	0	wt	168	2.26E+05	8	17	0.1	nd	135	2.08E+06
4	5	0	wt	127	4.81E+05	8	18	0.1	nd	113	2.25E+06
5	1	0	wt	195	4.41E+05	9	1	0	wr	270	6.97E+05
5	2	0	wt	215	1.41E+05	9	2	0	wr	269	1.10E+06
5	3	0	wt	205	2.53E+05	9	3	0	wr	328	1.46E+05
5	4	0	wt	185	1.20E+05	9	4	0	wr	295	4.61E+05
5	5	0	wt	175	1.39E+05	9	5	0	wr	344	2.79E+05
5	6	0	wt	200	9.32E+04	9	6	0	wr	278	9.19E+05
5	7	0	wt	165	5.59E+05	9	7	0	wr	291	6.92E+05

Table B.2: Laser-welded joint fatigue test data Part I

series	num.	rl []	failure	Sn [MPa]	cycles []
9	8	0	wr	278	5.63E+05
9	9	0	wr	297	1.76E+05
9	10	0	wr	345	1.31E+05
10	1	0.01	wr	119	7.23E+04
10	2	0.01	wr	119	5.86E+04
10	3	0.01	wr	119	6.62E+04
10	4	0.01	wr	119	6.90E+04
10	5	0.01	wr	119	6.58E+04
10	6	0.01	wr	99	1.42E+05
10	7	0.01	wr	99	1.43E+05
10	8	0.01	wr	99	1.04E+05
10	9	0.01	wr	99	1.19E+05
10	10	0.01	wr	99	1.15E+05
10	11	0.01	wr	79	4.23E+05
10	12	0.01	wr	79	3.93E+05
10	13	0.01	wr	79	2.94E+05
10	14	0.01	wr	79	3.04E+05
10	15	0.01	wr	79	3.26E+05
11	1	-1	wt	207	3.59E+06
11	2	-1	nd	207	2.03E+07
11	3	-1	nd	207	2.00E+07
11	4	-1	nd	207	2.00E+07
11	5	-1	wt	414	2.12E+05
11	6	-1	wt	414	2.22E+05
11	7	-1	wt	414	2.14E+05
11	8	-1	wt	414	2.63E+05
11	9	-1	wt	620	1.85E+04
11	10	-1	wt	620	1.85E+04
11	11	-1	wt	620	1.54E+04
11	12	-1	wt	620	1.32E+04
12	1	-1	wt	414	2.28E+04
12	2	-1	wt	414	2.64E+04
12	3	-1	wt	414	2.05E+04
13	1	-1	wt	414	4.35E+04
13	2	-1	wt	414	4.77E+04
14	1	0.1	wt	542	1.55E+05
14	2	0.1	wt	452	2.69E+05
14	3	0.1	wt	356	4.43E+05
14	4	0.1	wt	264	9.81E+05
14	5	0.1	nd	204	2.16E+06
14	6	0.1	wt	226	2.51E+06

Table B.3: Laser-welded joint fatigue test data Part II

$$C$$
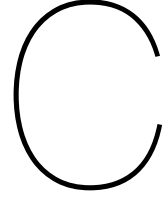
CBW fitting

C.1. Toe of single lap joint DS (614)

$$
\begin{aligned}
C_{bw-toe-614} = {} & 0.279r_s + 0.0953T + 0.0626O - 0.11W + 0.00945r_s - 0.00564Q \\
& - 0.000556T^2O^2 - 0.307r_sT - 0.0433r_sO - 0.15r_sW + 0.0148TO - 0.00779r_sr_s \\
& - 0.209TW - 0.0688r_sQ + 0.0405Tr_s + 0.0165OW + 0.238TQ - 0.00586Or_s - 0.0038OQ \\
& - 0.0194Wr_s + 0.0907WQ - 0.0601r_sQ + 0.543r_sT^2 - 0.188r_sT^3 + 0.0015r_sO^2 \\
& + 0.00246TO^2 - 0.0355T^2O - 0.215T^2W + 0.00896T^3O - 0.0286T^2r_s \\
& + 0.157T^3W - 0.0012O^2W - 0.0893T^2Q + 0.00507T^3r_s + 0.000218O^2r_s \\
& + 0.0288T^3Q + 0.0023O^2Q - 0.202T^2 + 0.161T^3 - 0.0029O^2 - 0.0366T^4 \\
& - 0.000646r_sTO^2 + 0.0165r_sT^2O - 0.0946r_sT^2W + 0.0222r_sT^2r_s - 0.000252r_sO^2W \\
& + 0.165r_sT^2Q - 0.000126r_sO^2r_s + 0.000597TO^2W - 0.0215T^2OW + 0.000158r_sO^2Q \\
& - 0.000084TO^2r_s + 0.001T^2Or_s - 0.000442TO^2Q + 0.0137T^2OQ + 0.00414T^2Wr_s \\
& - 0.0772T^2WQ + 0.000211O^2Wr_s - 0.0597T^2r_sQ + 0.00107O^2WQ + 0.000887O^2r_sQ \\
& - 0.0205r_sTO + 0.15r_sTW - 0.0551r_sTr_s - 0.0166r_sOW - 0.281r_sTQ + 0.00675r_sOr_s \\
& + 0.0275TOW + 0.0385r_sOQ + 0.0386r_sWr_s - 0.000627TOr_s + 0.174r_sWQ - 0.0572TOQ \\
& + 0.0168TWr_s - 0.0309r_sr_sQ + 0.0663TWQ + 0.00398OWr_s + 0.138Tr_sQ + 0.065OWQ \\
& + 0.00662Or_sQ + 0.0386Wr_sQ + 0.00994r_sTOW - 0.000992r_sTOr_s - 0.02r_sTOQ \\
& - 0.0195r_sTWr_s - 0.101r_sTWQ - 0.000384r_sOWr_s + 0.0246r_sTr_sQ + 0.0137r_sOWQ \\
& - 0.00433TOWr_s + 0.0144r_sOr_sQ - 0.023TOWQ - 0.0133r_sWr_sQ - 0.00783TOr_sQ \\
& - 0.0237TWr_sQ + 0.00781OWr_sQ + 0.035 \quad\quad\quad\quad\quad\quad\quad\quad\quad\quad\quad\quad (C.1)
\end{aligned}
$$

r_s	T	O	W	P	Q	coefficient
0	0	0	0	0	1	-5.64E-03
0	0	0	0	1	0	9.45E-03
0	0	0	0	1	1	-6.01E-02
0	0	0	1	0	0	-1.10E-01
0	0	0	1	0	1	9.07E-02
0	0	0	1	1	0	-1.94E-02
0	0	0	1	1	1	3.86E-02
0	0	1	0	0	0	6.26E-02
0	0	1	0	0	1	-3.80E-03
0	0	1	0	1	0	-5.86E-03
0	0	1	0	1	1	6.62E-03
0	0	1	1	0	0	1.65E-02
0	0	1	1	0	1	6.50E-02
0	0	1	1	1	0	3.98E-03
0	0	1	1	1	1	7.81E-03
0	0	2	0	0	0	-2.90E-03
0	0	2	0	0	1	2.30E-03
0	0	2	0	1	0	2.18E-04
0	0	2	0	1	1	8.87E-04
0	0	2	1	0	0	-1.20E-03
0	0	2	1	0	1	1.07E-03
0	0	2	1	1	0	2.11E-04
0	1	0	0	0	0	9.53E-02
0	1	0	0	0	1	2.38E-01
0	1	0	0	1	0	4.05E-02
0	1	0	0	1	1	1.38E-01
0	1	0	1	0	0	-2.09E-01
0	1	0	1	0	1	6.63E-02
0	1	0	1	1	0	1.68E-02
0	1	0	1	1	1	-2.37E-02
0	1	1	0	0	0	1.48E-02
0	1	1	0	0	1	-5.72E-02
0	1	1	0	1	0	-6.27E-04
0	1	1	0	1	1	-7.83E-03
0	1	1	1	0	0	2.75E-02
0	1	1	1	0	1	-2.30E-02
0	1	1	1	1	0	-4.33E-03
0	1	2	0	0	0	2.46E-03
0	1	2	0	0	1	-4.42E-04
0	1	2	0	1	0	-8.40E-05
0	1	2	1	0	0	5.97E-04
0	2	0	0	0	0	-2.02E-01
0	2	0	0	0	1	-8.93E-02

r_s	T	O	W	P	Q	coefficient
0	2	0	0	1	0	-2.86E-02
0	2	0	0	1	1	-5.97E-02
0	2	0	1	0	0	-2.15E-01
0	2	0	1	0	1	-7.72E-02
0	2	0	1	1	0	4.14E-03
0	2	1	0	0	0	-3.55E-02
0	2	1	0	0	1	1.37E-02
0	2	1	0	1	0	1.00E-03
0	2	1	1	0	0	-2.15E-02
0	2	2	0	0	0	-5.56E-04
0	3	0	0	0	0	1.61E-01
0	3	0	0	0	1	2.88E-02
0	3	0	0	1	0	5.07E-03
0	3	0	1	0	0	1.57E-01
0	3	1	0	0	0	8.96E-03
1	0	0	0	0	0	2.79E-01
1	0	0	0	0	1	-6.88E-02
1	0	0	0	1	0	-7.79E-03
1	0	0	0	1	1	-3.09E-02
1	0	0	1	0	0	-1.50E-01
1	0	0	1	0	1	1.74E-01
1	0	0	1	1	0	3.86E-02
1	0	0	1	1	1	-1.33E-02
1	0	1	0	0	0	-4.33E-02
1	0	1	0	0	1	3.85E-02
1	0	1	0	1	0	6.75E-03
1	0	1	0	1	1	1.44E-02
1	0	1	1	0	0	-1.66E-02
1	0	1	1	0	1	1.37E-02
1	0	1	1	1	0	-3.84E-04
1	0	2	0	0	0	1.50E-03
1	0	2	0	0	1	1.58E-04
1	0	2	0	1	0	-1.26E-04
1	0	2	1	0	0	-2.52E-04
1	1	0	0	0	0	-3.07E-01
1	1	0	0	0	1	-2.81E-01
1	1	0	0	1	0	-5.51E-02
1	1	0	0	1	1	2.46E-02
1	1	0	1	0	0	1.50E-01
1	1	0	1	0	1	-1.01E-01
1	1	0	1	1	0	-1.95E-02
1	1	1	0	0	0	-2.05E-02
1	1	1	0	0	1	-2.00E-02

r_s	T	O	W	P	Q	coefficient
1	1	1	0	1	0	-9.92E-04
1	1	1	1	0	0	9.94E-03
1	1	2	0	0	0	-6.46E-04
1	2	0	0	0	0	5.43E-01
1	2	0	0	0	1	1.65E-01
1	2	0	0	1	0	2.22E-02
1	2	0	1	0	0	-9.46E-02
1	2	1	0	0	0	1.65E-02
1	3	0	0	0	0	-1.88E-01
0	0	0	0	0	0	3.50E-02
0	4	0	0	0	0	-3.66E-02

Table C.1: Coefficients for C_{bw} of the toe of single lap joints DS (614)

$$
\begin{aligned}
C_{bw2-toe-614} = {}& 0.911 C_{bw} + 0.334 r_s + 0.383T + 0.0361O + 0.211W - 0.184 C_{bw} r_s \\
& - 0.327 C_{bw} T + 0.0869 C_{bw} O + 0.0548 r_s T - 0.623 C_{bw} W - 0.0526 r_s O - 0.118 r_s W \\
& - 0.0982 TO - 0.163 TW - 0.0123 OW - 0.212 C_{bw} T^2 + 0.129 C_{bw} T^3 - 0.205 r_s T^2 \\
& + 0.0463 r_s T^3 + 0.0512 T^2 O + 0.0225 T^2 W - 0.00729 T^3 O + 0.00488 T^3 W + 0.172 T^2 \\
& - 0.18 T^3 + 0.0288 T^4 + 0.0423 C_{bw} r_s T^2 - 0.0091 C_{bw} T^2 O + 0.159 C_{bw} T^2 W \\
& - 0.00819 r_s T^2 O + 0.00227 r_s T^2 W - 0.00391 T^2 OW - 0.0235 C_{bw} r_s T + 0.0285 C_{bw} r_s O \\
& + 0.0669 C_{bw} r_s W - 0.00476 C_{bw} TO - 0.209 C_{bw} TW + 0.0447 r_s TO + 0.0538 C_{bw} OW \\
& + 0.0529 r_s TW + 0.00905 r_s OW + 0.0168 TOW - 0.0143 C_{bw} r_s TO - 0.00568 C_{bw} r_s TW \\
& - 0.00328 C_{bw} r_s OW - 0.0329 C_{bw} TOW - 0.00426 r_s TOW - 0.344
\end{aligned}
\tag{C.2}
$$

C_{bw}	r_s	T	O	W	Coefficient
0	0	0	0	1	2.11E-01
0	0	0	1	0	3.61E-02
0	0	0	1	1	-1.23E-02
0	0	1	0	0	3.83E-01
0	0	1	0	1	-1.63E-01
0	0	1	1	0	-9.82E-02
0	0	1	1	1	1.68E-02
0	0	2	0	0	1.72E-01
0	0	2	0	1	2.25E-02
0	0	2	1	0	5.12E-02
0	0	2	1	1	-3.91E-03
0	0	3	0	0	-1.80E-01
0	0	3	0	1	4.88E-03
0	0	3	1	0	-7.29E-03
0	1	0	0	0	3.34E-01
0	1	0	0	1	-1.18E-01
0	1	0	1	0	-5.26E-02
0	1	0	1	1	9.05E-03
0	1	1	0	0	5.48E-02
0	1	1	0	1	5.29E-02
0	1	1	1	0	4.47E-02
0	1	1	1	1	-4.26E-03
0	1	2	0	0	-2.05E-01
0	1	2	0	1	2.27E-03
0	1	2	1	0	-8.19E-03
0	1	3	0	0	4.63E-02
1	0	0	0	0	9.11E-01
1	0	0	0	1	-6.23E-01
1	0	0	1	0	8.69E-02
1	0	0	1	1	5.38E-02
1	0	1	0	0	-3.27E-01
1	0	1	0	1	-2.09E-01
1	0	1	1	0	-4.76E-03
1	0	1	1	1	-3.29E-02
1	0	2	0	0	-2.12E-01
1	0	2	0	1	1.59E-01
1	0	2	1	0	-9.10E-03
1	0	3	0	0	1.29E-01
1	1	0	0	0	-1.84E-01
1	1	0	0	1	6.69E-02
1	1	0	1	0	2.85E-02
1	1	0	1	1	-3.28E-03
1	1	1	0	0	-2.35E-02

C_{bw}	r_s	T	O	W	Coefficient
1	1	1	0	1	-5.68E-03
1	1	1	1	0	-1.43E-02
1	1	2	0	0	4.23E-02
0	0	0	0	0	-3.44E-01
0	0	4	0	0	2.88E-02

Table C.2: Coefficients for C_{bw2} of the toe of single lap joints DS (614)

C.2. Root of single lap joint DS (614)

$$
\begin{aligned}
C_{bw-root-614} = {} & 0.386P - 6.1r_s + 36.8T + 11.8O + 9.28W - 0.914S + 0.00294P^2T^2 \\
& - 0.339Pr_s - 1.62PT - 2.39PO - 35.8r_sT + 11.8PW - 12.0r_sO - 0.0315PS - 8.89r_sW \\
& + 2.91TO - 0.118r_sS - 67.2TW - 4.52TS - 30.2OW - 1.42OS - 1.08WS + 0.22P^2r_s \\
& - 2.85PT^2 - 0.968P^2T - 0.00976PT^3 + 6.34r_sT^2 + 0.283P^2O + 10.8r_sT^3 - 1.42P^2W \\
& + 0.027P^2S - 0.703T^2O + 65.3T^2W - 0.0021T^3O + 0.777T^2S - 0.0346T^3W + 1.36T^3S \\
& - 0.22P^2 - 7.22T^2 - 10.5T^3 - 0.033T^4 + 2.88Pr_sT^2 + 0.958P^2r_sT - 0.281P^2r_sO \\
& - 0.00174PT^2O + 1.43P^2r_sW - 0.000632P^2TO - 0.0347PT^2W + 0.707r_sT^2O \\
& - 0.000266P^2r_sS - 0.00498P^2TW + 0.363PT^2S - 64.9r_sT^2W + 0.119P^2TS \\
& + 0.0000553P^2OW + 0.00617r_sT^2S - 0.035P^2OS + 0.18P^2WS + 0.0272T^2OW \\
& + 0.0913T^2OS - 8.14T^2WS + 1.59Pr_sT + 2.37Pr_sO - 12.0Pr_sW - 0.306PTO \\
& + 0.0182Pr_sS + 16.8PTW - 2.84r_sTO + 0.202PTS + 1.76POW + 66.1r_sTW \\
& + 0.295POS + 0.0419r_sTS + 30.5r_sOW - 1.51PWS + 0.0056r_sOS + 4.28TOW \\
& + 0.0857r_sWS - 0.388TOS + 8.38TWS + 3.79OWS + 0.317Pr_sTO - 16.6Pr_sTW \\
& + 0.000793Pr_sTS - 1.79Pr_sOW - 0.00102Pr_sOS + 0.00858PTOW - 0.00945Pr_sWS \\
& + 0.0397PTOS - 4.48r_sTOW - 2.08PTWS - 0.000993r_sTOS - 0.223POWS \\
& - 0.0318r_sTWS - 0.00507r_sOWS - 0.551TOWS + 6.59
\end{aligned}
$$

(C.3)

P	r_s	T	O	W	S	Coefficient
0	0	0	0	0	1	-9.14E-01
0	0	0	0	1	0	9.28E+00
0	0	0	0	1	1	-1.08E+00
0	0	0	1	0	0	1.18E+01
0	0	0	1	0	1	-1.42E+00
0	0	0	1	1	0	-3.02E+01
0	0	0	1	1	1	3.79E+00
0	0	1	0	0	0	3.68E+01
0	0	1	0	0	1	-4.52E+00
0	0	1	0	1	0	-6.72E+01
0	0	1	0	1	1	8.38E+00
0	0	1	1	0	0	2.91E+00
0	0	1	1	0	1	-3.88E-01
0	0	1	1	1	0	4.28E+00
0	0	1	1	1	1	-5.51E-01
0	0	2	0	0	0	-7.22E+00
0	0	2	0	0	1	7.77E-01
0	0	2	0	1	0	6.53E+01
0	0	2	0	1	1	-8.14E+00
0	0	2	1	0	0	-7.03E-01
0	0	2	1	0	1	9.13E-02
0	0	2	1	1	0	2.72E-02
0	0	3	0	0	0	-1.05E+01
0	0	3	0	0	1	1.36E+00
0	0	3	0	1	0	-3.46E-02
0	0	3	1	0	0	-2.10E-03
0	1	0	0	0	0	-6.10E+00
0	1	0	0	0	1	-1.18E-01
0	1	0	0	1	0	-8.89E+00
0	1	0	0	1	1	8.57E-02
0	1	0	1	0	0	-1.20E+01
0	1	0	1	0	1	5.60E-03
0	1	0	1	1	0	3.05E+01
0	1	0	1	1	1	-5.07E-03
0	1	1	0	0	0	-3.58E+01
0	1	1	0	0	1	4.19E-02
0	1	1	0	1	0	6.61E+01
0	1	1	0	1	1	-3.18E-02
0	1	1	1	0	0	-2.84E+00
0	1	1	1	0	1	-9.93E-04
0	1	1	1	1	0	-4.48E+00
0	1	2	0	0	0	6.34E+00
0	1	2	0	0	1	6.17E-03

P	r_s	T	O	W	S	Coefficient
0	1	2	0	1	0	-6.49E+01
0	1	2	1	0	0	7.07E-01
0	1	3	0	0	0	1.08E+01
1	0	0	0	0	0	3.86E-01
1	0	0	0	0	1	-3.15E-02
1	0	0	0	1	0	1.18E+01
1	0	0	0	1	1	-1.51E+00
1	0	0	1	0	0	-2.39E+00
1	0	0	1	0	1	2.95E-01
1	0	0	1	1	0	1.76E+00
1	0	0	1	1	1	-2.23E-01
1	0	1	0	0	0	-1.62E+00
1	0	1	0	0	1	2.02E-01
1	0	1	0	1	0	1.68E+01
1	0	1	0	1	1	-2.08E+00
1	0	1	1	0	0	-3.06E-01
1	0	1	1	0	1	3.97E-02
1	0	1	1	1	0	8.58E-03
1	0	2	0	0	0	-2.85E+00
1	0	2	0	0	1	3.63E-01
1	0	2	0	1	0	-3.47E-02
1	0	2	1	0	0	-1.74E-03
1	0	3	0	0	0	-9.76E-03
1	1	0	0	0	0	-3.39E-01
1	1	0	0	0	1	1.82E-02
1	1	0	0	1	0	-1.20E+01
1	1	0	0	1	1	-9.45E-03
1	1	0	1	0	0	2.37E+00
1	1	0	1	0	1	-1.02E-03
1	1	0	1	1	0	-1.79E+00
1	1	1	0	0	0	1.59E+00
1	1	1	0	0	1	7.93E-04
1	1	1	0	1	0	-1.66E+01
1	1	1	1	0	0	3.17E-01
1	1	2	0	0	0	2.88E+00
2	0	0	0	0	0	-2.20E-01
2	0	0	0	0	1	2.70E-02
2	0	0	0	1	0	-1.42E+00
2	0	0	0	1	1	1.80E-01
2	0	0	1	0	0	2.83E-01
2	0	0	1	0	1	-3.50E-02
2	0	0	1	1	0	5.53E-05
2	0	1	0	0	0	-9.68E-01

P	r_s	T	O	W	S	Coefficient
2	0	1	0	0	1	1.19E-01
2	0	1	0	1	0	-4.98E-03
2	0	1	1	0	0	-6.32E-04
2	0	2	0	0	0	2.94E-03
2	1	0	0	0	0	2.20E-01
2	1	0	0	0	1	-2.66E-04
2	1	0	0	1	0	1.43E+00
2	1	0	1	0	0	-2.81E-01
2	1	1	0	0	0	9.58E-01
0	0	0	0	0	0	6.59E+00
0	0	4	0	0	0	-3.30E-02

Table C.3: Coefficients for C_{bw} of the root of single lap joints DS (614)

$$
\begin{aligned}
C_{bw2-root-614} = {}& 0.861r_s - 0.849P - 1.99C_{bw} + 0.397T + 0.0676O + 5.95W - 0.0081P^2T^2 \\
& + 1.63C_{bw}P + 2.03C_{bw}r_s + 1.22C_{bw}T + 0.806Pr_s - 0.0716C_{bw}O + 1.21PT \\
& - 4.1C_{bw}W - 0.161PO + 0.126r_sT - 0.97PW - 0.572r_sO - 4.01r_sW + 0.0956TO \\
& - 6.0TW + 0.903OW - 0.154C_{bw}P^2 + 0.00165C_{bw}P^3 - 1.3C_{bw}T^2 - 0.384P^2r_s \\
& - 0.257PT^2 - 0.042P^2T + 0.0293P^3r_s + 1.26r_sT^2 - 0.00263P^2O - 0.00715P^3T \\
& - 0.0253P^2W + 0.000481P^3O + 0.00309P^3W - 0.00782T^2O + 2.06T^2W + 0.229P^2 \\
& - 0.00554P^3 - 0.000532P^4 - 0.297T^2 - 0.0166C_{bw}P^2r_s + 0.586C_{bw}PT^2 \\
& + 0.0721C_{bw}P^2T - 1.05C_{bw}r_sT^2 + 0.00114C_{bw}P^2O + 0.165C_{bw}P^2W \\
& + 0.0605Pr_sT^2 + 0.166P^2r_sT - 0.0295C_{bw}T^2O - 0.0157P^2r_sO - 2.48C_{bw}T^2W \\
& + 0.00511PT^2O - 0.188P^2r_sW + 0.00337P^2TO - 0.0284PT^2W - 0.019r_sT^2O \\
& + 0.023P^2TW - 0.771r_sT^2W - 0.00471P^2OW + 0.0108T^2OW - 0.428C_{bw}Pr_s \\
& - 1.52C_{bw}PT + 0.00718C_{bw}PO + 2.52C_{bw}r_sT - 0.981C_{bw}PW - 0.332C_{bw}r_sO \\
& - 1.57Pr_sT - 2.18C_{bw}r_sW + 0.094C_{bw}TO + 0.368Pr_sO + 5.5C_{bw}TW + 2.21Pr_sW \\
& + 0.0182PTO + 0.236C_{bw}OW + 0.403PTW + 0.116r_sTO + 0.0223POW + 3.54r_sTW \\
& - 1.57r_sOW - 0.341TOW + 0.0951C_{bw}Pr_sT - 0.00468C_{bw}Pr_sO + 0.405C_{bw}Pr_sW \\
& - 0.00514C_{bw}PTO - 0.204C_{bw}PTW + 0.103C_{bw}r_sTO - 0.0353C_{bw}POW \\
& - 0.546C_{bw}r_sTW - 0.0856Pr_sTO + 0.143C_{bw}r_sOW - 0.438Pr_sTW + 0.0504C_{bw}TOW \\
& + 0.0969Pr_sOW - 0.0135PTOW + 0.39r_sTOW - 1.55
\end{aligned}
$$

$$\text{(C.4)}$$

C_{bw}	P	r_s	T	O	W	Coefficient
0	0	0	0	0	1	5.95E+00
0	0	0	0	1	0	6.76E-02
0	0	0	0	1	1	9.03E-01
0	0	0	1	0	0	3.97E-01
0	0	0	1	0	1	-6.00E+00
0	0	0	1	1	0	9.56E-02
0	0	0	1	1	1	-3.41E-01
0	0	0	2	0	0	-2.97E-01
0	0	0	2	0	1	2.06E+00
0	0	0	2	1	0	-7.82E-03
0	0	0	2	1	1	1.08E-02
0	0	1	0	0	0	8.61E-01
0	0	1	0	0	1	-4.01E+00
0	0	1	0	1	0	-5.72E-01
0	0	1	0	1	1	-1.57E+00
0	0	1	1	0	0	1.26E-01
0	0	1	1	0	1	3.54E+00
0	0	1	1	1	0	1.16E-01
0	0	1	1	1	1	3.90E-01
0	0	1	2	0	0	1.26E+00
0	0	1	2	0	1	-7.71E-01
0	0	1	2	1	0	-1.90E-02
0	1	0	0	0	0	-8.49E-01
0	1	0	0	0	1	-9.70E-01
0	1	0	0	1	0	-1.61E-01
0	1	0	0	1	1	2.23E-02
0	1	0	1	0	0	1.21E+00
0	1	0	1	0	1	4.03E-01
0	1	0	1	1	0	1.82E-02
0	1	0	1	1	1	-1.35E-02
0	1	0	2	0	0	-2.57E-01
0	1	0	2	0	1	-2.84E-02
0	1	0	2	1	0	5.11E-03
0	1	1	0	0	0	8.06E-01
0	1	1	0	0	1	2.21E+00
0	1	1	0	1	0	3.68E-01
0	1	1	0	1	1	9.69E-02
0	1	1	1	0	0	-1.57E+00
0	1	1	1	0	1	-4.38E-01
0	1	1	1	1	0	-8.56E-02
0	1	1	2	0	0	6.05E-02
0	2	0	0	0	0	2.29E-01
0	2	0	0	0	1	-2.53E-02
0	2	0	0	1	1	-4.71E-03
0	2	0	1	0	0	-4.20E-02
0	2	0	1	0	1	2.30E-02
0	2	0	1	1	0	3.37E-03
0	2	0	2	0	0	-8.10E-03
0	2	1	0	0	0	-3.84E-01
0	2	1	0	0	1	-1.88E-01
0	2	1	0	1	0	-1.57E-02
0	2	1	1	0	0	1.66E-01
0	3	0	0	0	0	-5.54E-03
0	3	0	0	0	1	3.09E-03
0	3	0	0	1	0	4.81E-04
0	3	0	1	0	0	-7.15E-03
0	3	1	0	0	0	2.93E-02
1	0	0	0	0	0	-1.99E+00
1	0	0	0	0	1	-4.10E+00
1	0	0	0	1	0	-7.16E-02
1	0	0	0	1	1	2.36E-01
1	0	0	1	0	0	1.22E+00
1	0	0	1	0	1	5.50E+00
1	0	0	1	1	0	9.40E-02
1	0	0	1	1	1	5.04E-02
1	0	0	2	0	0	-1.30E+00
1	0	0	2	0	1	-2.48E+00
1	0	0	2	1	0	-2.95E-02
1	0	1	0	0	0	2.03E+00
1	0	1	0	0	1	-2.18E+00
1	0	1	0	1	0	-3.32E-01
1	0	1	0	1	1	1.43E-01
1	0	1	1	0	0	2.52E+00
1	0	1	1	0	1	-5.46E-01
1	0	1	1	1	0	1.03E-01
1	0	1	2	0	0	-1.05E+00
1	1	0	0	0	0	1.63E+00
1	1	0	0	0	1	-9.81E-01
1	1	0	0	1	0	7.18E-03
1	1	0	0	1	1	-3.53E-02
1	1	0	1	0	0	-1.52E+00
1	1	0	1	0	1	-2.04E-01
1	1	0	1	1	0	-5.14E-03
1	1	0	2	0	0	5.86E-01
1	1	1	0	0	0	-4.28E-01

C_{bw}	P	r_s	T	O	W	Coefficient
1	1	1	0	0	1	4.05E-01
1	1	1	0	1	0	-4.68E-03
1	1	1	1	0	0	9.51E-02
1	2	0	0	0	0	-1.54E-01
1	2	0	0	0	1	1.65E-01
1	2	0	0	1	0	1.14E-03
1	2	0	1	0	0	7.21E-02
1	2	1	0	0	0	-1.66E-02
1	3	0	0	0	0	1.65E-03
0	0	0	0	0	0	-1.55E+00
0	4	0	0	0	0	-5.32E-04

Table C.4: Coefficients for C_{bw2} of the root of single lap joints DS (614)

C.3. Toe of single lap joint SS (615)

$$
\begin{aligned}
C_{bw-toe-615} = {} & 0.791T - 1.1W + 0.448r_s + 0.0534T^2W^2 + 1.34TW - 1.59Tr_s + 1.03Wr_s \\
& - 0.938TW^2 - 0.781T^2W + 0.275TW^3 + 1.65T^2r_s + 0.281T^3W - 0.566T^3r_s - 1.07W^2r_s \\
& + 0.331W^3r_s - 0.885T^2 + 0.514T^3 + 1.04W^2 - 0.152T^4 - 0.307W^3 + 0.0876TW^2r_s \\
& + 0.15T^2Wr_s - 0.359TWr_s - 0.00343
\end{aligned} \tag{C.5}
$$

T	W	r_s	Coefficient
0	0	1	4.48E-01
0	1	0	-1.10E+00
0	1	1	1.03E+00
0	2	0	1.04E+00
0	2	1	-1.07E+00
0	3	0	-3.07E-01
0	3	1	3.31E-01
1	0	0	7.91E-01
1	0	1	-1.59E+00
1	1	0	1.34E+00
1	1	1	-3.59E-01
1	2	0	-9.38E-01
1	2	1	8.76E-02
1	3	0	2.75E-01
2	0	0	-8.85E-01
2	0	1	1.65E+00
2	1	0	-7.81E-01
2	1	1	1.50E-01
2	2	0	5.34E-02
3	0	0	5.14E-01
3	0	1	-5.66E-01
3	1	0	2.81E-01
0	0	0	-3.43E-03
4	0	0	-1.52E-01

Table C.5: Coefficients for C_{bw} of the toe of single lap joints SS (615)

$$
\begin{aligned}
C_{bw2-toe-615} = {}& -0.116 C_{bw}^3 T - 0.0715 C_{bw}^3 + 0.82 C_{bw}^2 T^2 + 0.426 C_{bw}^2 T \\
& - 0.0379 C_{bw}^2 - 1.22 C_{bw} T^3 + 1.01 C_{bw} T^2 + 0.542 C_{bw} T + 1.08 C_{bw} - 0.211 T^4 \\
& + 0.689 T^3 - 0.416 T^2 - 0.128 T - 0.0653
\end{aligned}
\tag{C.6}
$$

C_{bw}	T	Coefficient
0	1	-1.28E-01
0	2	-4.16E-01
0	3	6.89E-01
1	0	1.08E+00
1	1	5.42E-01
1	2	1.01E+00
1	3	-1.22E+00
2	0	-3.79E-02
2	1	4.26E-01
2	2	8.20E-01
3	0	-7.15E-02
3	1	-1.16E-01
0	0	-6.53E-02
0	4	-2.11E-01

Table C.6: Coefficients for C_{bw2} of the toe of single lap joints SS (615)

C.4. Root of single lap joint DS (615)

$$
\begin{aligned}
C_{bw-root-615} = {}& 74800.0T - 143000.0r_s - 35900.0P + 161000.0W - 3140.0S + 8340.0P^2r_s^2 \\
& - 0.00173P^2T^2 - 0.000628P^2W^2 - 3680.0r_s^2T^2 - 174000.0r_s^2W^2 + 0.043T^2W^2 \\
& + 116000.0Pr_s - 45400.0PT + 50000.0PW - 194000.0r_sT + 5130.0PS - 89200.0r_sW \\
& + 16900.0r_sS + 103000.0TW - 10700.0TS - 22900.0WS - 86100.0Pr_s^2 - 6380.0P^2r_s \\
& - 5180.0PT^2 - 1870.0P^2T - 721.0P^3r_s - 0.00386PT^3 - 3620.0PW^2 - 23900.0r_sT^2 \\
& + 1040.0P^2W + 0.000699P^3T + 124000.0r_s^2T - 0.00138PW^3 + 9300.0r_sT^3 \\
& + 603000.0r_sW^2 + 115.0P^2S + 0.000097P^3W - 108000.0r_s^2W - 112000.0r_sW^3 \\
& - 4900.0TW^2 - 90.1P^3S - 0.648r_s^2S + 305.0T^2W + 0.0152TW^3 - 3380.0T^2S \\
& + 0.0409T^3W + 1160.0T^3S + 56400.0W^2S - 14000.0W^3S - 805.0P^2 + 631.0P^3 \\
& + 135000.0r_s^2 + 0.000429P^4 + 23700.0T^2 - 8140.0T^3 - 394000.0W^2 - 0.0902T^4 \\
& + 98200.0W^3 + 5920.0Pr_sT^2 - 70800.0Pr_s^2T + 2140.0P^2r_sT + 4140.0Pr_sW^2 \\
& + 89000.0Pr_s^2W - 1190.0P^2r_sW + 0.00426PTW^2 + 0.205Pr_s^2S + 0.00488PT^2W \\
& + 1040.0P^2r_sS + 0.00284P^2TW + 740.0PT^2S + 5600.0r_sTW^2 - 348.0r_sT^2W \\
& + 267.0P^2TS + 165000.0r_s^2TW + 517.0PW^2S - 459.0r_sT^2S - 149.0P^2WS \\
& + 0.56r_s^2TS - 21800.0r_sW^2S + 0.505r_s^2WS + 700.0TW^2S - 43.5T^2WS \\
& + 114000.0Pr_sT - 135000.0Pr_sW - 10800.0Pr_sS + 17000.0PTW + 6490.0PTS \\
& - 262000.0r_sTW - 7150.0PWS + 15500.0r_sTS - 13500.0r_sWS - 14700.0TWS \\
& - 19400.0Pr_sTW - 8850.0Pr_sTS + 11100.0Pr_sWS - 2430.0PTWS + 20600.0r_sTWS \\
& + 22000.0
\end{aligned}
$$

$$ \text{(C.7)} $$

P	r_s	T	W	S	Coefficient
0	0	0	0	1	-3.14E+03
0	0	0	1	0	1.61E+05
0	0	0	1	1	-2.29E+04
0	0	0	2	0	-3.94E+05
0	0	0	2	1	5.64E+04
0	0	0	3	0	9.82E+04
0	0	0	3	1	-1.40E+04
0	0	1	0	0	7.48E+04
0	0	1	0	1	-1.07E+04
0	0	1	1	0	1.03E+05
0	0	1	1	1	-1.47E+04
0	0	1	2	0	-4.90E+03
0	0	1	2	1	7.00E+02
0	0	1	3	0	1.52E-02
0	0	2	0	0	2.37E+04
0	0	2	0	1	-3.38E+03
0	0	2	1	0	3.05E+02
0	0	2	1	1	-4.35E+01
0	0	2	2	0	4.30E-02
0	0	3	0	0	-8.14E+03
0	0	3	0	1	1.16E+03
0	0	3	1	0	4.09E-02
0	1	0	0	0	-1.43E+05
0	1	0	0	1	1.69E+04
0	1	0	1	0	-8.92E+04
0	1	0	1	1	-1.35E+04
0	1	0	2	0	6.03E+05
0	1	0	2	1	-2.18E+04
0	1	0	3	0	-1.12E+05
0	1	1	0	0	-1.94E+05
0	1	1	0	1	1.55E+04
0	1	1	1	0	-2.62E+05
0	1	1	1	1	2.06E+04
0	1	1	2	0	5.60E+03
0	1	2	0	0	-2.39E+04
0	1	2	0	1	-4.59E+02
0	1	2	1	0	-3.48E+02
0	1	3	0	0	9.30E+03
0	2	0	0	0	1.35E+05
0	2	0	0	1	-6.48E-01
0	2	0	1	0	-1.08E+05
0	2	0	1	1	5.05E-01
0	2	0	2	0	-1.74E+05

P	r_s	T	W	S	Coefficient
0	2	1	0	0	1.24E+05
0	2	1	0	1	5.60E-01
0	2	1	1	0	1.65E+05
0	2	2	0	0	-3.68E+03
1	0	0	0	0	-3.59E+04
1	0	0	0	1	5.13E+03
1	0	0	1	0	5.00E+04
1	0	0	1	1	-7.15E+03
1	0	0	2	0	-3.62E+03
1	0	0	2	1	5.17E+02
1	0	0	3	0	-1.38E-03
1	0	1	0	0	-4.54E+04
1	0	1	0	1	6.49E+03
1	0	1	1	0	1.70E+04
1	0	1	1	1	-2.43E+03
1	0	1	2	0	4.26E-03
1	0	2	0	0	-5.18E+03
1	0	2	0	1	7.40E+02
1	0	2	1	0	4.88E-03
1	0	3	0	0	-3.86E-03
1	1	0	0	0	1.16E+05
1	1	0	0	1	-1.08E+04
1	1	0	1	0	-1.35E+05
1	1	0	1	1	1.11E+04
1	1	0	2	0	4.14E+03
1	1	1	0	0	1.14E+05
1	1	1	0	1	-8.85E+03
1	1	1	1	0	-1.94E+04
1	1	2	0	0	5.92E+03
1	2	0	0	0	-8.61E+04
1	2	0	0	1	2.05E-01
1	2	0	1	0	8.90E+04
1	2	1	0	0	-7.08E+04
2	0	0	0	0	-8.05E+02
2	0	0	0	1	1.15E+02
2	0	0	1	0	1.04E+03
2	0	0	1	1	-1.49E+02
2	0	0	2	0	-6.28E-04
2	0	1	0	0	-1.87E+03
2	0	1	0	1	2.67E+02
2	0	1	1	0	2.84E-03
2	0	2	0	0	-1.73E-03
2	1	0	0	0	-6.38E+03

P	r_s	T	W	S	Coefficient
2	1	0	0	1	1.04E+03
2	1	0	1	0	-1.19E+03
2	1	1	0	0	2.14E+03
2	2	0	0	0	8.34E+03
3	0	0	0	0	6.31E+02
3	0	0	0	1	-9.01E+01
3	0	0	1	0	9.70E-05
3	0	1	0	0	6.99E-04
3	1	0	0	0	-7.21E+02
0	0	0	0	0	2.20E+04
4	0	0	0	0	4.29E-04
0	0	4	0	0	-9.02E-02

Table C.7: Coefficients for C_{bw} of the root of single lap joints DS (615)

$$
\begin{aligned}
C_{bw2-root-615} = {}& 6.28P - 23.9C_{bw} - 126.0r_s - 27.1T + 30.3W - 9.47C_{bw}P \\
& + 113.0C_{bw}r_s + 59.0C_{bw}T - 12.5Pr_s - 80.7C_{bw}W - 0.205PT + 1.1PW \\
& + 44.4r_sT - 55.5r_sW + 7.96TW + 1.67C_{bw}^2P - 90.2C_{bw}r_s^2 - 13.0C_{bw}^2r_s \\
& + 12.8C_{bw}T^2 + 5.92Pr_s^2 - 10.3C_{bw}^2T + 22.0C_{bw}W^2 - 0.137PT^2 \\
& + 29.4C_{bw}^2W + 0.0468PW^2 - 5.93r_sT^2 - 15.7r_s^2T + 4.98r_sW^2 + 22.7r_s^2W \\
& + 0.23TW^2 - 1.79T^2W - 8.55C_{bw}^2 + 166.0r_s^2 - 69.9r_s^3 + 1.07T^2 \\
& + 1.78T^3 - 5.66W^2 + 8.83C_{bw}Pr_s - 3.32C_{bw}PT - 2.98C_{bw}PW \\
& - 28.0C_{bw}r_sT + 62.9C_{bw}r_sW + 0.817Pr_sT - 49.5C_{bw}TW - 1.11Pr_sW \\
& - 0.106PTW - 2.24r_sTW + 29.7
\end{aligned}
\tag{C.8}
$$

C_{bw}	P	r_s	T	W	Coefficient
0	0	0	0	1	3.03E+01
0	0	0	0	2	-5.66E+00
0	0	0	1	0	-2.71E+01
0	0	0	1	1	7.96E+00
0	0	0	1	2	2.30E-01
0	0	0	2	0	1.07E+00
0	0	0	2	1	-1.79E+00
0	0	1	0	0	-1.26E+02
0	0	1	0	1	-5.55E+01
0	0	1	0	2	4.98E+00
0	0	1	1	0	4.44E+01
0	0	1	1	1	-2.24E+00
0	0	1	2	0	-5.93E+00
0	0	2	0	0	1.66E+02
0	0	2	0	1	2.27E+01
0	0	2	1	0	-1.57E+01
0	1	0	0	0	6.28E+00
0	1	0	0	1	1.10E+00
0	1	0	0	2	4.68E-02
0	1	0	1	0	-2.05E-01
0	1	0	1	1	-1.06E-01
0	1	0	2	0	-1.37E-01
0	1	1	0	0	-1.25E+01
0	1	1	0	1	-1.11E+00
0	1	1	1	0	8.17E-01
0	1	2	0	0	5.92E+00
1	0	0	0	0	-2.39E+01
1	0	0	0	1	-8.07E+01
1	0	0	0	2	2.20E+01
1	0	0	1	0	5.90E+01
1	0	0	1	1	-4.95E+01
1	0	0	2	0	1.28E+01
1	0	1	0	0	1.13E+02
1	0	1	0	1	6.29E+01
1	0	1	1	0	-2.80E+01
1	0	2	0	0	-9.02E+01
1	1	0	0	0	-9.47E+00
1	1	0	0	1	-2.98E+00
1	1	0	1	0	-3.32E+00
1	1	1	0	0	8.83E+00
2	0	0	0	0	-8.55E+00
2	0	0	0	1	2.94E+01
2	0	0	1	0	-1.03E+01

C_{bw}	P	r_s	T	W	Coefficient
2	0	1	0	0	-1.30E+01
2	1	0	0	0	1.67E+00
0	0	0	0	0	2.97E+01
0	0	3	0	0	-6.99E+01
0	0	0	3	0	1.78E+00

Table C.8: Coefficients for C_{bw2} of the root of single lap joints SS (615)

D
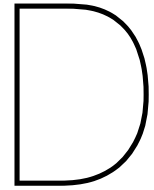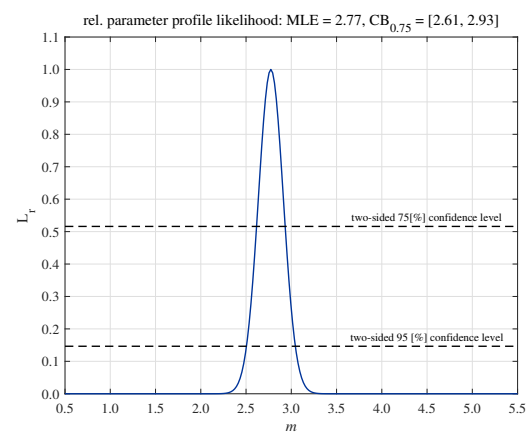
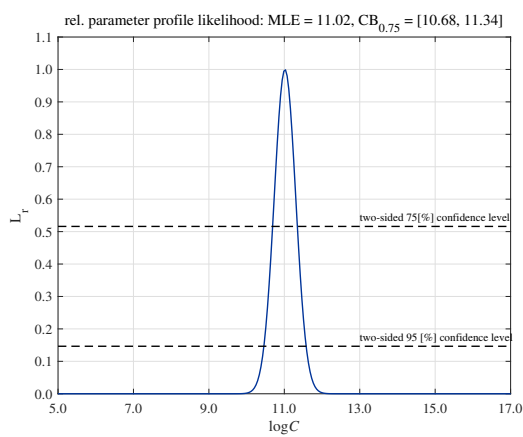# Arc-welded joints fatigue assessment

D.1. NSC

Figure D.1: Likelihood distribution for log(C) with NSC and log(normal)

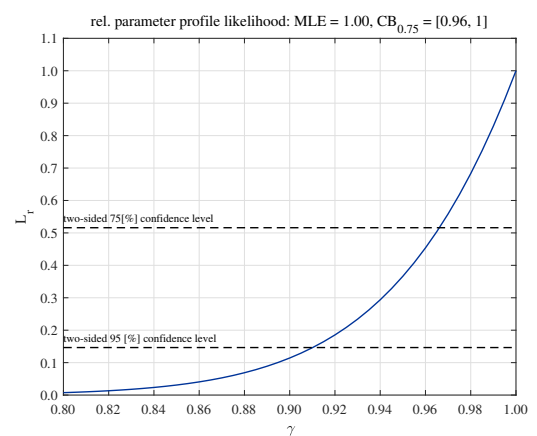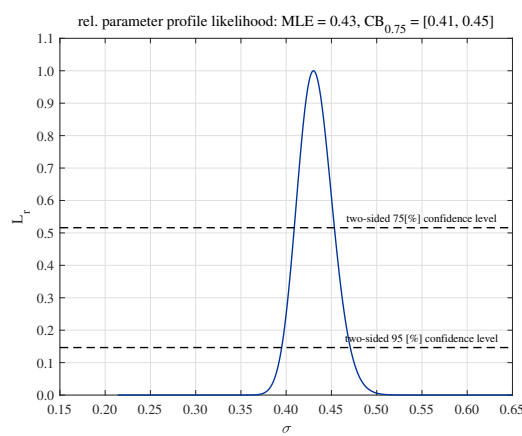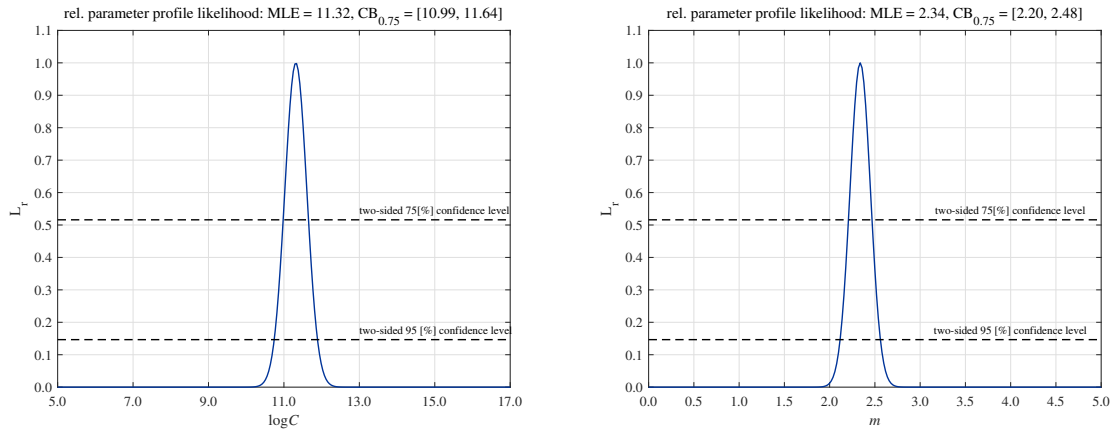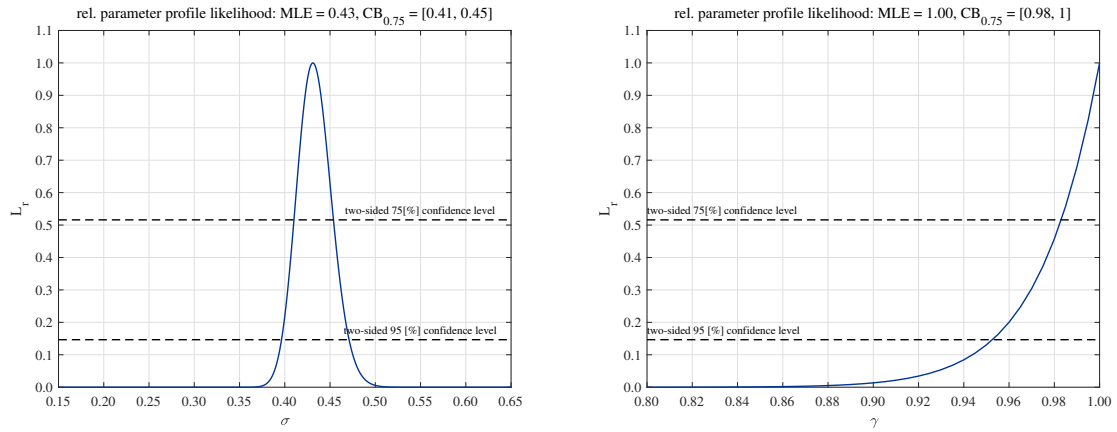Figure D.2: Likelihood distribution for m with NSC and log(normal)

Figure D.3: Likelihood distribution for σ with NSC and log(normal)

Figure D.4: Likelihood distribution for γ with NSC and log(normal)
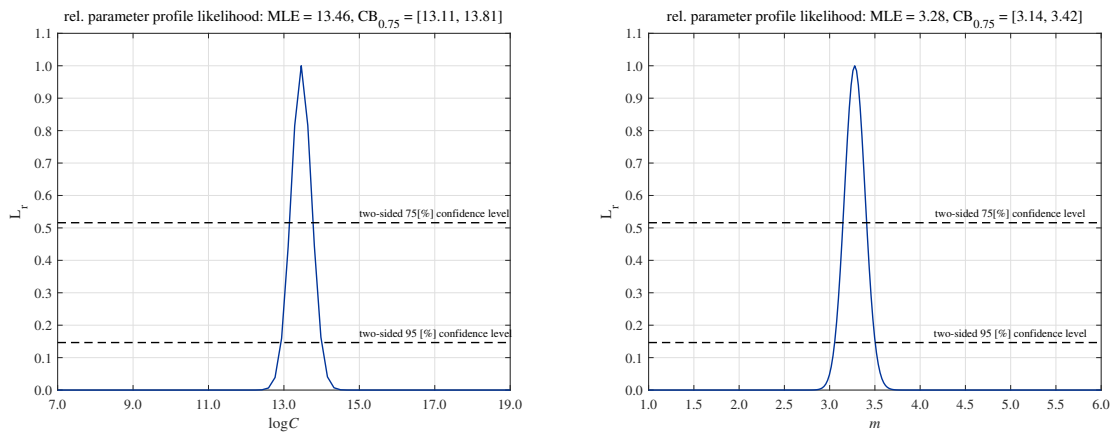
D.2. HSSSC

Figure D.5: Likelihood distribution for log(C) with HSSSC and log(normal)

Figure D.6: Likelihood distribution for m with HSSSC and log(normal)

Figure D.7: Likelihood distribution for σ with HSSSC and log(normal)

Figure D.8: Likelihood distribution for γ with HSSSC and log(normal)

D.3. LENSC

Figure D.9: Likelihood distribution for log(C) with LENSC and log(normal)

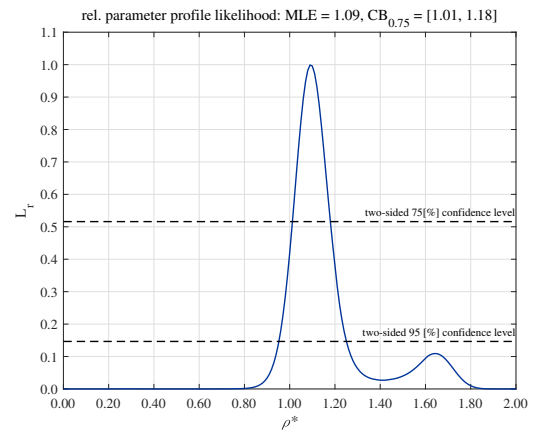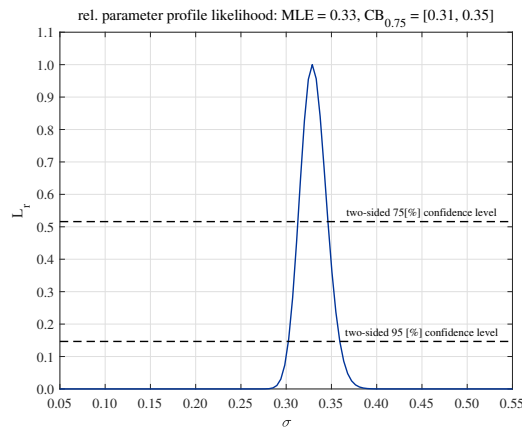Figure D.10: Likelihood distribution for m with LENSC and log(normal)

Figure D.11: Likelihood distribution for σ with LENSC and log(normal)

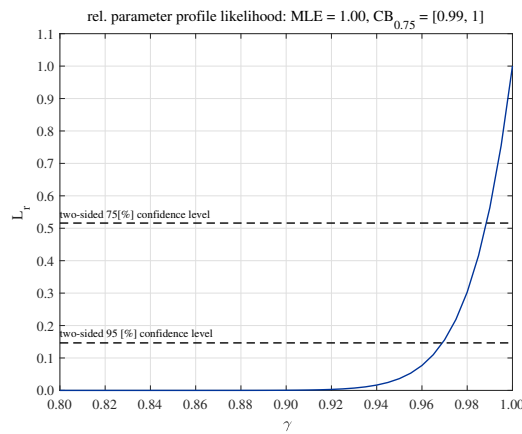Figure D.12: Likelihood distribution for ρ^* with LENSC and log(normal)

Figure D.13: Likelihood distribution for γ with LENSC and log(normal)
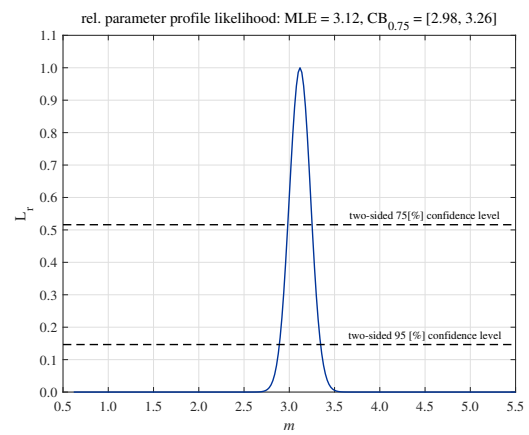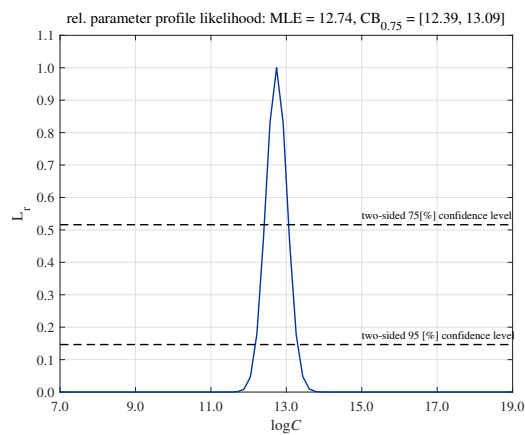
D.4. PENSC

Figure D.14: Likelihood distribution for log(C) with PM and log(normal)

Figure D.15: Likelihood distribution for m with PM and log(normal)
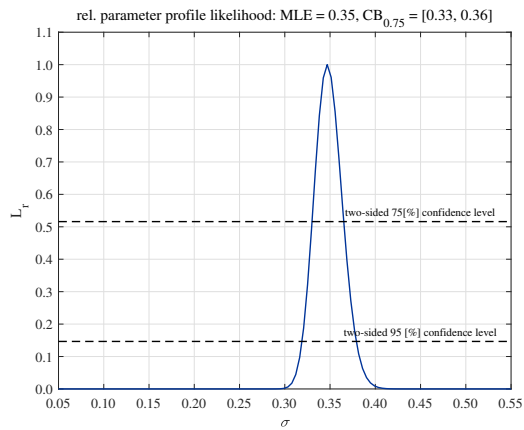
Figure D.16: Likelihood distribution for σ with PM and log(normal)
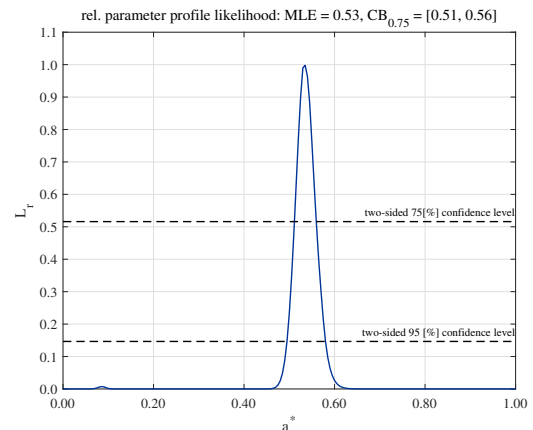

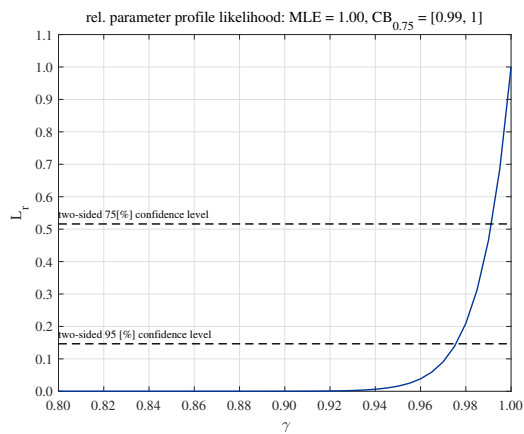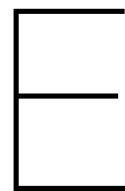Figure D.17: Likelihood distribution for a^* with PM and log(normal)

Figure D.18: Likelihood distribution for γ with PM and log(normal)

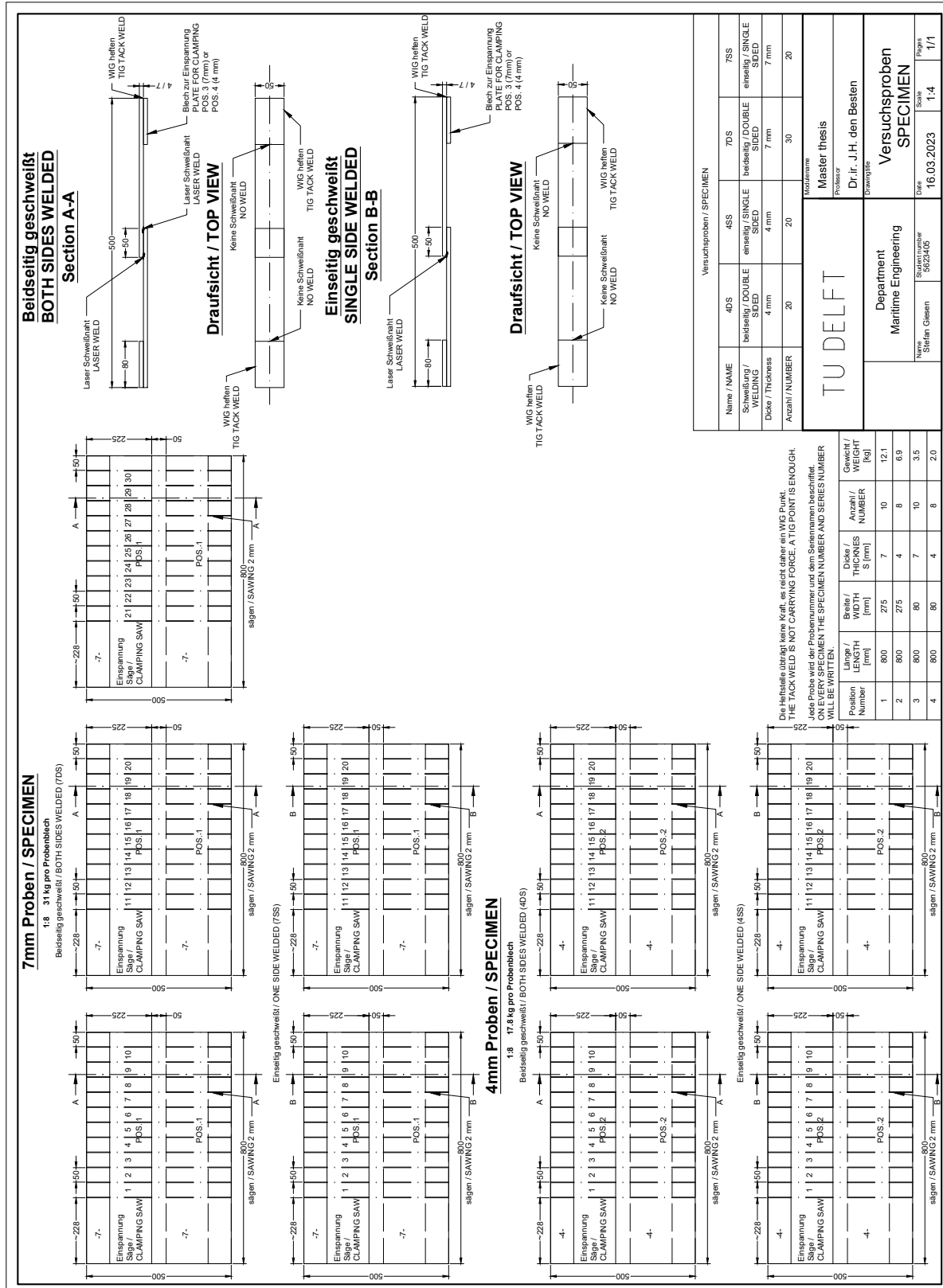# Laser-welded joints fatigue assessment

E.1. Experimental results

Beidseitig geschweißt
BOTH SIDES WELDED
Section A-A

Einseitig geschweißt
SINGLE SIDE WELDED
Section B-B

Draufsicht / TOP VIEW

WIG heften / TIG TACK WELD

Blech zur Einspannung PLATE FOR CLAMPING POS. 3 (7mm) or POS. 4 (4 mm)

Laser Schweißnaht LASER WELD

Keine Schweißnaht NO WELD

7mm Proben / SPECIMEN
1:8   31 kg pro Probenblech
Beidseitig geschweißt / BOTH SIDES WELDED (7DS)

Einseitig geschweißt / ONE SIDE WELDED (7SS)

4mm Proben / SPECIMEN
1:8   17.8 kg pro Probenblech
Beidseitig geschweißt / BOTH SIDES WELDED (4DS)

Einseitig geschweißt / ONE SIDE WELDED (4SS)

Einspannung Säge / CLAMPING SAW

sägen / SAWING 2 mm

Die Heftstelle übträgt keine Kraft, es reicht daher ein WIG Punkt.
THE TACK WELD IS NOT CARRYING FORCE, A TIG POINT IS ENOUGH.

Jede Probe wird der Probennummer und dem Seriennamen beschriftet.
ON EVERY SPECIMEN THE SPECIMEN NUMBER AND SERIES NUMBER WILL BE WRITTEN.

Position Number	Länge / LENGTH [mm]	Breite / WIDTH [mm]	Dicke / THICKNES S [mm]	Anzahl / NUMBER	Gewicht / WEIGHT [kg]
1	800	275	7	10	12.1
2	800	275	4	8	6.9
3	800	80	7	10	3.5
4	800	80	4	8	2.0

Versuchsproben / SPECIMEN

Name / NAME	4DS	4SS	7DS	7SS
Schweißung / WELDING	beidseitig / DOUBLE SIDED	einseitig / SINGLE SIDED	beidseitig / DOUBLE SIDED	einseitig / SINGLE SIDED
Dicke / Thickness	4 mm	4 mm	7 mm	7 mm
Anzahl / NUMBER	20	20	30	20

TU DELFT

Department
Maritime Engineering

Modulename
Master thesis
Professor
Dr.ir. J.H. den Besten

Drawingtitle
Versuchsproben
SPECIMEN

| Name Stefan Giesen | Studentnumber 5623405 | Date 16.03.2023 | Scale 1:4 | Pages 1/1 |

Figure E.1: Drawing test specimen

Name	rl	failure	Sn [Mpa]	cycles []	frequency [Hz]
4 DS I 1	0.1	wt	204	3.40E+04	15
4 DS I 13	0.1	wt	170	4.59E+04	15
4 DS I 2	0.1	wt	80	4.87E+05	15
4 DS I 12	0.1	nd	40	9.15E+06	15
4 DS I 3	0.1	wt	60	1.23E+06	20
4 DS I 11	0.1	wt	50	5.77E+06	20
4 DS I 4	0.1	wt	150	6.78E+04	20
4 DS I 10	0.1	wt	150	7.20E+04	20
4 DS I 5	0.1	wt	150	6.84E+04	20
4 DS I 9	0.1	wt	55	2.50E+06	20
4 DS I 6	0.1	wt	90	2.82E+05	20
4 DS I 8	0.1	wt	90	3.26E+05	25
4 DS I 7	0.1	wt	55	1.64E+06	25
4 DS II 1	0.1	wt	55	9.14E+05	25
4 DS II 13	0.1	wt	90	2.85E+05	20
7 DS I 1	0.1	wt	90	1.75E+05	20
7 DS I 13	0.1	wt	70	3.07E+05	20
7 DS I 2	0.1	wt	70	4.29E+05	20
7 DS I 12	0.1	wt	120	6.25E+04	20
7 DS I 3	0.1	wt	120	6.17E+04	20
7 DS I 11	0.1	nd	35	1.00E+07	25
7 DS I 4	0.1	wt	120	6.25E+04	20
7 DS I 10	0.1	wt	70	3.41E+05	20
7 DS I 5	0.1	wt	50	1.88E+06	25
7 DS I 9	0.1	wt	50	1.12E+06	20
7 DS I 6	0.1	nd	50	4.85E+06	20
7 DS I 8	0.5	wt	70	3.02E+05	20
7 DS II 1	0.5	wt	115	9.19E+04	20
7 DS II 13	0.5	wt	115	8.74E+04	20
7 DS II 2	0.5	wt	70	2.73E+05	20
7 DS II 12	0.5	wt	70	2.54E+05	20
7 DS II 3	0.5	wt	115	9.12E+04	20
7 DS II 11	0.5	wt	45	9.89E+05	20
7 DS II 4	0.5	wt	45	1.03E+06	20
7 DS II 10	0.5	wt	45	1.08E+06	20
7 SS I 1	0.5	wt	55	3.82E+05	15
7 SS I 9	0.5	wt	90	7.13E+04	15
7 SS I 2	0.5	wt	30	6.17E+06	20
7 SS I 8	0.5	wt	55	3.52E+05	20
7 SS I 3	0.5	wr	90	7.61E+04	15
7 SS I 7	0.5	wt	35	1.92E+06	20
7 SS I 4	0.5	wt	35	1.56E+06	20
7 SS I 6	0.1	wt	55	5.29E+05	20

Table E.1: Experimental fatigue resistance data of laser-welded lap joints Part I

Name	rl	failure	Sn [Mpa]	cycles []	frequency [Hz]
7 SS I 5	0.1	wt	55	5.46E+05	20
7 SS II 11	0.1	wt	40	2.11E+06	20
7 SS II 1	0.1	wt	40	1.40E+06	20
7 SS II 10	0.1	wt	95	6.84E+04	15
7 SS II 2	0.1	wt	95	8.08E+04	15
7 DS II 5	-1	wt	125	2.02E+05	15
7 DS II 9	-1	wt	105	4.31E+05	15
7 DS II 6	-1	wt	160	7.15E+04	15
7 DS II 7	-1	wt	160	6.51E+04	15
7 DS I 7	-1	wt	160	9.75E+04	15
7 DS II 8	-1	wt	80	7.78E+05	15
7 DS III 1	-1	wt	70	3.93E+06	18
7 DS III 13	-1	wt	105	3.76E+05	18
7 DS III 2	-1	wt	80	2.07E+06	18
7 DS III 12	-1	wt	105	4.51E+05	18
7 DS III 3	-1	wt	80	1.83E+06	18
4 DS II 2	0.5	wt	85	3.39E+05	20
4 DS II 12	0.5	wt	145	1.39E+05	20
4 DS II 3	0.5	wt	50	2.79E+06	20
4 DS II 11	0.5	wt	50	3.01E+06	20
4 DS II 4	0.5	wt	85	4.15E+05	20
4 DS II 10	0.5	wt	145	1.32E+05	20
4 DS II 5	0.5	wt	85	3.82E+05	20
4 DS II 9	0.5	wt	145	1.27E+05	20
4 SS I 1	0.5	wr	65	3.10E+05	20
4 SS I 10	0.5	wr	100	8.79E+04	20
4 DS II 6	0.5	wt	50	2.54E+06	20
4 SS I 2	0.5	wr	65	2.99E+05	20
4 SS I 9	0.5	wr	100	7.15E+04	20
4 SS I 3	0.5	wr	40	1.41E+06	20
4 SS I 8	0.5	wr	40	1.14E+06	20
4 SS I 4	0.1	wr	75	2.53E+05	20
4 SS I 7	0.1	wr	115	5.26E+04	20
4 SS I 5	0.1	wr	115	5.45E+04	20
4 SS I 6	0.1	wr	75	1.92E+05	20
4 SS II 1	0.1	wt	45	1.31E+06	20
4 SS II 7	0.1	wr	45	1.54E+06	20
7 SS I 2	0.5	wt	30	6.17E+06	20
7 SS I 8	0.5	wt	55	3.52E+05	20
7 SS I 3	0.5	wr	90	7.61E+04	15
7 SS I 7	0.5	wt	35	1.92E+06	20
7 SS I 4	0.5	wt	35	1.56E+06	20
7 SS I 6	0.1	wt	55	5.29E+05	20

Table E.2: Experimental fatigue resistance data of laser-welded lap joints Part II

Name	rl	failure	Sn [Mpa]	cycles []	frequency [Hz]
7 SS I 5	0.1	wt	55	5.46E+05	20
7 SS II 11	0.1	wt	40	2.11E+06	20
7 SS II 1	0.1	wt	40	1.40E+06	20
7 SS II 10	0.1	wt	95	6.84E+04	15
7 SS II 2	0.1	wt	95	8.08E+04	15
7 DS II 5	-1	wt	125	2.02E+05	15
7 DS II 9	-1	wt	105	4.31E+05	15
7 DS II 6	-1	wt	160	7.15E+04	15
7 DS II 7	-1	wt	160	6.51E+04	15
7 DS I 7	-1	wt	160	9.75E+04	15
7 DS II 8	-1	wt	80	7.78E+05	15
7 DS III 1	-1	wt	70	3.93E+06	18
7 DS III 13	-1	wt	105	3.76E+05	18
7 DS III 2	-1	wt	80	2.07E+06	18

Table E.3: Experimental fatigue resistance data of laser-welded lap joints Part III

E.2. FE-model validation
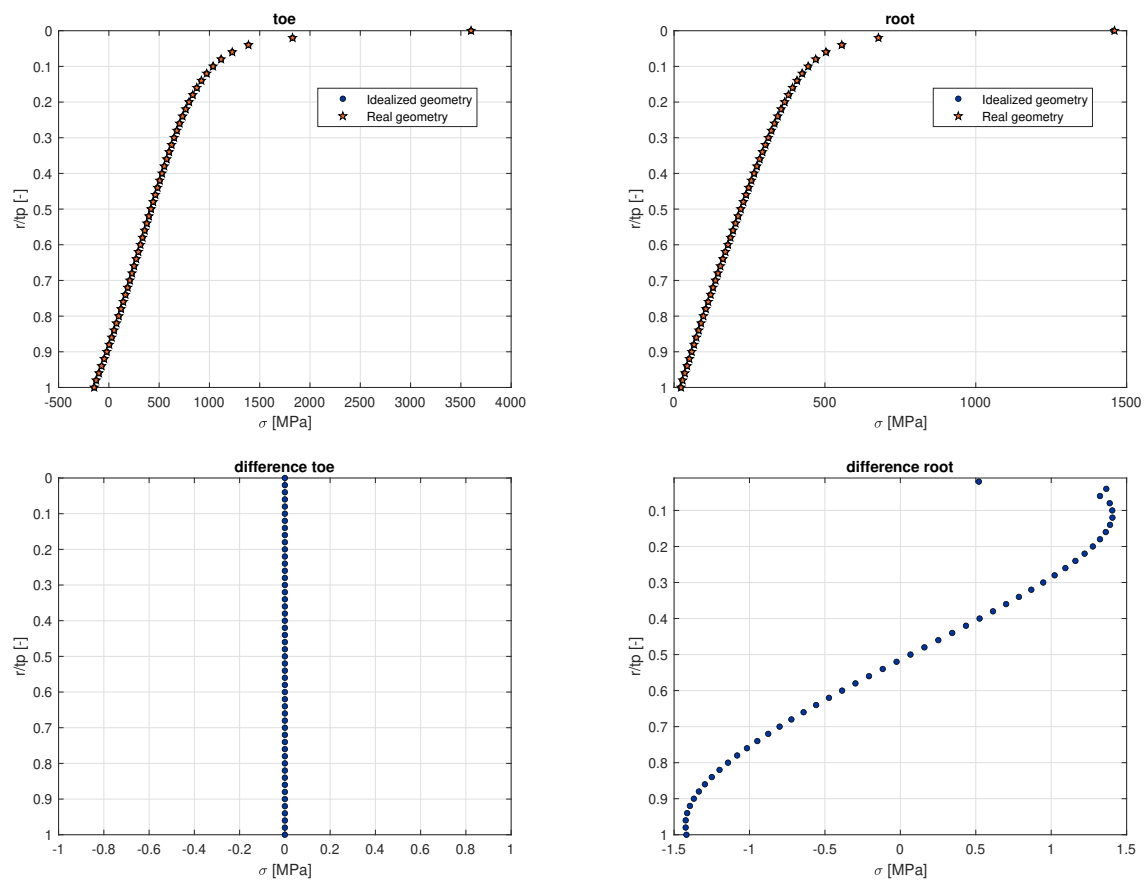
Figure E.2: Weld notch stress distribution for 4 DS series with $\sigma_n = 500 MPa$
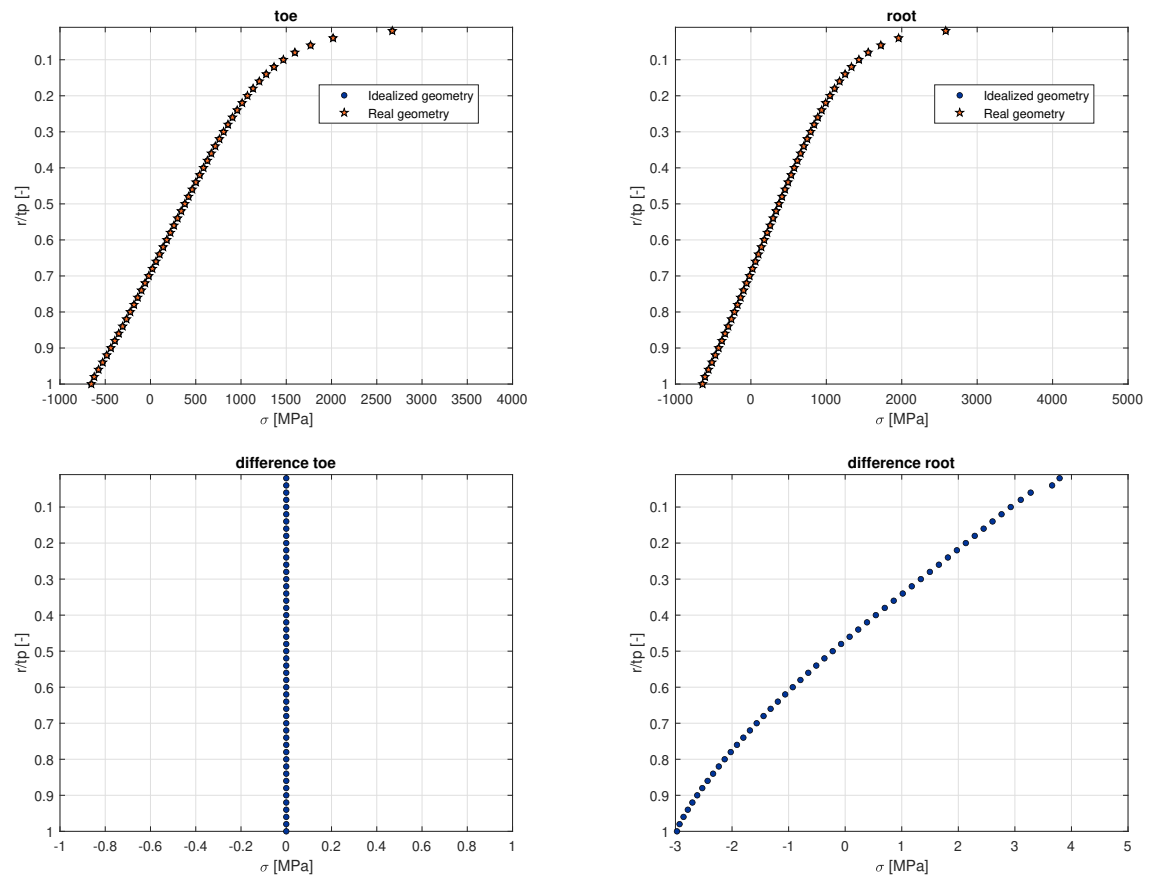
Figure E.3: Weld notch stress distribution for 4 SS series with $\sigma_n = 500MPa$
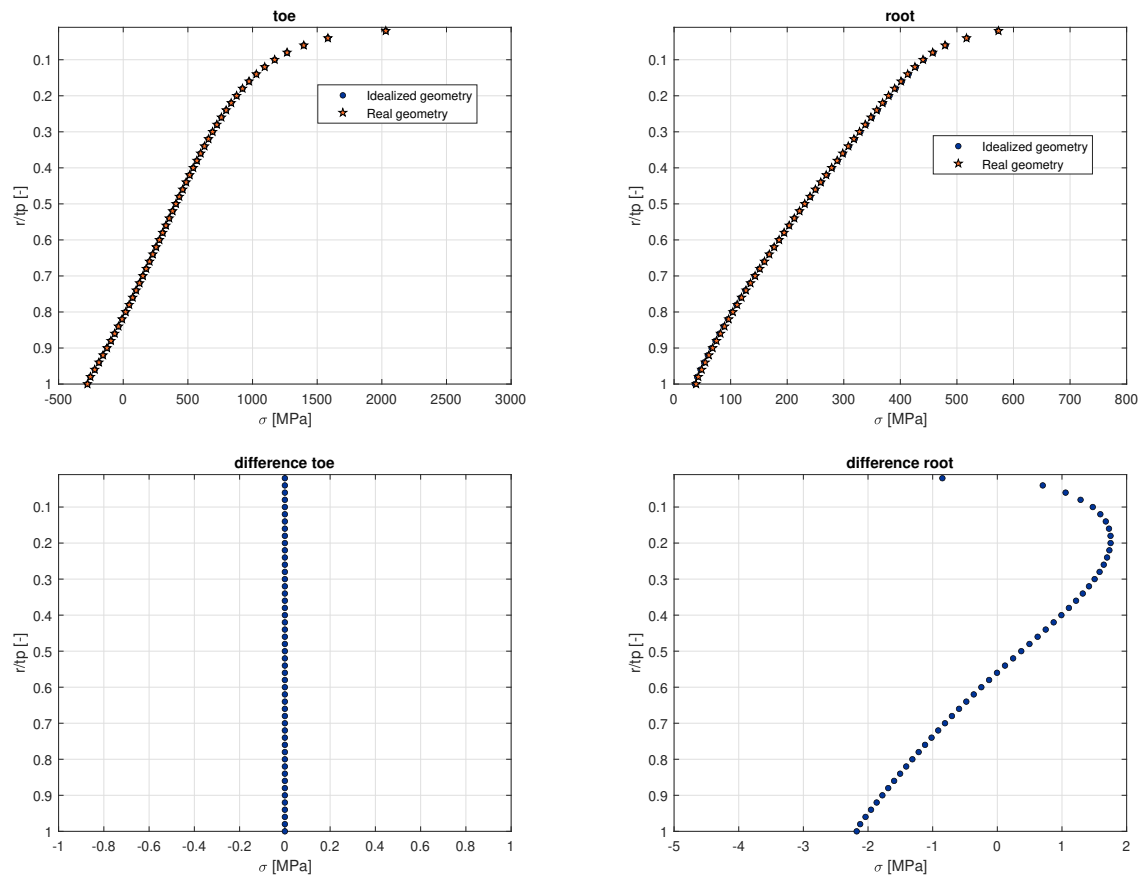
Figure E.4: Weld notch stress distribution for 7 DS series with $\sigma_n = 500 MPa$
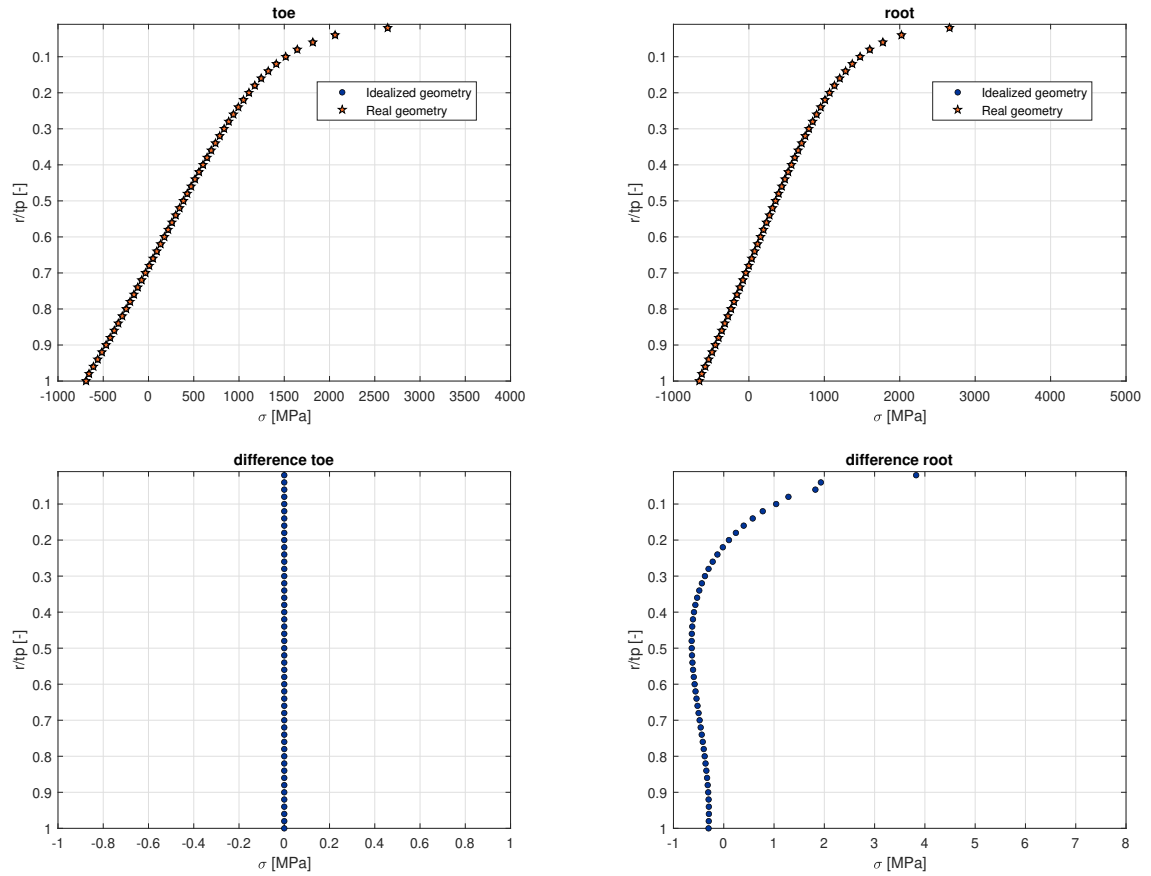
Figure E.5: Weld notch stress distribution for 7 SS series with $\sigma_n = 500 MPa$

E.3. NSC
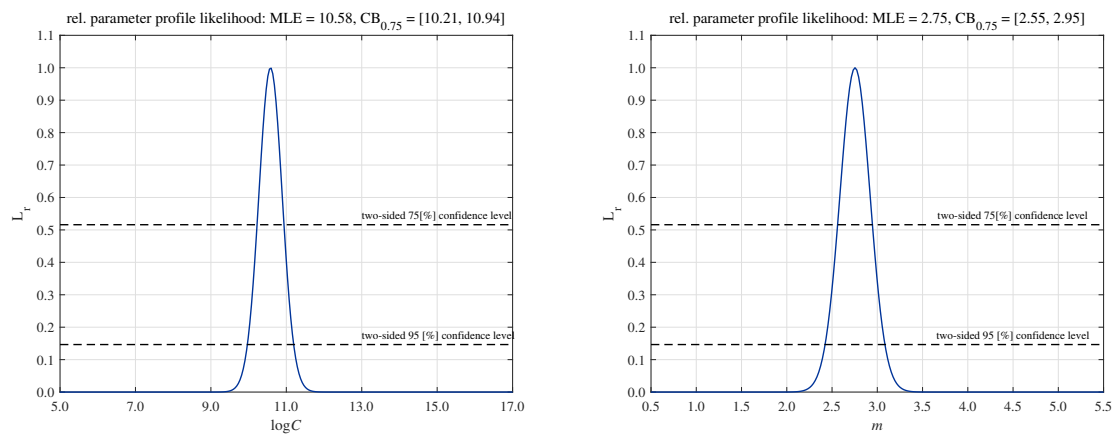
Figure E.6: Likelihood distribution for log(C) with NSC and log(normal)

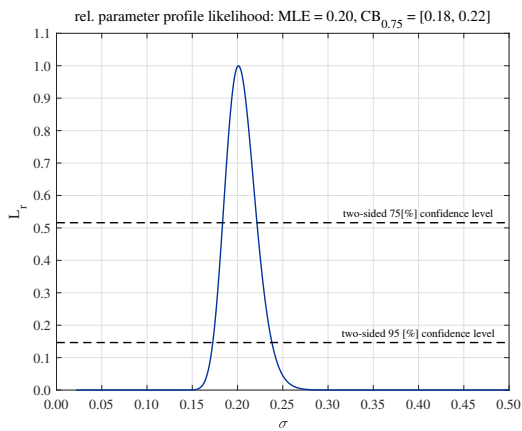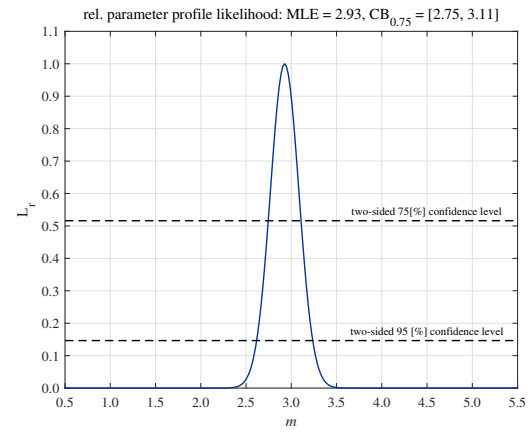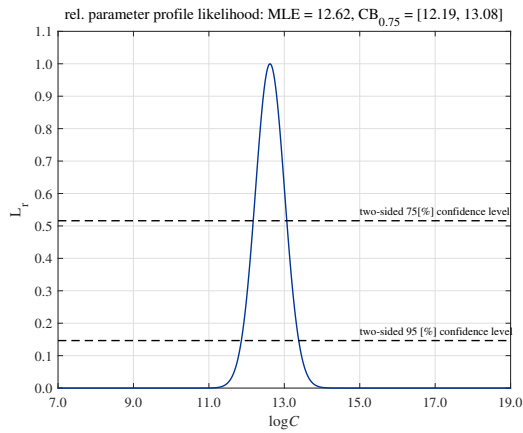Figure E.7: Likelihood distribution for m with NSC and log(normal)
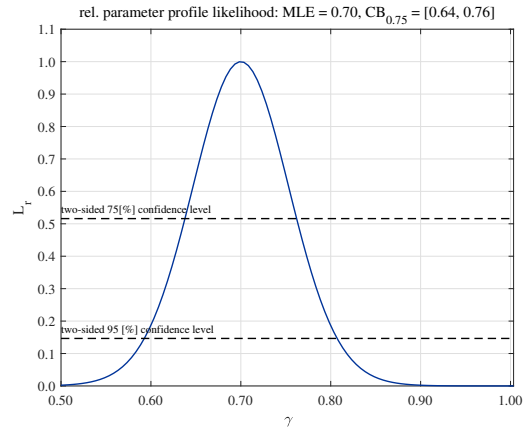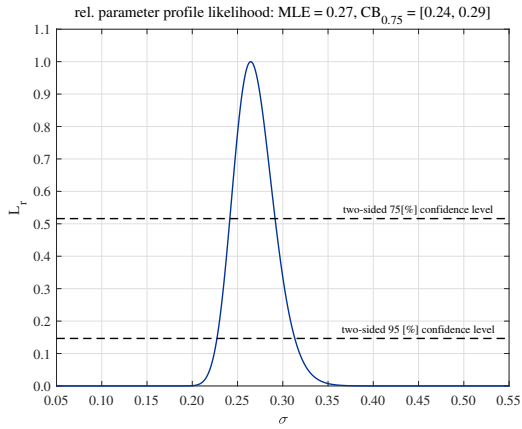
Figure E.8: Likelihood distribution for σ with NSC and log(normal)

Figure E.9: Likelihood distribution for γ with NSC and log(normal)

E.4. HSSSC
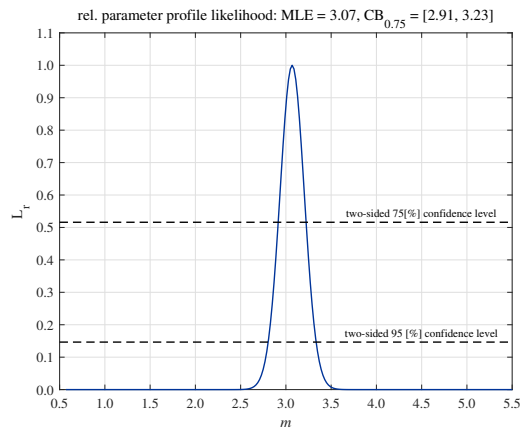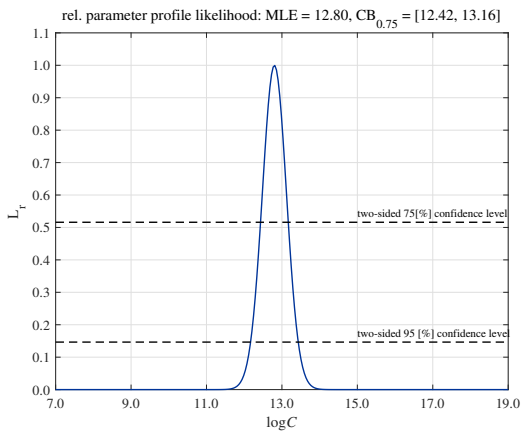
Figure E.10: Likelihood distribution for log(C) with HSSSC and log(normal)

Figure E.11: Likelihood distribution for m with HSSSC and log(normal)
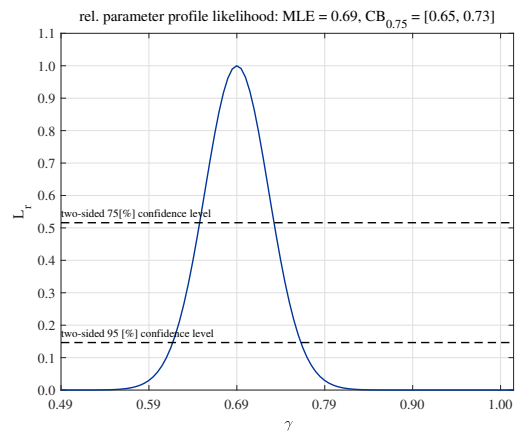
Figure E.12: Likelihood distribution for σ with HSSSC and log(normal)

Figure E.13: Likelihood distribution for γ with HSSSC and log(normal)

E.5. LENSC

Figure E.14: Likelihood distribution for log(C) with LENSC and log(normal)

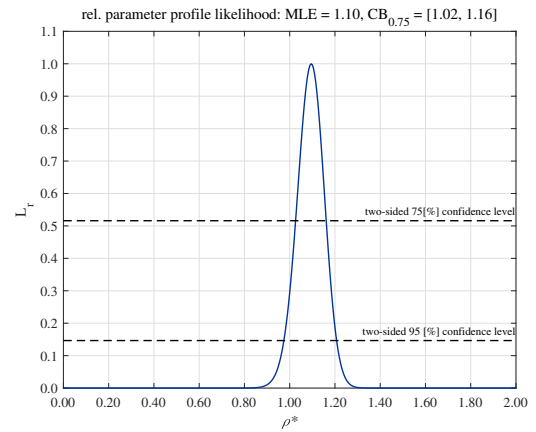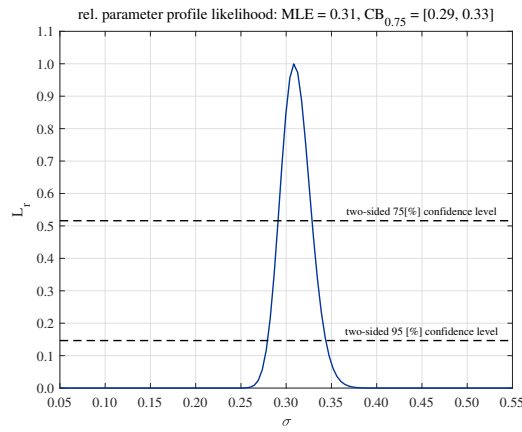Figure E.15: Likelihood distribution for m with LENSC and log(normal)

Figure E.16: Likelihood distribution for σ with LENSC and log(normal)

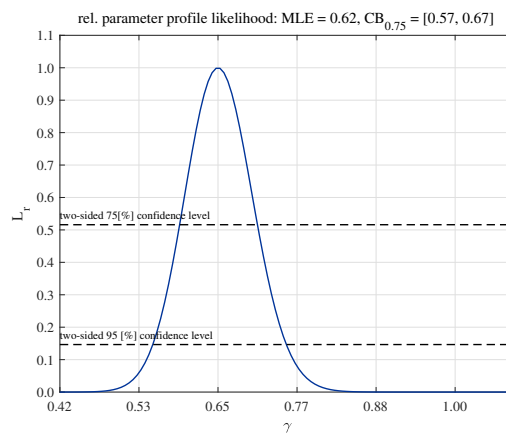Figure E.17: Likelihood distribution for ρ^* with LENSC and log(normal)

Figure E.18: Likelihood distribution for γ with LENSC and log(normal)

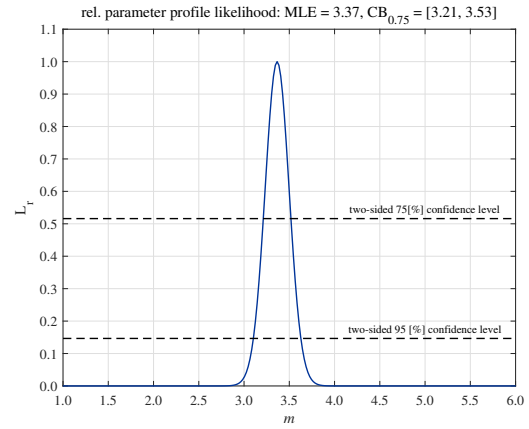Figure E.19: Likelihood distribution for for log(C) with LENSC and log(normal) of experimental data

Figure E.20: Likelihood distribution for m with LENSC and log(normal) of experimental data
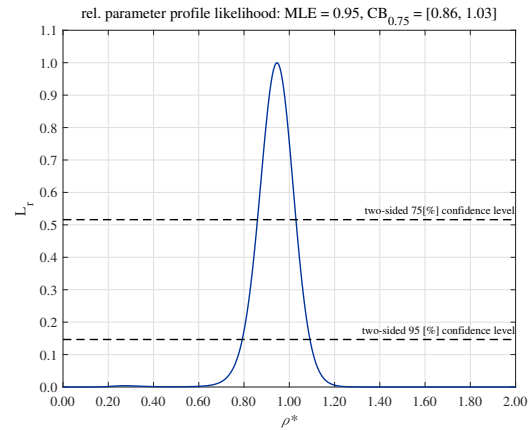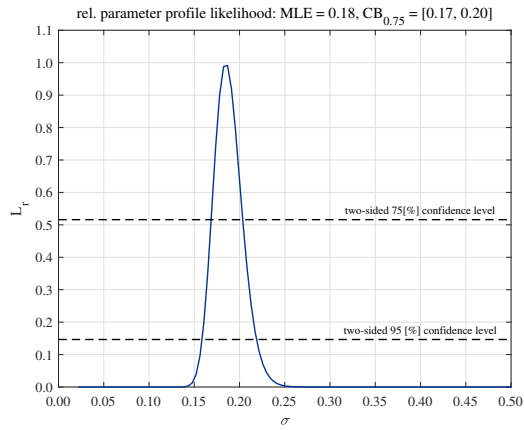
Figure E.21: Likelihood distribution for σ with LENSC and log(normal) of experimental data

Figure E.22: Likelihood distribution for ρ^* with LENSC and log(normal) of experimental data

Figure E.23: Likelihood distribution for γ with LENSC and log(normal) of experimental data
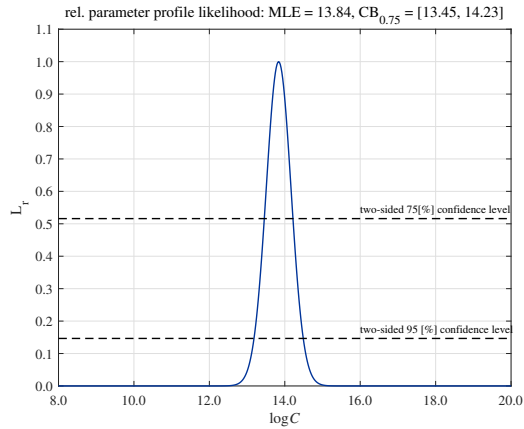
E.6. PENSC

Figure E.24: Likelihood distribution for log(C) with PENSC and log(normal)

Figure E.25: Likelihood distribution for m with PENSC and log(normal)
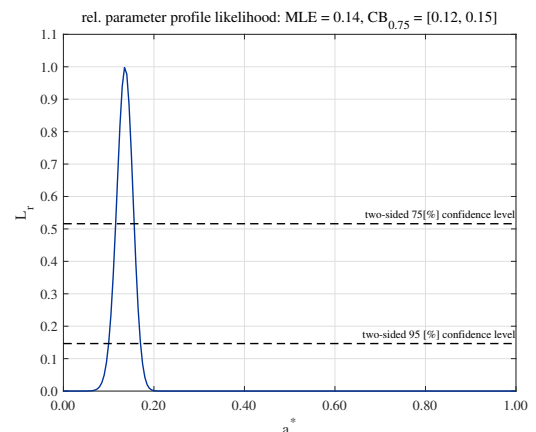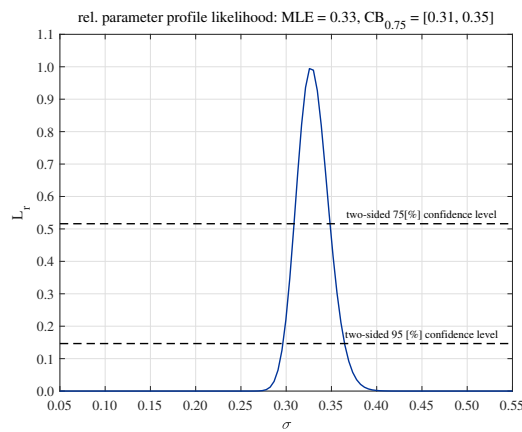
Figure E.26: Likelihood distribution for σ with PENSC and log(normal)

Figure E.27: Likelihood distribution for a^* with PENSC and log(normal)
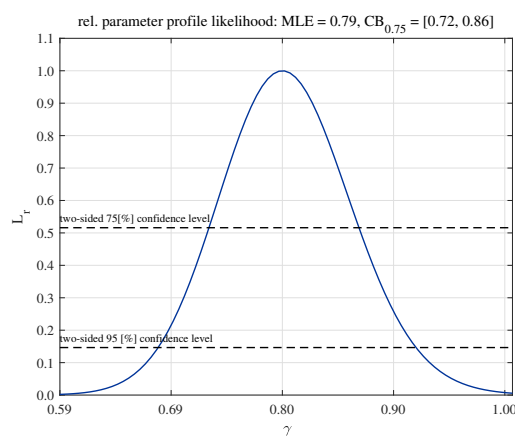
Figure E.28: Likelihood distribution for γ with PENSC and log(normal)
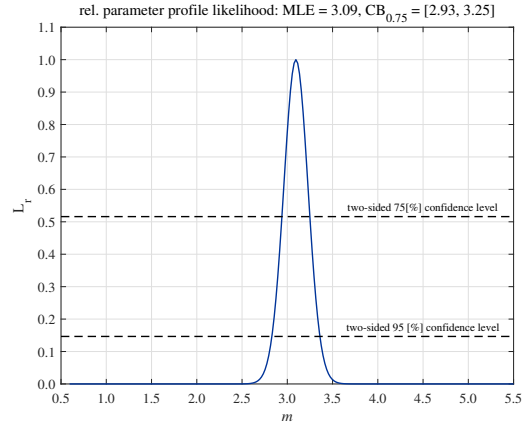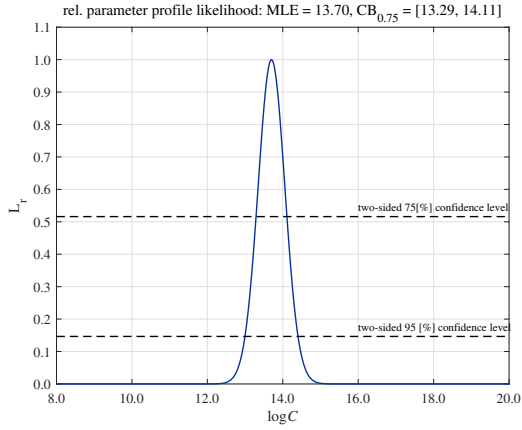
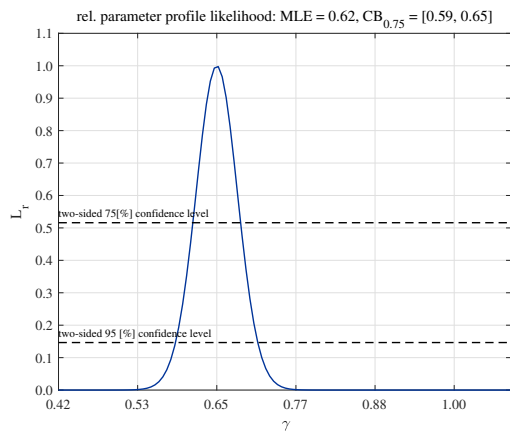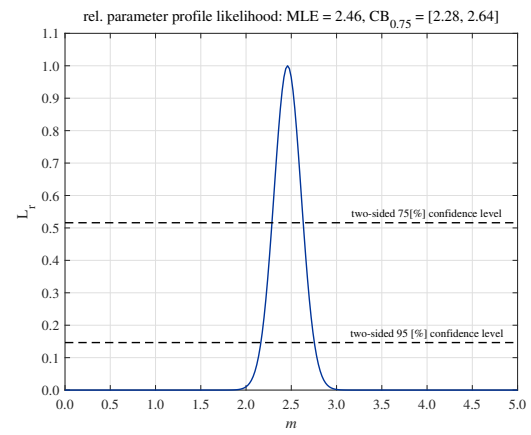Figure E.29: Likelihood distribution for log(C) with PENSC and log(normal) of experimental data

Figure E.30: Likelihood distribution for m with PENSC and log(normal) of experimental data
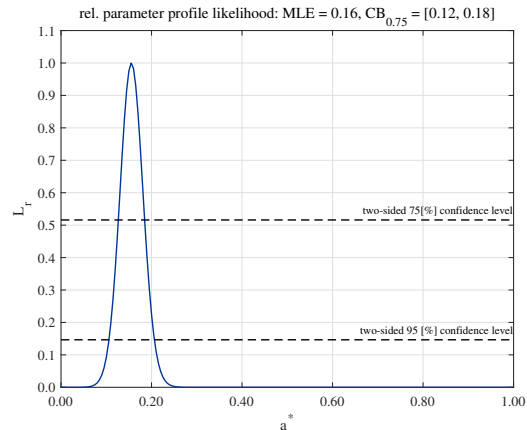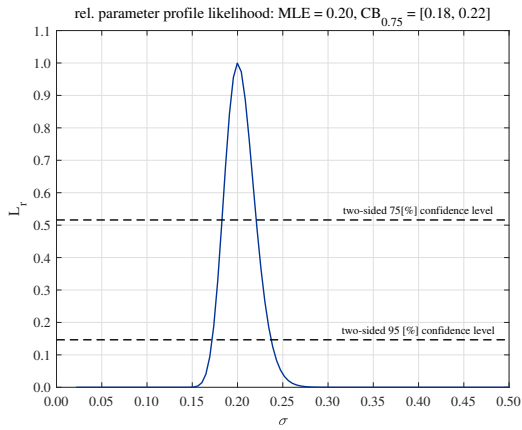
Figure E.31: Likelihood distribution for σ with PENSC and log(normal) of experimental data

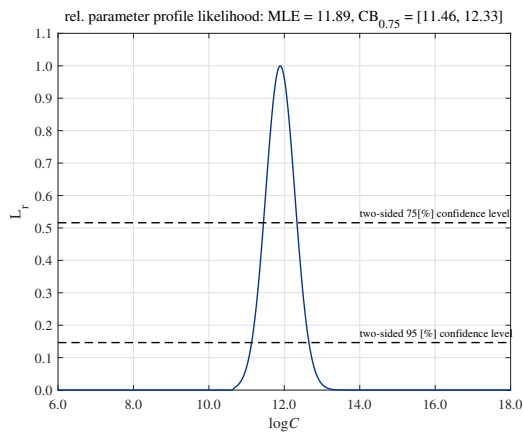Figure E.32: Likelihood distribution for a^* with PENSC and log(normal) of experimental data
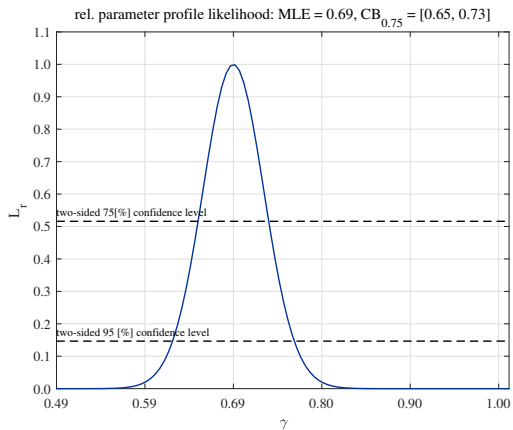
Figure E.33: Likelihood distribution for γ with PENSC and log(normal) of experimental data

F

Beam/shell model

Version 1

Version 2

Version 3

According to Turlier et al., 2014

Figure F.1: Weld geometries of unaccurate beam models

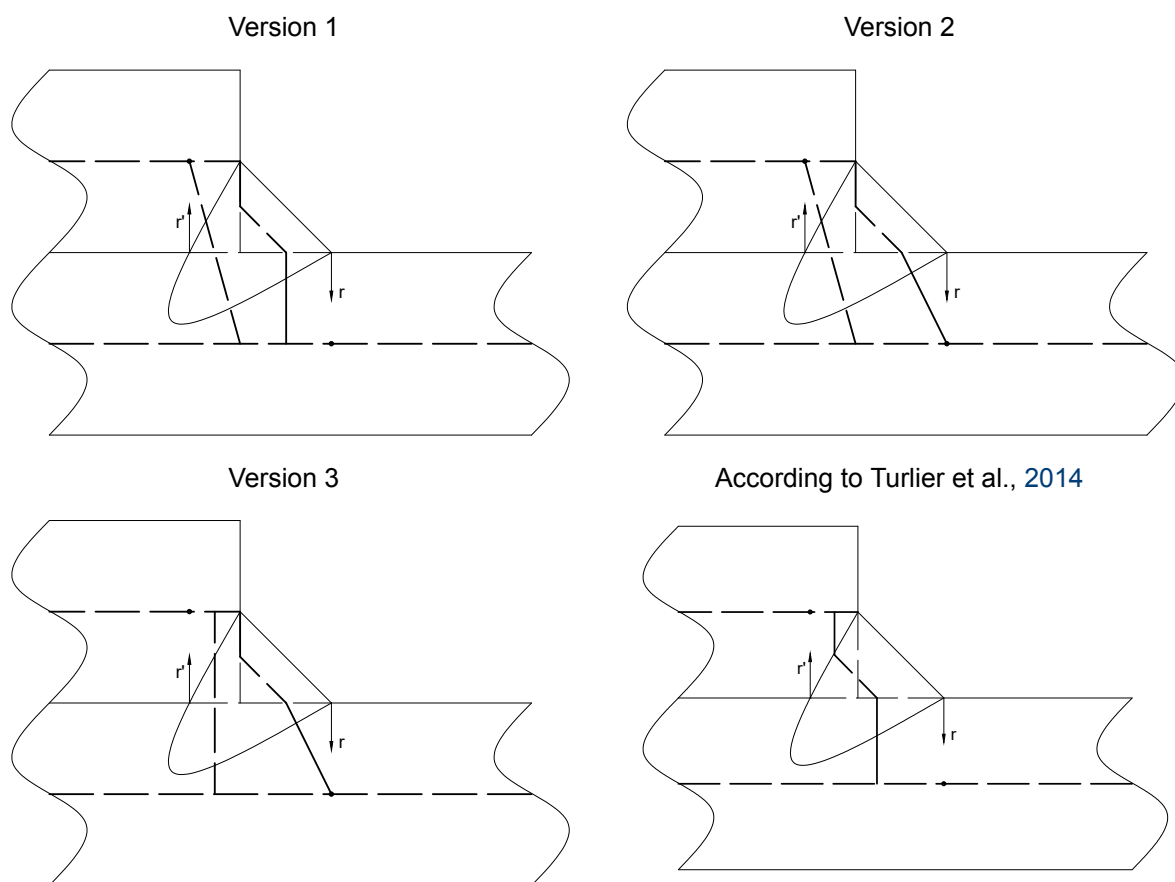| geometry	σn [Mpa]	toe				root			
		σm [-]	σb [-]	σs [-]	rs [-]	σm [-]	σb [-]	σs [-]	rs [-]
614 laser	1	0.00%	-0.47%	-0.33%	-0.14%	0.00%	46.53%	15.52%	26.85%
	100	0.00%	-1.40%	-0.93%	-0.48%	0.00%	34.52%	14.74%	17.23%
	200	0.00%	-1.76%	-1.13%	-0.64%	-0.01%	30.31%	14.19%	14.12%
	300	-0.01%	-2.35%	-1.47%	-0.89%	-0.06%	28.94%	14.15%	12.95%
	400	0.01%	-3.32%	-2.02%	-1.32%	-0.02%	29.05%	14.59%	12.61%
615 laser	1	0.00%	-0.13%	-0.09%	-0.03%	0.00%	-0.01%	-0.01%	0.00%
	100	-0.01%	-0.22%	-0.17%	-0.06%	-0.01%	-0.57%	-0.43%	-0.14%
	200	0.00%	-0.38%	-0.28%	-0.10%	0.00%	-0.93%	-0.69%	-0.24%
	300	0.01%	-0.53%	-0.39%	-0.14%	0.01%	-1.22%	-0.90%	-0.32%
	400	0.02%	-0.65%	-0.47%	-0.18%	0.02%	-1.48%	-1.08%	-0.40%
614 arc	1	0.00%	-2.72%	-1.70%	-1.04%	0.00%	10.67%	4.78%	5.63%
	100	0.00%	-3.32%	-2.04%	-1.31%	0.00%	10.99%	5.04%	5.66%
	200	0.00%	-3.85%	-2.33%	-1.56%	0.00%	11.17%	5.22%	5.65%
	300	0.00%	-4.32%	-2.58%	-1.79%	0.00%	11.27%	5.36%	5.62%
	400	0.00%	-4.75%	-2.79%	-2.01%	0.00%	11.32%	5.45%	5.57%
615 arc	1	0.00%	0.06%	0.04%	0.02%	0.00%	-0.17%	-0.13%	-0.04%
	100	0.00%	-0.24%	-0.17%	-0.06%	0.00%	-0.90%	-0.67%	-0.23%
	200	0.01%	-0.61%	-0.45%	-0.17%	0.01%	-1.31%	-0.96%	-0.35%
	300	0.06%	-0.65%	-0.46%	-0.19%	0.05%	-1.46%	-1.06%	-0.41%
	400	0.21%	1.49%	1.13%	0.35%	0.18%	0.29%	0.26%	0.03%
	Average	0.02%	1.66%	1.05%	0.62%	0.02%	11.66%	5.26%	5.70%

Table F.1: Bar model to capture far field stress version 1

geometry	σn [Mpa]	toe				root			
		σm [-]	σb [-]	σs [-]	rs [-]	σm [-]	σb [-]	σs [-]	rs [-]
614 laser	1	0.00%	-0.44%	-0.31%	-0.13%	0.00%	43.85%	14.62%	25.50%
	100	0.00%	-1.07%	-0.71%	-0.36%	0.00%	32.29%	13.79%	16.26%
	200	0.00%	-1.16%	-0.74%	-0.42%	-0.01%	28.16%	13.18%	13.23%
	300	-0.01%	-1.50%	-0.94%	-0.57%	-0.06%	26.75%	13.08%	12.09%
	400	0.01%	-2.26%	-1.37%	-0.90%	-0.02%	26.80%	13.46%	11.75%
615 laser	1	0.00%	0.08%	0.06%	0.02%	0.00%	-0.19%	-0.14%	-0.05%
	100	-0.01%	0.14%	0.10%	0.04%	-0.01%	-0.89%	-0.67%	-0.22%
	200	0.00%	0.10%	0.07%	0.03%	0.00%	-1.36%	-1.01%	-0.35%
	300	0.00%	0.05%	0.04%	0.01%	0.00%	-1.73%	-1.28%	-0.46%
	400	0.02%	0.01%	0.01%	0.00%	0.01%	-2.05%	-1.51%	-0.55%
614 arc	1	0.00%	-1.04%	-0.65%	-0.39%	0.00%	6.99%	3.13%	3.74%
	100	0.00%	-0.33%	-0.20%	-0.13%	0.00%	5.63%	2.58%	2.97%
	200	0.00%	0.36%	0.22%	0.14%	0.00%	4.48%	2.10%	2.34%
	300	0.00%	1.04%	0.62%	0.42%	0.00%	3.48%	1.65%	1.80%
	400	0.00%	1.69%	1.00%	0.69%	0.00%	2.60%	1.25%	1.33%
615 arc	1	0.00%	0.96%	0.70%	0.26%	0.00%	-0.92%	-0.70%	-0.23%
	100	0.00%	1.88%	1.38%	0.50%	0.00%	-2.76%	-2.05%	-0.72%
	200	0.01%	2.33%	1.71%	0.61%	0.01%	-3.88%	-2.86%	-1.05%
	300	0.05%	2.97%	2.18%	0.77%	0.04%	-4.58%	-3.34%	-1.28%
	400	0.20%	5.78%	4.23%	1.49%	0.17%	-3.33%	-2.37%	-0.98%
	Average	0.02%	1.26%	0.86%	0.39%	0.02%	10.14%	4.74%	4.85%

Table F.2: Bar model to capture far field stress version 2

geometry	σn [Mpa]	toe				root			
		σm [-]	σb [-]	σs [-]	rs [-]	σm [-]	σb [-]	σs [-]	rs [-]
614 laser	1	0.00%	-0.43%	-0.30%	-0.13%	0.00%	0.18%	0.06%	0.12%
	100	0.00%	-0.87%	-0.58%	-0.30%	0.00%	0.11%	0.05%	0.06%
	200	0.00%	-0.76%	-0.49%	-0.27%	-0.01%	-0.69%	-0.33%	-0.36%
	300	-0.01%	-0.90%	-0.56%	-0.34%	-0.06%	-0.81%	-0.43%	-0.38%
	400	0.01%	-1.46%	-0.89%	-0.58%	-0.02%	-0.34%	-0.18%	-0.16%
615 laser	1	0.00%	1.05%	0.77%	0.28%	0.00%	-1.03%	-0.78%	-0.25%
	100	-0.01%	1.85%	1.36%	0.49%	-0.01%	-2.42%	-1.81%	-0.62%
	200	0.00%	2.36%	1.73%	0.61%	0.00%	-3.40%	-2.52%	-0.90%
	300	0.00%	2.75%	2.02%	0.71%	0.00%	-4.17%	-3.08%	-1.12%
	400	0.02%	3.09%	2.27%	0.80%	0.01%	-4.83%	-3.56%	-1.32%
614 arc	1	0.00%	-1.09%	-0.68%	-0.41%	0.00%	0.97%	0.43%	0.54%
	100	0.00%	-0.42%	-0.26%	-0.16%	0.00%	-0.36%	-0.17%	-0.20%
	200	0.00%	0.22%	0.14%	0.09%	0.00%	-1.50%	-0.70%	-0.80%
	300	0.00%	0.85%	0.51%	0.34%	0.00%	-2.49%	-1.18%	-1.32%
	400	0.00%	1.46%	0.86%	0.60%	0.00%	-3.36%	-1.62%	-1.77%
615 arc	1	0.00%	1.39%	1.01%	0.37%	0.00%	-1.28%	-0.97%	-0.32%
	100	0.00%	2.80%	2.05%	0.73%	0.00%	-3.64%	-2.70%	-0.96%
	200	0.01%	3.56%	2.61%	0.93%	0.01%	-5.09%	-3.75%	-1.39%
	300	0.05%	4.45%	3.26%	1.15%	0.04%	-6.05%	-4.42%	-1.70%
	400	0.20%	7.51%	5.48%	1.92%	0.17%	-5.05%	-3.62%	-1.49%
	Average	0.02%	1.96%	1.39%	0.56%	0.02%	2.39%	1.62%	0.79%

Table F.3: Bar model to capture far field stress version 3

geometry	σn [Mpa]	toe				root			
		σm [-]	σb [-]	σs [-]	rs [-]	σm [-]	σb [-]	σs [-]	rs [-]
614 laser	1	0.00%	-1.71%	-1.20%	-0.52%	-9.85%	-68.06%	-29.26%	-54.85%
	100	0.00%	-5.50%	-3.65%	-1.92%	-11.40%	-51.37%	-28.47%	-32.02%
	200	0.00%	-7.71%	-4.93%	-2.92%	-12.51%	-45.50%	-27.96%	-24.34%
	300	-0.01%	-9.61%	-5.99%	-3.85%	-13.52%	-41.48%	-27.23%	-19.58%
	400	0.01%	-11.53%	-7.04%	-4.83%	-14.42%	-37.87%	-26.20%	-15.81%
615 laser	1	0.00%	10.64%	7.78%	2.65%	0.00%	-9.59%	-7.24%	-2.53%
	100	-0.01%	11.44%	8.40%	2.80%	-0.01%	-17.23%	-12.89%	-4.99%
	200	0.00%	11.18%	8.22%	2.73%	0.00%	-19.92%	-14.80%	-6.01%
	300	0.00%	10.53%	7.74%	2.59%	0.00%	-20.44%	-15.12%	-6.27%
	400	0.02%	10.44%	7.67%	2.58%	0.01%	-19.14%	-14.11%	-5.86%
614 arc	1	0.00%	-6.31%	-3.94%	-2.47%	-10.80%	-40.30%	-24.01%	-21.43%
	100	0.00%	-7.88%	-4.84%	-3.20%	-11.45%	-37.26%	-23.29%	-18.21%
	200	0.00%	-9.25%	-5.59%	-3.87%	-12.06%	-34.62%	-22.61%	-15.52%
	300	0.00%	-10.45%	-6.23%	-4.50%	-12.63%	-32.24%	-21.95%	-13.18%
	400	0.00%	-11.53%	-6.78%	-5.09%	-13.18%	-30.03%	-21.29%	-11.10%
615 arc	1	0.00%	11.94%	8.69%	2.99%	0.00%	-10.59%	-8.02%	-2.80%
	100	0.00%	10.55%	7.73%	2.61%	0.00%	-19.89%	-14.78%	-5.99%
	200	0.01%	9.78%	7.16%	2.44%	0.01%	-14.64%	-10.79%	-4.32%
	300	-17.79%	-3.53%	-7.39%	4.17%	-17.96%	-20.25%	-19.64%	-0.76%
	400	-32.64%	-15.60%	-20.33%	5.94%	-33.19%	-28.67%	-29.91%	1.77%
	Average	2.52%	9.36%	7.07%	3.23%	8.65%	29.95%	19.98%	13.37%

Table F.4: Bar model to capture far field stress according to Turlier et al., 2014